Multi-wavelength analysis to constrain the role of AGN in galaxy evolution

Miranda E. Jarvis

München 2020

Multi-wavelength analysis to constrain the role of AGN in galaxy evolution

Miranda E. Jarvis

Dissertation
der Fakultät für Physik
der Ludwig-Maximilians-Universität
München

vorgelegt von
Miranda E. Jarvis
aus Ontario, Canada

München, den July 23 2020

Erstgutachter: Prof. Dr. Eiichiro Komatsu

Zweitgutachter: Prof. Dr. Paola Caselli

Tag der mündlichen Prüfung: September 23 2020

This thesis has been carried out at the European Southern Observatory under the supervision of Dr. Vincenzo Mainieri and Dr. Chris Harrison

Image credit: ESO/M. Kornmesser

Contents

List of Figures

List of Tables

Zusammenfassung

Es ist weithin anerkannt, dass die Entstehung von Sternen in Galaxien auf eine gewisse Weise reguliert sein muss, um die beobachtete Demografie der Galaxien zu erreichen. Insbesondere in massereichen Galaxien sind die supermassereichen schwarzen Löcher, die sich bekanntermaßen in deren Zentren befinden, die wahrscheinlichste Quelle dieser Regulierung. Das Wachstum dieser schwarzen Löcher durch die Akkretion von Gas setzt beträchtliche Mengen von Energie in Form von Strahlung und/oder bipolaren Jets geladener Teilchen frei. Während dieser Wachstumsphase werden sie als „aktive Galaxienkerne“ (*active galactic nuclei*, AGN) bezeichnet. Diese Energie hat das Potential, die Sternentstehung in den Wirtsgalaxien mittels der Entfernung von Gas durch Ausflüsse, der Unterbindung der Akkretion neuen Gases durch die Galaxie und/oder der Beeinflussung der Gaseigenschaften, die es außerstande setzen, weitere Sterne zu bilden (z. B. durch Erhitzung/Turbulenz), zu regulieren. Dies wird kollektiv als AGN-Rückkopplung (*AGN feedback*) bezeichnet. Etwa 10 Prozent der AGN weisen eine extreme Leuchtkraft im Radiobereich aufgrund von starken Jets auf, welche in der Lage sind, die Gasakkretion der Galaxie zu verhindern. Für die restlichen ∼90 Prozent der AGN-Population, die sogenannten „radioleisen“ AGN, sind die involvierten physikalischen Prozesse hingegen weniger klar. Diese Dissertation befasst sich mit einer Stichprobe, die für die Mehrheit der AGN repräsentativ ist, und setzt Beobachtungen mehrerer Wellenlängen ein, um einige der offenen Fragen darüber aufzulösen, wie „radioleise“ AGN Energie in ihre Wirtsgalaxien übertragen und wie sie das mehrphasige Gas in der Umgebung und, folglich, die Entwicklung ihrer Wirtsgalaxien beeinflussen.

Im ersten Teil dieser Dissertation untersuche ich zehn lokale ($z < 0.2$), „radioleise“ AGN mit hoher Leuchtkraft ($L_{\mathrm{AGN}} \gtrsim 10^{45}\ \mathrm{erg\,s^{-1}}$), die aufgrund ihrer starken ionisierten Ausflüsse ausgewählt wurden, wobei Radio-Beobachtungen (mit bis zu 20-mal besseren räumlichen Auflösungen als bestehende Datensätze)

und optische Integralfeldspektroskopie kombiniert werden. Ich habe ~kpc Jet-ähnliche Radioemissionen in 70–80 Prozent der Stichprobe festgestellt und Signaturen enthüllt, die darauf hindeuten, dass diese Jets ionisierte Gasausflüsse in ihren Wirtsgalaxien antreiben. Dies hinterfragt die Erwartung, dass die Rückkopplung in diesen Systemen durch Strahlungsdruck dominiert sein sollte, und etabliert die Tatsache, dass Jets sogar in diesem „radioleisen“ Regime eine wichtige Rolle in der Entwicklung von Galaxien spielen. Daraufhin habe ich Beobachtungen der Gesamtemission von Kohlenstoffmonoxid in neun solcher Systeme verwendet um darzulegen, dass diese Ausflüsse und Jets keinen unmittelbaren, globalen Einfluss auf das Gesamtreservoir molekularen, in die Sternentstehung involvierten Gases in ihren Wirtsgalaxien haben. Um genau zu sein habe Ich ermittelt, dass sich mindestens sieben der beobachteten AGN in gasreichen Galaxien mit einem hohen Niveau von Sternentstehung befinden. Zum Abschluss präsentiere ich die ersten Ergebnisse des vollständigen *Quasar Feedback Survey*-Projekts, wobei die untersuchte Stichprobe auf 42 Ziele ausgeweitet und die Prä-Selektion nach bekannten Ausflüssen aufgehoben wurden. Anhand dieser ~4-mal größeren, erwartungstreuen Stichprobe habe ich gezeigt, dass die die Radio-Jet-ähnlichen Merkmale in der Mehrheit (66 Prozent) der Stichprobe weiterhin vorhanden sind und eine Korrelation zwischen Radiogröße und den Eigenschaften der ionisierten Gasausflüsse festgestellt, was auf Jet–Gas-Wechselwirkungen hindeutet. Diese Arbeit hat eine Verbindung zwischen Ausflüssen und Radioemissionen bestätigt und gezeigt, dass Jets sogar in „radioleisen“ AGN ein wichtiger Antriebsmechanismus von Ausflüssen sind. Ich habe außerdem herausgefunden, dass sogar in Systemen mit Ausflüssen und Jets kein *unmittelbarer*, *nennenswerter* Einfluss auf den globalen molekularen Gasgehalt vorliegt. Diese Ergebnisse werden die Aktualisierung von Simulationen von Rückkopplung erforderlich machen und und stellen einen maßgeblichen Schritt im Streben nach der Bildung eines vollständigen Verständnisses der Entwicklung von Galaxien dar.

Abstract

It is widely accepted that the formation of stars in galaxies must somehow be regulated to achieve the observed galaxy demographics. In massive galaxies in particular, the supermassive black holes that are known to reside at their centres are the most likely source of this regulation. The growth of these black holes through the accretion of gas releases considerable amounts of energy in the form of radiation and / or bipolar jets of charged particles. During these growth phases they are referred to as 'active galactic nuclei' (AGN). This energy has the potential to regulate star formation in the host galaxies, by removing gas through outflows, halting the accretion of new gas onto the galaxy, and / or rendering the gas incapable of forming stars (e.g. through heating / turbulence). This is collectively referred to as 'AGN feedback'. Around 10 percent of AGN have extreme radio luminosities due to powerful jets which are capable of preventing gas accretion onto the galaxy. However, for the remaining ~90 percent of the AGN population, the so called 'radio-quiet' AGN, the physical processes at play are less clear. This thesis targets a sample representative of the majority of AGN, and uses multi-wavelength observations to resolve some of the outstanding questions about how 'radio-quiet' AGN transfer energy into their host galaxies, impact the surrounding multi-phase gas and, consequently, impact the evolution of their host galaxies.

In the first part of this thesis I study ten local ($z < 0.2$), high luminosity ($L_{AGN} \gtrsim 10^{45}$ erg s^{-1}), 'radio-quiet' AGN selected to have powerful ionised gas outflows, combining radio observations (with spatial resolutions up to 20 times better than the pre-existing data), and optical integral field spectroscopy. Jet-like radio emission on ~kpc scales was discovered in 70–80 percent of the sample, and it was revealed that these jets are driving ionised gas outflows in their host galaxies. This challenges the expectation that photon pressure should dominate feedback in these systems, and establishes that jets are playing an important

role in the evolution of galaxies even in this 'radio-quiet' regime. I then used observations of the total carbon monoxide emission in nine of the sources studied in the radio to demonstrate that the outflows and jets do not have an immediate, global impact on the total reservoir of molecular, star-forming gas in their host galaxies. Specifically, at least seven of the AGN observed reside in gas-rich, highly star-forming galaxies. Finally, I present the first results on the full Quasar Feedback Survey, expanding the sample studied to 42 targets and removing the pre-selection for known outflows. In this ~four times larger, unbiased sample I showed that radio jet like features are still present in the majority (66 percent) of the sample and found a correlation between radio size and the ionised gas outflow properties, indicative of jet-gas interactions. This work has confirmed a connection between outflows and radio emission, and determined that jets are an important mechanism for driving outflows even in 'radio-quiet' AGN. I also discovered that even in systems with outflows and jets there is no *immediate*, *appreciable* impact on the global molecular gas content. These results will require simulations of feedback to be updated, and represent a significant step forward in the quest to form a complete understanding of how galaxies evolve.

Chapter 1

Introduction

The night sky is full of stars, which are all part of our home galaxy, the Milky Way. Over the course of the last century, astronomers have discovered that the Milky Way is just one among hundreds of billions of galaxies in the observable universe (Hubble, 1926; Gott et al., 2005). One of the greatest undertakings in astronomy is understanding the processes that determine how these distant collections of stars, gas, dust and dark matter are formed, interact and evolve. These discoveries, in turn, provide insight into our own Milky Way and its place in the universe.

Over the last few decades it has been established that at the heart of all massive galaxies is a supermassive massive black hole. Although these black holes are orders of magnitude smaller in both size and mass than their host galaxies, the evolution of the two seems to be closely linked, with the black hole likely controlling the eventual fate of the entire galaxy (e.g. Kormendy & Ho, 2013).

When provided with sufficient amounts of gas as fuel for growth, these supermassive black holes can reach luminosities trillions of times larger than that of our Sun, outshining entire galaxies (Schmidt, 1963; Wu et al., 2015). The energy released by these so-called active galactic nuclei (AGN) is in principle large enough to remove all of the gas from their host galaxies and completely halt the formation of new stars (Silk & Rees, 1998). However, the dominant form in which this energy is released (i.e. through photons and / or jets of charged particles), through what mechanisms it can couple with the different gas phases in the galaxy and the impact of this interaction on the fate of the galaxy are topics of ongoing debate.

In this thesis I present a multi-wavelength study of local, highly energetic

AGN and their host galaxies, and provide answers to some of these questions. I use imaging and spectroscopy across the optical, sub-mm and radio wavebands to create a detailed picture of the impact that these AGN have on their host galaxies and the mechanisms through which this is achieved. The remainder of this Chapter provides background information explaining the main concepts, terms and techniques used throughout this thesis.

1.1 Galaxies

Galaxies exist in a wide variety of masses, radii, morphologies and colours. One of the main challenges of extragalactic astronomy is attributing physical meaning to these observable quantities and building a consistent model connecting the different types of galaxies. This is achieved through a combination of imaging, spectroscopy and simulations, focusing both on large populations, and detailed studies of individual galaxies.

One of the key features of a galaxy is the rate at which it forms stars (the star formation rate – SFR). This can be measured in multiple ways, with the two most relevant for this thesis being the emission in the infrared (*IR*) and radio bands (see review in Kennicutt & Evans, 2012). A significant fraction (~50 percent) of the optical and ultraviolet (*UV*) light from young stars is absorbed by interstellar dust and re-emitted in the *IR*. As such, the infrared luminosity of a galaxy is a good tracer of its star formation rate (e.g. Sauvage & Thuan, 1992; Kennicutt et al., 2009; Hao et al., 2011). In the radio, supernovae (i.e. the explosive deaths of massive stars) accelerate charged particles, resulting in synchrotron emission which dominates the low frequency (~1.4 GHz) radio emission of star-forming galaxies. Since the rate of supernovae is tied directly to the recent star formation history of the galaxy, this makes the 1.4 GHz radio luminosity an effective star formation rate tracer (Helou et al., 1985; Condon, 1992).

One of the key features used to characterise and classify galaxies is the amount of star formation they have compared to their stellar mass (see Fig. 1.1). This is often quantified either by the star formation rate of the galaxy or equivalently, by the specific star formation rate (sSFR – defined as SFR/$M_\star$), as a function of their stellar mass ($M_\star$). In these planes galaxies that are actively forming large numbers of stars (star-forming galaxies) are clearly separated from those which

are not (passive galaxies). Star-forming galaxies form the so-called 'star-forming main sequence', a tight ($\sigma \approx 0.3$ dex) log linear relation between star formation rate and stellar mass (see e.g. Brinchmann et al., 2004; Daddi et al., 2007; Elbaz et al., 2007; Noeske et al., 2007; Salim et al., 2007; Wyder et al., 2007; Renzini & Peng, 2015). The most extreme star-forming galaxies are referred to as starbursts and are commonly defined based on their distance above the star-forming main sequence. Specifically, I define starbursts in this thesis as galaxies with specific star formation rates four times higher than the main sequence value for their stellar mass following e.g. Elbaz et al. (2011) and Rodighiero et al. (2011). Finally, between the density peaks in the star formation rate versus stellar mass plane occupied by star-forming and passive galaxies, lies a low density region often referred to as the green valley. Green valley galaxies are typically interpreted as being in the process of 'quenching', where their global star formation is being halted by some internal or external process. One possible mechanism leading to this quenching is feedback from AGN.

1.2 Active Galactic Nuclei

At the centre of all massive galaxies, including our own Milky Way, lies a supermassive black hole (SMBH; $M \gtrsim 10^5 M_\odot$; see e.g. Genzel et al., 1997; Kormendy & Ho, 2013; Gravity Collaboration et al., 2018). Like all black holes these are infinitely dense objects from whose gravitational pull even light is unable to escape.

The primary growth mechanism for these SMBHs is by the accretion of the surrounding gas (Soltan, 1982; Marconi et al., 2004). Through this accretion process, gravitational potential energy is released as radiation across the electromagnetic spectrum, with the bolometric[1] accretion luminosity given by: $L_{acc} = \eta \dot{M} c^2$, where η is the efficiency with which mass is converted to energy (typically assumed to be ~0.1; Davis & Laor, 2011), $\dot{M}$ is the accretion rate of the SMBH and c is the speed of light. Thus a moderate accretion rate of 10^{-3} $M_\odot$ yr^{-1} gives a luminosity of approximately 10^9 $L_\odot$, comparable to the luminosities from entire galaxies. These accreting black holes are known as AGN. In this section I discuss the basic structure of AGN.

[1] i.e. total across all wavelengths

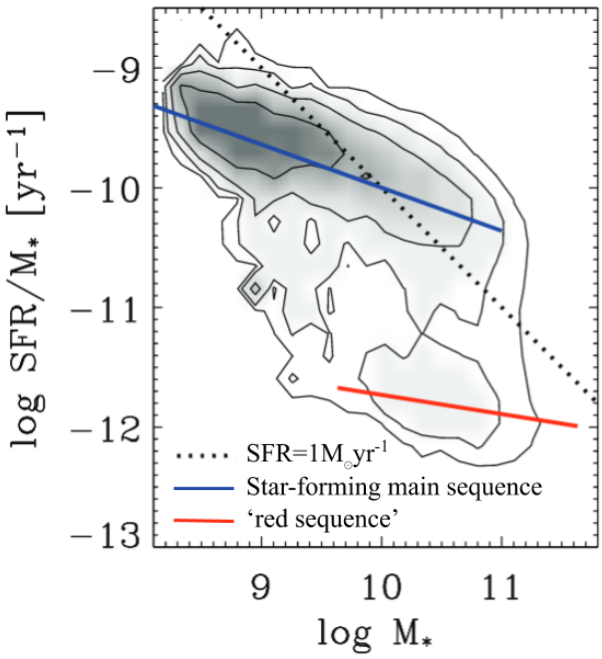

Figure 1.1: The specific star formation rate ($SFR/M_\star$) versus stellar mass ($M_\star$) for the Sloan Digital Sky Survey (SDSS) spectroscopic sample of galaxies with contours enclosing 38, 68, 87, and 95 percent of the distribution, from Schiminovich et al. (2007). The blue line marks the star-forming main sequence and the red line at lower specific star formation rates marks an approximate 'red sequence' of passive galaxies. The black dotted line marks SFR=1 $M_\odot$ yr^{-1}. Galaxies in the lower density region above the main sequence are starbursts, and the low density region between the main sequence and the passive galaxies is sometimes referred to as the green valley.

The defining feature of the AGN is of course, the central supermassive black hole; however, several other key components make up the larger structure generally encompassed in the discussion of AGN. The main features (see Fig. 1.2), working roughly from the SMBH itself to larger scales are the:

Accretion disc: A thin, rotating disc extending to ~1 pc from the SMBH that funnels material onto the SMBH and emits thermally due to viscosity (Shakura & Sunyaev, 1973).

X-ray corona: A region of hot (T $\approx 10^9$ K) electrons directly around the black hole that produces X-ray emission via inverse Compton scattering (Haardt & Maraschi, 1991). This corona may also contribute to the radio emission from AGN (see Section 1.3.1; Laor & Behar, 2008).

Broad line region (BLR): The BLR is composed of clouds of gas gravitationally bound to the SMBH. This results in high gas velocities producing very broad emission lines (full width at half maximum – FWHM – of approximately 10^3–10^4 km s^{-1}). The observation of these broad emission lines is one of the defining features of type 1 AGN (see Section 1.4). This region typically extends 0.1–1 pc from the SMBH (Peterson et al., 2004).

Torus: A large optically thick and potentially clumpy torus of dust and gas that surrounds the broad line region (between ~0.1 and 10 pc from the central SMBH; Burtscher et al. 2013). The hot dust in the torus reprocesses the higher energy radiation of the AGN into thermal emission, which is the main contributor to the infrared emission from the AGN and can be used to measure the AGN bolometric luminosity (see Section 1.3).

Narrow line region (NLR): A region of low electron density (10^6 cm^{-3}), starting from ~100–300 pc from the black hole (Netzer, 1990). The NLR is often defined as all gas that is ionized by the AGN and can extend out to kpc scales, where it is sometimes referred to as the extended narrow line region (Tadhunter et al., 1989; Greene et al., 2011; Sun et al., 2017). Permitted and forbidden, narrow (approximately 100<FWHM<1000 km s^{-1}) emission lines originate from this region. Of greatest importance for this work is the [O III]λ5007 μm line, which as a forbidden line, can not exist in higher density regions (such as the BLR). Observations of the NLR can be used to

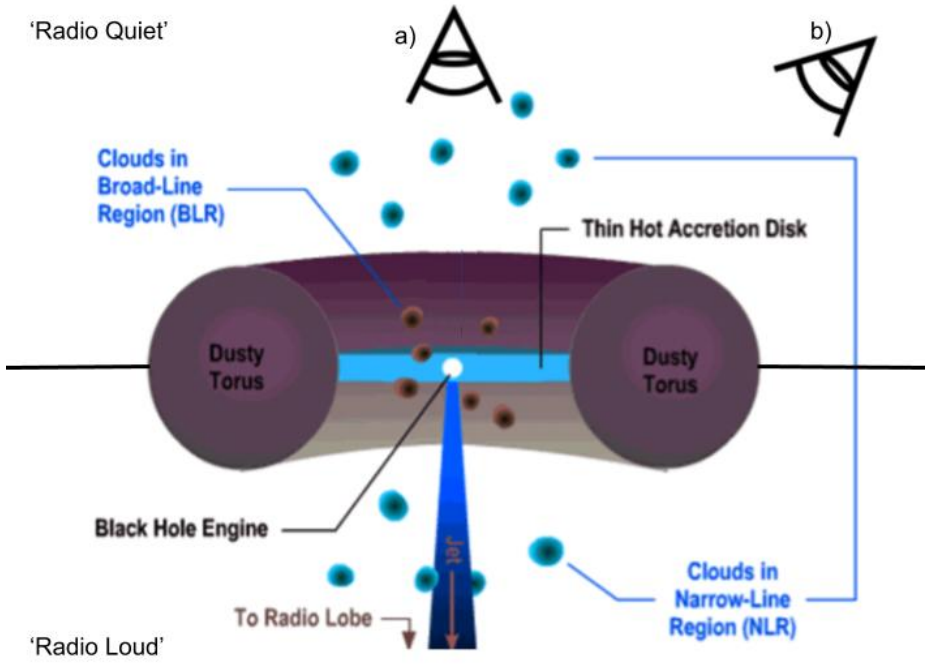

Figure 1.2: The basic structure of an AGN adapted from Gillessen et al. (2010). The individual components shown are described in Section 1.2. The top half of the figure represents a traditionally 'radio-quiet' or non-jetted AGN and the bottom half shows a 'radio-loud' AGN with a powerful, relativistic jet. Finally, according to the AGN unification models, the AGN is either a type 1 or type 2 AGN depending on the angle from which it is viewed (e.g. Urry & Padovani, 1995). Type 1 are viewed from a), causing the BLR to be visible and type 2 AGN are viewed from b), where the BLR is obscured by the dusty torus.

identify outflows of gas powered by the AGN (see Section 1.5.1) and can be used to estimate the bolometric luminosity of the AGN (see Section 1.3).

Jet: Approximately 10 percent of AGN produce jets of highly collimated, relativistic, charged particles which can extend out to Mpc scales, and are powerful radio emitters ($L_{1.4GHz} \gtrsim 10^{25}$ W Hz^{-1}; see e.g. Zakamska et al., 2004; Blandford et al., 2019). One of the main topics of this thesis is the possibility of weaker jets existing in the other 90 percent of AGN (see Section 1.3.1 and Chapters 2 and 4).

All of these components contribute to the overall energy released by the AGN. This is discussed in more detail in the following section.

1.3 The release of energy by AGN

AGN release massive amounts of energy, both through radiation across the electromagnetic spectrum and mechanical energy (from jets), which can then interact with the gas and dust within the host galaxy (the interstellar medium – ISM; see Section 1.5).

Fig. 1.3 shows a schematic spectral energy distribution (SED) from the radio to gamma rays, for a type 1 AGN compared to that of a starburst galaxy. By fitting models to observed SEDs, important properties of the AGN and the underlying host galaxy can be determined (see e.g. Walcher et al., 2011; Calistro Rivera et al., 2016; Circosta et al., 2018). In this thesis in particular, I use SED fitting to determine the bolometric luminosity of the AGN and the stellar mass and star formation rate of the host galaxy (see Chapters 2 and 3).

As can be seen from Fig. 1.3, one of the wavelength ranges dominated by emission from the AGN (from the dusty torus in particular), is the mid-infrared (*MIR*; ∼7.5–14.5 μm). In fact, one method used to identify AGN (although not used in this thesis), is based off of their *IR* colours (e.g. Stern et al. 2005, see also Padovani et al. 2017 for a general review of the different ways AGN are detected). The 6 μm flux in particular is often (including in this thesis) used as a proxy for the AGN bolometric luminosity using a bolometric conversion factor of 8× (Richards et al., 2006; Suh et al., 2019).

The radiation emitted from the AGN is powered directly by the accretion of matter onto the central black hole (Soltan, 1982). The resultant radiation pressure couples with the surrounding gas, limiting the accretion onto the SMBH (the so-called 'Eddington limit' – L_{edd}; Eddington 1916) and may even completely remove gas from the galaxy (see Section 1.5; Moe et al., 2009; Saez et al., 2009; Dunn et al., 2010). The majority of AGN seem to be accreting at relatively high accretion rates (Eddington ratios – $L_{AGN}/L_{edd} \gtrsim 1 \times 10^{-3}$; Hickox et al. 2009), and emit most of their energy through radiation (also referred to as 'radiatively efficient' or 'radiative mode' AGN). This thesis focuses on local ($z < 0.2$) radiatively efficient AGN, specifically quasars (see Section 1.4).

Radiatively efficient AGN also have powerful emission lines, originating from the broad and narrow line regions (see Section 1.2). This allows their optical spectra to be easily distinguished from normal star-forming galaxies and is one of the primary ways in which AGN are identified (including in this thesis; see Section

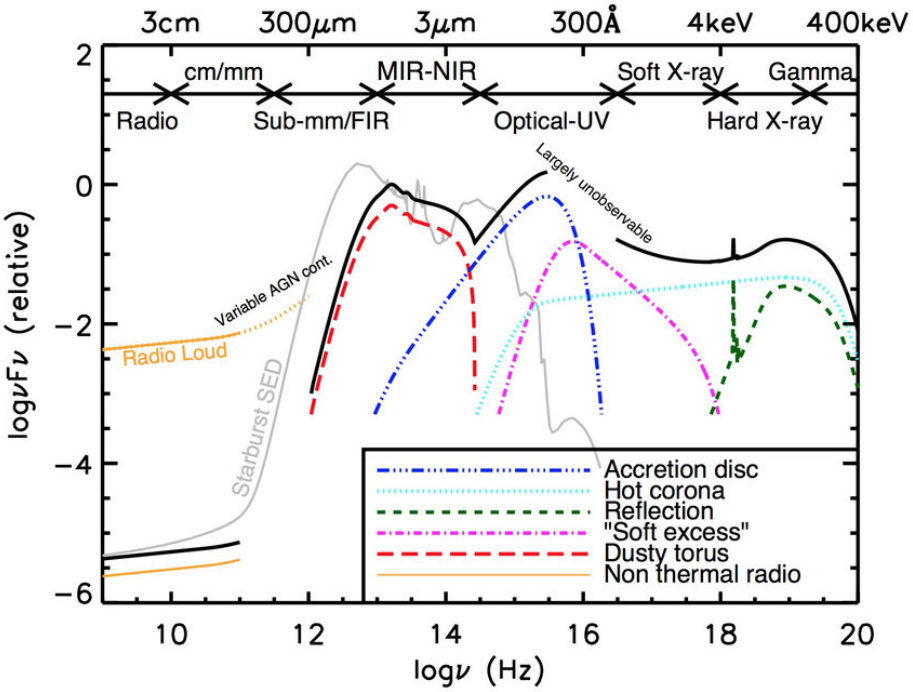

Figure 1.3: A schematic spectral energy distribution for a type 1 AGN (black curve) compared to that of a starburst galaxy (grey line) from Harrison (2014). The various components that make up the emission from an AGN are shown as different coloured curves. The AGN is the dominant source of emission compared to the host galaxy at almost all wavelengths. Type 2 AGN, due to the obscuration of the central accretion disc, are significantly dimmer in the optical–*UV*, facilitating study of the underlying host galaxy properties.

1.6). Specifically, AGN can be distinguished from star-forming galaxies based on the identification of broad lines (for type 1 AGN; see Section 1.4) or based on the ratios of various emission lines (see Section 1.6). The [O III] luminosity in particular is sometimes used as a proxy for the AGN bolometric luminosity with a bolometric correction factor of 3500× (Heckman et al., 2004). However, this is known to be an unreliable tracer of the AGN luminosity, and can over predict it by $\gtrsim$1 dex. This is particularly true in [O III] luminous ($L_{[OIII]} \gtrsim 10^{42}$ ergs s^{-1}), type 2 AGN such as are primarily studied in this thesis (Schirmer et al., 2013; Hainline et al., 2013; Harrison et al., 2014).

Approximately 10 percent of AGN, however, emit the majority of their energy mechanically through their radio jets, which also dominate their SED. These so-called radiatively inefficient AGN have typically lower Eddington ratios than radiatively efficient AGN ($L_{AGN}/L_{edd} \lesssim 1 \times 10^{-3}$; Hickox et al. 2009) and are also referred to as 'radio mode' or 'jet mode' AGN. The high radio luminosities from the jets results in these AGN additionally being classified as 'radio-loud' (see section 1.4). The radio emission from AGN, and radio jets in particular, are one of the main topics of this thesis and are discussed in more detail below.

1.3.1 Radio emission from AGN

The radio emission from an AGN is primarily non-thermal synchrotron radiation. The radio luminosity of an AGN relative to other bands varies widely which resulted in the distinction between 'radio-loud' and 'radio-quiet' AGN (see also Section 1.4). Specifically, in 'radio-loud' AGN, powerful jets cause them to emit large amounts of radio emission; these are also typically radiatively inefficient AGN. For 'radio-quiet' AGN (which are also typically radiatively efficient), the origin of the radio emission is less clear (discussed further below and in Chapters 2 and 4).

The spectra of continuum radio sources can be characterised by a quantity called the spectral index (α). Throughout this thesis I define the spectral index as $S_\nu \propto \nu^\alpha$, where S_ν is the flux at a given frequency (ν). The spectral index is used in this Section and the rest of the thesis to describe the radio emission from AGN.

Prototypical Jets

AGN jets are collimated streams of charged particles launched at relativistic speeds in both directions from the SMBH / accretion disc. Most of our knowledge of AGN jets comes from the study of 'radio-loud' AGN, even though lower power jets can exist in 'radio-quiet' AGN (discussed in the next section).

The exact physical mechanism(s) responsible for the launching of AGN jets is currently debated. The key ingredient seems to be the generation of a magnetic field by the rotation of the highly conducting accretion disc, with the energy to launch the jets either coming from the accretion energy of the disc or the rotational energy of the SMBH itself (see e.g. Romero et al., 2017, and references therein). Additionally, the composition of the jets (see e.g. Sol et al., 1989) and the mechanism(s) by which they are collimated (see e.g. Marscher, 2006) are unclear.

The spiralling of electrons around the magnetic field lines in the jet produces synchrotron radiation, which can be observed from the radio to the optical wavebands with a typical spectral index of $\alpha \approx -0.7$. Inverse Compton scattering (where the relativistic electrons in the jet scatter low energy photons to high energies) causes radio jets to be bright gamma ray emitters (see e.g. Maraschi et al., 1992; Blandford et al., 2019). The high speeds of the particles in AGN jets can result in relativistic / Doppler boosting, where the side of the jet pointed towards the observer appears brighter than the receding side. This causes many AGN jets to be observed as one sided, when the Doppler boosted approaching side is above the detection limit of the observations and the dimmer receding side is not (Kellermann et al., 2007).

AGN jets, and the various large scale structures that make them up (see Fig. 1.4), are important to this thesis. The term 'jet' in particular can be used to describe the tightly collimated structure specifically or the entire large scale structure fuelled by this jet. Additional components are:

Core: A point source at the base of the jet (i.e. the SMBH). The core is characterised by synchrotron self-absorbed radiation resulting in a 'flat' radio spectrum ($\alpha \approx 0$).

Lobe: As the jet passes through the ISM, or on larger scales the intergalactic medium (IGM), the material at its head can be slowed, forming a shock,

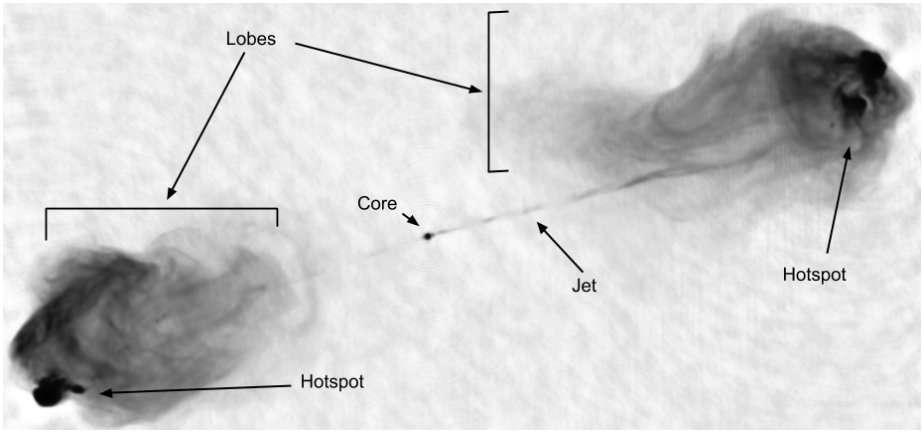

Figure 1.4: A radio image of the galaxy Cygnus A, with the various components of the 'jet' labelled (see Section 1.3.1). Image credit: NRAO/AU.

which causes the jet to become disordered and form a large, roughly ellipsoidal 'lobe'. These lobes typically have steep spectra ($\alpha \lesssim -0.7$), with the steepest spectra found in lobes which are no longer powered by an active jet (so-called 'relics'; see e.g. Roettiger et al., 1994; Carilli & Barthel, 1996).

Hotspot: These are bright, compact regions within the lobes formed at the head of the shocked jet. They have typical spectral indices of $\alpha \approx -0.5$ (Carilli & Barthel, 1996).

Radio emission in 'radio-quiet' AGN

In the majority (~90 percent) of AGN the radio emission is weaker ($L_{1.4GHz} \lesssim 10^{25}$ W Hz^{-1}) and powerful ~Mpc jets are not observed (e.g. Zakamska et al., 2004). The origin of the radio emission in these 'radio-quiet' AGN is widely debated (e.g. Bonzini et al., 2013; White et al., 2017; Laor et al., 2019; Panessa et al., 2019), and is one of the main topics addressed by this thesis (see Chapters 2 and 4). Below I discuss the four main possible sources of the radio emission:

Star formation: As mentioned in Section 1.1, supernovae are radio emitters. Since 'radio-quiet' AGN often reside in star-forming galaxies (e.g. Ellison et al., 2016; Kauffmann et al., 2003b), this is a common explanation for their radio emission (e.g. Kimball et al., 2011b; Padovani et al., 2011; Condon et al., 2013). This radio emission is expected to trace the star formation in

the host galaxy, both in its morphology and intensity. In particular, radio emission in normal galaxies is typically smooth, tracing spiral arms and central starbursts; however, in dwarf irregular and merger galaxies it can be more lumpy and irregular (e.g. Condon, 1992). The radio luminosity from supernovae has been found to be tightly correlated with the infrared emission (which is also a product of massive stars; de Jong et al., 1985; Helou et al., 1985; Condon et al., 1991; Yun et al., 2001). This radio – infrared correlation is discussed in more detail below.

Coronal emission: As mentioned in Section 1.2, the hot corona around the SMBH is a source of X-rays. It has been shown that the radio emission in 'radio-quiet' AGN correlates with the X-ray luminosity (e.g. Brinkmann et al., 2000; Salvato et al., 2004; Wang et al., 2006; Panessa et al., 2015), and follows the same scaling relation as has been found for coronally active stars (Laor & Behar, 2008). This suggests that the radio emission is also originating from the corona. Radio emission from the corona is expected to be compact (∼pc scales) and optically thick, with a GHz spectral index of ∼0 (e.g. Raginski & Laor, 2016).

Shocks from winds: Radiation-driven AGN winds (discussed further in Section 1.5.1) can drive shocks in the galactic ISM, which may accelerate electrons to relativistic speeds, resulting in synchrotron emission (e.g. Jiang et al., 2010; Nims et al., 2015). This would naturally result in a relationship between the outflow properties (e.g. the width of the [O III] line) and the radio luminosity (e.g. Zakamska & Greene, 2014; Hwang et al., 2018). Due to the typical bi-conical morphology of AGN winds, the radio emission associated with them is also expected to show bi-conical structure, possibly mimicking the double lobed morphology of radio jets (e.g. Harrison et al., 2015; Alexandroff et al., 2016; Panessa et al., 2019).

Jets: Finally, 'radio-quiet' AGN may host compact, low luminosity jets. Many works have found evidence of radio jets in low optical luminosity 'radio-quiet' AGN (Seyferts and LINERS – see Section 1.4; e.g. Kukula et al., 1995; Ulvestad et al., 1981; Ho & Ulvestad, 2001; Schmitt et al., 2001; Gallimore et al., 2006; Baldi et al., 2018; Pierce et al., 2020). However, relatively few works have looked for jets in 'radio-quiet' quasars (Kellermann et al.,

1994; Kukula et al., 1998; Blundell & Rawlings, 2001; Leipski et al., 2006; Harrison et al., 2015, are among the few exceptions).

The origin of the radio emission in 'radio-quiet' AGN is further complicated by the fact that these mechanisms are likely to coexist. For example Inoue & Doi (2018) finds coronal activity superimposed on jet-like radio emission and Giroletti et al. (2017) finds evidence of an accretion disc outflow coexisting with a jet.

One technique that is often use to separate sources where the radio emission is dominated by the AGN from those where star formation dominates, is by using the so-called: 'radio excess'. This is done by comparing the observed radio emission to that expected from star formation (see Section 1.1), where excess radio emission must originate from the AGN. More specifically, the infrared emission is typically used as the star formation rate tracer for this analysis, with the radio emission predicted from the star formation calculated using the 'radio-*IR* correlation' (e.g. Helou et al., 1985; Bell, 2003). The main complication of this technique is that the infrared emission of the AGN (see Fig. 1.3) dominates the total *MIR* emission, and can contribute significantly to the far-infrared emission as well (up to 50 percent at 70μm; Shi et al., 2007; Shimizu et al., 2017). This can cause AGN to fall onto (or below) the radio-*IR* correlation for star-forming galaxies, even if their radio emission is dominated by the AGN, because the *IR* emission is contaminated by the AGN (Morić et al., 2010; Zakamska et al., 2016). As such, using an infrared measurement that has accounted for AGN contamination (e.g. through SED fitting) is the best way to identify all sources with an AGN contribution to their radio emission. Radio excess is used in Chapters 2 and 4 to identify the source of the radio emission.

Radio interferometry

The study of radio emission and jets in particular relies almost entirely on the use of radio interferometry: where the signals from multiple radio telescopes (or antennas; often referred to as an array) are combined. This technique can result in observations with much better spatial resolution than with a single telescope. Specifically, the angular resolution (Θ; in radians) is determined by: $1.22\ \lambda/D$, where λ is the wavelength of the light and D is either the diameter of the telescope, or in the case of interferometry, the distance between the most distant telescopes

in the array. The most extreme instances of this are called 'very-long-baseline interferometry' (VLBI), where the radio antennas are separated by thousands of kilometres, on different continents or even in space (e.g. the European VLBI Network, the Event Horizon Telescope and RadioAstron). The main limitations of interferometry are: 1) the collecting area is often small compared to using single larger telescopes, making it hard to observe dim targets; 2) the largest structures that can be observed are limited by the minimum distance between antennas (D_{min}) such that flux emitted by structures larger than λ/D_{min} are resolved out; and 3) the quality of the image is limited by how well the telescopes can cover the plane of the sky (i.e. the *uv* plane) with better images achieved from having more telescopes and observing for longer periods. By combining high spatial resolution and high sensitivity images, the radio structures of AGN can be studied in great detail. Specifically, this thesis uses ~0.25 arcsec resolution images from the NSF's Karl G. Jansky Very Large Array (VLA) to identify jet-like radio emission in 'radio-quiet' AGN (see Chapters 2 and 4).

1.4 AGN types

As can be seen from the discussion so far in this thesis, there are various overlapping terms used to describe different types of AGN. Furthermore, the meanings of these terms are often inconsistently defined or change with time. In this section, I describe the main classes of AGN pertinent to this thesis, as they are defined throughout the work. A more detailed description of AGN types can be found in Padovani et al. (2017).

Type 1 versus type 2: This classification of AGN is generally understood to depend purely upon the angle at which the AGN is viewed, and hence is not a fundamental property of the AGN itself (Fig. 1.2; see e.g. Urry & Padovani, 1995). Specifically, in type 1 AGN, the very central regions of the AGN are visible (e.g. the accretion disc and BLR). Observationally, this results in broad emission lines in their optical spectra and a bright, point-like optical continuum (see Section 1.3). In type 2 AGN, the central regions are obscured by the dusty torus, so that the NLR is visible but not the BLR, resulting in only narrow emission lines being observable and significantly less optical continuum emission.

Quasar: In this thesis, the term 'quasar' is used to describe optically bright AGN, specifically those with bolometric luminosities larger than 10^{45} erg s^{-1} (Reyes et al., 2008), where the AGN bolometric luminosity is typically calculated from the [O III] or mid-infrared emission (see Section 1.3). Historically, however, 'quasars' (also known as 'quasi-stellar objects' or QSOs) have been exclusively type 1 AGN (optically bright point sources) distinguished from the lower luminosity 'Seyferts' based on whether or not the host galaxy is observable (Schmidt, 1963). I note additionally that lower luminosity AGN can be split into the Seyfert and LINER types based on the ratios of their emission lines (Baldwin et al., 1981, see Section 1.6), however, these distinctions are not significant for this thesis.

Radio-quiet versus radio-loud: These classes are gradually falling out of favour, as the physical differences between them becomes less clear (Cirasuolo et al., 2003; Padovani, 2017; Padovani et al., 2017; Gürkan et al., 2018). Traditionally, these classes have been defined by comparing the emission of the AGN in the radio to that in other wavelengths, such as the optical or [O III] luminosity (see e.g. Kellermann et al., 1989; Xu et al., 1999). 'Radio-loud' AGN (also sometimes called radio-AGN) are characterised by powerful radio jets, and typically have low accretion rates and weak emission lines (radiatively inefficient; see Section 1.3). Since the main physical feature separating 'radio-loud' and 'radio-quiet' AGN is the presence of a radio jet, it has been suggested that a more physically meaningful classification would be separating jetted from non-jetted AGN (Padovani et al., 2017), however, as I explore in Chapters 2 and 4 of this thesis, it is non-trivial to identify jets. Furthermore, 'radio-loud' AGN have often been selected from radio surveys whereas 'radio-quiet' AGN are generally identified in other bands (e.g. optical, X-ray, infrared). This results in different selection effects complicating comparisons of the two populations, and a general disagreement as to whether or not these represent two distinct groups or one continuous population (e.g. Cirasuolo et al., 2003; Gürkan et al., 2018). I use the term 'radio-quiet' throughout this thesis, following the definition of Xu et al. (1999), to describe my sample purely to highlight the fact that the *expectation* was that they should be radiatively dominated, with radio jets playing at most a secondary role (which may not, in reality, be the case; see

Chapters 5).

In the radio band in particular there are several other sub-classes which play minor roles in this thesis. Classical radio-loud AGN are divided into two categories: Fanaroff-Riley class I and II (FRI, FRII; Fanaroff & Riley, 1974). Although primarily a morphological classification, FRI and FRII galaxies also show systematically different radio luminosity, optical emission line and SMBH accretion properties (see e.g. Tadhunter, 2016). Compact Steep Spectrum (CSS) and Gigahertz-peaked spectrum (GPS) sources are radio-loud AGN characterised by their small sizes ($\lesssim$20 kpc), high radio luminosities ($L_{1.4GHz}>10^{25}$ W Hz^{-1}) and convex radio spectra (O'Dea, 1998). CSS and GPS sources are generally believed to be young jets (e.g. Orienti, 2016).

1.5 AGN feedback

At the heart of the theory of AGN feedback, is that just a small fraction of the vast amounts of energy released by AGN, both through radiation and jets (see Section 1.3), coupling to the gas in the host galaxy would result in AGN having a significant influence on galaxy evolution (e.g. Silk & Rees, 1998).

The first indications that supermassive black holes may impact their host galaxies came in the form of observations of so-called SMBH–galaxy co-evolution. Initially, this was observed as scaling relations between the SMBH and the properties of the spheroidal component of the host galaxy (see review in Kormendy & Ho, 2013). Namely, the mass of the SMBH is correlated with the luminosity (which itself is correlated to the mass) of the host galaxy spheroid (e.g. Dressler, 1989; Kormendy, 1993), with a tight relationship also found between the SMBH mass and the velocity dispersion of the shperoid (e.g. Ferrarese & Merritt, 2000; Gebhardt et al., 2000). The co-evolution of black holes and their host galaxies can also be seen through the similar cosmic evolution of the star formation rate and the growth of black holes, with both peaking between $z \approx 1$–3 (see Fig. 1.5; Marconi et al., 2004; Hopkins et al., 2007; Shankar et al., 2009; Madau & Dickinson, 2014; Aird et al., 2015). This result suggests that the peak period of AGN feedback occurred at $z \approx 2$. However, these relationships do not necessarily imply a causal connection between SMBH growth (AGN) and galaxy growth.

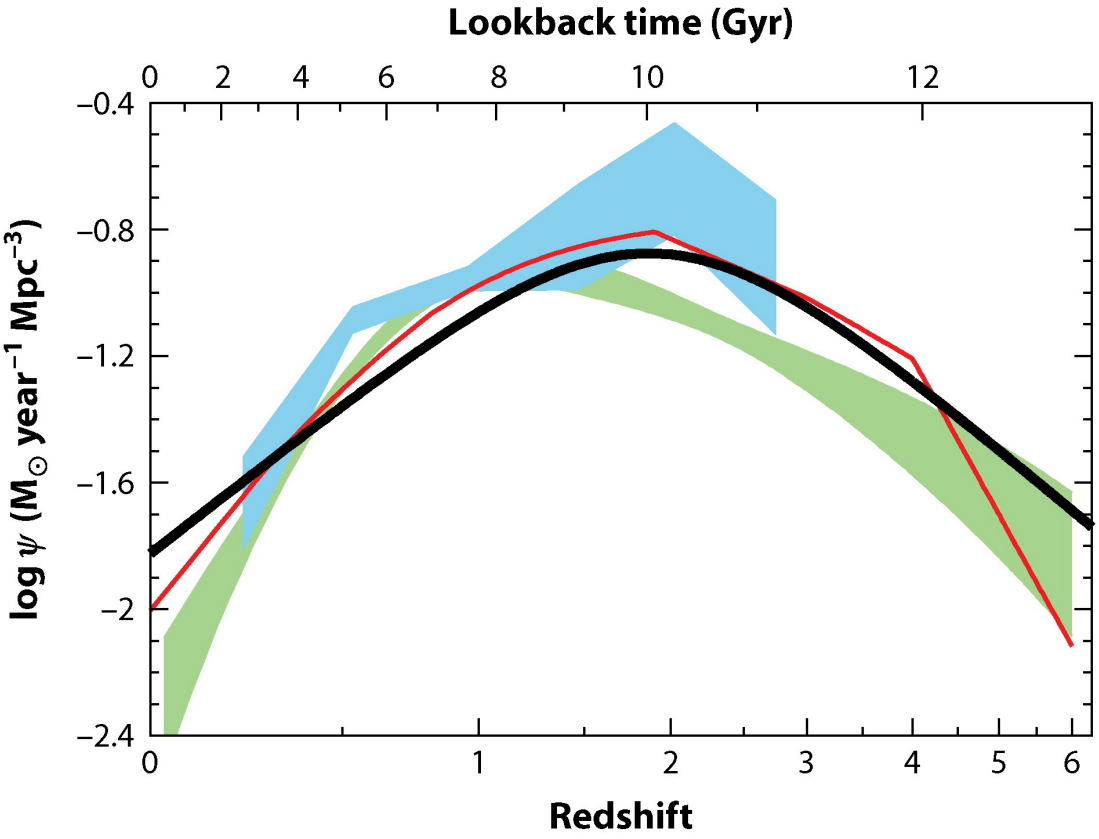

Figure 1.5: Comparison of the cosmic evolution of the star formation history (black curve) to the supermassive black hole accretion history from several methods scaled up by a factor of 3300 (other curves) from Madau & Dickinson (2014). In particular, the SMBH accretion history is shown using data from the: X-ray (red curve: Shankar et al. 2009; light green shading: Aird et al. 2010) and infrared (light blue shading: Delvecchio et al. 2014), with the shaded regions showing the $\pm 1\sigma$ uncertainty on the bolometric luminosity density.

The evidence for a causal connection between SMBH growth and galaxy evolution, in the form of 'AGN feedback', comes from direct observations of its effects (e.g. outflows) and simulations. In particular, feedback is generally accepted to occur in two distinct modes: 'quasar mode', in which the radiation from powerful radiation-dominated AGN (i.e. quasars; also typically 'radio-quiet') couples to the nearby gas. This results in high-velocity winds that propagate through the host galaxy, and ultimately results in the removal or destruction of the star-forming fuel (e.g. Faucher-Giguère & Quataert, 2012; King & Pounds, 2015; Costa et al., 2018a). Since the initial energy from the AGN comes from radiation pressure, this is also referred to as radiative feedback. Secondly, there is 'maintenance mode' or 'radio mode', in which the jets from low accretion rate, 'radio-loud' AGN regulate the cooling of gas in the IGM, slowing or stopping the accretion of gas onto the host galaxy, and hence regulating the level of star formation (Churazov et al., 2005; Alexander & Hickox, 2012; McNamara & Nulsen, 2012). This is also referred to as mechanical feedback, since it is mechanical energy from the particles in the jet which ultimately impacts the host galaxy.

Maintenance mode feedback has been well studied using cosmological simulations and observations. Early simulations were found to overproduce massive galaxies. The implementation of maintenance mode AGN feedback was needed to simulate a realistic mass distribution of galaxies (e.g. Bower et al., 2006; Croton et al., 2006; Somerville et al., 2008). Maintenance mode feedback can be observed by combining X-ray and radio observations of galaxy clusters. Cavities in the X-ray gas can be seen expanding outwards from galaxy centres, spatially coincident with radio emission from jets which are likely inflating the cavities (e.g. Churazov et al., 2000; Bîrzan et al., 2004; Forman et al., 2007).

This thesis is primarily concerned with 'quasar mode' feedback, which takes the form of powerful outflows and is discussed in more detail below.

1.5.1 Outflows

The majority (as high as 80 percent) of radiatively efficient AGN are thought to host high velocity (up to $\sim 0.1c$) winds launched close to the accretion disc ($\lesssim 1$ pc from the SMBH; Crenshaw et al., 2003; Ganguly & Brotherton, 2008; Tombesi et al., 2012). These ultra-fast outflows are typically observed through *UV* and X-ray absorption lines (see review in King & Pounds, 2015, and references

therein).

In order for these outflows to have an impact on the overall evolution of their host galaxy however, they must impact the gas on ~kpc scales. These larger scale outflows are typically observed using forbidden emission lines such as [O III], since they are produced in the NLR but not by the high density gas in the direct vicinity of the AGN. This thesis focuses on ionized gas outflows as traced through the [O III] emission line. Outflows have been additionally observed in multiple gas phases including the molecular and atomic gas (e.g. Morganti et al., 2016; Feruglio et al., 2010; Alatalo et al., 2011; Lehnert et al., 2011; Rupke & Veilleux, 2011; García-Burillo et al., 2014; Cicone et al., 2014; Morganti et al., 2015). Although the outflows in different gas phases are most often observed in different objects, making the mass distribution uncertain, there is evidence that molecular gas might represent the most massive component in the majority of AGN outflows (see Morganti, 2017; Fiore et al., 2017). Outflows in all phases are most commonly identified through line profiles showing broad, blue shifted features. In particular, velocities $\gtrsim 500\,\mathrm{km\,s^{-1}}$ are not typically achieved through stellar processes and so can be attributed to the AGN (Fabian, 2012).

Some of the earliest observations of AGN outflows came from dedicated spectroscopic observations of small samples of galaxies (e.g. Weedman, 1970; Stockton, 1976; Veron, 1981; Heckman et al., 1981). Later, large spectroscopic surveys such as the Sloan Digital Sky Survey (SDSS; York et al., 2000) provided spectra for thousands of AGN and enabled larger studies, which statistically constrained the properties of outflows (e.g. Boroson, 2005; Greene & Ho, 2005; Komossa et al., 2008; Zhang et al., 2011).

However, to properly identify and study galaxy-wide outflows requires spatially resolved spectroscopy, namely long slit or integral field spectroscopy (IFS). These observational techniques provide simultaneous spectral and spatial information in one (long slit) or two dimensions (IFS). IFS in particular provides a 2D image where each pixel is a spectrum, and allows for the creation of maps tracing the line kinematics, which can be used to measure the size and shape of [O III] outflows (Rupke & Veilleux, 2011; Liu et al., 2013; Harrison et al., 2014; Perna et al., 2015; Husemann et al., 2016; Kakkad et al., 2016; Wylezalek et al., 2017). This technique is used to study the outflows in Chapter 2 of this thesis. The spatial resolution of modern ground based IFS observations is typically limited

by blurring from the turbulent mixing in the Earth's atmosphere (i.e. astronomical seeing). Higher spatial resolution is only possible by using adoptive optics (combining deformable mirrors and wavefront sensors to correct for the atmospheric distortions; which can be used with e.g. The Multi Unit Spectroscopic Explorer – MUSE; see Chapter 5) or in the near future, by observing from space (using e.g. The Near InfraRed Spectrograph or the The Mid-Infrared Instrument on the James Webb Space Telescope).

Driving mechanisms of outflows

The typical scenario for the launching of wide angle winds by AGN is that outflows are driven from the accretion disc due to radiation pressure on dust (see review in Morganti, 2017). Particularly in radiatively powerful AGN, these winds then interact with and shock the ISM, creating an energy-conserving expanding bubble, which in turn sweeps up gas and drives an outer shock (e.g. Zubovas & King, 2012; Faucher-Giguère & Quataert, 2012). Alternatively, radiation pressure on dust may directly drive large scale outflows (Ishibashi & Fabian, 2015; Thompson et al., 2015; Bieri et al., 2017; Costa et al., 2018a,b). Molecular gas is either formed as the swept up shocked gas cools or is entertained directly by the expanding shocked wind without being destroyed (e.g. Costa et al., 2018b; Richings & Faucher-Giguère, 2018; Scannapieco, 2017). Of particular relevance to this thesis, is that the shocks caused by these radiation-driven winds can produce non-thermal synchrotron emission with radio luminosities similar to those observed in typical 'radio-quiet' AGN ($L_{1.4GHz} \lesssim 10^{24}\,W\,Hz^{-1}$; see also Section 1.3.1; Nims et al. 2015; Jiang et al. 2010).

Jets can also drive outflows in the ISM. There have been many observations of jet-driven outflows both in the warm ionized gas (e.g. Emonts et al., 2005; Morganti et al., 2007; Holt et al., 2011) and the cold neutral / molecular gas (Morganti et al., 2005, 2015; Lehnert et al., 2011; Dasyra & Combes, 2012). Simulations of jet-driven outflows suggest that as jets interact with and collide with the clumpy ISM, they form energy driven bubbles of expanding gas which drive shock fronts and outflows throughout the galaxy (i.e. on kpc scales; Wagner et al., 2012; Mukherjee et al., 2016). Such jet-gas interactions can impact the star formation in their host galaxies, and possibly disrupt the evolution of the jet itself (e.g. Mukherjee et al., 2016; Kunert-Bajraszewska & Labiano, 2010). Of

particular relevance to this thesis is the discovery that low-power and compact jets might have a larger impact on the gas within their host galaxies than their more extended or higher power counterparts (Mukherjee et al., 2016; Holt et al., 2008; Molyneux et al., 2019).

1.5.2 The radio – outflow connection

With both radio jets and radiation-driven winds capable of driving large scale gas outflows in their host galaxies, the classical divisions between feedback modes are less clear. Furthermore, since both jets and shocks from radiation-driven winds can produce radio emission, the radio emission of AGN and their outflow proprieties are indisputably entwined.

The connection between the radio and outflow properties of AGN has been studied in the most detail by Mullaney et al. (2013) (see also Husemann et al., 2013). SDSS spectroscopy was used to explore the [O III] outflow properties of 24 264 AGN at $z < 0.4$. The 1.4 GHz radio luminosity ($L_{1.4GHz}$) was found to have a stronger influence on the prevalence of powerful outflows (as traced by the FWHM of the [O III] line) than bolometric luminosity, Eddington ratio, radio-loudness or optical class (type 1 versus type 2). Specifically, stacked spectra were used to find that AGN with moderate radio luminosity ($L_{1.4GHz} > 10^{23}$ W Hz^{-1}) have the broadest [O III] line profiles. For individual spectra, AGN with $L_{1.4GHz} > 10^{23}$ W Hz^{-1} are ∼five times more likely to have powerful [O III] outflows (FWHM > 1000 km s^{-1}) than their less radio luminous counterparts (see Fig. 1.6). Similar results were found by Zakamska & Greene (2014), who attributed the correlation of ionized gas outflows and radio luminosity to the radio produced by shocks from radiation-driven outflows, and by Villar Martín et al. (2014), who claimed that the turbulent outflows in their higher radio luminosity sources are due to unresolved jets (see Section 1.5.1). Finally, Molyneux et al. (2019) found that sources with compact radio emission (within the SDSS fibre in particular) have signatures of more extreme outflows and are twice as likely to show powerful (FWHM > 1000 km s^{-1}) outflows than the sources with more extended radio luminosity, implying a direct connection between the radio emission and the outflows.

Although the outflow properties of AGN (and 'radio-quiet' / intermediate radio luminosity AGN in particular) are clearly linked to their radio emission, the

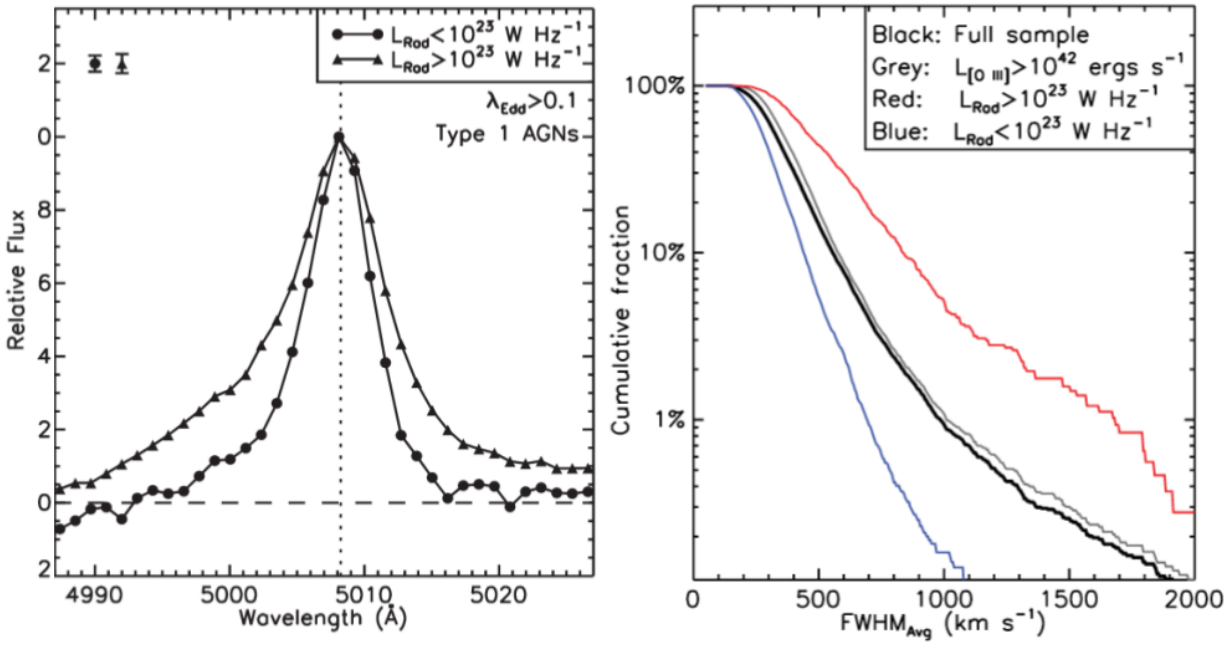

Figure 1.6: Two figures from Mullaney et al. (2013) demonstrating the relationship between the radio luminosity of AGN and their ionized gas outflows. *Left:* The average [O III] line profiles for high-Eddington-ratio (λ_{Edd}=L_{AGN}/L_{Edd} > 0.1) type 1 AGN, in bins of radio luminosity (with circles for L_{rad}=$L_{1.4GHz}$ < 10^{23} W Hz^{-1} and triangles for $L_{1.4GHz}$ > 10^{23} W Hz^{-1}). Representative error bars are shown in the top left. A strong blue wing indicative of outflows can be seen in the higher radio luminosity bin. *Right:* The fraction of AGN where the average FWHM from a two Gaussian fit to their [O III] line profile (FWHM$_{Avg}$) is greater than a given value. Values of FWHM$_{Avg}$ > 1000 km s^{-1} are approximately five times more likely for the AGN with $L_{1.4GHz}$ > 10^{23} W Hz^{-1} (red line) than for the overall sample (black line), with only a negligible difference seen for the AGN with higher [O III] luminosity (grey line).

physical mechanisms behind the radio emission, the outflows and their interconnectedness are unclear. This thesis addresses these questions by constraining the origin of the radio emission and the nature of the outflows through detailed, spatially resolved observations at multiple wavelengths (see Chapters 2 and 4).

1.5.3 The impact of outflows

Since stars form through the gravitational collapse of giant clouds of molecular gas, in order for the AGN to cause an immediate quenching of star formation, they must remove, destroy or prevent the formation of molecular gas in their host galaxy. Although primarily composed of H_2, the cold molecular gas in galaxies is typically observed using carbon monoxide (^{12}CO; the second most abundant molecule; see e.g. Bolatto et al. 2013; Carilli & Walter 2013, and references therein). This is because at the typical temperatures of molecular clouds ($\sim$10 K) H_2 does not have any emission or absorption lines at easily observable wavelengths. CO, however, has a permanent dipole moment and is excited by collisions with H_2 (see e.g. Combes, 1999). Specifically, the ground level CO rotational transition (J=1–0) has an excitation temperature of just 5.53 K, making it a good tracer of cold molecular gas (see e.g. Bolatto et al., 2013). It is worth noting that observing multiple CO transitions (i.e. the CO ladder or spectral line energy distribution – SLED) can reveal the temperature and density of the molecular gas, since the relative excitation of the different CO transitions depends strongly on the conditions of the gas (e.g. Weiß et al., 2005; Le Petit et al., 2006; Papadopoulos, 2010; Kamenetzky et al., 2018). This can be used to trace the heating / excitation of the CO gas by outflows (e.g. Dasyra et al., 2016; Zhang et al., 2019).

Since CO outflows typically only represent $\sim$10 percent of the molecular gas luminosity (e.g. Fluetsch et al., 2019; Lutz et al., 2020), they are difficult to observe directly. However, if outflows can remove, destroy or heat the molecular gas sufficiently, the effects will be observable through the total CO emission in multiple transitions. In particular, measurements of the total CO emission from low J transitions (ideally J=1) in AGN host galaxies can be compared to non-AGN galaxies with similar properties to look for a decreased molecular gas mass and / or star formation efficiency in the AGN host galaxies (e.g. Simpson et al., 2012; Husemann et al., 2017; Kakkad et al., 2017; Perna et al., 2018; Rosario et al.,

2018; Shangguan et al., 2020; Kirkpatrick et al., 2019). The main challenge with this type of study is controlling for the many host galaxy properties that can impact the molecular gas content (e.g. SFR, redshift, stellar mass). Chapter 3 of this thesis takes advantage of recent work which studied in detail the key factors that impact the molecular gas in galaxies to isolate the possible effect of the AGN (e.g. Tacconi et al., 2018; Liu et al., 2019, and references therein).

Finally, if the molecular gas is being heated by the AGN, this will be observable through increased emission in higher CO transitions relative to lower ones (e.g. Pereira-Santaella et al., 2013; Carniani et al., 2019; Papadopoulos et al., 2010). By modelling CO measurements at multiple transitions, the specific impact of the AGN on the molecular gas can be identified (e.g. van der Werf et al., 2010; Mashian et al., 2015; Carniani et al., 2019). However, these studies are typically limited to high redshift galaxies, where the CO lines are red-shifted into the infrared. This thesis presents some of the first work constraining the CO excitation mechanisms in low redshift quasars (see Chapter 3).

1.6 The Quasar Feedback Survey

The Quasar Feedback Survey is a sample of 42 local ($z < 0.2$), luminous AGN (i.e. quasars) which was designed to answer some of the key questions about AGN feedback and outflows presented in Section 1.5. This thesis presents the first results on the full sample (see Chapter 4).

The parent sample for this survey was the 24 264 SDSS spectroscopically identified, $z < 0.4$ AGN from Mullaney et al. (2013). The type 1 AGN in this sample were selected based on the presence of a broad Hα emission line in their SDSS spectra, and the type 2 by their location in the AGN regions of "Baldwin, Phillips & Terlevich" (BPT) diagrams (Baldwin et al., 1981; Kauffmann et al., 2003a; Brinchmann et al., 2004; Tremonti et al., 2004). BPT diagrams use the [O III]λ5007 / Hβ and [N II]λ6583 / Hα line ratios to separate spectra whose emission lines are dominated by ionization from hot stars (i.e. HII regions in star-forming galaxies) from those which are ionized by an AGN (with other emission line ratios sometimes additionally used; Kewley et al., 2001; Kauffmann et al., 2003b; Kewley et al., 2006). This separation occurs because the radiation from AGN is stronger at higher energies than that from stars, and so more efficiently

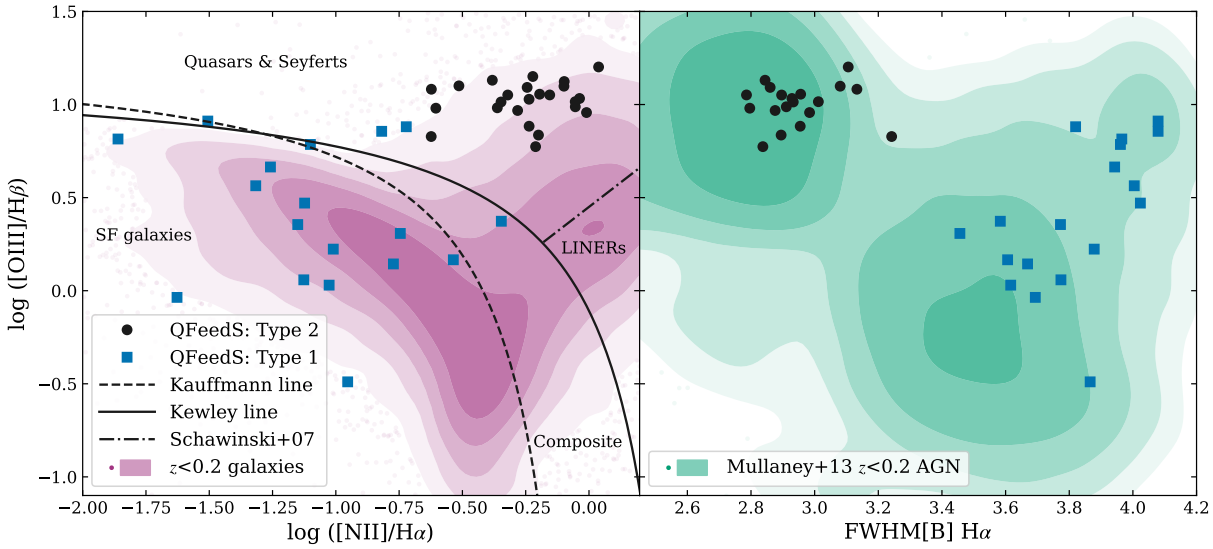

Figure 1.7: Properties used to select / classify the Quasar Feedback Survey sample (QFeedS) with the type 1 (broad line; see Section 1.4) sources as blue squares and the type 2s as black circles. *Left:* Shows the sample's location on the BPT diagram. The magenta contours are log density contours of the $z < 0.2$ SDSS galaxies from the NASA-Sloan Atlas (`http://www.nsatlas.org/`). The Kewley et al. (2001) and Kauffmann et al. (2003b) lines typically used to separate star-forming galaxies (SF galaxies) from AGN are shown as solid and dashed lines respectively, with all sources falling between the two classified as 'composite' systems. The dot-dashed line marks the boundary between Seyfert and quasar type AGN from LINERs, from Schawinski et al. (2007). *Right*: [O III]/ Hβ versus the FWHM of the Hα line. Specifically, the FWHM of the broadest Gaussian containing at least 50 percent of the line flux from three Gaussian fits from Mullaney et al. (2013). The green contours are log density contours of the $z < 0.2$ AGN from Mullaney et al. (2013).

excites higher energy transition lines. I show the locations of the Quasar Feedback Survey sources on the BPT diagram and the width of their Hα lines in Fig. 1.7.

The Quasar Feedback Survey sample was selected from the Mullaney et al. (2013) AGN using 4 selection criteria:

1. $z < 0.2$: This criterion primarily serves to allow for spatially resolved observations of the targets (with 1 arcsec $\approx$ 3.3 kpc at $z = 0.2$). Secondly, when combined with the luminosity cuts described below, it ensures that the targets can be observed with reasonable integration times.

2. $L_{[O\ III]} > 10^{42}$ ergs s^{-1}: In high optical luminosity AGN (i.e. quasars; Reyes et al., 2008) radiation-driven outflows are expected to be ubiquitous (Ganguly & Brotherton, 2008). Furthermore, these [O III] luminosities

correspond to bolometric AGN luminosities that are representative of typical AGN at $z \approx 1$–2, where the majority of AGN feedback is thought to have taken place (Hopkins et al., 2007; Aird et al., 2015, see also Fig. 1.5).

3. $L_{1.4GHz} > 2{\times}10^{23}$ W Hz^{-1}: This cut, on the observed radio luminosity from the NRAO VLA Sky Survey (NVSS; using the catalogue matches from Mullaney et al. 2013; Condon et al. 1998) is above the flux limit of NVSS, which ensures that the sample is representative within the selection criteria. Additionally, this is the radio luminosity range where the most powerful outflows were observed in Mullaney et al. (2013), making it an ideal sample to study the relationship between radio luminosity and outflows.

4. Observable from VLA: The final selection criteria was that the sources needed to be observable from the VLA. This limited the sample to sources within 10<RA<300 and 24<Dec<44 degrees.

The main selection criteria of this sample are shown in Chapter 4 Fig. 4.1, with the basic sample properties tabulated in Table 4.1. I additionally note that the majority (all but 5) of the Quasar Feedback Survey sources are classified as 'radio-quiet' by the [O III]–radio diagnostic of Xu et al. (1999).

Nine sources in this survey have been previously studied as part of the sample presented in Harrison et al. (2014). Specifically, these sources all have $FWHM_{OIII} > 700$ km s^{-1} to preferentially select sources with powerful outflows. Using IFS observations, Harrison et al. (2014) found ~kpc ionized gas outflows in the complete sample. These nine, high FWHM sources, are studied in greater detail in Chapters 2 and 3 of this thesis, with Chapter 4 considering the full Quasar Feedback Survey sample.

By combining the observational potential of a luminous nearby sample (see selection criteria above) with the diagnostic capabilities of a sample selected to potentially impact their host galaxies both mechanically and radiativly, the Quasar Feedback Survey is an ideal laboratory for studying both the mechanisms by which AGN impact their host galaxies and the extent of their impact. This thesis provides some of the first steps towards this goal and is described in more detail below.

1.7 This thesis

This thesis addresses two main questions: 1) What is the origin of the radio emission in traditional 'radio-quiet' AGN? and, 2) How are these AGN impacting their host galaxies? Specifically, I use the origin of the radio emission as a probe of the feedback mechanisms at work in these AGN. By combining this with information about the ionized gas outflows, the direct impact of feedback on the ISM can be traced and the driving mechanisms at work can be constrained. Finally, for feedback to ultimately be effective at reducing star formation, it must influence the molecular gas supply of the host galaxy, which I explore in this thesis using total CO measurements. Overall, this thesis combines data from multiple wavelengths (with particular emphasis on the radio, optical and sub-mm) and predominantly uses spatially resolved data, to provide the most complete picture possible of AGN feedback in these sources.

The remainder of this thesis is structured as follows:

Chapter 2: This Chapter identifies compact radio jets in seven to eight of the nine Quasar Feedback Survey sources previously studied in Harrison et al. (2014), by combining high spatial resolution radio imaging (~0.25 arcsec resolution) and *UV–IR* SED fitting (it also includes one additional source: J1338+1503). Radio imaging and IFS observations are combined to directly link the radio structures / jets observed to the ionised gas outflows, finding strong evidence of jet-ISM interactions. This Chapter is published as Jarvis et al. (2019).

Chapter 3: This Chapter builds directly off of the work presented in Chapter 2, looking for a potential impact of the AGN and jets on the molecular gas, for the nine Quasar Feedback Survey sources. Specifically, total (spatially unresolved) CO measurements of the (2–1) transition are used to discover that these quasars reside in gas-rich galaxies, with no signatures of immediate gas depletion by the AGN. Furthermore, the AGN are found to not significantly excite the molecular gas, using CO(6–5) measurements for three of these sources. This Chapter is published as Jarvis et al. (2020).

Chapter 4: In this Chapter I present the first results on the full Quasar Feedback Survey sample of 42 AGN. I place constraints on the origin of the radio

emission, by combining the radio morphology and spectral index measured using high spatial resolution radio images (~0.25 arcsec resolution) and the detection of excess radio emission beyond what can be predicted from star formation. Additionally, I find evidence of a direct connection between the radio features observed and the ionized gas outflows.

Chapter 5: Here I summarize the results of this thesis while putting the work into the context of larger astronomical discoveries and future / ongoing research being led by myself and my collaboration.

Chapter 2

Prevalence of radio jets associated with galactic outflows and feedback from quasars

M. E. Jarvis, C. M. Harrison, A. P. Thomson, C. Circosta, V. Mainieri,
D. M. Alexander, A. C. Edge, G. B. Lansbury, S. J. Molyneux
and J. R. Mullaney

Monthly Notices of the Royal Astronomical Society, Volume 485, Issue 2, May 2019, Pages 2710–2730

Abstract: We present 1–7 GHz high-resolution radio imaging (VLA and e-MERLIN) and spatially-resolved ionized gas kinematics for ten z<0.2 type 2 'obscured' quasars ($\log[L_{\rm AGN}$ / erg s$^{-1}] \gtrsim 45$) with moderate radio luminosities ($\log[L_{1.4\,\rm GHz}$/W Hz^{-1}]=23.3–24.4). These targets were selected to have known ionized outflows based on broad [O III] emission-line components (FWHM≈800–1800 km s^{-1}). Although 'radio-quiet' and not 'radio AGN' by many traditional criteria, we show that for nine of the targets, star formation likely accounts for $\lesssim$10 per cent of the radio emission. We find that ∼80–90 percent of these nine targets exhibit extended radio structures on 1–25 kpc scales. The quasars' radio morphologies, spectral indices and position on the radio size-luminosity relationship reveals that these sources are consistent with being low power compact radio galaxies. Therefore, we favour radio jets as dominating the radio emission in the majority of these quasars. The radio jets we observe are associated with morphologically and kinematically distinct features in the ionized gas, such as increased turbulence and outflowing bubbles, revealing jet-gas interaction on

galactic scales. Importantly, such conclusions could not have been drawn from current low-resolution radio surveys such as FIRST. Our observations support a scenario where compact radio jets, with modest radio luminosities, are a crucial feedback mechanism for massive galaxies during a quasar phase.

2.1 Introduction

Growing supermassive black holes at the hearts of massive galaxies, i.e. active galactic nuclei (AGN), are widely believed to be able to impact galaxy evolution by facilitating a global shut-down or regulation of star formation (e.g. see reviews in Alexander & Hickox, 2012; Fabian, 2012; Harrison, 2017). Galaxy formation models require this 'AGN feedback' to inject energy or momentum into the surrounding gas, in order to reproduce key observables of galaxy populations and the intergalactic material (e.g. Hopkins et al., 2006; Bower et al., 2006; McCarthy et al., 2010; Gaspari et al., 2011; Dubois et al., 2013; Vogelsberger et al., 2014; Hirschmann et al., 2014; Schaye et al., 2015; Henriques et al., 2015; Taylor & Kobayashi, 2015; Choi et al., 2018).

Historically, 'AGN feedback' was considered to come in two flavours: 'quasar mode', and 'maintenance mode' or 'radio mode' e.g. see Croton, 2009; Bower et al., 2012. The former mode is associated with powerful radiatively-dominated AGN, which are often referred to as quasars e.g. see Harrison, 2017. The energetic photons are predicted to couple to the nearby gas, resulting in high-velocity winds that propagate through the host galaxy and ultimately in the removal or destruction of the star forming fuel (e.g. Faucher-Giguère & Quataert, 2012; King & Pounds, 2015; Costa et al., 2018a). Conversely, maintenance mode is associated with low accretion rate AGN that release most of their energy in the form of radio jets (McNamara & Nulsen, 2012). These jets regulate the cooling of gas in the halos, and hence the level of star formation in their host galaxies. In reality feedback is unlikely to be simply divided into two modes (e.g. Churazov et al., 2005; Ciotti et al., 2010; Cielo et al., 2018) and observations are ultimately required to determine the processes by which AGN impact upon their galaxies.

Observationally, the details of 'quasar mode' feedback are not clear. On the one hand, winds driven in the vicinity of the accretion disc are common, if not ubiquitous (e.g. Silk & Rees, 1998; King & Pounds, 2015) and multi-phase AGN-

driven outflows have been observed on galaxy-wide scales (i.e. $\gtrsim$0.6 kpc) using integral field spectroscopy (IFS) and interferometric observations e.g. Veilleux et al., 2013; Husemann et al., 2013; Liu et al., 2013; Rupke & Veilleux, 2013; Cicone et al., 2014; Harrison et al., 2014; Fiore et al., 2017; Bae & Woo, 2018; Morganti et al., 2018; Fluetsch et al., 2019. However, determining how these galactic-outflows are driven is challenging; with accretion-disc winds, radio jets and star-formation all potential candidates e.g. Harrison et al., 2018; Wylezalek & Morganti, 2018.

Whilst radio jets are unambiguously associated with galaxy-wide outflows in rare, extremely radio luminous quasars (i.e. $L_{1.4\mathrm{GHz}}>10^{25}$ W Hz^{-1}; Nesvadba et al., 2017); the majority of quasars ($\gtrsim$90 percent) have lower radio luminosities. Particularly at moderate luminosities (i.e. $10^{23}\lesssim L_{1.4\mathrm{GHz}}\lesssim 10^{25}$ W Hz^{-1}), the dominant origin of radio emission is a matter of ongoing debate (e.g. Condon et al., 2013; Padovani et al., 2015; Zakamska et al., 2004; Zakamska et al., 2016). Furthermore, studies using spatially-unresolved radio emission and spectroscopy are unable to definitively distinguish between winds and radio jets as driving galactic outflows in typical quasars (Mullaney et al., 2013; Villar Martín et al., 2014; Zakamska & Greene, 2014).

As part of an ongoing programme, in this work we use spatially-resolved radio observations and spectroscopy to assess the dominant producer of radio emission and drivers of galactic ionized outflows in quasars. Using a sample of ∼24,000 $z < 0.4$ AGN we already discovered a strong relationship between the radio luminosity and the prevalence of ionized outflows based on measuring the [O III] emission-line profiles (Mullaney et al. 2013; also see Zakamska & Greene 2014; Villar Martín et al. 2014). Here, we combine follow-up high-resolution radio observations and integral field spectrograph observations of ten $z < 0.2$ quasars with moderate radio luminosities.

In Section 2.2 we describe the sample selection criteria and characterise the sample's host galaxy and AGN properties, using spectral energy distributions (SEDs). In Section 2.3 we describe the radio and IFS data sets we used and reduction steps taken and in Section 2.4 we describe the details of our analyses. In Section 2.5 we discuss our results in the context of previous work. Finally, in Section 2.6 we give our conclusions. We adopt H_0=71km s^{-1}Mpc^{-1}, Ω_M=0.27, Ω_Λ=0.73 throughout, and define the radio spectral index, α, using $S_\nu \propto \nu^\alpha$. We

assume a Chabrier (2003) initial mass function (IMF).

2.2 Target selection and characterisation

2.2.1 Sample selection

In this work we focus on ten type 2 ('obscured') $z < 0.2$ AGN, that have quasar-like luminosities (i.e. $L_{[\mathrm{O\ III}]}{>}10^{42}\,\mathrm{erg\,s^{-1}}$; Reyes et al., 2008). These were originally selected by Harrison et al. (2014) from our parent sample of 24 264 $z < 0.4$ spectroscopically identified AGN presented in Mullaney et al. (2013). We originally selected 16 sources for follow-up IFS observations that exhibit a luminous broad [O III] component in the one dimensional spectra, indicative of a powerful ionized outflow (see Fig. 2.1; Harrison et al., 2014). These IFS data revealed ∼kpc scale ionized outflows. The present text focuses on the subset of ten of these targets with a luminosity of $L_{[\mathrm{O\ III}]} > 10^{42}\,\mathrm{erg\,s^{-1}}$ (referred to as the primary sample; see Fig. 2.1). In Fig. 2.2 we show three-colour SDSS images for the ten quasars discussed in this work with the IFS field of view over-plotted.

The positions, redshifts, [O III] properties and radio properties (from the FIRST Survey; Becker et al. 1995) of the ten targets studied in this paper are presented in Table 2.1. As can be seen in Fig. 2.3 all of the primary sample discussed here are classified as 'radio-quiet' AGN based upon the criteria of Xu et al. (1999). Furthermore, as can be seen from the radio contours from FIRST in Fig. 2.2, the spatial resolution (∼5 arcsec) of these data, compared to our IFS observations (i.e. ∼0.6–0.9 arcsec; Section 2.3.3), is insufficient to unambiguously relate the kinematic features observed in the IFS data to the radio morphology. This motivated us to observe all of our targets with interferometric radio observations (as described in Section 2.3) to obtain higher resolution radio images (also see Harrison et al., 2015).

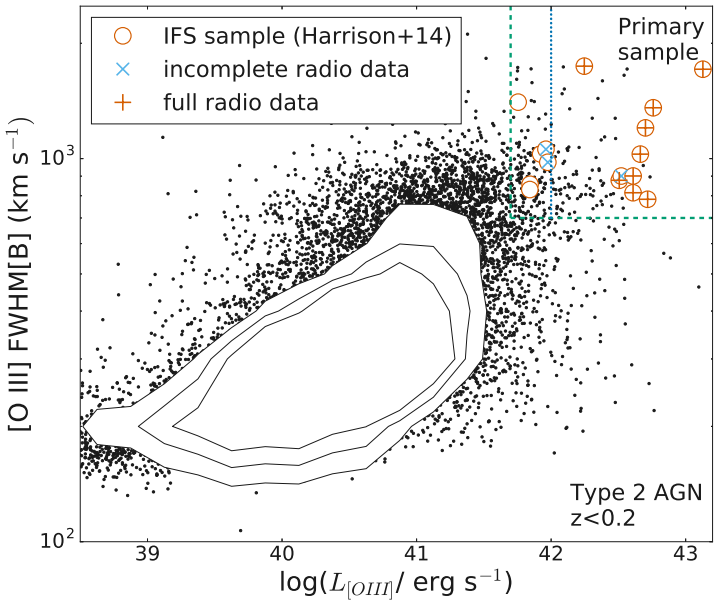

Figure 2.1: The FWHM of the broadest, luminous [O III] emission-line component versus the total [O III] luminosity (see Table 2.1 and Section 2.2.1). Our parent population of $z < 0.2$ type 2 AGN are shown as black data points and contours (Mullaney et al., 2013). The dashed green lines show the selection criteria used in Harrison et al. (2014) to select sources with spectral signatures of ionized outflows, the dotted blue line marks the additional criteria for the primary sample considered for most of the analysis presented here ($L_{[\mathrm{O\ III}]} > 10^{42}$ erg s^{-1}). The IFS targets are shown as red circles, with red plus symbols marking those with full radio data and cyan crosses marking those with incomplete radio data (see Section 2.3).

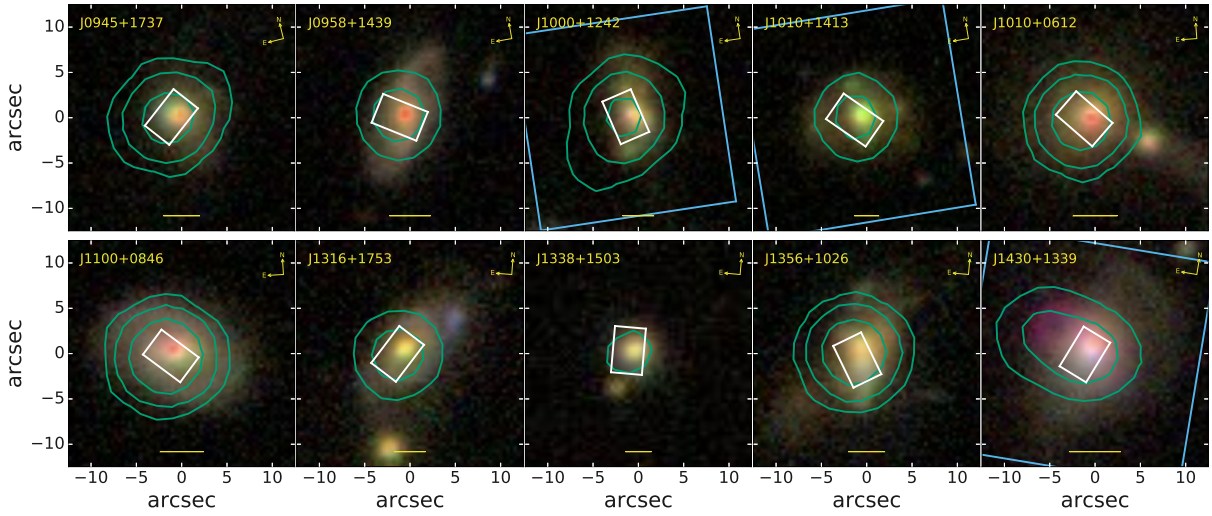

Figure 2.2: An overview of the ten quasars presented here. A three-colour (*gri*) SDSS image is shown (Alam et al., 2015). The green contours show the FIRST 1.4 GHz, ~5 arcsec resolution data, with contours at $\pm[8, 32, 128]\sigma$. The rectangles mark the field of view of our IFS data (GMOS in white and VIMOS in blue). The scale bar in each marks 9 kpc. Based on the FIRST data (also see Table 2.1), only one source shows unambiguous extended radio emission (J1430+1339) and two show marginal evidence for extended emission (J0945+1737; J1000+1242) and in all cases the resolution is too poor to connect to the ionized gas kinematics observed in the IFS data.

Table 2.1: Target list and basic properties.

Name	RA (J2000)	Dec (J2000)	z	$\log(L_{[\mathrm{O\,III}]})$ (erg s^{-1})	FWHM[B] (km s^{-1})	$S_{1.4}$ (mJy)	$\log(L_{1.4})$ (W Hz^{-1})	Θ_{FIRST}
(1)	(2)	(3)	(4)	(5)	(6)	(7)	(8)	(9)
J0945+1737	09:45:21.33	+17:37:53.2	0.1281	42.66	1027	44.5[4]	24.3	1.072[3]
J0958+1439	09:58:16.88	+14:39:23.7	0.1091	42.51	878	10.4[4]	23.5	1.006[9]
J1000+1242	10:00:13.14	+12:42:26.2	0.1479	42.61	815	31.8[4]	24.2	1.111[4]
J1010+1413	10:10:22.95	+14:13:00.9	0.1992	43.13	1711	8.8[5]	24.0	1.04[1]
J1010+0612	10:10:43.36	+06:12:01.4	0.0982	42.25	1743	99.3[3]	24.4	1.038[3]
J1100+0846	11:00:12.38	+08:46:16.3	0.1004	42.70	1203	61.3[3]	24.2	1.023[1]
J1316+1753	13:16:42.90	+17:53:32.5	0.1504	42.76	1357	11.4[4]	23.8	1.04[1]
J1338+1503	13:38:06.53	+15:03:56.1	0.1859	42.52	901	2.4[4]	23.3	1.06[5]
J1356+1026	13:56:46.10	+10:26:09.0	0.1233	42.72	783	59.6[4]	24.4	1.014[2]
J1430+1339	14:30:29.88	+13:39:12.0	0.0852	42.61	901	26.4[4]	23.7	1.400[9]

Notes: (1) Object name; (2)-(3) optical RA and Dec positions from SDSS (DR7); (4) Systemic redshifts from the GMOS data (see Section 2.4.2); (5) Total observed [O III]λ5007 luminosity from Mullaney et al. (2013). Absorption corrections would increase the values by on average 0.6 dex (with a maximum increase of 1.4 dex); (6) FWHM of the broad component of the [O III] line fit from Mullaney et al. (2013); (7) 1.4 GHz flux densities obtained from the FIRST survey (Becker et al., 1995) and uncertainties that are defined as 3× the RMS noise of the radio image at the source position; (8) Rest-frame radio luminosities using a spectral index of $\alpha = -0.7$ and assuming $S_\nu \propto \nu^\alpha$ (we note that a range of $\alpha = -0.2$ to -1.5 introduces a spread of ± 0.1 dex on the radio luminosity); (9) Radio morphology parameter, where sources with $\Theta > 1.06$ are classified as extended in the 1.4 GHz FIRST data (Harrison et al., 2014).

2.2.2 Star-formation rates and SED fitting

In Fig. 2.3 we show that all of the quasars in our sample would be classified as 'radio-quiet' by the Xu et al. (1999) criterion. However, there is significant debate in the literature as to whether this division marks two populations or one continuous distribution and if these divisions are physically motivated (Cirasuolo et al., 2003; Padovani, 2017; Padovani et al., 2017; Gürkan et al., 2019). A more meaningful measure is to select 'radio AGN' by assessing if the observed radio emission is dominated by star formation or by the AGN (e.g. Morić et al., 2010; Best & Heckman, 2012). Although our sources would be classified as star forming by the method of Best & Heckman (2012), the method that we use in this work is to look for an excess of radio emission in relation to the *FIR*–radio correlation for star-forming galaxies (e.g. Helou et al., 1985; Bell, 2003).

An important consideration in using the *FIR*–radio correlation to identify so called 'radio excess' galaxies is separating the *FIR* contribution from star formation and the AGN. This is because if both the *FIR* emission and radio emission are dominated by the AGN, this could produce another correlation, artificially causing AGN to follow the relation set by star-forming galaxies (Morić et al., 2010; Zakamska et al., 2016). We therefore make use spectral energy distribution (SED) fitting from the *UV* to *FIR* to isolate the *FIR* luminosity associated with star formation ($L_{\rm IR,SF}$) in addition to getting stellar masses ($M_\star$) and AGN bolometric luminosities ($L_{\rm AGN}$). The details of the archival photometric data we used are provided in the online supplementary information (Appendix A). We note that five of our targets do not have photometric measurements at wavelengths $\gtrsim$60μm; we flag these targets in Table 2.2 and assess the reliability of our key parameters for these targets below.

To fit the SEDs we used the Code Investigating GALaxy Emission (CIGALE[1]; Noll et al., 2009; Buat et al., 2015; Ciesla et al., 2015). We followed the basic procedure described in Circosta et al. (2018) but provide specific details of our implementation of the code in the online supplementary information (Appendix A). In short, the code simultaneously fits attenuated stellar emission, dust emission heated by star formation, AGN emission (both primary accretion disc emission and dust heated emission) and nebular emission from the *UV* to *FIR*. The code builds up a probability distribution function (PDF) for each parameter

[1] https://cigale.lam.fr

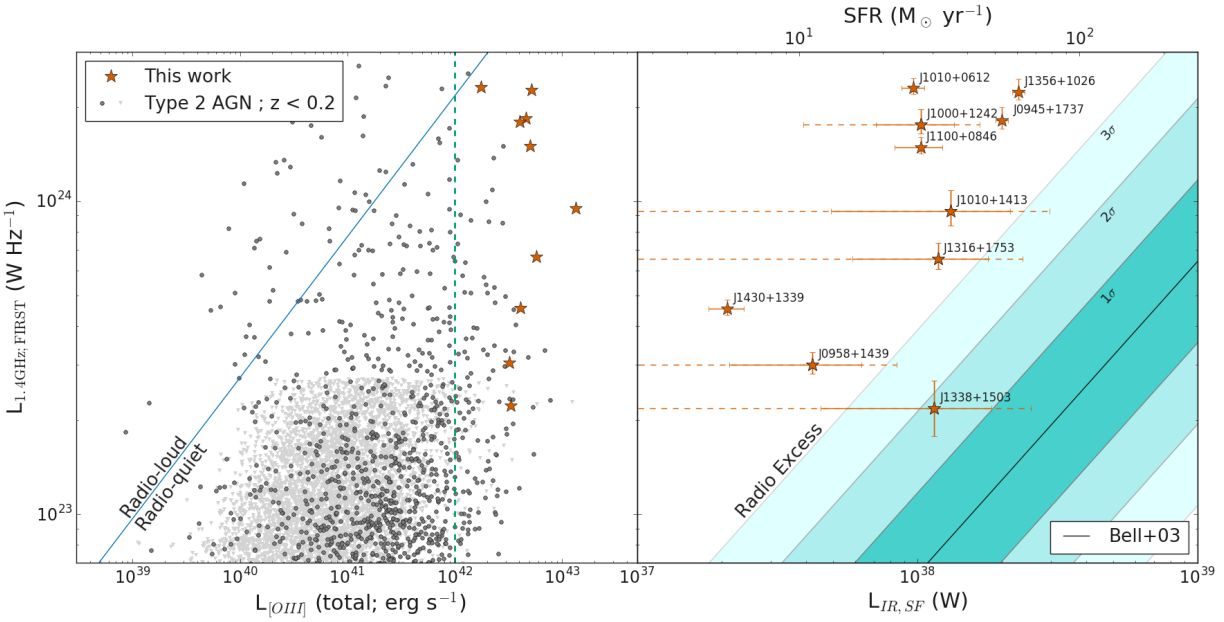

Figure 2.3: Left: Radio luminosity (from FIRST fluxes) versus [O III] luminosity for our galaxies (red stars) with the division between 'radio-loud' and 'radio-quiet' AGN from Xu et al. (1999) (blue line; see Section 2.2.1). Also shown is our parent sample of type 2 AGN with $z < 0.2$ (black points, grey for upper limits; Mullaney et al., 2013). Our selection criterion of $L_{[\mathrm{OIII}]} > 10^{42}$ erg s^{-1} is shown as a dashed green line. Right: The *FIR*–radio correlation of Bell (2003) compared to the values for our primary sample. We plot the far-infrared luminosity of the star formation component only ($L_{IR,SF}$). For those sources without good *FIR* coverage the 2σ errors are also plotted as dashed lines (see Section 2.2.2 and Table 2.2). The solid black line is the average correlation from Bell (2003) with the cyan regions marking 1, 2 and 3σ regions respectively. Although all of our targets are classified as radio-quiet, all but one are consistent with having excess radio emission above that predicted from star formation alone (see Section 2.2.2).

of interest, taking into account the variations from the different models. These fits are an improvement on those previously presented in Harrison et al. (2014), most notably, the increased wavelength range used allowed the attenuated stellar emission and dust emission due to star formation to be coupled, increasing the accuracy of $L_{\rm IR,SF}$, particularly in the cases with limited *FIR* coverage. Our results show that our targets have $L_{\rm IR,SF}$ that are broadly consistent with luminous infrared galaxies (i.e. $10^{11}\,L_{\odot}\lesssim L_{\rm IR,SF}\lesssim 10^{12}\,L_{\odot}$).

SED fits, especially with limited FUV coverage and an AGN component, can be difficult to determine (see e.g. Bongiorno et al., 2012; Zakamska et al., 2016). Indeed, it is well known that the uncertainties from standard SED-fitting procedures can be artificially small, with the true values being sensitive to, for example, the 'discretization' of the template grids used in the fitting procedure. The systematic uncertainties on stellar masses and far infrared luminosities are likely to be around 0.3 dex (Gruppioni et al., 2008; Mancini et al., 2011; Santini et al., 2015). As $L_{\rm IR,SF}$ is important for our interpretation we also tested how reliable our values are for the targets that lack far infrared photometric detections, by re-fitting all of the other SEDs (with good FIR coverage) but removing the longer wavelength data. Through this exercise we find that even with no data at $\geq 22\mu$m, the new values vary by no more than $\sim 2\sigma$ from the values derived using all the available *FIR* data[2]. This is likely due to the additional constraints on the star formation that come from the optical part of the SEDs in our fitting procedure. These boosted (2σ) errors also make the values consistent with the $L_{\rm IR,SF}$ values presented for the same sources in Harrison et al. (2014). We flag these affected sources in Table 2.2 and show the 2σ error bars in Fig. 2.3. We note that these additional systematic uncertainties do not affect the conclusions drawn in this paper.

To estimate the star formation rates of our targets we used the SED-derived $L_{\rm IR,SF}$ and the relationship from Kennicutt & Evans (2012), correcting to a Chabrier IMF by dividing by 1.7 (Chabrier, 2003). In Table 2.2 the quoted uncertainties are only from the SED-derived $L_{\rm IR,SF}$ uncertainties. We note that there is an additional systematic uncertainty on the star formation rates due to the conversion factor from the far-infrared luminosity (i.e. ~0.3 dex; Kennicutt & Evans, 2012).

[2] σ is the formal error recorded in Table 2.2.

Table 2.2: Galaxy and AGN parameters derived from SED fitting for the primary sample.

Name	$\log[L_{\rm AGN}]$ (erg s^{-1})	$\log[{\rm M}_\star]$ (M$_\odot$)	$\log[L_{\rm IR,SF}]$ (erg s^{-1})	SFR (M$_\odot$yr^{-1})	$S^{\rm predicted}_{1.4,{\rm SF}}$ (mJy)	% SF	q_{IR}	Radio Excess
(1)	(2)	(3)	(4)	(5)	(6)	(7)	(8)	(9)
J0945+1737	45.7	$10.1^{+0.09}_{-0.12}$	45.3±0.02	46±2	3.0±0.2	6.9±0.4	1.6±0.02	Y
J0958+1439†	45.2	$10.74^{+0.09}_{-0.12}$	$44.6^{+0.2}_{-0.3}$	10±5	0.9±0.5	9±4	$1.7^{+0.2}_{-0.5}$	P
J1000+1242†	45.3	$9.9^{+0.3}_{-0.7}$	$45.0^{+0.1}_{-0.2}$	24±7	1.1±0.4	4±1	$1.3^{+0.2}_{-0.4}$	Y
J1010+1413†	46.2	11.0±0.1	$45.1^{+0.2}_{-0.4}$	30±20	0.8±0.5	9±5	$1.8^{+0.3}_{-0.7}$	P
J1010+0612	45.3	$10.5^{+0.3}_{-0.9}$	44.99±0.04	22±2	2.6±0.2	2.6±0.2	1.15±0.04	Y
J1100+0846	46.0	–††	$45.01^{+0.08}_{-0.09}$	24±5	2.6±0.5	4.3±0.8	$1.37^{+0.08}_{-0.09}$	Y
J1316+1753†	44.4	$11.0^{+0.2}_{-0.3}$	$45.1^{+0.2}_{-0.3}$	30±10	1.3±0.6	11±6	$1.8^{+0.2}_{-0.5}$	P
J1338+1503†	45.7	$10.6^{+0.1}_{-0.2}$	$45.1^{+0.2}_{-0.4}$	30±20	0.8±0.5	–	$2.3^{+0.3}_{-0.7}$	N
J1356+1026	45.2	$10.64^{+0.09}_{-0.11}$	45.36±0.02	53±3	3.8±0.2	6.4±0.3	1.56±0.02	Y
J1430+1339	45.5	$10.86^{+0.05}_{-0.06}$	$44.32^{+0.06}_{-0.07}$	4.8±0.7	0.8±0.1	2.9±0.4	$1.18^{+0.06}_{-0.07}$	Y

Notes: All values are given with 1σ formal errors from the SED fit (see Section 2.2.2 for systematic uncertainties). (1) Object name; (2) Bolometric AGN luminosity; (3) Stellar mass; (4) Infrared luminosity from star formation in the range 8–1000 μm; (5) Star formation rate; (6) 1.4 GHz flux predicted from star formation following the radio – L_{IR} relation (Bell, 2003); (7) Percentage of the FIRST luminosity accounted for by star formation in the radio excess sources; (8) The q_{IR} ('radio excess') parameter, where $q_{IR} \leq 1.8$ denotes radio excess (see Section 2.2.2); (9) Flag to define if the target is radio excess, where: 'Y' means radio excess, 'P' means probably radio excess and 'N' means not radio excess. †These sources do not have photometric measurements at wavelengths longer than 60μm, with J1316+1753 having no photometry above 22μm (see Section 2.2.2 for a discussion on the additional uncertainties on the parameters for these sources). †† For this target the AGN contribution is particularly high in the *NIR* regime and the estimate of the stellar mass is unconstrained, with an uncertainty larger than the parameter value itself. We therefore do not report a value of M$_\star$.

Our targets are type 2 AGN, and consequently, we do not detect the primary AGN disc emission in the *UV*–optical part of the SED. Therefore, to estimate the bolometric AGN luminosity ($L_{\rm AGN}$) we converted the 6μm luminosity from the AGN emission component using a bolometric correction of 8× following Richards et al. (2006). The uncertainties on these $L_{\rm AGN}$ values are dominated by a ∼1 dex systematic uncertainty on the bolometric corrections. This confirms that our targets are consistent with having quasar luminosities (i.e. $L_{\rm AGN}\gtrsim10^{45}$ erg s^{-1})[3], which we also find by using $L_{\rm [OIII]}$ and the bolometric correction from Heckman et al. (2004) (see Table 2.2).

Two example SEDs are shown in Fig. 2.4 and the remainder are provided in online supplementary material. Although the SEDs are only fit using the *UV*–*FIR* photometry we also show the radio fluxes from three radio surveys, when available: FIRST (1.4 GHz); TIFR GMRT Sky Survey Alternative Data release (TGSS; 150MHz; Intema et al., 2017); and the GaLactic and Extragalactic All-sky MWA Survey (GLEAM; 200MHz; Hurley-Walker et al., 2017), as well as the total flux from our measurements at 1.5, 5.2 and 7.2 GHz (see Section 2.4.1 and Table 2.4). These additional radio data allow for visual comparison to the level of emission expected from star formation alone (Bell, 2003) and the identification of spectral turnovers in the radio SEDs (Section 2.5.2).

In Fig. 2.3 we show $L_{IR,SF}$ as a function of radio luminosity (see Table 2.1) for our targets and compare these values to the *FIR*–radio correlation of star-forming galaxies from Bell (2003). It can be seen that nine of our ten targets lie well above the *FIR*–radio correlation[4] (the exception is J1338+1503). We note that for three of the targets, which all have poor *FIR* photometry, the uncertainties could cause them to be consistent with star-forming galaxies, within the 3σ scatter on that relation, and we highlight these targets in Table 2.2. However, based on our spatially-resolved radio images presented in Section 2.3.1, we are confident that these sources have significant radio emission that is not associated with star formation. The distance of points from this relation can be quantified using the

[3]We note that the bolometric luminosity calculated in this way is below the quasar limit for J1316+1753, however it is consistent with being equal to or above 10^{45} erg s^{-1} within the 1 dex error mentioned above. Additionally, it is clearly a quasar using the [O III] luminosity (Reyes et al., 2008).

[4]If we instead used the *FIR*–radio correlation from Delhaize et al. (2017) the nine targets lie even further above the relationship of star-forming galaxies.

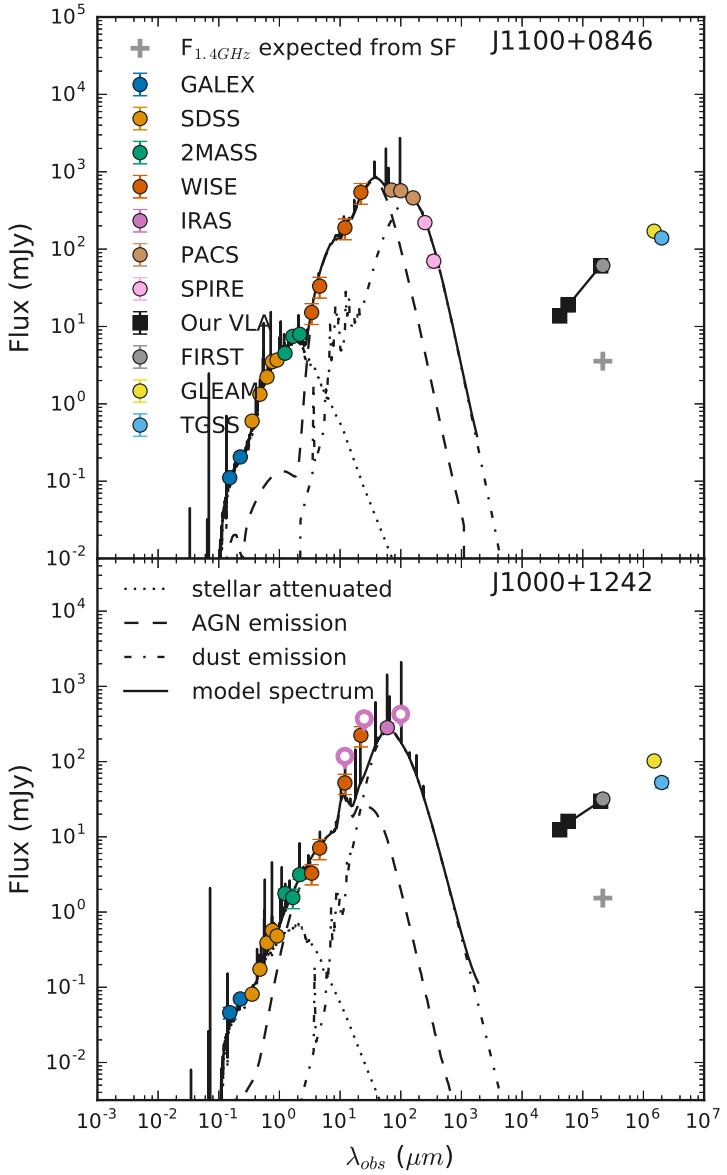

Figure 2.4: Two of the SEDs of our targets (J1100+0846; an example with good *FIR* photometry and J1000+1242; an example without *FIR* detections). The other SEDs are included in the supplementary online material. The data are plotted as circles colour coded by survey, with upper limits as open circles. The available radio photometry are shown but are not included in the fit. The solid curve shows our best total fit that is decomposed into attenuated stellar (dotted line), AGN (dashed line), and star-formation heated dust (dot-dashed line) components. An additional nebular component, not plotted separately, is responsible for the emission-lines visible in the total fit. A grey cross marks the predicted 1.4 GHz flux from star formation following Bell (2003). We find that all but one of targets have excess radio emission above that expected from star formation (Section 2.2.2).

$q_{\rm IR}$ parameter, defined as

$$q_{IR} = \log \left[\frac{L_{IR}/3.75 \times 10^{12}\mathrm{W}}{L_{1.4}/\ \mathrm{W\ Hz^{-1}}} \right], \tag{2.1}$$

where L_{IR} is the rest-frame far-infrared (8–1000 μm) luminosity, and sources with $q_{IR} \lesssim 1.8$ are considered radio excess (see Table 2.2; e.g. Bell, 2003; Del Moro et al., 2013; Delhaize et al., 2017).

In Table 2.2 we also show the radio flux that we expect from star formation following Bell (2003) and we find that for our nine 'radio excess' targets, the star formation is expected to contribute ∼3–11 percent of the total observed radio emission (also see Fig. 2.4). We discuss this in more detail in Section 2.5.2.

2.3 Observations and data reduction

2.3.1 VLA observations, and imaging

Observations and data reduction

We observed with VLA under two proposals: programme 13B-127, with observations carried out 2013 December 1– 2014 May 13 and programme 16A-182 with observations carried out 2016 May 30 – 2017 January 20. For 13B-127 we observed nine targets, from our primary sample of ten, in four configuration–frequency combinations: (1) A-array in L-band (1–2 GHz; ∼1.3 arcsec resolution); (2) A-array in C-band (4–8 GHz; ∼0.3 arcsec resolution); (3) B-array in L-band (1–2 GHz; ∼4.3 arcsec resolution) and (4) B-array in C-band (4–8 GHz; ∼1.0 arcsec resolution). The final target in our primary sample (J1338+1503)[5], was observed by VLA during our 16A-182 project. Due to incomplete observations, this was only observed in one configuration–frequency combination: B-array configuration in the C-band (i.e. 4–8 GHz; ∼1.0 arcsec resolution).

The 13B-127 observations comprise 2 hours (∼5 minutes on each target) of L-band observations in the A-configuration, and 2.5 hours (∼7–10 minutes on each target) of L-band observations in the B-configuration. For the C-band, 2.5 hours (∼7 minutes on each target) and 2 hours (∼5 minutes on each target)

[5]along with two other targets from the Harrison et al. (2014) sample not included in the primary sample (J1355+1300 and J1504+0151; see supplementary information)

of observations were taken in A- and B-configurations, respectively. During our 16A-182 observations C-band data in B-configuration were taken of three targets. These were taken with 2× or 3× repeats of 1 hour observing blocks (with 35, 32 and 26 minutes on target for each J1338+1503; J1355+1300 and J1504+0151, respectively).

We perform amplitude and bandpass calibration at L- and C-band at the start of each observing block using a ∼10 minute scan on the standard calibration source J1331+3030 (3C 286), and determine complex gain solutions via ∼3 minute scans (including slew-time) of nearby calibration sources every ∼ 10–15 minutes (typically within ∼10° of our targets). We choose calibration sources from the list of VLA calibrators website[6] with codes which deem them suitable for each combination of array configuration/observing frequency. The 13B-127 observations were reduced using the Common Astronomy Software Applications (CASA[7]) package (version 4.1.0), along with version 1.2.0 of the VLA scripted pipeline. We reduced the later 16A-182 observations using CASA version 4.5.2, and version 1.3.5 of the VLA scripted pipeline.

Imaging

When imaging the VLA data we had two goals: (1) identify any morphological features that are present in the radio emission and (2) measure the fluxes / spectral indices of these features. These goals required different approaches to the imaging of the data and we describe them both here. In order to take into account the broad and varying bandwidths of our observations, all of the VLA images we present were made using the Multi-Frequency Synthesis (MFS) mode of the CLEAN function in CASA version 4.7.1. We chose the weighting of the baselines to obtain the desired compromise between sensitivity and beam size to achieve our science goals (see Briggs 1995). In some cases we additionally applied Gaussian tapering to achieve the desired resolution. Because of the relatively short observing times of our targets and resultant limited *uv* coverage our cleaned images sometimes still suffer from relatively strong beam residuals. However, in order to test the validity of these features we ensured that they were identified at multiple frequencies and using different combinations of weighting and tapering

[6] https://science.nrao.edu/facilities/vla/observing/callist
[7] https://casa.nrao.edu/

Table 2.3: Summary of the radio images used in Fig. 2.5.

Object Name	Img.	Beam HPBW (arcsec)	Beam PA (deg)	Noise (μJy/beam)	Data	Weighting
(1)	(2)	(3)	(4)	(5)	(6)	(7)
J0945+1737	HR	0.22×0.21	−18	19	C-A	uniform
J0945+1737	LR	1.17×0.94	52	18	C-B	briggs 0.5
J0958+1439	HR	0.22×0.21	−27	12	C-A	uniform
J0958+1439	LR	1.22×0.94	51	9	C-B	briggs 0.5
J1000+1242	HR	0.30×0.26	−12	23	C-A	briggs 0.5
J1000+1242	LR	1.44×1.21	39	22	C-A+C-B†	nat.+150kλtaper
J1010+1413	HR	0.22×0.21	−41	16	C-A	uniform
J1010+1413	LR	1.21×0.95	51	9	C-B	briggs 0.5
J1010+0612	HR	0.25×0.22	−68	79	C-A	uniform
J1010+0612	LR	1.55×0.93	50	83	C-B	briggs 0.5
J1100+0846	HR	0.23×0.22	−67	48	C-A	uniform
J1100+0846	LR	1.24×0.94	48	58	C-B	briggs 0.5
J1316+1753	HR	0.26×0.22	78	14	C-A	uniform
J1316+1753	LR	1.01×0.86	29	16	C-B	briggs 0.5
J1338+1503	LR	1.01×0.91	51	6	C-B	briggs 0.5
J1356+1026	HR	0.37×0.29	−47	100	C-A	briggs 0.5
J1356+1026	LR	1.05×0.92	4	36	C-A+C-B††	natural
J1430+1339	HR	0.33×0.23	−88	23	C-A	uniform
J1430+1339	LR	1.00×0.88	16	12	C-B	briggs 0.5

Notes: (1) object name; (2) resolution of the image; (3-5) details of the synthesised beams and noise of the radio images; (6) describes the measurement set(s) used, where C-A indicates the VLA C-band A-configuration data (etc.); (7) describes the weighting scheme used to image the data. †a concatenation of the C-band A and B-array data were used with relative weighting of 4:1; ††a concatenation of the C-band A and B-array data were used with even weight.

(see Section 2.4.1).

For our first goal, we aimed to identify both diffuse and compact morphological features in the radio emission. To do this we made two C-band (6 GHz) 'showcase images' for each galaxy in the primary sample: one with a ∼1 arcsec beam (i.e. ∼2 kpc at z=0.1; referred to as 'low-resolution' or LR) and one with a ∼0.25 arcsec beam (i.e. ∼0.5 kpc at z=0.1; referred to as 'high-resolution' or HR)[8]. Fig. 2.5 shows the low and high-resolution images for each source, which are also made available as FITS (Flexible Image Transport System) files in the online supplementary material. For these showcase images, the imaging parameters (weighting, tapering and concatenating data sets) were tweaked to best reveal the morphological features found in each galaxy (details in Table 2.3). The σ (noise) values are calculated using 8σ clipping repeated ten times across a region of the images that is 50 times the size of the beam major axis.

For our second goal we measured the flux densities and spectral indices (over 1-7GHz) for each morphological feature identified. To do this we required multi-frequency images with the same spatial resolution. We produced images at 1.5, 5.2 and 7.2 GHz, where the 5.2 and 7.2 GHz images were made by evenly splitting the 16 VLA C-band spectral windows. We created two sets of these resolution-matched multi-frequency images using weighting and tapering to match the beams as closely as possible, one set at high-resolution (∼0.25 arcsec; using e-MERLIN for the 1.5 GHz data; see Section 2.3.2) and one set at low-resolution (∼1 arcsec; using the VLA L-band A-configuration data for the 1.5 GHz images). Full details of the data used, applied weighting schemes/tapering, the resultant properties of the images (i.e. beam sizes, noise levels; see Table B1) and all 56 of these images, are presented in the online supplementary material.

For the two sources observed with our VLA 16A-182 programme but not included in the primary sample (J1355+1300 and J1504+0151), the details of the imaging, the images themselves and a brief discussion of the features seen are presented in the online supplementary material (Appendix C).

[8]For J1338+1503 only a low-resolution image was created due to there being no available A-configuration VLA data.

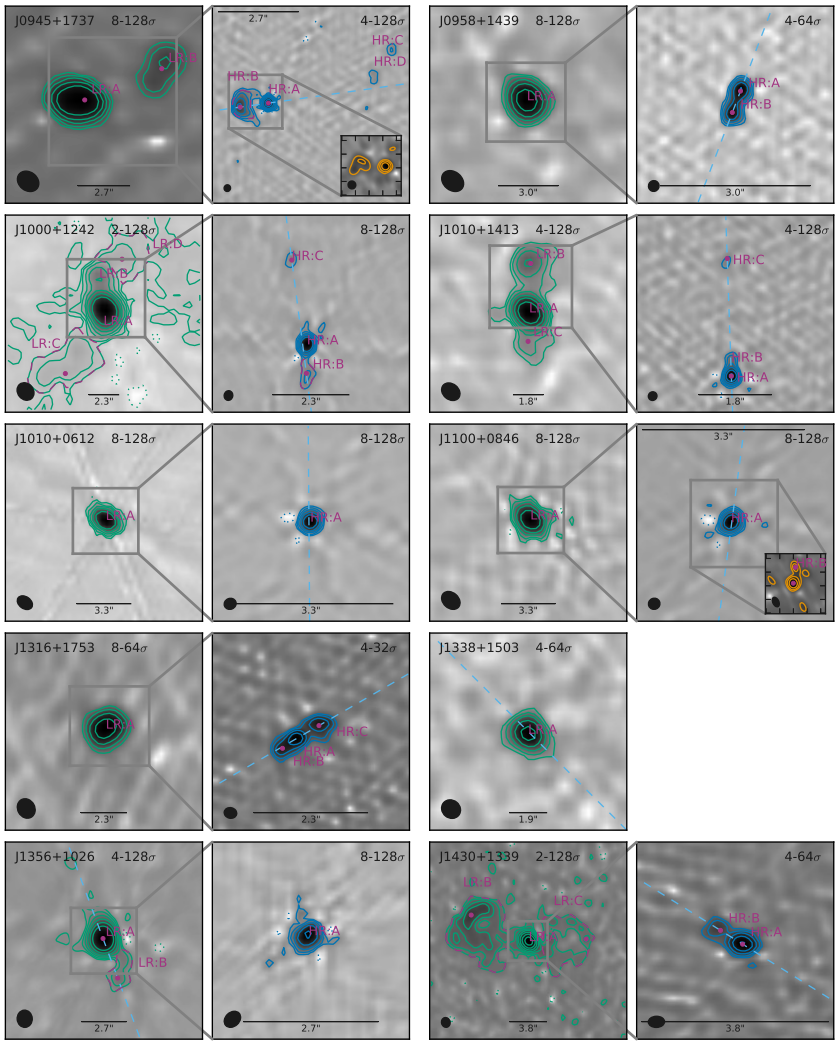

Figure 2.5: VLA 6 GHz images and contours for our primary sample. The low-resolution images (∼1 arcsec beam; green contours) are shown to the left and on the right are the high-resolution images (∼0.25 arcsec beam; blue contours) that cover the region marked with grey boxes in the low-resolution images. For J0945+1737 and J1100+0846, we also inset the 1.5 GHz e-MERLIN images (orange contours). Contours are at $\pm[2, 4, 8, 16, 32, 64, 128]\sigma$ with the minimum and maximum contour in each image given in the top right (see Section 2.3.1; the e-MERLIN contours always start at 8σ). The synthesised beams are shown as black ellipses and the scale bars represent 6 kpc. We label the radio morphological features and when a region is used to calculate the flux it is shown by a dashed magenta outline (Section 2.4.1). Magenta dots show the positions used to calculate sizes, distances, and the major axis of the radio emission (light-blue dashed line ; see Section 2.4.1). In seven sources we see unambiguous multiple radio features. Additionally, J1100+0846 shows one ambiguous feature, only seen in the e-MERLIN image. Only for J1338+1503, which lacks a high-resolution image, and for J1010+0612 do we see no evidence of multiple radio features.

2.3.2 e-MERLIN observations and imaging

We obtained 1.5 GHz (L-band) e-MERLIN observations with ~40–172 minutes on-source per target in Cycle 1 (ID: CY 1022; observed on 2013 December 19) and ~1.5–3 hours on-source per target in Cycle 2 (ID: CY 2217; observed between 2015 January 21–23). Each observing block entailed ~30 minute scans of 0319+415 and 1407+284 for flux density and bandpass calibration, respectively. Target scans were ~8 minutes, interspersed with ~3 minute scans of bright, nearby phase reference sources. We processed the data in AIPS version 31DEC15, with most steps being carried out using the e-MERLIN pipeline (Argo, 2015), but with extensive additional manual flagging of bad data using the AIPS tasks SPFLG and IBLED.

We created 4096×4096 pixel maps from our calibrated *uv* data using IMAGR with a pixel size of 0.05 arcsec (i.e. a 3 arcminute postage stamp around each source), and iteratively deconvolved the point spread function (PSF) within manually-defined CLEAN boxes around sources of bright emission. Our typical synthesised beam is ~0.2–0.3 arcsec and in all cases the beams have axial ratios of $b/a > 0.5$.

Unfortunately, a combination of strong, persistent radio frequency interference (RFI) and hardware failures resulted in the loss of >50 percent of our Cycle 1 data, covering both target and calibrator fields. The resulting loss of point-source sensitivity and *uv* coverage severely limited the quality of the final images, leaving us unable to achieve our science goals of establishing the radio morphologies at 1.5 GHz. Consequently we do not use these data in our analyses. Fortunately, only one of our primary targets (J1338+1503) was part of this Cycle 1 programme. Improvements in both the hardware performance and observing strategies for Cycle 2 lowered our loss-rate to ~20 percent (with significantly improved *uv* coverage), yielding improved imaging ($\sigma \approx 300\,\mu$Jy beam^{-1}) and allowing us to study the 1.5 GHz morphologies on sub-kpc scales of the nine of our primary targets, that were all observed in this cycle.

2.3.3 IFS observations and data reduction

All of our quasars have published IFS data obtained using Gemini-GMOS (Harrison et al., 2014). These observations covered the O [III]λ4959, 5007 and Hβ

emission-lines using 25×20 lenslets sampling a 5×3.5 arcsec field of view. The spectral resolution of ~3700 gives a line FWHM of 80 km s^{-1}. The observations were performed with a typical V band seeing of ~ 0.7 arcsec. More details about these observations are given in Harrison et al. (2014).

As part of an uncompleted ESO programme, three of our targets (J1430+1339, J1010+1413 and J1000+1242) also have IFS observations with VIMOS on the ESO/VLT telescope observed from 2014 January 23–24 and 2014 March 9–10 (Program ID: 092.B-0062). The VIMOS observations, which benefit from a ~20×20 arcsec field of view, were motivated by the kinematic and morphological structures that appeared to extend beyond the GMOS field of view (i.e. on $\gtrsim$5 arcsec scales; Harrison et al., 2014, see Fig. 2.2). The data for J1430+1339 are already published in Harrison et al. (2015) and we combine these data with the rest of the sample here.

We used VIMOS in IFS mode, using the HR-Orange grism, which provides a wavelength range of 5250–7400Å at a spectral resolution of ~2650, giving a line FWHM of 110 km s^{-1} at 5007Å, which we confirmed within $\pm$10 km s^{-1} by measurements of sky-lines. During the observations the targets were dithered around the four quadrants of the VIMOS field of view. The on-source exposure times were 6480 seconds for J1430+1339 and J1010+1413; and 2160 seconds for J1000+1242. The V-band seeing ranged between 0.8–0.9 arcsec. Standard stars were taken under similar conditions to the science observations. The standard ESOREX pipeline was used to reduce the data, which includes bias subtraction, flat-fielding, wavelength calibration and flux calibration. Data cubes were constructed from the individually sky-subtracted, reduced science frames. The final data cubes were created by median combining the individual exposure cubes using a three-sigma clipping threshold.

2.4 Analyses

Here we describe the techniques used to identify and characterise morphological and kinematic features observed in our radio and optical IFS data. In Section 2.4.1 we identify the radio features seen at different resolution and measure the location, flux and spectral index for each feature. In Section 2.4.2, we describe the non-parametric characterisation of the [O III]λ5007 emission-line profiles and explain

how we produced emission-line kinematic maps.

2.4.1 Radio analyses

Radio features, flux densities and spectral indices

As can be seen in Fig. 2.5 our sources are typically composed of multiple spatially-distinct radio features. In order to constrain the source of the radio emission in each of these morphological features (discussed in Section 2.5.2), we calculated flux densities and spectral indices for each. We note that we tested our overall approach to flux calibration and to obtaining flux densities by verifying that the total fluxes of the sources from our imaged VLA L-band B-array data (average spatial resolution of 4.3 arcsec) are consistent with the FIRST values (5 arcsec beam) within errors. We note that the variations in flux densities by converting between the difference in the central frequency of our observations and FIRST (i.e. 1.5 GHz to 1.4 GHz) is smaller than the errors on our fluxes.

We name each morphologically distinct feature (detected at $\geq 3\,\sigma$) in the high-resolution images as HR:A, HR:B etc., and similarly for the low-resolution images with LR:A, LR:B etc. For the low significance features (e.g. HR:C in J1000+1242) we verified that they are real by ensuring that they were significantly detected in images produced using multiple weighting schemes and/or in independent observations. In general the e-MERLIN images (see Section 2.3.2) did not reveal any new information on the morphological features. The exceptions are: for J0945+1737, where the HR:B feature shows a bent 'jet like' appearance in the e-MERLIN image; and for J1100+0846, which shows a $\sim 7\sigma$ feature (HR:B; see Table 2.4) in the e-MERLIN image that is not identified in the 6 GHz VLA images. We show the e-MERLIN images for these two sources in Fig. 2.5. The e-MERLIN images for all sources are presented in the supplementary online material. We discuss the origin of the identified radio features in Section 2.5.2.

Due to the range of morphologies seen in our data (see Fig. 2.5), we were required to use two approaches to obtain the flux densities of each feature. The first approach was to model the emission as a series of two-dimensional Gaussian components. All of the parameters of the fits were left free[9]. We note that

[9]For the LR-C component of J1010+1413 we were required to fix the peak position of the Gaussians to within 0.5 pixels to obtain a reasonable fit. We flag this feature as having unreliable flux density measurements.

the feature LR:A in both J0945+1737 and J1000+1242 needed two component Gaussians to provide an adequate fit, which is easily explained by the multiple HR components that they are composed of (see Fig. 2.5).

The second approach was to sum the emission in regions motivated by the lowest-level contours of the appropriate resolution image in Fig. 2.5. We verified that the flux density measurements are consistent within the errors (described below) if we vary the defined region sizes up or down by 25 percent. These regions were primarily used for diffuse/irregular structures that are not well described by a Gaussian and are referred to as 'region components'. Where it was possible to apply both approaches, we further verified that they gave consistent results, but favoured the Gaussian fitting method. In the cases where a compact nuclear component was seen in addition to a more diffuse structure, the flux in the diffuse regions was calculated after subtracting off the Gaussian fits to the compact component(s) in order to minimize contamination. Figures showing the data, our best-fit models and the corresponding residuals for all multi-frequency images can be found in the online supplementary material.

To calculate the random noise on our flux density measurements for each feature, we took the standard deviation of 100× repeats of extracting flux densities from inside appropriately sized regions randomly positioned within the central 10 arcsec (for high-resolution images) or 20 arcsec (for the low-resolution images) avoiding source emission. For the 'region components' the regions used in this procedure were the same size and shape as those used to extract the flux densities. For the Gaussian components we used an ellipse with axis sizes equal to twice the semi-minor and semi-major axes of the fits. To establish if a feature was detected in each of the 1.5, 5.2 and 7.2 GHz images, we imposed a 5σ detection limit. For each of the detected components, we added an additional 10 percent systematic error, in quadrature, to the uncertainties to account for the random variations we found when extracting flux densities when changing the weighting scheme used to image the data. The final flux densities (or 5σ upper limits) and their 1σ uncertainties at 1.5, 5.2 and 7.2 GHz are presented in Table 2.4.

The spectral index (α, which we define as $S_\nu \propto \nu^\alpha$) is used to help interpret the source of the radio emission for each feature in Section 2.5.2. We measured this by fitting a line through all of the detected frequencies (1.5, 5.2 and 7.2 GHz) for each radio structure. The errors given for α in Table 2.4 are the 1σ

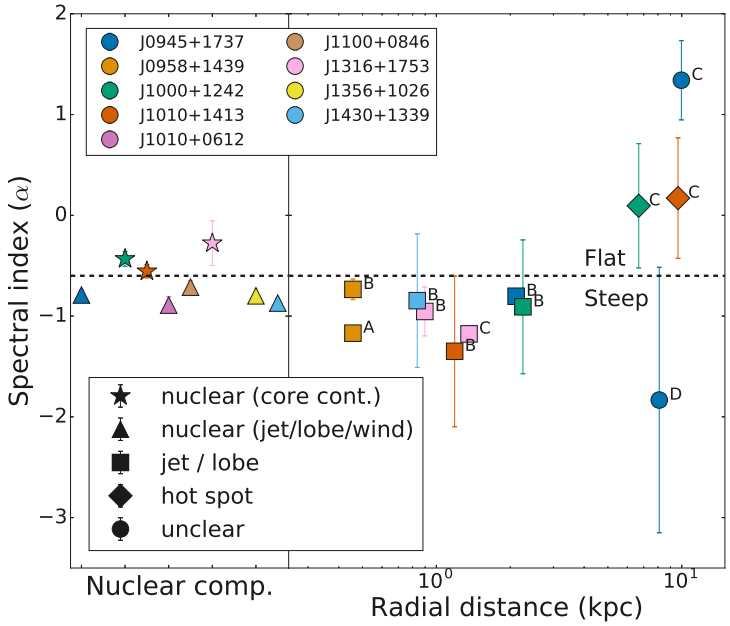

Figure 2.6: Spectral index (α) of each high-resolution morphological radio component with detections in more than one band verses its distance to the brightest high-resolution radio component (i.e. nuclear/HR-A; Fig. 2.5 ; Table 2.4). The α values for the nuclear components are plotted on the left with an arbitrary separation. Each are colour coded based on their source, with the shape corresponding to our classification (see Section 2.5.2). The nuclear components are noted as either jet/wind dominated or with a possible core contribution based on if they are steep ($\alpha < -0.6$) or flat ($\alpha > -0.6$; dashed line). Non-nuclear components are labelled as either 'jet/lobe' or as 'hot spot' depending on if they are steep or flat. Two components have an 'unclear' origin and are discussed in more detail in Section 2.5.2.

errors on the fit, except for where the component was only detected in two bands, then the error is the propagated error from the two measured fluxes. Some of our data were observed at different epochs (e.g. when combining our e-MERLIN and VLA C-band B-configuration data) which risks unknown variability of the fluxes affecting the spectral index values. However, we find that our α values are consistent to those calculated using only our single-epoch VLA C-band data (within the errors on the VLA C-band values). The 1-7 GHz radio SEDs for each radio component are presented in the supplementary material. The spectral indices for the high-resolution components are plotted in Fig. 2.6 along with their distance from the central brightest component (HR:A; see Section 2.4.1).

Table 2.4: Radio properties of the morphological structures (see Fig. 2.5), extracted from resolution matched e-MERLIN and VLA images.

Name	S_{FIRST} (mJy)	Structure	Interpretation or LLS	$S_{1.5GHz}$ (mJy)	$S_{5.2GHz}$ (mJy)	$S_{7.2GHz}$ (mJy)	α
(1)	(2)	(3)	(4)	(5)	(6)	(7)	(8)
J0945+1737	44.5±0.4	HR:A	nuclear (jet/wind)	16±2	6.3±0.6	4.6±0.5	-0.79±0.05
		HR:B	jet / lobe	13±2	4.8±0.5	3.9±0.4	-0.8±0.02
		HR:C	unclear	<7.5	0.24±0.04	0.37±0.04	1.3±0.4
		HR:D	unclear	<1.6	0.26±0.04	0.15±0.03	-2±1
		HR:Total	LLS=2.1kpc	29±2	11.7±0.9	9.0±0.8	-0.76±0.02
		LR:A	composite	42±2	13±1	9±1	-0.927±0.007
		LR:B	lobe	4.5±0.5	1.9±0.2	1.4±0.2	-0.74±0.03
		LR:Total	LLS=11kpc	47±1	15±1	11±1	-0.906±0.008
J0958+1439	10.4±0.4	HR:A	jet / lobe	5.8±0.7	1.3±0.1	0.97±0.1	-1.17±0.07
		HR:B	jet / lobe	3.7±0.7	1.6±0.2	1.2±0.1	-0.7±0.1
		HR:Total	LLS=0.9kpc	10±1	2.9±0.5	2.1±0.4	-0.959±0.001
		LR:A	composite	11±1	2.9±0.3	2.1±0.2	-1.057±0.005
J1000+1242	31.8±0.4	HR:A	nuclear (core cont.)	20±2	13±1	9±1	-0.43±0.07
		HR:B	jet / lobe	<2.1	1.0±0.1	0.73±0.08	-0.9±0.7
		HR:C	hot spot	<1.1	0.65±0.08	0.7±0.1	0.1±0.6
		HR:Total	LLS=8.9kpc	20±1	14±1	11±1	-0.35±0.09
		LR:A	composite	25±2	14±1	11±1	-0.52±0.05
		LR:B	lobe	3.1±0.3	1.2±0.1	1.0±0.1	-0.742±0.006
		LR:C	lobe	1.3±0.3	0.7±0.1	0.6±0.1	-0.5±0.1

Continued on next page

Continuation from previous page

		LR:D[‡]	lobe	<0.69	<0.52	<0.44	–
		LR:Total	LLS=25kpc	30±1	16±1	12±1	-0.54±0.05
J1010+1413	8.8±0.5	HR:A	nuclear (core cont.)	5.9±0.7	3.2±0.3	2.4±0.2	-0.55±0.07
		HR:B	jet / lobe	<2.4	0.41±0.04	0.27±0.03	-1.3±0.7
		HR:C	hot spot	<3.4	0.22±0.03	0.23±0.03	0.2±0.6
		HR:Total	LLS=9.7kpc	5.9±0.8	3.8±0.6	2.9±0.5	-0.43±0.1
		LR:A	composite	7.5±0.8	3.7±0.4	2.7±0.3	-0.63±0.06
		LR:B	lobe	1.1±0.1	0.72±0.09	0.56±0.06	-0.43±0.08
		LR:C[†]	lobe	<0.48	0.2±0.04	0.27±0.04	0.9±0.6
		LR:Total	LLS=15kpc	8.6±0.9	4.6±0.6	3.6±0.5	-0.55±0.05
J1010+0612	99.3±0.3	HR:A	nuclear (jet/wind)	80±10	30±3	20±2	-0.89±0.08
		LR:A	–	97±10	29±3	20±2	-1.01±0.05
J1100+0846	61.3±0.3	HR:A	nuclear (jet/wind)	42±5	19±2	13±1	-0.71±0.07
		HR:B	artefact / variable[††]	20±3	<0.1	<0.13	–
		HR:Total	LLS=0.8kpc	62±2	19±1	13±1	-0.98±0.01
		LR:A	composite[††]	61±6	19±2	14±1	-0.95±0.02
J1316+1753	11.4±0.4	HR:A	nuclear (core cont.)	1.3±0.3	1.1±0.1	0.83±0.08	-0.3±0.2
		HR:B	jet / lobe	1.8±0.3	0.69±0.07	0.4±0.04	-1.0±0.2
		HR:C	jet / lobe	4.2±0.6	0.92±0.09	0.67±0.07	-1.18±0.05
		HR:Total	LLS=1.4kpc	7.2±0.9	2.7±0.4	1.9±0.3	-0.85±0.08
		LR:A	composite	11±1	3.0±0.3	2.2±0.2	-1.019±0.001
J1338+1503	2.4±0.4	LR:A	star formation?	–	0.7±0.07	0.53±0.05	-0.9±0.6
J1356+1026	59.6±0.4	HR:A	nuclear (jet/wind)	49±5	19±2	14±1	-0.8±0.07
		LR:A	–	58±6	20±2	15±1	-0.88±0.03

Continued on next page

Continuation from previous page

		LR:B	unclear	<0.88	0.57±0.07	0.4±0.06	-1.1±0.8
		LR:Total	LLS=5.6kpc	58±2	21±1	15±1	-0.86±0.03
J1430+1339	26.4±0.4	HR:A	nuclear (jet/wind)	6.3±0.9	2.3±0.2	1.6±0.2	-0.87±0.05
		HR:B	jet / lobe	<2.1	0.69±0.08	0.53±0.06	-0.8±0.7
		HR:Total	LLS=0.8kpc	6.3±0.9	2.9±0.5	2.1±0.4	-0.69±0.1
		LR:A	composite	12±1	3.4±0.3	2.4±0.2	-1.02±0.01
		LR:B	lobe	10±1	3.1±0.3	2.2±0.2	-0.97±0.03
		LR:C	lobe	1.8±0.2	0.7±0.08	0.59±0.07	-0.72±0.03
		LR:Total	LLS=19kpc	24±1	7.2±0.7	5.2±0.6	-0.97±0.02

Notes: (1) object name; (2) the flux density from the FIRST survey; (3) name of structure; (4) interpretation of structure (see Section 2.5.2), or largest linear size observed at that resolution in kpc; (5)-(7) flux density in mJy at 1.5, 5.2 and 7.2 GHz. The errors given are a combination of 1σ random errors and a 10 percent systematic (see Section 2.4.1). 5σ upper limits are given for non-detections; (8) the spectral index (α) defined as $S_\nu \propto \nu^\alpha$ and found by fitting a line through all detected points between 1.5–7.2GHz. The errors quoted are discussed in Section 2.4.1. ‡ Although this component is not detected at 5σ significance in any individual band it is detected in all three at 3σ resulting in a spectral index of -0.5. † Due to the fitting constraints needed to get this component to be well fit by a Gaussian in all three images the fluxes and spectral index for this source are unreliable (see Section 2.4.1). †† We determine that HR:B is either a high S/N beam artefact or a variable component, which then determines if LR:A is a composite or not (see Section 2.5.2).

Radio sizes and position angles of the major axes

Here we provide two quantitative measures of the large scale radio morphology for each source: (1) the largest linear size (LLS) and (2) the position angle of the major axis. For the size measurements, our method is motivated by comparing to published radio sizes for other samples (see Section 2.5.2). Therefore, for both the high and low-resolution showcase images (Fig. 2.5) the largest linear size is calculated as the distance between the peak emission of the two farthest morphological features (see e.g. Kunert-Bajraszewska & Labiano, 2010). For the features well described by Gaussian components the peak of the Gaussian fits are used and for region components the brightest pixel within the region is used to motivate the peak position. These peak positions are shown as magenta points in Fig. 2.5. For the components with only one observed morphological feature in our highest resolution radio images (J1010+0612, J1338+1503 and J1356+1026) we used CASA's IMFIT function to calculate the deconvolved size. The sizes used for these components are the major axis size from these fits which are 115±7.8 marcsec (∼0.2 kpc), 595±41 marcsec (∼2 kpc) and 133±34 marcsec (∼0.3 kpc) respectively. We plot all these sizes in Fig. 2.7.

To obtain the position angle (PA) of the major axis of the radio emission, we defined an axis by a line connecting the two peaks used to calculate the largest linear sizes. To check for consistency with the method used to calculate the position angle of the ionized gas emission (see Section 2.4.2), and to estimate the reliability of these position angles, we fit two dimensional Gaussians to the showcase image (Fig. 2.5) of each target after first applying a Gaussian filter with σ = 0.5 arcsec[10]. We then used the difference between the fit PA and that from connecting the two farthest peaks as an error on the position angle. These errors are between ∼0.2 and 9° (in all cases this was larger than the formal error on the fit). In most cases, the high-resolution radio images were used to identify the positional angle. The two exceptions are J1338+1503 (where we have no high-resolution image) and J1356+1026 where an extended feature is only visible in the low-resolution image. In the two cases where no extended radio features were identified in any of our radio images (J1010+0612 and J1338+1503), the two-dimensional fit in CASA was used to identify the deconvolved PA and its error.

[10]For J1100+0846 we used the e-MERLIN image for this and only burred by a σ = 0.2 arcsec Gaussian filter so as to not completely remove the effect of HR:B.

These radio major axes are indicated by the blue dashed lines in Fig. 2.5.

2.4.2 Ionized gas maps and analyses

Here we describe the steps taken to analyse the ionized gas morphologies and kinematics using our optical IFS data from GMOS and VIMOS (see Section 2.3.3), and how we align these data to our radio maps. We trace the ionized gas kinematics using the [O III]λ5007 emission-line profile and follow the procedures described in detail in Harrison et al. (2014, 2015), with brief details given here.

To map the dominant gas kinematics across the galaxies and compare to the radio morphologies, following Harrison et al. (2014, 2015), we use the following non-parametric definitions to characterise the overall [O III] emission-line profiles:

1. The peak signal-to-noise ratio (S/N), which is the S/N of the emission-line profile at the peak flux density. This allows us to identify the spatial distribution of the emission-line gas, including low surface-brightness features.

2. The 'median velocity' (v_{50}), which is the velocity at 50 percent of the cumulative flux. This allows the 'bulk' ionized gas velocities to be traced.

3. The line width, W_{80}, which is the velocity width that contains 80 percent of the overall emission-line flux. This characterises the overall width of the emission-line, irrespective of the underlying profile shape. For comparison to other work (Section 2.5.4) we also calculate W_{90}, which contains 90 percent of the overall emission-line flux.

4. The asymmetry value (A; see Liu et al., 2013), which is defined as:

$$A \equiv \frac{(v_{90} - v_{50}) - (v_{50} - v_{10})}{W_{80}}, \tag{2.2}$$

   where v_{10} and v_{90}, are the velocities at 10 percent, and 90 percent of the cumulative flux, respectively. A very negative (positive) value of A means that the emission-line profile has a strong blue (red) wing.

To minimize the effect of noise on the broad wings of the emission-lines even in regions of low S/N, we fit the [O III]4959,5007 emission-line profile with multiple

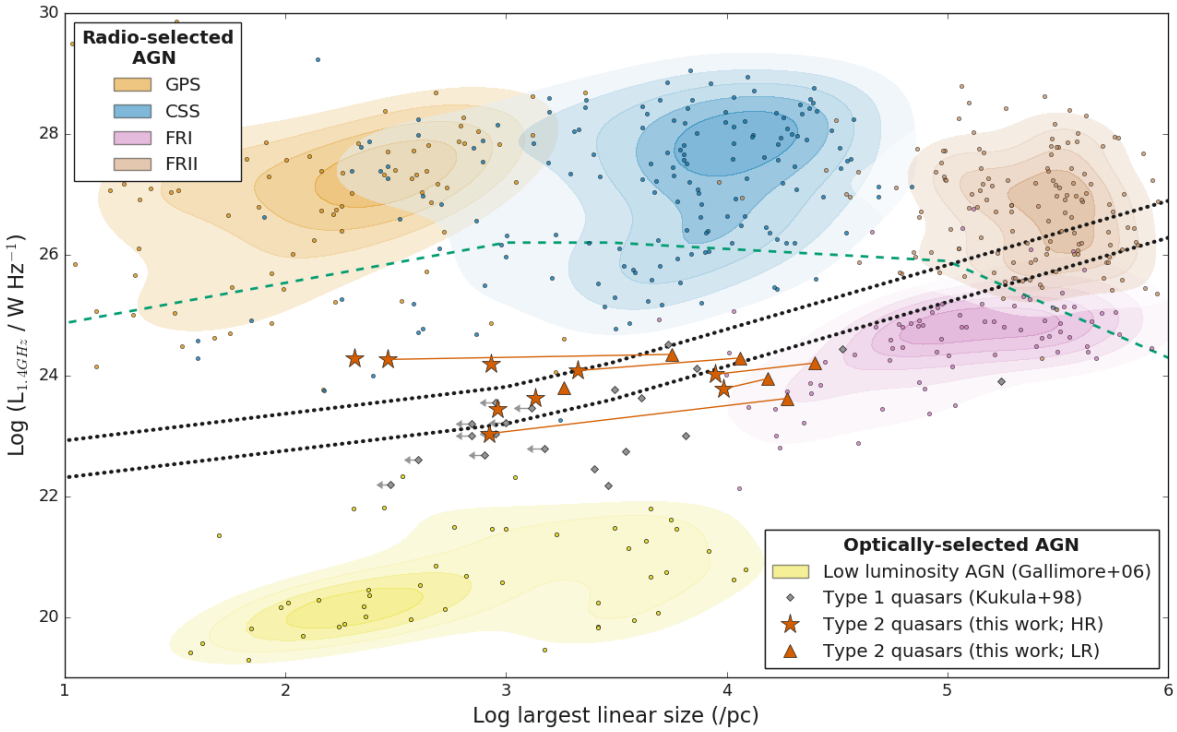

Figure 2.7: Radio luminosity versus largest linear size for our primary sample. The data for radio-selected AGN are from an extensive sample compiled by An & Baan (2012), shown by points and density clouds of the appropriate colour. Seyfert and LINER galaxies ('low luminosity AGN'; Gallimore et al., 2006) and type 1 quasars (Kukula et al., 1998) are also shown as representative optically-selected AGN for comparison. For our data, we show the sizes and total luminosity from both the high-resolution images (HR; stars) and low-resolution images (LR; triangles). Where both are shown for the same source they are connected by a red line. The two black dotted lines approximately separate the area where laminar jet flows are stable (above the lines) and or unstable and turbulent (below) and the green dashed line shows a possible evolutionary track (see Section 2.5.4; An & Baan, 2012). Our quasars and the type 1 quasars share properties with the lowest luminosity compact radio galaxies (CSS; GPS) and low luminosity small FRI radio galaxies.

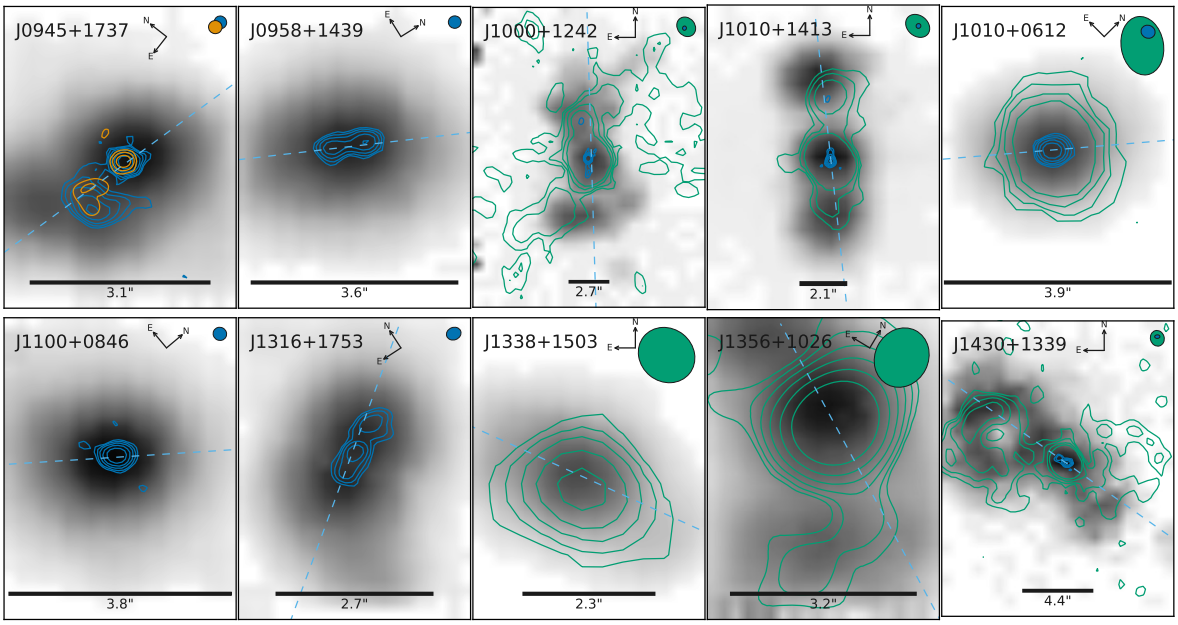

Figure 2.8: The distribution of [O III] emission (S/N maps) with contours overlaid from the radio images shown in Fig. 2.5, colour coded as in that figure. The beam for each radio image is shown as an appropriately coloured ellipse in the top right corner. The dashed line marks the major axis of the [O III] emission (see Section 2.4.2). The scale bar in each panel represents 7 kpc. We observe a close connection between the radio and ionized gas morphologies.

Gaussian components, correcting for the instrumental dispersion, following the methods described in Harrison et al. (2014, 2015). We produce maps of each of the parameters described above by fitting the emission-line profiles in ~0.6 arcsec spatial regions (i.e. comparable to the seeing of the observations). The (S/N) maps are shown in Fig. 2.8 and the other maps are presented in Section 2.5.3.

The systemic redshifts quoted in Table 2.1 are derived using the v_{50} values of the [O III] emission-line profiles extracted from a 3×3 arcsec aperture centred on the quasar's SDSS position in the GMOS data cubes. This corresponds roughly to the velocity of the narrow component, which is often attributed to galaxy kinematics (e.g. Greene & Ho, 2005; Rupke & Veilleux, 2013) or in the case of multiple peaks, lies roughly at the central velocity which, assuming the peaks are dominated by either rotation or symmetric outflows (e.g. Holt et al., 2008), should give a good estimate of the systemic velocity. We note that the values used here vary from the quoted SDSS redshifts by a maximum of ~100 km s^{-1}.

To compare the morphology of the ionized gas quantitatively to our radio

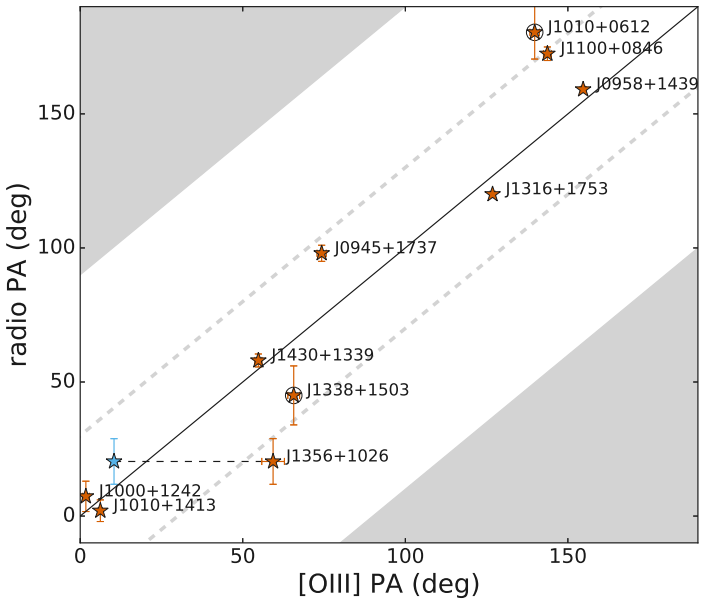

Figure 2.9: Comparison of the position angle of the major axis of the [O III] gas and the radio emission for the galaxies in the primary sample (red stars; black circles surround the two soures where only one radio component is observed and the radio PA is from fitting in CASA). The black line marks x=y, with ±30° separation marked by grey dashed lines. The areas where the two axes would be separated by ≥ 90° is shaded out. For J1356+1026 a light-blue star, connected to the main point by a black dashed line, marks the position angle of the [O III] emission if the outflowing bubble is used (which is not covered by our IFS observations; Greene et al., 2012). There is a close relationship between the spatial distribution of ionized gas and radio emission.

images, we measure a position angle from our S/N maps. We define the major axis of the [O III] emission by fitting a single Gaussian to the S/N map for each galaxy. This method is slightly biased to passing through the brightest features in the [O III]; however, based on visual inspection provides a sufficient measurement of the position angle for our broad comparison to the distribution of radio emission presented in Section 2.5.3. The main exception is J1356+1026 for which the position angle we measure for the ionized gas is determined primarily by a bright region to the north-east of the core with no radio counterpart observed. However, if we define the position angle using the location of the base of the bubble identified by Greene et al. (2012) (see Section 2.5.3), the radio and [O III] emission are well aligned, with a PA separation of ∼10 degrees. These positional angles are shown on the [O III] S/N maps in Fig. 2.8 and are plotted against the radio PAs in Fig. 2.9.

We aligned the IFS data to the SDSS astrometry by creating pseudo-broad band images from the IFS cubes using the common wavelength coverage with SDSS r band[11]. We then anchored the astrometric information of the IFS peak pixel location to the associated position from the SDSS image peak, after blurring each with a 0.2 arcsec Gaussian filter to minimize the impact of bad pixels. We used the brightest morphological components in our high-resolution VLA images (HR:A) to confirm that the SDSS and VLA astrometry were consistent[12]. We found the SDSS positions were scattered around the peak VLA emission with a median offset of 0.13 arcsec, corresponding to 0.24 kpc at a representative redshift of z=0.1. This is sufficient for the comparison we make between the radio morphologies and our $\sim$0.6–0.7 arcsec resolution ionized gas kinematics in this work (Section 2.5.3).

2.5 Results and discussion

In the previous section we presented our 1–7 GHz radio imaging and optical integral field spectroscopy for a sample of ten z<0.2 'radio-quiet' quasars, that were known to host $\gtrsim$kpc-scale ionized outflows based on our previous work (Fig. 2.8; Harrison et al., 2014, 2015). The aim of this section is to establish the origin of the radio emission (Section 2.5.1 and Section 2.5.2), to explore the relationship between the radio and the ionized gas (Section 2.5.3) and to discuss the implication of our results for understanding the radio emission and feedback in the context of the overall AGN population (Section 2.5.4).

2.5.1 Properties of the observed radio emission

We observe radio structures with a range of morphologies from compact features with spatial extents of $\sim$1 kpc (e.g. see the high-resolution image of J0958+1439 in Fig. 2.5) to diffuse lobes extending over $\sim$25 kpc (e.g. see the low-resolution radio image of J1000+1242 in Fig. 2.5). In particular five of our targets show distinctly jet like radio morphologies (J0945+1737, J0958+1439, J1000+1242,

[11]for J1338+1503 the g band filter was used because the r was too effected by bad pixels near the edge of the IFS wavelength range.

[12]J0958+1439 was excluded from this since it seems likely, due to their similar brightness and steep spectral indices, that both of the radio components in this source are lobes around a central, core below our detection threshold.

J1010+1413 and J1316+1753) with three more showing more irregular radio features (J1100+0846, J1356+1026 and J1430+1339; see Section 2.5.2 and Harrison et al., 2015). Specifically, this means that of the nine quasars in the sample consistent with being radio excess in Section 2.2.2 (i.e. all except J1338+1503; see Fig. 2.3 and Table 2.2) 90 percent show spatially resolved radio structures with linear sizes on ∼1–25 kpc scales (see Fig. 2.5 and Fig. 2.7).

To estimate the significance of the features that we have identified in our high-resolution VLA and e-MERLIN data in terms of their contribution to the total radio luminosity at 1.5 GHz, we compare the radio emission from these morphologically-distinct features to the total radio emission (extracted from FIRST but consistent with our observations, see Section 2.4.1; Table 2.1). For the radio excess sources, we find that the total combined fluxes of the high-resolution components, including the central nuclear components, (i.e. HR:Total in Table 2.4) contain ∼60–90 percent of the total radio flux. The exception is J1430+1339 for which the high-resolution components only make up ∼22 percent of the total flux with ∼50 percent of the FIRST flux located in the diffuse low-resolution lobes/bubbles. Below, we discuss how the radio emission that is resolved out on these ∼0.25 arcsec scales may be attributed to star formation.

Importantly, as can be seen by eye in Fig. 2.2 and quantitatively using the Θ_{FIRST} parameter (see Table 2.1), only J1430+1339 is definitively extended and two other sources (J0945+1737 and J1000+1242) are tentatively extended based upon their ∼5 arcsec resolution FIRST data. This is supported by the 'FIRST Classifier' (Alhassan et al., 2018), which automatically identifies FIRST sources as compact or not, and determines that all of our sources are compact except for J1430+1339. This cautions against only relying on low-resolution radio data to identify low power/compact radio structures not associated with star formation in such systems (e.g. see Kimball et al., 2011a; Le et al., 2017).

2.5.2 Origin of the radio emission

Star formation

All of our targets are classified as being 'radio-quiet' based on standard criteria (e.g. Xu et al., 1999, see Fig. 2.3). Furthermore, based on many standard criteria, our sources would *not* be classified as 'radio AGN' (e.g. Best & Heckman, 2012,

Section 2.2.2). The radio emission in such sources is often attributed to being dominated by star formation processes (e.g. Best & Heckman, 2012; Condon et al., 2013). However, through unresolved *UV*–to–*FIR* SED fitting we found that nine of our ten type 2 quasars have more radio emission than can be explained from star formation alone (Section 2.2.2). For these nine targets, star formation estimates from SED fitting imply that only ∼3–11 percent of the observed radio emission at 1.4 GHz are produced by star formation (see Table 2.2).

A comparison of the total 1.4 GHz flux density in our high-resolution images to the total flux obtained from FIRST reveals that ∼10–40 percent of the total radio flux is resolved out across the sample. In all cases, the amount of flux resolved out in the high-resolution images is greater than the 1.4 GHz flux predicted from our calculated star-formation rates using the *FIR*–radio correlation (see Table 2.2; Bell, 2003). This means that the radio emission from star formation can be fully accounted for with a diffuse component not identified in our high-resolution images. Although convincing, we note that these arguments are based upon SED fitting results which are subject to some systematic uncertainties (see Section 2.2.2).

Another piece of evidence that star-formation does not dominate the radio emission in the nine radio excess targets is their complex radio morphologies (see Fig. 2.5; e.g. Colbert et al., 1996). However, it is plausible that star formation could contribute to the central/nuclear emission we see in our high-resolution images. We assess this possibility independently of our SED fitting results. We initially measured the nuclear (HR:A) radio sizes from two-dimensional beam-deconvolved Gaussian fits on the high-resolution images shown in Fig. 2.5 using CASA. We obtain major axis sizes of ∼100–200 marcsec, with errors at least 4 times lower than these values. If we then *assume* that all of the radio emission observed is due to star formation, following Bell (2003) and Kennicutt & Evans (2012); corrected to a Chabrier IMF (Chabrier, 2003) the inferred SFR surface densities are consequently $\log \Sigma \approx 2$–$4[M_\odot/yr/kpc^2]$. These values straddle the physical cut-off set by the Eddington limit from radiation pressure on dust grains (i.e. $\log \Sigma \approx 3.5$), with five of the nine sources lying above the Eddington limit (Murray et al., 2005; Thompson et al., 2005; Hopkins et al., 2010). These results strengthen our SED-based arguments that the radio structures observed in our high-resolution images, including the nuclear components, are not dominated by

star formation processes.

In summary, for all but one of our ten targets we have strong evidence that only ∼3–11 percent of the total flux can be attributed to star formation. All of the radio structures that we see in the high-resolution images appear to be dominated by other processes associated with the AGN.

Quasar winds

Another largely discussed source of the radio emission in radio-quiet quasars is radiatively-driven accretion disc winds which result in synchrotron emitting shocks through the inter-stellar medium (e.g. Jiang et al., 2010; Zakamska & Greene, 2014; Nims et al., 2015; Zakamska et al., 2016; Hwang et al., 2018). Currently there are only rough predictions for this scenario and these are only for spatially-integrated radio properties (i.e. not spatially-resolved). One prediction we can use is that the simple energy conserving outflow model presented by Faucher-Giguère & Quataert (2012), when launched by a quasar with $L_{\rm AGN} \approx 10^{45}$ erg s^{-1}, could plausibly produce radio luminosities consistent with our targets (i.e. $L_{1.4\rm GHz} \approx 10^{23}$–$10^{24}$ W Hz^{-1}) when it interacts with the interstellar medium (Nims et al., 2015). These modelled outflows can reach velocities of ∼1000 km s^{-1}, consistent with those seen in our IFS data (see Section 2.5.3). The predicted steep-spectral index from this model ($\alpha \approx -1$), is also broadly consistent with many of the radio features seen in our observations (see Fig. 2.6 and Table 2.4; Jiang et al., 2010). However there are a large number of assumptions needed to obtain this conclusion and, importantly, we can now use our high-resolution radio data to further investigate quasar winds as the producer of the radio emission in these quasars.

An outflow driven by a quasar wind may produce loosely collimated radio structures on large scales due to the galactic disc collimating the outflow (Alexandroff et al., 2016). However, the shocked wind scenario described above does not seem sufficient to explain the highly collimated radio structures seen in our high-resolution radio images (e.g. particularly see J1000+1242 and J1010+1413 in Fig. 2.5). Furthermore, for J0958+1439, the radio structure appears to be directed *into* the disc (based on the SDSS morphology and [O III] kinematics; see Fig. 2.2 and Fig. 2.10) which also disfavours the wind scenario, but be consistent with randomly oriented radio jets (e.g. Gallimore et al., 2006; Kharb et al.,

2006). Unfortunately, it is challenging to identify the galaxy major axes based on the available imaging for most of our sources (see Fig. 2.2) and our optical IFS data of the targets are not deep enough to model the orientation of the stellar discs (Kang & Woo, 2018). Another alternative to asses the relative orientations would be to identify a molecular galactic disc in these systems using resolved CO observations (Thomson+in prep; Sun et al., 2014).

Jets

Given the ubiquity of jets in radio-loud AGN it is reasonable to assume that low luminosity jets can, at least, contribute to the radio emission observed in AGN with lower radio powers. Indeed, radio jets can be identified in 'radio-quiet' Seyfert galaxies when using sufficiently deep and high-resolution radio observations (Gallimore et al., 2006; Baldi et al., 2018).

Our sample of 'radio-quiet' quasars (see Fig. 2.3) have many properties in common with jetted radio-loud AGN. Specifically, the radio morphologies of our targets as seen in our high-resolution images (Fig. 2.5), in general, look very similar to jetted compact radio galaxies, with a combination of hot spots, jets and cores (e.g. Kimball et al., 2011a; Baldi et al., 2018). The jet interpretation is particularly strong for J1000+1242 and J1010+1413 due to the presence of compact, flat spectrum components (i.e. $\alpha \gtrsim -0.6$; likely to be hot spots; see e.g. Meisenheimer et al., 1989; Carilli et al., 1991) inside the more diffuse steep spectrum lobes which are apparent in our low-resolution images (see Fig. 2.5). For the more compact jet-like structures that we see (e.g. J0958+1439 and J1316+1753) we would require higher spatial resolution images to separate out possible hot spots from steep spectrum lobes (see Table 2.4).

To quantify our comparison to the traditional radio AGN population, we investigate the radio size (LLS; see Section 2.4.1) versus radio luminosity plane for our sources and a literature compilation of radio selected AGN from An & Baan (2012) in Fig. 2.7. In terms of radio luminosity, our targets are consistent with the lowest luminosity radio-identified AGN samples (e.g. Fanti et al., 1987; Kunert-Bajraszewska & Labiano, 2010) and fill in the gap between these 'radio-loud' AGN and Low-Luminosity AGN (e.g. Gallimore et al., 2006). Based on our low-resolution images, where we can see ∼6–20 kpc radio structures, four of our targets overlap with Fanaroff-Riley class I (FRI; Fanaroff & Riley, 1974) galaxies

in the luminosity–size plane. However, the morphologies that we observe in our targets are not clearly consistent with this class of objects, which are more dominated by 'lossy' jets and have relatively weaker hot spots (e.g. as seen in 3C 31; Laing et al., 2008). We discuss possible reasons in Section 2.5.4.

It can be seen in Fig. 2.7 that most of our sources have radio sizes spanning those seen in compact steep spectrum (CSS) radio galaxies (i.e. ∼1–25 kpc; O'Dea, 1998). In the most compact case of J1010+0612, we see no features beyond the nuclear component and the deconvolved radio size is ∼200 pc, such that it is more consistent with those seen in Gigahertz Peak Spectrum (GPS) objects (O'Dea, 1998). Interestingly, there is an observed relationship between radio sizes and the frequency of peak emission in the radio SEDs of compact radio galaxies (Orienti & Dallacasa, 2014). Within our limited ability to identify a turnover in the radio SEDs and to constrain the turnover frequency, our targets are consistent with this relation, with three or four of our targets in particular showing a turnover in the radio SEDs somewhere between FIRST (1.4 GHz) and TGSS (150 MHz; see SEDs in Fig. 2.4 and the supplementary information)[13]. Further multi-frequency radio observations are required to accurately identify the turnover frequencies in our targets.

In a few cases, we see that the brightest nuclear radio component has a moderately flat spectral index (i.e. $\alpha > -0.6$), which may indicate a contribution from radio emission associated directly with an AGN 'core' / accretion disc (Padovani, 2016). Although we do not see strong evidence of flat spectrum AGN cores across the full sample, with most sources showing steep spectral indices in their nuclear regions, there are several possible explanations. For example, the radio core could have recently turned off which would cause its spectral slope to steepen and simultaneously could explain their low radio luminosities (Kunert-Bajraszewska & Labiano, 2010). Alternatively, multiple episodes of jet activity would produce a similar effect with the unresolved, younger jets/lobes outshining the core (e.g. Kharb et al., 2006; Gallimore et al., 2006; Orienti, 2016). Higher resolution images, particularly at higher frequencies, where the relative contribution from a flat spectrum core would be higher, are required for a thorough search for radio cores in our targets (see e.g. Middelberg et al., 2004).

[13]These are J1000+1242, J1100+0846 and J1356+1026, and possibly J1010+0612

Final classification of radio features

Our final classifications of the radio structures that we have observed are given in the 'interpretation' column of Table 2.4. These classifications are based on the morphology, spectral index and distance of the features from the optical centre (Fig. 2.6).

We have presented multiple pieces of evidence that support a jet origin for the majority of the non-nuclear morphological radio features we observe in our targets. However, for the nuclear, central components that have steep spectral indices (i.e. $\alpha < -0.6$), it is plausible that some fraction of the radio emission could be due to radiative winds that have shocked the interstellar medium (Section 2.5.2). Only in J1338+1503 can we not rule out that star-formation dominates the radio emission.

In the high-resolution components the name 'nuclear' was applied to the component closest to nucleus (based on the SDSS position), which in every case was also the brightest radio component (HR:A). We further split the nuclear components by either having a core contribution or being jet/wind dominated based on whether its spectral index was steep ($\alpha < -0.6$) or flat ($\alpha > -0.6$), respectively (see Fig. 2.6)[14]. The non-nuclear high-resolution components are labelled either as jet/lobe or as hot spot depending on if they are steep or flat (see e.g. Dallacasa et al., 2013).

There are a few exceptions to these clean divisions of the high-resolution components, which we label as 'unclear' in Table 2.4. In J0945+1737, HR:C and HR:D are low signal-to-noise features, which may not be truly individual components. Furthermore, HR:B in J1100+0846 which only appears in the e-MERLIN image, is either an extremely high significance artefact or a variable component which is below the detection limit at the epoch of the high resolution VLA observations. Assuming that it is real and non-variable would require a nonphysical spectral index of $\lesssim -4$ using the 5σ upper limits given in Table 2.4. The artefact explanation is supported by HR:B containing ~30 percent of the peak flux, which is comparable to the highest peak in the synthesised beam; however in this case we would expect a symmetric feature on the other side of the core (that we do not see). Assuming a conservative, yet not un-physical, spectral index

[14]For J0958+1439 whose two roughly equal brightness components are approximately equidistant to the optical centre (0.6 vs 0.8 kpc), both are labelled jet / lobe.

of $\lesssim -2$ (Harwood et al., 2017) for HR:B over a ∼1 year period, a factor of ten variability at 5.2 GHz would be required for it to be un-detected in our VLA image (see Table 2.4). Similar scale (1-2 orders of magnitude) variability has been seen on month-year time-scales in radio-quiet quasars (Barvainis et al., 2005). Further multi-epoch observations would be needed to confirm this interpretation.

For the low-resolution radio components, they are generally either labelled as composites, when they are composed of multiple observed high-resolution components, or lobes. Additionally, LR:A in J1338+1503 is classified as probably star formation dominated due to the lack of high-resolution data for this target and it not being classified as radio excess. The final exception to the low-resolution classifications is LR:B in J1356+1026. Its lack of any high-resolution counterpart makes its identification as a jet or a lobe more tenuous.

2.5.3 Connection between ionized gas and radio

We have previously identified $\gtrsim$kpc scale ionized gas outflows in our sample of type 2 quasars (Harrison et al., 2014, 2015). With our new radio images, we are now in a position to compare the radio morphology with the morphological and kinematic structures of the ionized gas that we can obtain from our IFS data of each of these targets (Section 2.4.2).

Morphological alignment of radio and ionized gas

In Fig. 2.8, we compare the spatial distribution of the ionized gas, as traced by [O III], to the distribution of radio emission in each of our ten targets. Specifically for J0945+1737, J1000+1242, J1010+1413 and J1316+1753, where we see extended, distinct ionized gas structures, we see [O III] bright regions in front of, or co-spatial with, the hot spots and jet-like features we identified in Section 2.4.1. Additionally in J1430+1339 we see co-incident bubbles of radio emission and ionized gas (discussed in detail in Harrison et al., 2015; Lansbury et al., 2018). Finally, in J1356+1026, we see a radio structure that is difficult to classify (Section 2.5.2), but is a possible radio jet/lobe. It is located at the top of a ∼12 kpc [O III] bright region extending to the south, not covered by our IFS data, but clearly seen in *HST* imaging (see supplementary material) and confirmed to be an outflowing bubble by Greene et al. (2012).

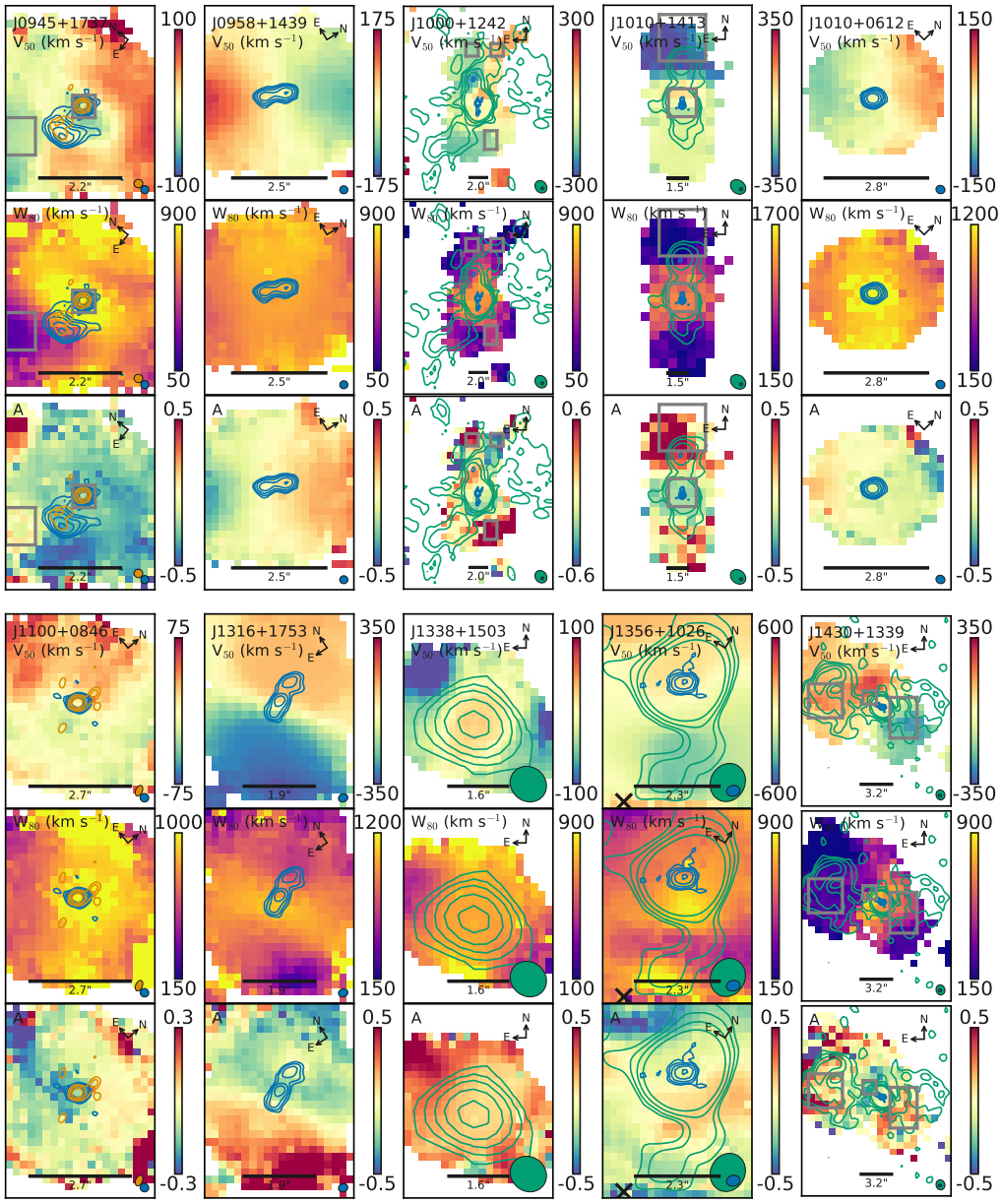

Figure 2.10: For each of the targets in our primary sample, we show maps of three non-parametric emission-line properties measured from the [O III] profile in our optical IFS data (see Section 2.4.2). These are given in columns for each target starting with the 'median velocity' (v_{50}), then the line width (W_{80}) and the asymmetry (A), with each having their respective scale bar shown to the right. In each case, the relevant radio contours are overlaid with the low-resolution VLA in green, the high-resolution VLA in blue and e-MERLIN in orange; in each case the beam(s) are shown in the lower right corner. The scale bar in each image represents 5 kpc. Relevant features / regions discussed in Section 2.5.3 are shown as either grey boxes or black crosses; [O III] emission-line profiles extracted from each of these boxes are shown in the online supplementary material.

The alignment between the ionized gas and radio emission in all ten of our targets is quantified in Fig. 2.9 by comparing the position angle of the semi-major axis of the radio data (blue dashed lines in Fig. 2.5) and ionized gas (blue dashed line in Fig. 2.8). We find that nine targets have alignments within 30 degrees. The exception is J1010+0612, which shows no distinct morphological features on $\sim$ kpc scales in either our radio or [O III] images.

Similar alignments between radio emission and ionized gas have been seen by other studies of 'radio-quiet' quasar and Seyfert populations. These are generally interpreted as the radio jet interacting with the ISM, causing outflows, bow-shocks and sometimes deflecting the jet e.g. Ulvestad & Wilson, 1983; Ferruit et al., 1999; Whittle & Wilson, 2004; Leipski et al., 2006.

Connection between jets and ionized gas kinematics

In Fig. 2.10, we overlay our radio images on top of the kinematics maps from our IFS data (described in Section 2.4.2). We provide further visualisations of the [O III] emission-line profiles at the locations of the radio structures in the supplementary online material. We defer a detailed kinematic analyses of the ionized gas in our targets, and a quantitative comparison to e.g. jet power to future work (also see Harrison et al., 2015). Here we provide a first overview of the relationship between the large-scale kinematic properties of the warm ($\sim 10^4$ K) ionized gas and the radio features we identified in Section 2.4.1.

It can be seen in Fig. 2.10 that the ionized gas shows distinct kinematics at the location of the spatially-extended jet/lobe structures that we have identified in our sources. For J1430+1339, we have already presented (in earlier work) the presence of a broad, high-velocity ionized gas component ($W_{80} \approx 900\,\mathrm{km\,s^{-1}}$ and $v_p \approx 600\,\mathrm{km\,s^{-1}}$; marked by a small central grey box in Fig. 2.10) co-spatial with the HR:B radio jet/lobe structure (Harrison et al., 2015). In addition, the $\sim$20 kpc scale bubbles observed in both the ionized gas and radio emission (see Fig. 2.8; also marked by grey boxes in Fig. 2.10) have narrow emission-line profiles but offset velocities possibly indicative of outflows ($\approx \pm 150$ km s^{-1} respectively). Coronal line measurements in these regions by Villar-Martín et al. (2018) confirm this velocity offset and suggest that the north-east bubble may contain ionization level dependent kinematic substructure.

The potential jets we observe in J0945+1737 and J1010+1413 (HR:B and

HR:C respectively), terminate at brightened blue-shifted [O III] clouds (with $v_p = -27$ and $v_p = -316$ km s^{-1}, respectively; see grey boxes in Fig. 2.10). This is evidence of jets hitting a cloud of gas, both pushing the gas away and deflecting the jet (see e.g. Leipski et al., 2006). For J1010+1413 this supports the interpretation that the ionized gas region in the north is part of an outflow rather than being passively illuminated by the AGN (see also Sun et al., 2017). In J1316+1753, we see strong double peaked [O III] emission, offset in velocity by ∼400 km s^{-1}, with the blue and red shifted gas being brightest at the termination of each jet (also see additional figures in the supplementary material). J0958+1439 shows a similar kinematic line splitting structure and co-spatial jets/lobes. Such observations indicate possible jet-driven outflows similar to that seen in Rosario et al. (2010).

Striking evidence of outflowing bubbles of gas being launched near the base of likely jets/lobes is observed in both J1000+1242 and J1356+1026 (HR:B and LR:B, respectively; Fig. 2.10). For J1000+1242, this is seen in the kinematic maps by the blue-to-red ∼200 km s^{-1} velocity shift in the v_{50} map from east–west (extracted from the two northerly regions in Fig. 2.10) and the large asymmetry values in both the north and south (A≈1). This bubble is characterised by velocity splitting of the [O III] emission-line seen using a pseudo-slit extracted from our IFS data in Fig. 2.11. We find that the base of this southern bubble corresponds to the location of the southern jet (HR:B). No sign of this bubble was seen in long-slit observations with a similar alignment in Sun et al. (2017), possibly due to the longer exposure time and better spectral resolution of our data. A ∼12 kpc outflowing bubble in J1356+1026 was discovered by long-slit observations in Greene et al. (2012), with a very similar kinematic structure to the one we see for J1000+1242 in Fig. 2.11. For J1356+1026, the bubble is beyond the field-of-view covered by our GMOS data cube. However, here we have discovered a radio feature that terminates at the base of the outflowing bubble (LR:B; see the black 'x' in Fig. 2.10). Although the origin of this radio structure is ambiguous (see Section 2.5.2), this may also be due to a jet that terminates at this location and drives the outflow.

We note that the spatial extent of the outflows in many of our sources (J1000+1242, J1010+1413, J1356+1026 and J1430+1339 in particular) are underestimated, if the outflow size is based solely upon the spatial extent of the

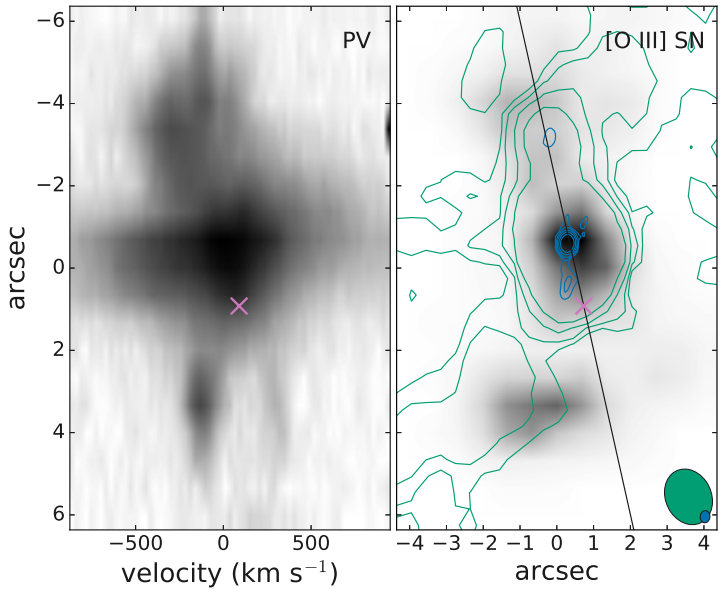

Figure 2.11: A position velocity diagram for J1000+1242 (left) extracted along a 2 arcsec wide pseudo-long slit from our VIMOS data with the slit position shown as the black line on the [O III] S/N map, with radio contours from Fig. 2.5 over-plotted (right). We see the signature line splitting of a quasi-spherical outflow starting approximately at the pink 'x' in both panels. This bubble seems to begin roughly at the base of a probable radio jet (HR:B). We have also identified a radio structure at the base of a similar outflowing bubble in J1356+1026 (identified by Greene et al. (2012); see black 'x' in Fig. 2.10).

broad [O III] emission-line component (see e.g. Kang & Woo, 2018) and highlights the need for careful analysis when establishing outflow properties (e.g. see Harrison et al., 2018).

In summary, we observe a strong relationship between the radio jets/lobes and the ionized gas kinematics in all seven of the targets where we see unambiguous radio structures on 1–25 kpc scales.

2.5.4 Radio jets associated with quasar outflows and feedback

In this section, we put our work into the context of observational and theoretical studies of other AGN and quasars. In particular, we focus on the properties of the likely radio jets in our sources compared to other samples and theoretical predictions. We explore the implication of our results for understanding the impact of jets on the host galaxies of our targets, and how that relates to the quasar population as a whole.

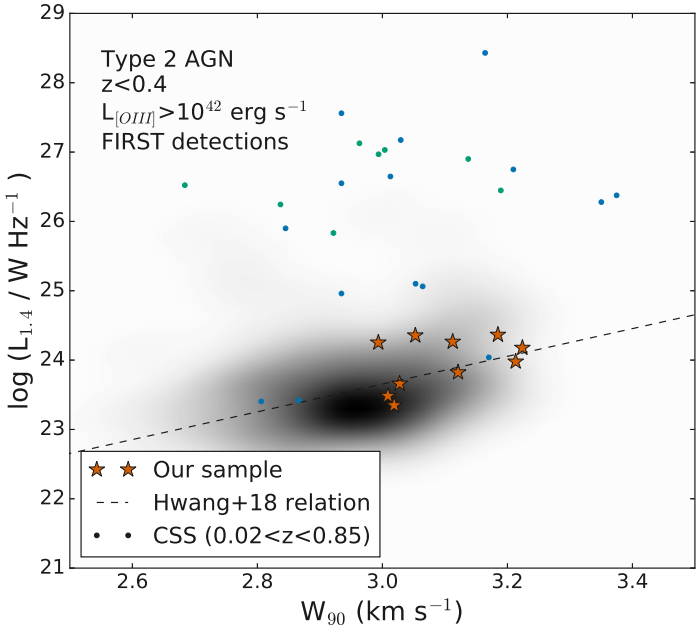

Figure 2.12: The width of the [O III] line (W_{90}) as a function of radio luminosity. The grey-scale shows the underlying distribution of type 2 AGN (Mullaney et al., 2013) with z<0.4 and a luminosity cut of $L_{[\mathrm{OIII}]} > 10^{42}$ erg s^{-1} (i.e. the selection criterion of our sample; Fig. 2.1) that are detected in FIRST. A similar selection criterion was used by Hwang et al. (2018), using the z<0.8 quasars from Zakamska & Greene (2014), to produce the relationship shown by the dashed line. Our sample is shown as red stars, where W_{90} is measured from our GMOS data in a 3 arcsec aperture (approximating the SDSS fibre). Circles mark the CSS radio AGN from Holt et al. (2008) (green; using the FWHM of their single Gaussian component fits), and Gelderman & Whittle (1994) (blue). Our sources have more representative radio luminosities compared to CSS radio galaxies; however, we have shown that they also contain compact radio jets. Consequently, radio jets should be explored as a crucial feedback mechanism for all quasars.

Our sources share many properties with the typically more powerful, compact radio galaxies (see Section 2.5.2; Fig. 2.7). It has been postulated that the compact radio galaxies (with $\lesssim$10 kpc scale jets) could evolve into traditional $\approx$100 kpc double radio galaxies (e.g. see discussion in An & Baan, 2012, and the dashed track in Fig. 2.7). However, not all compact radio sources may be destined to evolve into traditional radio galaxies. Of particular relevance here is the idea that jets can get frustrated/stagnated by the dense interstellar medium (e.g. van Breugel et al., 1984; O'Dea et al., 1991; Bicknell et al., 2018) and that these jets may consequently become unstable at small sizes (see dotted tracks in Fig. 2.7; An & Baan, 2012). Our targets, along with a sample of type 1 quasars from Kukula et al. (1998) straddle this instability criterion at sizes of only a few kpc (Fig. 2.7). Within the model presented by An & Baan (2012), a characteristic of obstructed jets would be a hot spot and a plume-like diffuse structure beyond the hot spot – a strikingly good description of what we sometimes see in our targets, in particular for J1010+1413 and J1000+1242 (Fig. 2.5). We see further evidence that jets are interacting with the interstellar medium in their host galaxies due to the highly disturbed ionized gas, outflowing bubbles and brightened [O III] structures observed co-incident with the jets/lobes (Fig. 2.8 and Fig. 2.10; Section 2.5.3).

It has been observed for several decades that jets interact with their interstellar medium in 'radio-loud' samples as well as 'low-luminosity' AGN and Seyferts (e.g. van Breugel et al., 1984; Whittle et al., 1986; Pedlar et al., 1989; Capetti et al., 1996; Steffen et al., 1997; Ferruit et al., 1998; Mahony et al., 2013; Riffel et al., 2014; Morganti et al., 2015; Rodríguez-Ardila et al., 2017; Nesvadba et al., 2017; May et al., 2018; Morganti et al., 2018). It has further been noted that compact radio galaxies may host the most extreme ionized gas kinematics because the radio jets are confined in the interstellar medium (e.g. Holt et al., 2008). In this work, we have provided observational evidence that compact radio jets may be crucial for interacting with the interstellar medium and driving outflows, even in 'radio-quiet' quasars, sources where radiatively driven winds are often assumed to be the most important (e.g. Zakamska & Greene, 2014; Hwang et al., 2018).

Hwang et al. (2018) suggest that the source of the radio emission in radio-quiet quasars (suggested to be winds) is distinct from their radio-loud counterparts (suggested to be jets). This is largely based on a sample of radio-quiet AGN for which the width of the [O III] and the radio luminosity are roughly correlated,

while the jetted CSS sources from Holt et al. (2008) have more radio emission for a given [O III] width (see Fig. 2.12). However, these results are based on low-resolution radio data, which are insensitive to small-scale jets. We find that our targets lie on the relationship seen by 'radio-quiet' sources and we have presented several pieces of evidence that our sources contain jets that are interacting with the interstellar medium. Furthermore, the lower power end of the sample of jetted CSS sources studied by Gelderman & Whittle (1994) also lie on the 'radio-quiet' relationship in Fig. 2.12.

Cutting-edge models show that compact jets interacting with the interstellar medium may be a crucial aspect of 'AGN feedback' and possibly the most efficient mechanism for driving powerful outflows (e.g. Wagner et al., 2012; Mukherjee et al., 2016; Bicknell et al., 2018; Cielo et al., 2018). For example, Mukherjee et al. (2018) show that jets can increase the turbulence of the gas within the disc and simultaneously drive larger-scale outflowing bubbles, in qualitative agreement with the observations presented here for some of our targets (e.g. J1000+1242; J1356+1026; J1430+1339; see Fig. 2.10 and 2.11). In future work, we will use our IFS data and radio imaging to measure the detailed outflow energetics in relation to the jet power and assess if the jets have a negative or positive impact on the star formation in their host galaxies (e.g. Mukherjee et al., 2018).

Our results support a scenario where compact radio jets are a crucial feedback mechanism during a quasar phase. Further work is now needed to decouple the relative roles of jets and winds in contributing to the total radio emission in a larger sample of quasars and their relative importance for feedback on their host galaxies. To this end, we are already working on an expanded sample selected from Mullaney et al. (2013), removing the pre-selection on sources with known outflows (see Fig. 2.1). Future, higher spatial resolution radio images (e.g. VLBI) will also help to disentangle the two forms of emission.

2.6 Conclusions

We have presented 0.25–1 arcsecond resolution, 1–7 GHz radio images and integral field spectroscopy of a sample of ten z<0.2 type 2 quasars ($\log[L_{\rm AGN}/{\rm erg\ s^{-1}}] \gtrsim 45$) selected to have ionized gas outflows based on their broad [O III] line widths (Fig. 2.1). Our previous work revealed that the outflows in these sources were

located on $\gtrsim$kpc scales (Harrison et al., 2014, 2015). The targets have moderate radio luminosities ($\log[L_{1.4\,\mathrm{GHz}}/\mathrm{W\,Hz^{-1}}]$=23.3–24.4) and are classified as 'radio-quiet' and not as 'radio AGN' using many traditional criteria (e.g. Xu et al., 1999; Best & Heckman, 2012). However, based on our *UV–FIR* SED fitting, all but one of these targets are classified 'radio excess', with $\gtrsim$90% of the total 1.4 GHz radio luminosity not accounted for by star formation (Fig. 2.3). In this work, we have explored the origin of this radio emission and its relationship to the ionized gas distribution and kinematics. Our main conclusions are the following:

- Of the nine radio excess sources, we identify radio features associated with the AGN (lobes, jets, hot spots) separated by 1–25 kpc in 7 or 8 (see Section 2.4.1; Fig. 2.5).

- Based on the radio size–luminosity relationship, these quasars are consistent with radio-identified AGN hosting radio jets: low power compact radio galaxies or small FRI galaxies. Furthermore, the collimated appearance of many of the radio structures we observe leads us to favour radio jets as the dominant cause of the extended radio structures in the majority of our sample (see Section 2.5.2; Fig. 2.5; Fig. 2.7).

- For eight of the targets, we identify compact nuclear radio components ($\lesssim$400 pc) that also appear to be dominated by processes associated with the AGN. Most of these nuclear regions have a steep 1–7 GHz radio spectral index (i.e. $\alpha < -0.6$) which could be attributed to small-scale jets/lobes or shocked interstellar medium from quasar winds. Three have flatter spectral indices, possibly revealing a contribution from an AGN core (see Section 2.5.2; Fig. 2.6).

- We show that there are strong indications of interactions between the observed radio jet structures and the warm ionized gas (as traced by the [O III] emission-line). In particular, the two phases are spatially coincident and the radio jets/lobes we observed are co-spatial with distinct kinematic components. These observations are consistent with jet–ISM interactions resulting in galactic outflows and deflected jets (see Section 2.5.3; Fig. 2.8; Fig. 2.9; Fig 2.10).

In this work we provide evidence that compact radio jets ($\approx$1–25 kpc) are a common feature in radiatively dominated ('radio-quiet') quasar systems and an important mechanism for driving outflows. We have demonstrated the importance of deep high-resolution radio imaging to identify the origin of the radio emission in such systems and to search for jet–ISM interactions. Our observations are in qualitative agreement with models where radio jets become stagnated as they plough into the host galaxy material, and simultaneously increase turbulence and drive large-scale outflows. Future work, in particular focusing on the energetics of both the jets and the outflows is needed to quantitatively test these models and to establish the impact of compact jets on the evolution of massive galaxies.

Acknowledgements

We thank Tao An for graciously sharing the compiled radio data used to make Fig. 2.7. We thank the referee for their prompt and constructive comments. The National Radio Astronomy Observatory is a facility of the National Science Foundation operated under cooperative agreement by Associated Universities, Inc. e-MERLIN (enhanced Multi-Element Radio Linked Interferometer Network) is a National Facility operated by the University of Manchester at Jodrell Bank Observatory on behalf of the Science and Technology Facilities Council. Based on observations collected at the European Southern Observatory under ESO programmes 092.B-0062. Based on observations made with the NASA/ESA Hubble Space Telescope, obtained from the data archive at the Space Telescope Science Institute. STScI is operated by the Association of Universities for Research in Astronomy, Inc. under NASA contract NAS 5-26555. MEJ and CC acknowledge support from the IMPRS on Astrophysics at the LMU (Munich).

Chapter 3

High molecular gas content and star formation rates in local galaxies that host quasars, outflows and jets

M. E. Jarvis, C. M. Harrison, V. Mainieri, G. Calistro Rivera, P. Jethwa, Z.-Y. Zhang, D. M. Alexander, C. Circosta, T. Costa, C. De Breuck, D. Kakkad, P. Kharb, G. B. Lansbury, A. P. Thomson

Monthly Notices of the Royal Astronomical Society, Volume 498, Issue 2, October 2020, Pages 1560–1575

Abstract: We use a sample of powerful $z\approx0.1$ type 2 quasars ('obscured'; $\log[L_{\rm AGN}/{\rm erg\,s^{-1}}]\gtrsim45$), which host kiloparsec-scale ionized outflows and jets, to identify possible signatures of AGN feedback on the total molecular gas reservoirs of their host galaxies. Specifically, we present Atacama Pathfinder EXperiment (APEX) observations of the CO(2–1) transition for nine sources and the CO(6–5) for a subset of three. We find that the majority of our sample reside in starburst galaxies (average specific star formation rates of 1.7 $\rm Gyr^{-1}$), with the seven CO-detected quasars also having large molecular gas reservoirs (average $\rm M_{gas}$=1.3×10^{10} $\rm M_{\odot}$), even though we had no pre-selection on the star formation or molecular gas properties. Despite the presence of quasars and outflows, we find that the molecular gas fractions ($\rm M_{gas}/M_{\star}$=0.1–1.2) and depletion times ($\rm M_{gas}$/SFR=0.16–0.95 Gyr) are consistent with those expected for the overall galaxy population with matched stellar masses and specific star formation rates. Furthermore, for at least two of the three targets with the required measurements, the CO(6–5)/CO(2–1) emission-line ratios are consistent with star formation

dominating the CO excitation over this range of transitions. The targets in our study represent a gas-rich phase of galaxy evolution with simultaneously high levels of star formation and nuclear activity; furthermore, the jets and outflows do not have an immediate appreciable impact on the global molecular gas reservoirs.

3.1 Introduction

The energy from accreting supermassive black holes (i.e. active galactic nuclei: AGN) is widely accepted to be responsible for the global quenching of star formation in massive galaxies (AGN feedback; e.g. see reviews in Alexander & Hickox, 2012; Fabian, 2012; Harrison, 2017). However, the physical mechanisms by which this energy couples to the gas on galactic scales and its precise impact on the host galaxy remains unclear. Multi-wavelength studies are proving to be vital in both determining the mechanism and impact of feedback (see e.g. Cicone et al., 2018; Cresci & Maiolino, 2018).

AGN are thought to be able to remove gas from their host galaxies via outflows. These outflows can be powered by the interaction between interstellar gas and small-scale accretion disc winds (Faucher-Giguère & Quataert, 2012; Zubovas & King, 2012) or directly via radiation pressure on dust (Ishibashi & Fabian, 2015; Thompson et al., 2015; Bieri et al., 2017; Costa et al., 2018a,b), particularly for AGN with high Eddington ratios ('quasar' or 'radiative mode'). While typically thought to operate primarily by preventing hot halo gas from cooling, via the so called 'radio' or 'maintenance mode' (e.g. Churazov et al., 2005), collimated jets are also likely to drive outflows of interstellar gas (Wagner et al., 2012; Mukherjee et al., 2016), blurring the division between 'quasar' and 'maintenance' modes (see e.g. Chapter 2, Jarvis et al., 2019).

In particular, the potential impact of AGN is most commonly observed through high velocity ionized gas outflows (see e.g. Karouzos et al., 2016; Morganti, 2017; Davies et al., 2020). However, if the direct impact of AGN upon star formation is to be understood, it is the cold (~10 K) molecular gas (primarily composed of H_2) which forms the fuel for star formation, that must be considered (Morganti, 2017). Since cold molecular gas is not directly observable in H_2 emission, carbon monoxide (^{12}CO which has a permanent dipole moment), is most often used as a tracer of these cold molecular clouds (see e.g. Bolatto et al., 2013; Carilli &

Walter, 2013, and references therein). Specifically, the ground level transition (J=1–0) has an excitation temperature of just 5.53 K, making it a good tracer of the total cold molecular gas (see e.g. Bolatto et al., 2013), while higher-J CO lines (i.e. J$\gtrsim$4–3) are produced from warmer, denser gas (see e.g. van der Werf et al., 2010; Daddi et al., 2015; Mashian et al., 2015; Kamenetzky et al., 2017).

Molecular gas outflows traced by CO gas have been identified in both radio and quasar mode AGN (see e.g. Cicone et al., 2014; King & Pounds, 2015; Morganti et al., 2015; Bischetti et al., 2019; Fotopoulou et al., 2019; Oosterloo et al., 2019; Lutz et al., 2020; Veilleux et al., 2020). However these outflows typically only represent ∼10 per cent of the molecular gas luminosity (see e.g. Fluetsch et al., 2019; Lutz et al., 2020) and so are difficult to observe. Instead, the impact of AGN on the molecular gas in their host galaxies is often probed through the total molecular gas content (see e.g. Bertram et al., 2007; Xia et al., 2012; Husemann et al., 2017; Rosario et al., 2018). Specifically, the gas mass and the molecular gas fraction relative to the star formation rate are used to assess the potential impact of the AGN on the star formation efficiency and / or their ability to deplete the molecular gas supply within the host galaxies (e.g. Kakkad et al., 2017; Perna et al., 2018). In addition to removing molecular gas through outflows, AGN and mechanical feedback from jets, can heat the molecular gas, which both inhibits star formation and causes the CO to emit in higher transitions (see e.g. Papadopoulos et al., 2010).

Our recent results, combining integral field spectrographic (IFS) and radio observations, have identified a sample of luminous ($L_{[O\ III]} > 10^{42}$ erg s^{-1}) type 2 (obscured) AGN with signatures of jets and extended ionized gas outflows. These systems represent the ideal environment to search for signatures of feedback since they have the strong potential to interact with their environments both mechanically and radiatively (Harrison et al., 2014, 2015; Lansbury et al., 2018; Jarvis et al., 2019). In this work we use unresolved CO measurements of the (2–1) and (6–5) transitions, to investigate the molecular gas content of these systems and look for signatures of the impact of the AGN and jet in particular, through thermal excitation and depletion of the gas reservoir.

In Section 3.2 we introduce our sample, describe our spectral energy distribution (SED) fitting approach used to determine key galaxy and AGN properties (Section 3.2.1), and compare our sample to the star forming main sequence (Sec-

tion 3.2.2). Section 3.3 describes our data, data reduction (Section 3.3.1) and analysis (Section 3.3.2). In Section 3.4 we describe our results and in Section 3.5 we compare the total molecular gas and CO excitation in our systems to literature results (Sections 3.5.1 and 3.5.2 respectively) and we discuss these results in the wider context of galaxy evolution in Section 3.5.3. We present our conclusions in Section 3.6. We adopt H_0=70km s^{-1}Mpc^{-1}, Ω_M=0.3, Ω_Λ=0.7 throughout, and assume a Chabrier (2003) initial mass function (IMF).

3.2 Sample selection and properties

Here we present observations of the molecular gas in nine type 2 quasars. This sample was designed to be representative of powerful local AGN, with signatures of feedback, and therefore is ideal for identifying the impact of the AGN on the molecular gas reservoir. In particular, by selecting sources with previously identified ionized gas outflows and radio jets, the AGN should be able to impact the molecular gas through radiative and / or mechanical feedback by exciting and / or removing the molecular gas.

In Fig. 3.1 we show how our targets were selected from the parent sample of 24 264 $z < 0.4$ spectroscopically identified AGN[1] presented in Mullaney et al. (2013). In Harrison et al. (2014) we selected 16 $z < 0.2$ type 2 AGN with luminous [O III] outflows: $L_{[O\ III]} > 10^{41.7}$ erg s^{-1} and full width half maximum (FWHM) $\gtrsim$700 km s^{-1} (see Fig. 3.1). The only other selection criteria was an ra / dec cut to select sources observable from Gemini-South. Using IFS data we revealed that these outflows are extended on $\gtrsim$kpc scales. For this work, we selected the nine of these 16 targets with the highest [O III] luminosities (i.e. $L_{[O\ III]} > 10^{42}$ erg s^{-1}) and radio luminosities ($\log[L_{1.4GHz}/W\,Hz^{-1}] \geq 23.5$; see Fig. 3.1). In Chapter 2 (Jarvis et al., 2019) we established that the radio luminosity of these targets is dominated by emission from the AGN, with eight of the nine exhibiting extended radio structures on 1–25 kpc scales, which are likely radio jets (J1010+0612 is the only target without any evidence for an extended radio structure). The spatial coincidence of these radio features to outflows and disturbed ionized gas features visible in the IFS data strongly suggests jet–gas interactions in the majority of this sample (see Harrison et al., 2015; Jarvis et al.,

[1] using a combination of 'BPT' diagnostics (Baldwin et al., 1981), and emission-line widths.

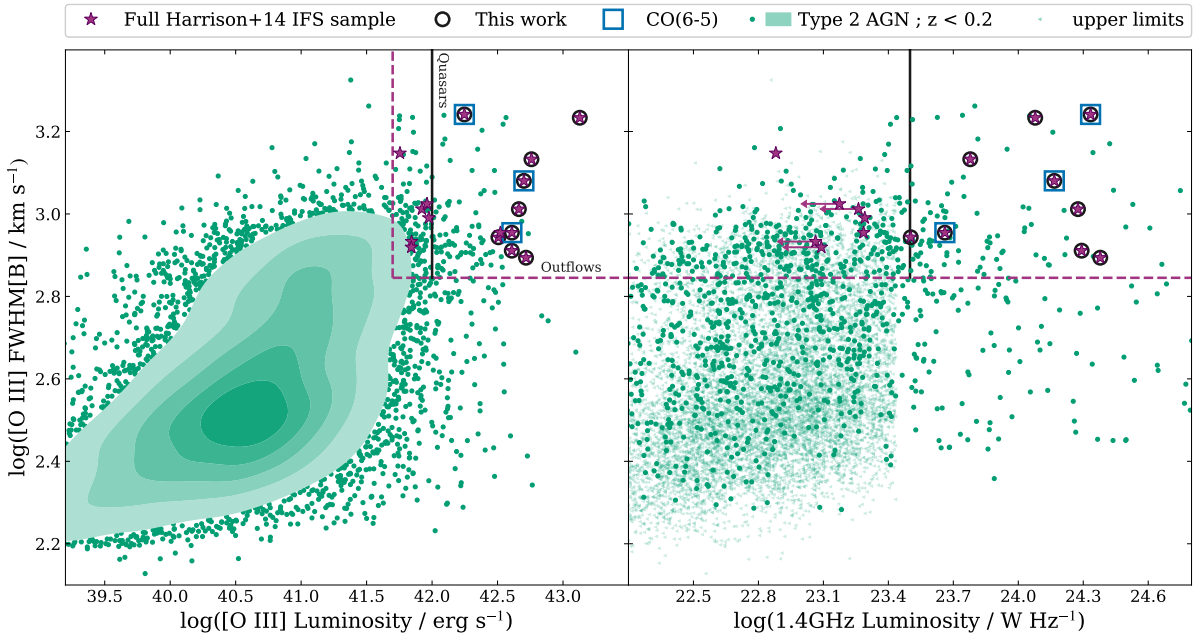

Figure 3.1: This figure shows the basic sample properties and selection criteria. In each panel the full Harrison et al. (2014) sample are shown as magenta stars with the sources studied here highlighted with black circles and the APEX CO(6–5) sample additionally highlighted with blue squares (values tabulated in Table 2.1 Jarvis et al., 2019). Our parent population of $z < 0.2$ type 2 AGN are shown as green data points and contours (Mullaney et al., 2013). The dashed magenta lines show the selection criteria used in Harrison et al. (2014) and the black solid lines mark the additional selection criteria applied for the sample in this work. *Left*: The FWHM of the broadest, luminous [O III] emission-line component versus the total [O III] luminosity (see Harrison et al., 2014; Jarvis et al., 2019). *Right*: The FWHM versus the radio luminosity (from FIRST fluxes), where the parent sample sources with only upper limits on their radio luminosity are shown as light green triangles.

2019). The basic sample properties are provided in Table 3.1.

3.2.1 SED fitting

A significant amount of the analysis in this paper relies on having reliable estimates of the star formation rates and stellar masses in our systems without contamination from the AGN. Since the AGN in this work are all type 2, the AGN has only a small contribution to the *UV* – optical emission but may still contribute significantly to the infrared emission. As such, in Chapter 2 (Jarvis et al., 2019) we performed *UV–IR* SED fitting using the 'Code Investigating

GALaxy Emission' (CIGALE[2]; Noll et al. 2009; Buat et al. 2015; Ciesla et al. 2015) to derive the host galaxy and AGN properties of this sample. We used data from GALEX, SDSS, 2MASS, WISE, IRAS, and where available archival, *Herschel* PACS and SPIRE, for these SED fits, corrected for Galactic extinction (see Chapter 2, Jarvis et al., 2019). Specifically, CIGALE simultaneously fits the attenuated stellar emission, star formation heated dust emission, AGN emission (from the accretion disc and dust heating) and nebular emission. Of particular relevance for this work are the stellar mass ($M_\star$) and the star formation rate (SFR) of the host galaxies, which are listed in Table 3.1. We calculated these star formation rates from the SED-derived infrared luminosity due to star formation ($L_{\rm IR,SF}$) and the relationship from Kennicutt & Evans (2012), converting from a Kroupa to a Chabrier IMF by multiplying by 0.94 (Madau & Dickinson, 2014), specifically: SFR=$L_{\rm IR}/(2.57\times10^{43})\times0.94$, with $L_{\rm IR}$ in erg s^{-1} and SFR in $M_\odot$ yr^{-1}. For further details of the SED fitting, derived quantities and uncertainties we refer the reader to Chapter 2 (Jarvis et al., 2019).

In Table 3.1 the quoted uncertainties are 1σ formal errors from the CIGALE fits and do not include systematics. However, there is a 0.3 dex systematic uncertainty expected on the infrared luminosity and stellar mass from the SED fitting (Gruppioni et al., 2008; Mancini et al., 2011; Santini et al., 2015). This results in a 0.42 dex systematic uncertainty for the star formation rate values, from adding in quadrature the systematic uncertainties from the SED fitting and the 0.3 dex systematic uncertainty on the conversion between $L_{\rm IR}$ and SFR (Kennicutt & Evans, 2012). Our sources have stellar masses in the range $8\times10^9 < M_\star < 1.1\times10^{11} M_\odot$ and star formation rates in the range $8 < {\rm SFR} < 84\ M_\odot {\rm yr}^{-1}$. All but one of our sources (J1430+1339) are classified as Luminous Infrared Galaxies (LIRGs) based upon their infrared luminosities due to star formation (10^{11}–10^{12} $L_\odot$; see Fig. 3.2).

[2]https://cigale.lam.fr

Table 3.1: Target list and properties.

Name	RA (J2000)	Dec (J2000)	z	$\log(M_\star)$ ($M_\odot$)	$\log(L_{IR,SF})$ (erg s^{-1})	SFR ($M_\odot$ yr^{-1})	Δ_{MS}	[O III]/Hβ
(1)	(2)	(3)	(4)	(5)	(6)	(7)	(8)	(9)
J0945+1737	09:45:21.33	+17:37:53.2	0.1281	$10.1^{+0.09}_{-0.12}$	45.3±0.02	73±4	36.1	1.015±0.005
J0958+1439	09:58:16.88	+14:39:23.7	0.1091	$10.74^{+0.09}_{-0.12}$	$44.6^{+0.2}_{-0.3}$	15±8	2.4	1.124±0.005
J1000+1242	10:00:13.14	+12:42:26.2	0.1479	$9.9^{+0.3}_{-0.7}$	$45.0^{+0.1}_{-0.2}$	40±10	24.8	0.988±0.008
J1010+1413	10:10:22.95	+14:13:00.9	0.1992	11.0±0.1	$45.1^{+0.2}_{-0.4}$	50±30	3.7	1.1±0.005
J1010+0612	10:10:43.36	+06:12:01.4	0.0982	$10.5^{+0.3}_{-0.9}$	44.99±0.04	35±3	8.7	0.828±0.005
J1100+0846	11:00:12.38	+08:46:16.3	0.1004	$10.7^{+0.3}_{-2.4}$	45.0±0.1	34±9	6.2	1.098±0.005
J1316+1753	13:16:42.90	+17:53:32.5	0.1504	$11.0^{+0.2}_{-0.3}$	$45.1^{+0.2}_{-0.3}$	40±20	4.3	1.082±0.005
J1356+1026	13:56:46.10	+10:26:09.0	0.1233	$10.64^{+0.09}_{-0.11}$	45.36±0.02	84±4	15.3	0.982±0.004
J1430+1339	14:30:29.88	+13:39:12.0	0.0852	$10.86^{+0.05}_{-0.06}$	$44.32^{+0.06}_{-0.07}$	8±1	1.0	0.883±0.004

Notes: (1) Object name; (2)–(3) optical RA and Dec positions from SDSS (DR7); (4) Systemic redshifts from GMOS IFS data ([O III]; Chapter 2, Jarvis et al., 2019); (5)–(8) are directly from, or are derived from, the CIGALE SED fits first presented in Chapter 2 (Jarvis et al., 2019) and discussed here in Section 3.2.1: (5) Stellar mass from SED fitting (there is an additional ~0.3 dex systemic uncertainty not included in the quoted errors); (6) Infrared luminosity from star formation in the range 8–1000 μm (i.e. excluding the AGN contribution; there is a ~0.3 dex systemic uncertainty not included in the quoted errors); (7) Star formation rate calculated from $L_{IR,SF}$ (there is a ~0.42 dex systematic uncertainty not included in the quoted errors; see Section 3.2.1); (8) distance of the source from the Sargent et al. (2014) main sequence, defined as sSFR/sSFR$_{MS}$ (see Section 3.2.2); (9) Ratio of the [O III]5007 to Hβ emission lines from SDSS DR7 catalogues (single Gaussian fits; Abazajian et al., 2009). Additional details of these sources (e.g. radio luminosity and AGN bolometric luminosity) are given in Chapter 2 (Jarvis et al., 2019).

We verified these values by performing independent SED fits using another code: AGNfitter (Calistro Rivera et al., 2016). The main difference between this code and the CIGALE code is that CIGALE assumes an energy balance between the *IR* and optical emission for the host galaxy, where AGNfitter considers the two almost independently with a prior that the energy from the *IR* must be at least equal to the energy attenuated from the stellar emission. For the three of our sources with *Herschel* observations, which have the best available coverage of the *FIR* emission (namely J1100+0846, J1356+1026 and J1430+1339; see Chapter 2, Jarvis et al., 2019), the *IR* derived SFRs agree within 0.27 dex (i.e. within the systematic uncertainty). For the remaining six sources the best SFR from AGNfitter is based on the optical emission alone and as such is a lower limit on the actual SFR (Calistro Rivera et al., 2016). In each case this limit is consistent with our SFR from CIGALE. The stellar masses from AGNfitter are on average 0.19 dex higher than those from CIGALE (i.e. within the systematic uncertainty), and the only significant outliers are J1000+1242 and J1010+0612 which have AGNfitter derived stellar masses 0.67 and 0.48 dex larger than those from CIGALE respectively. We note that using the AGNfitter stellar masses and SFRs would not change the main conclusion of this work. In summary, we trust the CIGALE SED-derived stellar masses and SFRs used throughout this work, within the limitations of the unavoidable systematic uncertainties discussed above.

3.2.2 Our targets in the context of the star-forming main sequence

There is a long established trend observed between star formation rate and stellar mass for star-forming galaxies, which is commonly referred to as the "star-forming main sequence" (see e.g. Brinchmann et al., 2004; Daddi et al., 2007; Elbaz et al., 2007; Noeske et al., 2007; Salim et al., 2007; Wyder et al., 2007). This relation provides a useful comparison to put our sample into the wider context of star-forming galaxies. Specifically, we consider where our galaxies lie in comparison to the redshift dependent main sequence of Sargent et al. (2014) (see Fig. 3.2). We chose this parametrization as it visually provided the best fit to galaxies selected from SDSS (the parent sample of our work); where the other main sequences checked were: Bauermeister et al. (2013), Speagle et al. (2014), Whitaker et al. (2014), Genzel et al. (2015), and Schreiber et al. (2015). In Fig. 3.2

we show the Sargent et al. (2014) main sequence compared to all SDSS sources defined as star-forming based on BPT emission-line ratios (Kauffmann et al., 2003a; Brinchmann et al., 2004; Tremonti et al., 2004) within z = 0.08–0.2 (i.e. the redshift range spanned by our sources) using the MPA-JHU measurements[3] converted from a Kroupa to Chabrier IMF (Madau & Dickinson, 2014). We define the distance from the main sequence ($\Delta_{\rm MS}$) for each source as the ratio of its specific star formation rate (sSFR $\equiv$ SFR/M$_\star$) compared to that of the main sequence at its redshift and stellar mass (Sargent et al., 2014). Following the literature, we define our targets as "starbursts" if they have $\Delta_{\rm MS}$>4 (see e.g. Elbaz et al., 2011); however, we note that we use this definition for a comparison to the overall population only and do not claim that they are physically different to the rest of the population for this work.

Using the definitions described above, all of our sources are on or above their local main sequence with seven classified as starbursts[4], even though we applied no pre-selection on SFR or infrared luminosity (see Table 3.1).

3.3 Observations and data reduction

3.3.1 Data reduction

We use the Atacama Pathfinder EXperiment (APEX) to observe the spatially un-resolved molecular gas emission in the CO(2–1) and CO(6–5) transitions. We observed CO(2–1) for the whole sample presented here and CO(6–5) for a representative sub-sample (J1010+0612, J1100+0846 and J1430+1339; see Figs. 3.1 and 3.2). These specific transitions were selected based on a combination of scientific and observational constraints. Specifically, lower CO transitions (CO(1–0) in particular) are best used to trace the total cold molecular gas content (e.g. Bolatto et al., 2013; Carilli & Walter, 2013) and the CO(2–1) transition is the lowest observable at the redshift of our targets with the available APEX instrumentation. Higher CO transitions trace molecular gas that has been excited by star formation, shocks and the AGN (e.g. Mashian et al., 2015; Carniani et al., 2019; Vallini et al., 2019). Specifically the CO(6–5) transition was selected

[3] https://www.sdss.org/dr12/spectro/galaxy_mpajhu/

[4] J1010+1413 is right on the transition between normal star forming and starburst with $\Delta_{\rm MS}$=3.7. In the rest of this paper we assume $\Delta_{\rm MS}$~4 and consider it as a starburst.

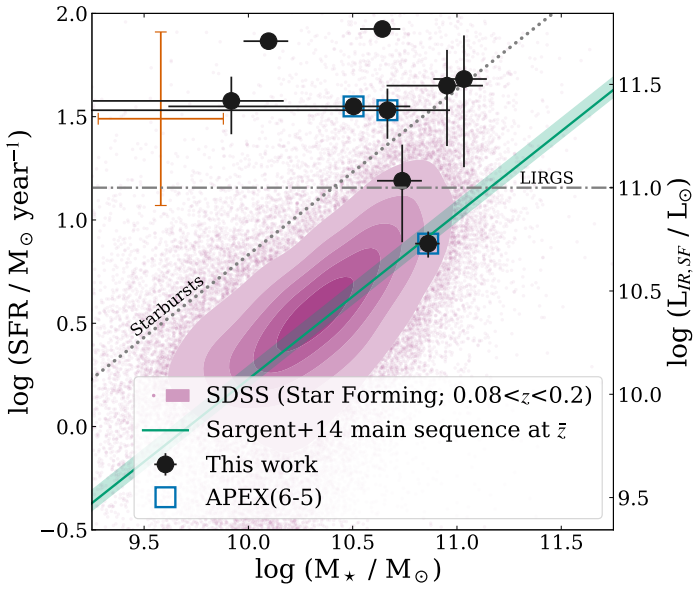

Figure 3.2: Our sources compared to the star forming main sequence, as shown by the comparison of stellar mass ($M_\star$) and star formation rate (SFR). Our sample is shown as black circles and the APEX CO(6–5) sample is highlighted with blue squares. The red error bar in the top left corner shows the systematic errors (see Section 3.2.1). The magenta contours and small translucent points show values for star-forming galaxies from SDSS. The solid green line is the main sequence as given in Sargent et al. (2014) at the mean redshift of our sources (z=0.127), with the width showing the variation across the redshift spanned by our sources. The black dotted line marks the region occupied by starbursts (Δ_{MS}>4) and the black dot-dashed lines marks the limit for LIRGs ($L_{IR} \geq 10^{11}$ $L_\odot$). All of our sources lie on or above the main sequence with seven being classified as starbursts.

based on indications that it can be boosted by AGN activity and jets in particular (Papadopoulos et al., 2010), and because it was the highest transition that could be observed for our targets in a reasonable time using APEX, due to available instrumentation and the atmospheric transmission. Due to observing constraints (e.g. the need for good weather for these observations; see Table 3.2) we only observed three of our targets in CO(6–5), however these three are representative of the overall population (see Figs. 3.1 and 3.2).

We observed CO(2–1) for our targets under proposal id. E-0100.B-0166 [PI: Jarvis] with the observations carried out between 2017 July 7 and 2018 December 29 with precipitable water vapours (PWV) between 0.6 and 4.7 mm. Three different instruments were used for these observations due to the redshift range of the targets and changes in the available instrumentation over the period of observation, namely, the Swedish-ESO PI receiver for APEX (SEPIA180; Belitsky et al., 2018), the Max Planck Institute for Radio Astronomy's PI230 and the APEX-1 receiver (SHeFI 230 GHz band; Vassilev et al., 2008). The instrument used for each source, the dates they were observed and the PWV values during the observations are listed in Table 3.2. The CO(6–5) data was observed under proposal id. E-0104.B-0292 [PI: Harrison] and observed between 2019 August 31 and December 10 using the SEPIA660 band 9 instrument with PWVs between 0.4 and 0.6.

The data were reduced and analysed using the Continuum and Line Analysis Single-dish Software (CLASS; version mar19a).[5] For many of our sources spectral spikes (due to bad channels) were found in at least one polarisation. To correct for this while losing the minimum amount of data for each source, for each day of observations we examined the average spectrum from each of the spectrometers separately and flagged, by eye, any channels affected by spikes. We also flagged the leading 150 channels (80 for the CO(6–5) data) and trailing 10 (in the overlap region) of each individual spectra. We combined the two spectrometers in the same sideband and polarisation using Zhiyu Zhang's CLASS extension file: combineTwoIFsAPEX.class which is made available online at `https://github.com/ZhiyuZhang/gildas_class_libraries`. From each of these combined scans we subtracted a linear baseline using the CLASS BASE command, excluding a velocity range ~500 km s^{-1} to either side of the

[5]from the GILDAS software package `http://www.iram.fr/IRAMFR/GILDAS/`

observed line position or the expected line position from the SDSS redshift if no line was obviously seen in the total binned spectrum. We then removed scans with poor baselines based on the ratio of their rms in 50 km s^{-1} bins (selected to best reveal the baselines) compared to the theoretical rms (rms$_t$) calculated by the following equation:

$$\mathrm{rms}_t \equiv \frac{T_{sys}}{\sqrt{|d\nu \times 10^6 \times t|}}, \tag{3.1}$$

where T_{sys} is the system temperature, t is the integration time and $d\nu$ is the frequency step size. The cutoff value for each was selected based on a combination of visual examination and minimizing the resultant final rms of the combined data in 100 km s^{-1} bins (selected to best reveal the emission lines) and ranged from rms / rms$_t$=1.25–2. Each day's data were then multiplied by the appropriate Kelvin to Jansky conversion factor. For each time frame and instrument the K/Jy conversion was determined using the APEX telescope efficiencies tool (`http://www.apex-telescope.org/telescope/efficiency/`), supplemented by private communications with Juan-Pablo Perez-Beaupuits (see Table 3.2 for the values used). Finally, the spectra were combined into a single spectrum and re-sampled to 1 km s^{-1} bins with a final linear baseline removed.

We show the final reduced APEX data in the velocity range around the CO(2–1) emission line in Fig. 3.3 and around the CO(6–5) emission line in Fig. 3.4.

3.3.2 Data analysis

We fit each averaged spectrum using Bayesian fitting and MCMC implemented through EMCEE (Foreman-Mackey et al., 2013).[6] This Bayesian method is preferred over frequentist fitting techniques for this analysis since it is less sensitive to binning, provides realistic uncertainties, and for the upper limits in particular requires only minimal assumptions on the line profile (see Appendix B.1). We assume a single Gaussian profile for the line, and fit for the line flux (f; integral under the line), peak velocity (v_p; central line velocity offset from the systemic redshift in Table 3.1), and standard deviation (σ; the width of the line) as well as the standard deviation of the noise in the spectrum (σ_N) which we assume to be

[6] `http://dfm.io/emcee/current/`

Table 3.2: Details of the observations.

Target	Instrument	t_{on} (min)	Date	K/Jy	pwv (mm)
(1)	(2)	(3)	(4)	(5)	(6)
CO(2–1); proposal id. E-0100.B-0166 [PI: Jarvis]					
J0945+1737	SEPIA180	126	2018-10-24	36±5	0.7
			2018-11-11	36±5	1.4
			2018-12-27	36±5	2.1
			2018-12-28	36±5	4.7
			2018-12-29	36±5	3.0
J0958+1439	SEPIA180	71.6	2018-10-26	36±5	0.6
			2018-12-27	36±5	2.1
			2018-12-28	36±5	4.7
J1000+1242	SEPIA180	261	2018-10-24	36±5	0.7
			2018-11-01	36±5	1.3
			2018-11-02	36±5	1.3
			2018-11-04	36±5	1.5
			2018-11-05	36±5	0.7
			2018-11-08	36±5	0.9
J1010+1413	SEPIA180	28.5	2018-10-26	36±5	0.6
			2018-10-31	36±5	0.9
			2018-11-02	36±5	1.3
			2018-11-03	36±5	1.5
J1010+0612	PI230	167	2018-10-29	42±6	0.8
J1100+0846	SEPIA180	51.4	2017-07-27	40±6	0.9
			2018-11-03	36±5	1.5
J1316+1753	SEPIA180	78.5	2017-07-28	40±6	0.9
			2018-12-28	36±5	4.7
J1356+1026	SEPIA180	35.8	2017-07-27	40±6	0.9
			2017-07-28	40±6	0.8
J1430+1339	APEX-1	101	2017-07-29	38±6	0.7
			2017-07-30	38±6	0.9
			2017-07-31	38±6	1.0
			2017-08-02	38±6	0.7
			2017-08-03	38±6	0.9
			2017-08-31	38±6	1.7
			2017-09-01	38±6	1.6
CO(6–5); proposal id. E-0104.B-0292 [PI: Harrison]					
J1010+0612	SEPIA660	145.2	2019-10-29	69±6	0.5
J1100+0846	SEPIA660	220.6	2019-11-05	69±6	0.4
			2019-11-06	69±6	0.4
			2019-12-10	69±6	0.5
J1430+1339	SEPIA660	118	2019-08-31	69±6	0.6

Notes: This table is divided into two parts with the details of our APEX CO(2–1) data given first and our CO(6–5) data at the bottom. (1) Object name; (2) Instrument; (3) On source time of the final total spectrum; (4) Date observed (year-month-day); (5) Conversion factor used to convert the observed antenna temperature (in K) to flux density (in Jy); (6) Average precipitable water vapour (PWV; mm) during the observations.

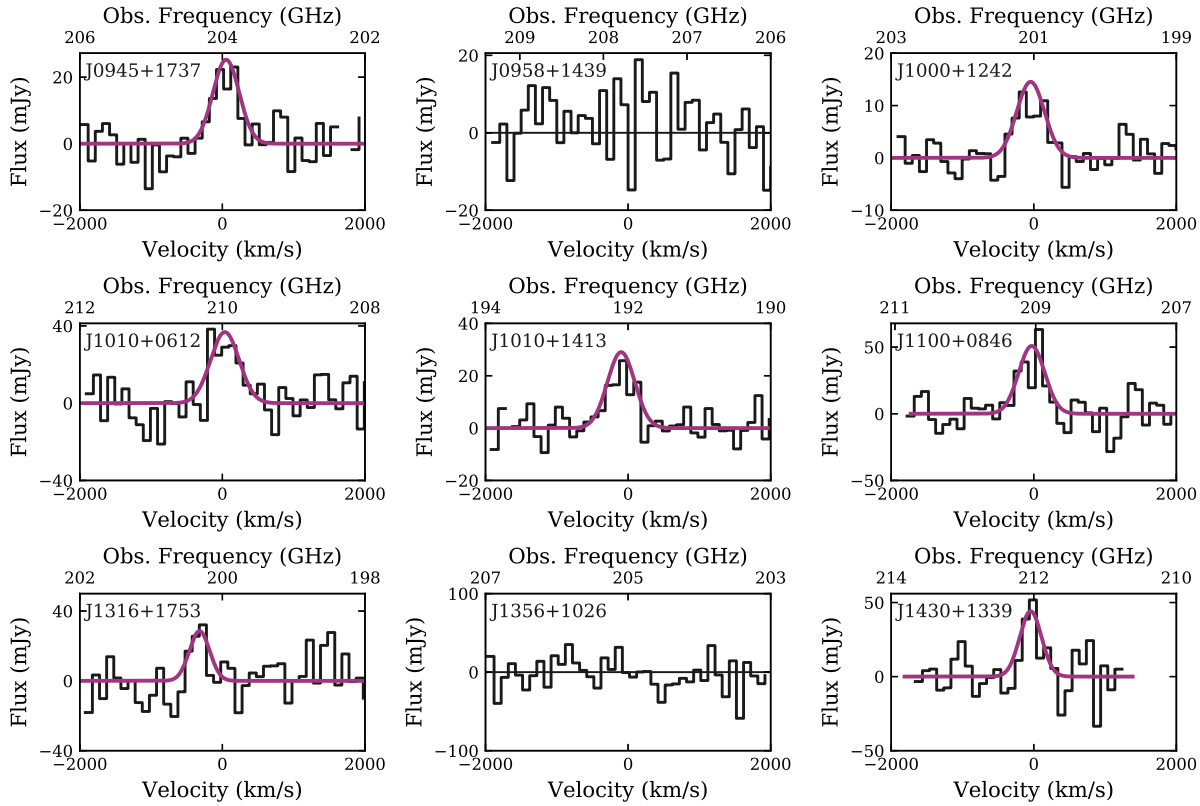

Figure 3.3: Our APEX CO(2–1) data (black curve) for each source. Over plotted for each is the results of our Bayesian fitting to the emission line, specifically the Gaussian constructed from the 50th percentile value from the posteriors for each parameter (magenta; see Table 3.3). For the two non detections a black horizontal line at flux=0 is plotted to help guide the eye.

Gaussian. The results of the fitting are listed in Table 3.3 and shown in Fig. 3.3 and 3.4. The full details of this analysis are given in Appendix B.1.

3.3.3 Evaluating contamination from other sources and beam corrections

The beams of the APEX observations discussed here are ~28 arcsec (~52 kpc at a representative redshift of $z = 0.1$) for the CO(2–1) data and ~9 arcsec (~17 kpc at z=0.1) for the CO(6–5) data. Based on the relatively large beams of the APEX data and considering the optical sizes of our targets we do not expect any CO flux to fall beyond our observed beams, making beam corrections unnecessary. However, the large CO(2–1) beam raises the possibility that other CO bright objects may be contaminating our flux measurements. To check for this

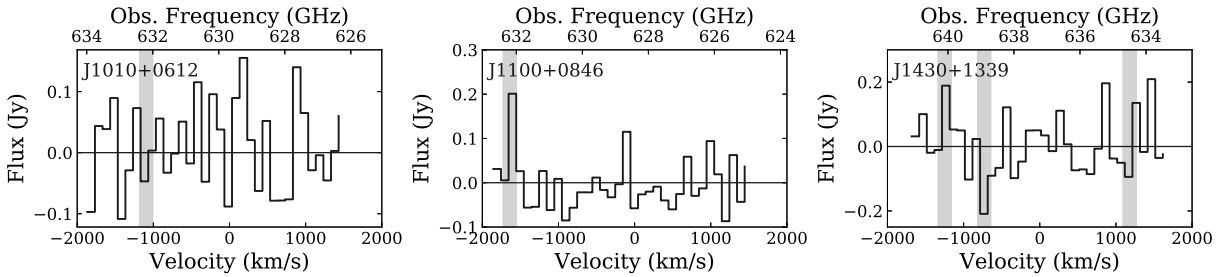

Figure 3.4: Our APEX CO(6–5) data. All three are undetected. Grey vertical bands highlight frequencies where there are narrow atmospheric absorption features that can cause slightly higher noise. A black horizontal line at flux=0 is plotted to help guide the eye.

scenario, we used higher spatial resolution ALMA CO observations. Specifically, we use the CO(1–0) and CO(3–2) images published in Sun et al. (2014) for J1356+1026 and for the other targets we use preliminary CO(3–2) images from two proposals carried out by our group[7] which have spatial resolution of ∼0.3–0.5 arcsec and a maximum recoverable scale of ∼4 arcsec.[8] The only target where a possible contaminating CO source was identified is J1010+0612 which has a CO(3–2) bright companion ∼7 arcsec away, which is within our CO(2–1) beam. Preliminary flux measurements from the ALMA data reveal that ∼82 per cent of the total flux is in our primary target of J1010+0612, a difference which is within the 1σ error bars from our Bayesian fit.[9] We highlight this source in subsequent figures.

3.4 Results

We show the final reduced APEX data, in 100 km s^{-1} bins, around the CO(2–1) line (for all nine targets) in Fig. 3.3 and around the CO(6–5) line in Fig. 3.4 (for the three targets observed). In the online supplementary data for this paper we provide corner plots displaying the posterior probability distributions of each of the parameters for each source (Jarvis et al., 2020). For the CO(2–1) data all but J0958+1439 and J1356+1026 show distinct peaks in the probability distribution for each parameter, indicating a detection. Therefore we detect seven of our nine

[7]Specifically, id. 2016.1.01535.S (PI. Lansbury), and id. 2018.1.01767.S (PI. Thomson)

[8]For J1430+1339, the ALMA data has a maximum recoverable scale of ∼19 arcsec.

[9]This is supported by the percent of the total system flux in J1010+0612 from 2MASS which is 87, 92 and 91 per cent, of the combined fluxes of these two sources, in the J, H and K_S bands, respectively.

targets in CO(2–1). None of the three sources observed in CO(6–5) show distinct peaks in the posterior probability distributions of all parameters and are clearly undetected.

For the detected emission lines we quote the 50th percentile (median) of the posterior distribution for each parameter in Table 3.3, and use the 16th and 84th percentile as errors. We note there is an additional ∼13 percent systematic uncertainty on the line flux from the error on the temperature to flux density conversion factors (Section 3.3.1). The values derived from our Bayesian analysis are consistent within errors to those derived from fitting a Gaussian directly to the data in 100 km s^{-1} bins. In Fig. 3.3 we show the resulting line profiles from our Bayesian procedure as Gaussians constructed using the 50th percentile value for each parameter. These parameter values will be adopted for the analyses throughout this work.

For the non-detected emission lines we derived 3σ upper limits on the line flux from the 99.7th percentile on the posterior distribution (see values in Table 3.3). Our upper limit for J1356+1026 (i.e. $L'_{CO(2-1)}<6\times10^9$ K km s^{-1} pc^2) is consistent with the observed value obtained by converting the total $L'_{CO}(1–0)$ reported for this source in Sun et al. (2014) to CO(2–1) (i.e. $L'_{CO}(2–1)=0.82\times10^9$ K km s^{-1} pc^2), where we have assumed $L'_{CO}(2–1)/(1–0)\equiv r_{21}=0.8$ (see Section 3.5.1 for a discussion of the choice of r_{21}). J1356+1026 is discussed in more detail in Section 3.5.1 and Section 3.5.3. We have no prior knowledge of the total CO emission for J0958+1439.

Overall we detect the CO(2–1) line for seven of our nine targets with fluxes in the range 7–23 Jy km s^{-1}. The two non detected targets have upper limits of 21.5 and 33.1 Jy km s^{-1} (for J0958+1439 and J1356+1026, respectively). Our upper limits on the CO(6–5) fluxes are 110, 74 and 135 Jy km s^{-1} for J1010+0612, J1100+0846 and J1430+1339, respectively. For the CO(2–1) detections we measured peak line velocities between −320 and 50 km s^{-1} relative to the systematic redshifts in Table 3.1, and line widths (σ) between 150 and 200 km s^{-1}; however, we defer a discussion of the molecular gas kinematics to future work.

We calculate the CO luminosities (following e.g. Solomon et al., 1997) for each source using:

$$L'_{CO}[\mathrm{K\ km\ s^{-1}pc^2}] = \frac{3.25\times10^7}{\nu^2_{\mathrm{co,rest}}}\left(\frac{D_L^2}{1+z}\right)\mathrm{f}, \tag{3.2}$$

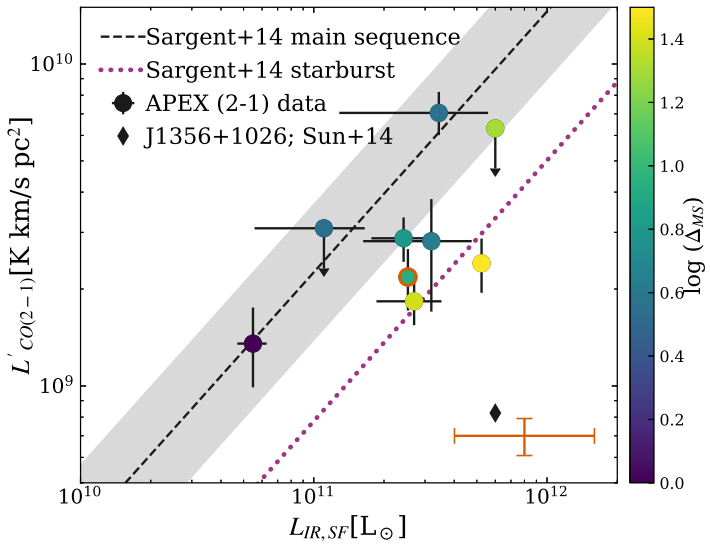

Figure 3.5: L'_{CO}(2–1) compared to the infrared emission produced by dust-heated star formation between 8–1000 μm ($L_{IR,SF}$; see Section 3.2.1). Our sample are shown as circles, colour coded by their distance from the main sequence (Δ_{MS}; see section 3.2.2). In the bottom right is a representative error bar showing the systematic uncertainties (see Sections 3.2.1 and 3.4). The Sun et al. (2014) value for L'_{CO}(1–0), converted to (2–1) using r_{21}=0.8, for J1356+1026 is shown as a black diamond. The black dashed and magenta dotted lines show the relationships from Sargent et al. (2014) for main sequence and starburst galaxies, respectively (see Section 3.5.1). Our quasars appear to follow the trend of star-forming galaxies, with those further from the main sequence agreeing more closely with starburst relation. J1010+0612 is highlighted with a red outline because the L'_{CO} may be $\lesssim$18 per cent overestimated (see Section 3.3.2).

where D_L is the luminosity distance in Mpc, $\nu_{co,rest}$ is the rest-frame frequency of the CO line in GHz (230.538 and 691.473 GHz for the CO(2–1) and CO(6–5) lines respectively), and f is the flux of the CO line in Jy km s^{-1}. This results in L'_{CO}(2–1) values of (1.4–7)$\times10^9$ K km s^{-1} pc^2 for the seven detected sources (see Table 3.3). These are plotted as a function of infrared luminosity in Fig. 3.5 and are discussed in the following section.

3.5 Discussion

In this work we look for signatures of AGN feedback on the molecular gas in our quasar sample. They are luminous AGN with ionized outflows and jets which may be able to impact upon the gas supply either radiatively or mechanically (see e.g. Harrison, 2017, for a review). We stress that although molecular outflows

Table 3.3: CO emission-line measurements.

Name	f	v_p	σ	σ_N	L'_{CO}
	(Jy km s^{-1})	(km s^{-1})	(km s^{-1})	(Jy)	($1\times10^9\times$ K km s^{-1} pc^2)
(1)	(2)	(3)	(4)	(5)	(6)
CO(2–1)					
J0945+1737	12±2	50^{+50}_{-40}	180^{+50}_{-40}	0.062	$2.3^{+0.5}_{-0.4}$
J0958+1439	<21.5	–	–	0.086	<3.0
J1000+1242	7±1	-40±40	200^{+40}_{-30}	0.031	1.9±0.3
J1010+1413	14±2	-100±30	190^{+40}_{-30}	0.11	7±1
J1010+0612†	19±4	30^{+60}_{-50}	200^{+60}_{-50}	0.052	$2.1^{+0.5}_{-0.4}$
J1100+0846	23±4	-30±40	180^{+40}_{-30}	0.12	2.8±0.4
J1316+1753	10^{+5}_{-4}	-320^{+90}_{-60}	140^{+110}_{-50}	0.13	3±1
J1356+1026	<33.1	–	–	0.23	<6.0
J1430+1339	17±5	-40^{+60}_{-50}	150^{+60}_{-40}	0.16	1.4±0.4
CO(6–5)					
J1010+0612	<110	–	–	0.56	<1.4
J1100+0846	<74	–	–	0.48	<0.98
J1430+1339	<135	–	–	0.90	<1.2

Notes: This table is divided into two parts with the details of our fits to the APEX CO(2–1) data given first then our fits to the CO(6–5) data are in the bottom portion. (1) Object name; (2–5) are values derived from our Bayesian fits to the APEX data, consisting of the 50th percentile (median) value with errors derived from the 16th and 84th percentiles: (2) line flux in Jy. For non-detections 3σ upper limits are given; (3) Peak velocity in km s^{-1} with respect to the systematic redshift given in Table 3.1; (4) Width of the line as a standard deviation in km s^{-1}; (5) Standard deviation of the noise in the final 1 km s^{-1} binned spectrum (see Section 3.3.2); (6) L'_{CO}/ 10^{9} in K km s^{-1} pc^2.

† Due to a nearby CO bright companion which is included within the CO(2–1) beam, the true CO(2–1) flux of this source could be up to 18 per cent lower than the value given here (see Section 3.3.3; the other line parameters are not used in the discussion of this paper).

are commonly observed directly through broad, generally blue shifted emission line components (see e.g. Fluetsch et al., 2019; Lutz et al., 2020); they are typically weak in CO emission (contributing $\lesssim$10 per cent of the total emission-line profile), which would be undetectable in our data. Here we focus on the galaxy-wide molecular gas content (Section 3.5.1) and CO excitation (Section 3.5.2) of our sample of extreme quasars and compare them to redshift-matched literature galaxy samples both with and without AGN.

3.5.1 Molecular gas content

In order to assess if our AGN have depleted their host galaxies' gas reservoir or decreased their star formation efficiency, we compare our results to studies of general galaxy populations and other AGN samples. Specifically, we consider: (1) their total CO luminosities (L'_{CO}) compared to their infrared luminosities (L_{IR}; corrected for the AGN contribution; Section 3.5.1); (2) how the molecular gas fractions ($M_{gas}/M_{\star}$) and depletion times (M_{gas}/SFR) compare to other samples when star-formation rates, stellar masses and offsets from the star-forming main sequence (Δ_{MS}) are taken into account (section 3.5.1) and (3) the relationship between AGN properties and the molecular gas content and star formation of the host galaxy (Section 3.5.1).

L'_{CO} / L_{IR} relations

The correlation of L'_{CO} (which traces the molecular gas mass) and L_{IR} (which traces star formation) in star-forming galaxies is well studied (e.g. Kennicutt 1998; Genzel et al. 2010; Greve et al. 2014; Sargent et al. 2014). By directly comparing observable quantities, this analysis removes many of the assumptions that are needed to convert these values into physical parameters. A complication to this analysis, which is not always accounted for, is that AGN can contribute significantly to the *IR* emission (see e.g. Kirkpatrick et al., 2019). The careful SED fitting technique implemented in our work allows us to reliably consider only the IR luminosity from the star formation component which is free from AGN contamination (i.e. $L_{IR,SF}$; see Section 3.2.1).

Numerous works have parametrized the L'_{CO} – L_{IR} relation using different samples of galaxies and different CO transitions. Here we focus on the work of

Sargent et al. (2014) which used CO observations of 130 z<3 massive ($M_\star > 10^{10}$ $M_\odot$) star-forming and starburst galaxies collected from a range of surveys. The size of the Sargent et al. (2014) sample and its coverage of similar galaxy properties as in this work make it an ideal comparison sample. They find a redshift-invariant log-linear relation between the L'_{CO} and L_{IR}. We convert their relation from CO(1–0) to CO(2–1) using r_{21}=0.8 (Leroy et al. 2009; Sargent et al. 2014; Daddi et al. 2015; Tacconi et al. 2018)[10]. We compare the L'_{CO} and L_{IR} values for the nine targets in our sample to this relation in Fig. 3.5.

We find that two out of the seven CO(2–1) detected quasars are consistent with the L'_{CO} – L_{IR} relationship for main sequence star-forming galaxies, whilst the other five have L'_{CO} values up to a factor of ∼4 lower than the relation would predict for their L_{IR} (see Fig. 3.5). However, as highlighted by the colour scaling in Fig. 3.5, all of the targets with low L'_{CO} compared to the Sargent et al. (2014) main sequence relationship have high star formation rates in relation to the main sequence (i.e. they have high Δ_{MS} values; see Section 3.2.2). This is consistent with Sargent et al. (2014), which finds that starbursts are offset to lower L'_{CO}values by a factor of ∼2.9, on average, compared to main sequence galaxies (see dotted line in Fig. 3.5). Indeed, all of our quasars which fall below the L'_{CO}– L_{IR} relationship for main sequence galaxies are classified as starbursts (i.e. $\Delta_{MS} \gtrsim 4$) and fall within 0.3 dex of the Sargent et al. (2014) relationship for starburst galaxies. We note that similar results are found when comparing our sample to the LIRG and merger L'_{CO} – L_{IR} relationships of Greve et al. (2014) and Genzel et al. (2010), respectively.

Based on our data, the two CO(2–1) non-detected targets could still be consistent with the expected relationships for star-forming galaxies (the main sequence and starburst relations for J0958+1439 and J1356+1026, respectively); but could also lie significantly lower. Specifically, we note that using the Sun et al. (2014) CO(1–0) luminosity for J1356+1026 would place it ∼4 times lower than the Sargent et al. (2014) starburst relation (see Fig. 3.5). This source is discussed in more detail in Section 3.5.1 and Section 3.5.3.

In summary, we find that at least seven of our nine targets have L'_{CO} values consistent with those of the star-forming galaxy population at matched infrared luminosities and at similar distance to the main sequence. From this analyses

[10]Sargent et al. (2014) use r_{21}=0.8 to convert from observed CO(2–1) to CO(1–0) in their analysis (where needed). Possible biases introduced by the choice of r_{21} are discussed in Section 3.5.1.

there is no evidence that the observed ionized outflows and jets in our powerful quasars have had an instantaneous impact on the observed CO luminosities.

Molecular gas comparisons

The more physically motivated quantities to study are the gas fraction (ratio of the molecular gas mass to stellar mass) and the depletion time (ratio of the molecular gas mass to the star formation rate), which relates to how efficiently stars are being formed for a given molecular gas mass. Based on large galaxies samples, these molecular gas properties scale with redshift, stellar mass and distance from the star-forming galaxy main sequence (see e.g. Tacconi et al., 2018; Liu et al., 2019, and references therein). In this work we are not concerned with the physical significance of these relations, but use them as a tool to compare the molecular gas properties of our sample to the wider galaxy population.

We compare our data to the homogenised sample of Tacconi et al. (2018) limited to within ±0.05 of the maximum and minimum redshift of our sample and only using their CO based measurements.[11] Specifically, the data compiled comes from the xCOLD GASS (Saintonge et al., 2017), EGNOG (Bauermeister et al., 2013) and GOALS (Armus et al., 2009) surveys and from the sample presented in Combes et al. (2011). We identified AGN hosts for each sample using BPT-based AGN classifications (the same as used to identify our sample; see Section 3.2), where available, and including all AGN classes (e.g. LINERS, Seyferts, quasars, composite; Baldwin et al., 1981). The galaxies in this redshift-matched comparison sample span the complete range of stellar mass, sSFR and Δ_{MS} found for our sample (see Fig. 3.6).

To ensure consistency with the comparison sample, we calculate the molecular gas masses of our samples using the same procedure as in Tacconi et al. (2018). Specifically, we follow the metallicity dependent α_{CO} and mass-metallicity relation used by Tacconi et al. (2018) (see also Genzel et al., 2015) to calculate molecular gas masses following $M_{gas} = \alpha_{CO} \times L'_{CO}(1–0)$. The resultant α_{CO} values for our sample range from 4.0 to 4.2. We convert from $L'_{CO}(2–1)$ to $L'_{CO}(1–0)$ using r_{21}=0.8. The full details of the equations used and a table of derived values are presented in Appendix B.2. For our seven CO(2–1) detected targets, the derived molecular gas masses fall in the range of $9.9 < \log(M_{gas}/M_{\odot}) < 10.5$, with

[11] Combined CO(1–0) and (3–2).

corresponding ranges of gas fractions and depletion times of $M_{gas}/M_{\star}$=0.1–1.2 and M_{gas}/SFR=0.16-0.95 Gyr, respectively.

In Fig. 3.6 we compare our derived gas masses and depletion times to the Tacconi et al. (2018) population as a function of stellar mass, sSFR and Δ_{MS}. We note that the dependence on the choice of main sequence relation adds additional uncertainty to Δ_{MS} compared to sSFR; however, Δ_{MS} has been shown to be more closely related to the molecular gas properties (see e.g. Tacconi et al., 2018; Liu et al., 2019) and we obtain consistent conclusions if we just consider sSFR. Within errors, our sources overlap with the comparison sample (non-AGN and AGN) in all of the common diagnostic planes shown in Fig. 3.6. To quantify this comparison, we perform a simple log linear fit to the Tacconi et al. (2018) sample with AGN removed (see Fig. 3.6). Our sample have a median log vertical offset of +0.1 in the gas fraction versus Δ_{MS} plane and +0.04 in the depletion time versus Δ_{MS} plane (ignoring the non-detections).[12] This provides some evidence for moderately high (∼0.1 dex) gas fractions in our sample, with respect to their position relative to the main sequence. However, we can not rule out that the two non detected sources in our sample could bring our average down. Specifically, calculating the gas mass for J1356+1026 using the total L'_{CO}(1–0) from Sun et al. (2014) would place it among the most gas poor systems in the Tacconi et al. (2018) population, with a log vertical distance from the Tacconi et al. (2018) line of −0.61 and −0.66 in gas fraction and depletion time respectively (see Section 3.5.3).

The AGN included in Tacconi et al. (2018), which have no selection for high bolometric luminosity or outflows, go in the opposite direction to our CO-detected targets, with median log vertical offsets of −0.12 in the gas fraction versus Δ_{MS} plane and −0.07 in the depletion time versus Δ_{MS} plane. We explore the possible role of AGN power further in Section 3.5.1.

It is important to consider possible systematic uncertainties in comparing AGN to non AGN samples due to the assumptions required to calculate gas masses.[13] For example, there is no consensus on if AGN have systematically different ratios of L'_{CO}(2–1) and (1–0), which is used to convert between the two

[12]Where the log vertical offset for a point (a,b) from a line y=f(x) with both in log space, is defined as b-f(a).

[13]We also note that, although the Tacconi et al. (2018) work does not directly account for an AGN contribution to their stellar mass and SFR calculations, their sample does not include type 1 quasars and are typically low power AGN (and therefore the AGN do not dominate the optical–UV part of the SEDs) so the impact is not expected to be strong.

(r_{21}; see e.g. Ocaña Flaquer et al. 2010; Papadopoulos et al. 2012; Xia et al. 2012; Husemann et al. 2017; Shangguan et al. 2020); however, we note that the observed range is modest ($0.4<r_{21}<1.2$) and we have adopted the mean value of 0.8 throughout this work (see e.g. Braine et al., 1993; Leroy et al., 2009). A larger uncertainty comes from α_{CO}, which, for most galaxies appears to have a value of ∼4, with slight dependencies on metallicity and SFR (see e.g. Bolatto et al., 2013; Sandstrom et al., 2013, and references therein). However α_{CO} may be significantly lower in LIRGs, submillimetre galaxies, mergers, starbursts and AGN (as low as ∼0.6; see e.g. Bolatto et al., 2013; Sargent et al., 2014; Calistro Rivera et al., 2018). In our comparison to literature results we have controlled for many of these differences, i.e. we are comparing like-for-like in sSFR and Δ_{MS} and made consistent assumptions (see Appendix B.2). However, we can not rule out some level of systematic differences in α_{CO} for AGN which could shift our sources to systematically lower gas masses than the non-AGN comparison sample. Finally, we note that a limitation of our comparison to the Tacconi et al. (2018) catalogue is that it does not provide information on detection fractions or report upper limits. However, if anything, this limitation will strengthen our suggestion that the majority of the quasars in our sample, are comparatively gas rich.

To summarize, although we can not control for unknown systematic variations in α_{CO}, our quasar sample has molecular gas fractions and depletion times that are consistent with, or slightly higher than, the redshift matched comparison sample when considered in terms of their stellar masses, sSFRs or distances to the main sequence. This implies no significant rapid depletion of the molecular gas supply despite the presence of kpc ionized gas outflows and jets.

The impact of AGN on the molecular gas content

To investigate the relationship between AGN and the molecular gas content in more detail, we build upon the work of Saintonge et al. (2017) which found that the BPT selected AGN in the xCOLD GASS sample with the highest [O III] / Hβ ratios (taken as a proxy of the power of the AGN radiation field) tend towards higher gas fractions. In Fig. 3.7 we plot gas fractions as a function of the [O III] / Hβ ratio for both the xCOLD GASS sample and the quasars presented in this work. For a fair comparison with the Saintonge et al. (2017) data we, again, use

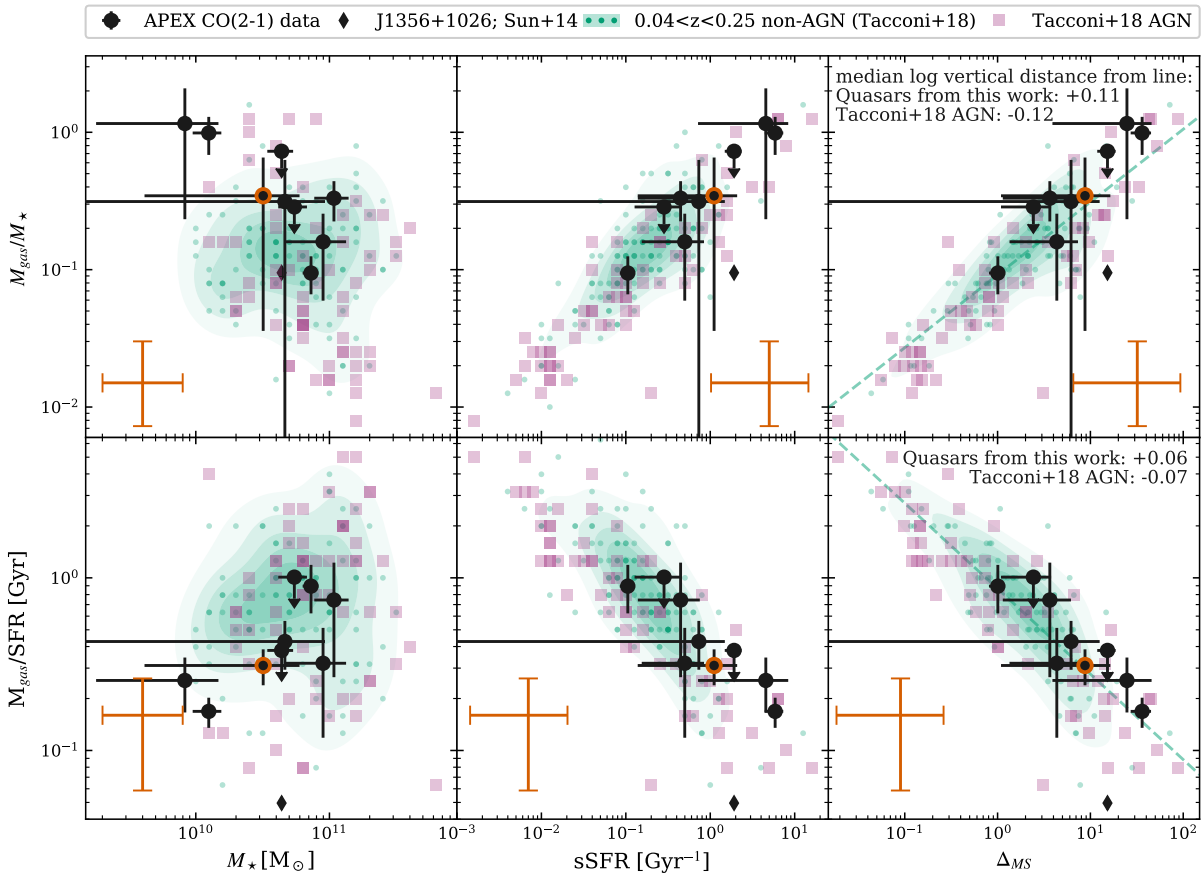

Figure 3.6: A comparison of the molecular gas content of our quasars (black circles) to literature values taken from Tacconi et al. (2018), within z ±0.05 of the full range of redshifts spanned by our sample. Galaxies without an identified AGN are represented by green points and density contours and AGN host galaxies by magenta squares (see Section 3.5.1). We show how the molecular gas fractions ($M_{gas}/M_\star$; top row) and depletion times (M_{gas}/SFR; bottom) vary with: stellar mass ($M_\star$; left column), sSFR (middle column) and distance to the main sequence (Δ_{MS}; right column; see Sect. 3.2). J1010+0612 is highlighted with a red circle following Fig. 3.5 and a black diamond in each panel marks the value for J1356+1026 using L'_{CO}(1–0) from Sun et al. (2014) instead of the limit from this work. In each panel a representative error bar is shown which factors in the systematic errors that could cause relative shifts between this work and the comparison sample (i.e. the conversion from L_{IR} to SFR and the error on the K/Jy conversion from APEX; see Sections 3.2.1 and 3.4). In the Δ_{MS} column (right) the median log vertical distance from a linear fit to the Tacconi et al. (2018) non-AGN (green dashed line) is given. Our powerful CO detected quasars, containing both outflows and jets, follow the overall trends seen in the comparison sample in all panels.

r_{21}=0.8, and follow their method to obtain α_{CO}. That is, we use the metallicity and Δ_{MS} dependent function of Accurso et al. (2017), which results in α_{CO} values between 3.3 and 6.0, and gas masses of $9.8<\log(M_{gas}/M_{\odot})<10.5$ (for the seven detected targets; see Appendix B.2 for full details).[14]

Fig. 3.7 reveals that our sample, extending to the most extreme local AGN, with no pre-selection on molecular gas or star forming properties, agrees with and strengthens the previous results from xCOLD GASS: the more extreme AGN (i.e. those with log ([O III] / Hβ)$\gtrsim$0.6) tend to have the highest gas fractions. On average, for the combined samples we find $(M_{gas}/M_{\star})_{average}$=0.02 for the sources with log([O III]/ Hβ)<0.6 and $(M_{gas}/M_{\star})_{average}$=0.16 for the sources with log([O III]/Hβ)>0.6 (excluding non-detections). We note that a similar trend is observed for our sample when the bolometric AGN luminosity from our SED fits (see Chapter 2, Jarvis et al., 2019) is used instead of [O III] / Hβ.

As highlighted by the colour-coding in Fig. 3.7, the most extreme AGN with the highest gas fractions are hosted in galaxies with high levels of concurrent star formation. Specifically we find increasingly high Δ_{MS} values for increasing [O III] / Hβ values. Indeed when considering instead of the gas fraction, the log vertical offset of each AGN from linear fits to redshift and stellar mass matched Tacconi et al. (2018) samples in the gas fraction versus Δ_{MS} plane (see Section 3.5.1), the trend with [O III]/ Hβ disappears. Specifically, the median vertical offset of the combined sample with log([O III]/Hβ)<0.6 is −0.05 while the median value for the sources with log([O III]/Hβ)>0.6 is ∼0 (see also Section 3.5.1 and Fig. 3.6). We note however, that our sample covers a very narrow range of [O III] / Hβ and xCOLD GAS is not designed as an AGN survey and so due to volume and redshift limits does not contain any powerful AGN. Larger samples, uniformly covering AGN with a range of powers would be needed to strengthen this observation. We discuss the impact of these results on the relationships between AGN activity, molecular gas masses and star formation rates in Section 3.5.3.

3.5.2 CO excitation

The relative luminosity of different CO lines contains information about the conditions of the molecular gas and the mechanisms that are exciting it. Through

[14]We note that J0945+1738, J1000+1242 and J1356+1026, are strong starbursts and might be better described with a lower α_{CO} (see Appendix B.2); however, this would not change our conclusions.

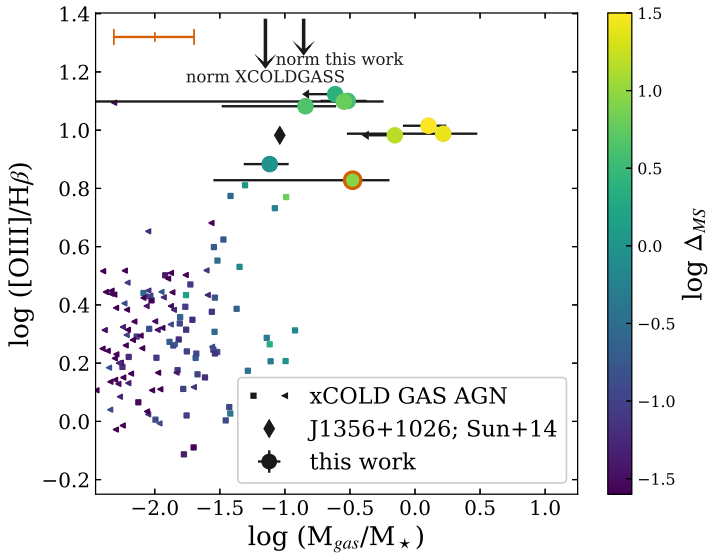

Figure 3.7: [O III] 5007 to Hβ emission line ratio versus gas fraction ($M_{gas}/M_\star$) of our quasars (circles) and xCOLD GASS AGN (squares, with triangles for upper limits; from the catalogues provided with Saintonge et al., 2017). The errors on the [O III]/ Hβ ratios for our sample are smaller than the point size. A representative systematic error bar is shown in the top left as in Fig. 3.6. J1010+0612 is highlighted with a red outline as per Fig. 3.5 and a black diamond marks the value for J1356+1026 using L'_{CO}(1–0) from Sun et al. (2014) instead of the limit from this work. Data points are colour-coded by their distance to the Sargent et al. (2014) main sequence (Δ_{MS}). The two arrows show the average gas fraction from the Tacconi et al. (2018) sample matched in stellar mass and redshift to each population, to demonstrate that the observed trend is not dominated by differences in these parameters between the two samples. Sources with high [O III] / Hβ ratios tend to have high gas fractions and have sSFR's above the main sequence.

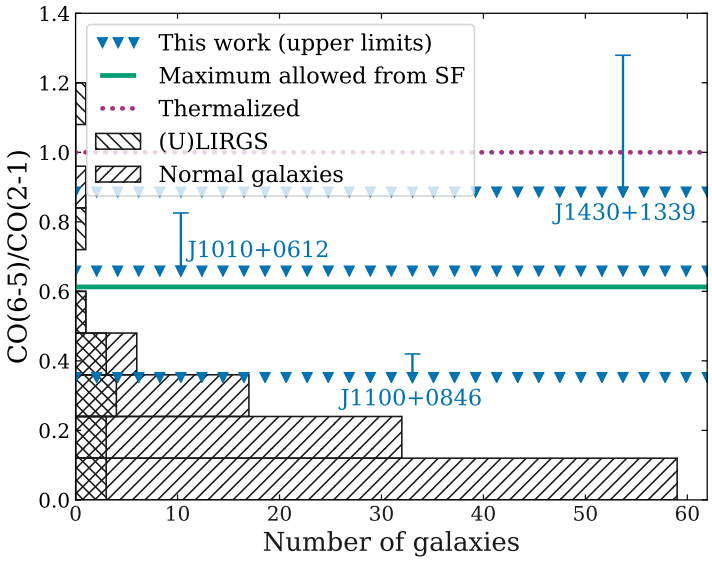

Figure 3.8: Upper limits of L'_{CO}(6–5) / L'_{CO}(2–1) ratios, for the three sources with these observations, represented as lines of blue triangles. Corresponding error bars represents the maximum values given the uncertainty on the measured CO(2–1) flux. The green line marks a maximum ratio achievable from star formation alone assuming a maximum star formation rate surface density of 1000 $M_{\odot}yr^{-1}kpc^{-2}$ following Narayanan & Krumholz (2014). The dotted magenta line marks where the molecular gas becomes thermalized. The histograms show the distribution of L'_{CO}(6–5) / CO(2–1) ratios for literature galaxy samples from Papadopoulos et al. (2012) ([U]LIRGs only) and Kamenetzky et al. (2016). For at least two of our sources (J1010+0612 and J1100+0846) we do not have any evidence for highly excited CO SLEDs (see Sec. 3.5.2).

our APEX observations we put constraints on the ratio of the CO(6–5) to the CO(2–1) luminosity (L'_{CO}; r_{62}) for three sources in our sample. Specifically, we find r_{62}<0.66, 0.35 and 0.89 for J1010+0612, J1100+0846 and J1430+1339 respectively (see Fig. 3.8). For J1010+0612 if an 18 per cent lower CO(2–1) flux is assumed to account for possible blending with its close companion, the limit on r_{62} increases marginally to 0.8 (which is within the error bar shown in Fig. 3.8).

The most ubiquitous source of CO excitation is photodissociation regions (PDRs) from the UV photons emitted from young stars. However this mechanism is inefficient at exciting higher CO transitions. Shocks and / or X-ray emission (through X-ray-Dominated Region models; XDR), both of which can be powered by AGN or jets, are needed to further excite the CO gas (see e.g. Pereira-Santaella et al., 2013; Carniani et al., 2019).

The CO spectral line energy distribution (SLED) modelled by Narayanan

& Krumholz (2014), which depends solely on the star formation rate surface density (Σ_{SFR}), predict values of $r_{62} \lesssim 0.24$ for typical star formation rate surface densities of $\lesssim 10$ $M_\odot yr^{-1} kpc^{-2}$, and even for an exceptionally high limit of Σ_{SFR}=1000 $M_\odot yr^{-1} kpc^{-2}$, $r_{62} \gtrsim 0.6$ can not be achieved. Our observed limit for J1100+0846 in particular suggests that the excitation of its total molecular gas could be explained by star formation alone, even at the highest end of the possible r_{62} ratio for this source. For J1010+0612 the observed limit of r_{62}<0.66 could be explained by star formation alone; however, some contribution of shocks and XDR, possibly powered by the AGN can not be ruled out.

In Fig. 3.8 we also show the distribution of observed r_{62} ratios from Kamenetzky et al. (2016) and Papadopoulos et al. (2012). This shows that the majority of sources are consistent with their CO(6–5) emission being caused by PDR. However, for the galaxies with $r_{62} \gtrsim 0.24$, it is worth noting that their relatively excited state would require either fairly high star formation rate surface densities (>10 $M_\odot yr^{-1} kpc^{-2}$) or imply the presence of another excitation mechanism (i.e. shocks or XDR). The three most extreme sources in these samples ($r_{62} \gtrsim 0.6$; IRAS 08572+3915 at 1.1, NGC 34 at 0.92 and 3C 293 at 0.78) all have a strong indication that AGN activity is responsible for the abnormally high r_{62} (see e.g. Cicone et al., 2014; Mingozzi et al., 2018; Emonts et al., 2005; Floyd et al., 2006; Papadopoulos et al., 2010). Our observed r_{62} limits on J1010+0612 and J1100+0846 can rule out such an extreme AGN excitation as seen in these sources. Unfortunately our weaker limit on J1430+1339, which of the three targets observed in CO(6–5) shows the clearest indications of jet activity (Jarvis et al., 2019, Chapter 2,), does not allow us to place any constraints on the excitation source for the CO(6–5) emission.

In summary, despite the fact that our targets containing kpc-scale ionized outflows (Fig. 3.1; Harrison et al., 2014; Jarvis et al., 2019), we see no evidence that the CO emission is extremely excited based on the L'_{CO}(6–5)/CO(2–1) ratios. This result is not entirely unexpected. For example, Rosenberg et al. (2015) found that the infrared colours of galaxies is a strong predictor of their CO excitation. Based on this, our galaxies (with *IRAS* 60/100μm flux $\lesssim 1$) should not have highly excited CO. Also, the effect of the AGN is expected to be most clearly seen at J>10 (e.g. Mashian et al., 2015; Lu et al., 2017) or at extreme gas densities (e.g. Lamperti et al., 2020). Observations of higher CO transitions could provide a

more complete constraint on the influence of the AGN (see e.g. van der Werf et al., 2010; Mashian et al., 2015; Carniani et al., 2019) and spatially resolved observations at multiple CO transitions would enable a study of any localised impact on the gas by the AGN or jets which could be undetectable in the total galaxy-wide emission (see e.g. Dasyra et al., 2016; Zhang et al., 2019).

3.5.3 The role of AGN in galaxy evolution

Many works have explored the total molecular gas content of AGN host galaxies compared to non-AGN galaxies (e.g. Simpson et al., 2012; Husemann et al., 2017; Kakkad et al., 2017; Perna et al., 2018; Rosario et al., 2018; Shangguan et al., 2020; Kirkpatrick et al., 2019); however, due to the huge amount of variation in the data used, the analysis conducted and the different selection criteria for comparison samples, creating a unified picture of these results is challenging. The most consistent conclusion seems to be that the molecular gas content for low-redshift ($z \ll 1$) AGN populations, is broadly consistent with matched non-AGN galaxies (see e.g. Xia et al., 2012; Krips et al., 2012; Villar-Martín et al., 2013).[15] Our comparison to non-AGN samples generally supports these broad conclusions: we find, at most, moderate differences in observed or derived molecular gas properties for our quasar sample compared to galaxy samples matched in redshift, stellar mass, sSFR and $\Delta_{\rm MS}$ (see Fig. 3.5 and Fig. 3.6). Additionally, our results suggest that powerful type 2 AGN with signatures of ionized gas outflows and jets, reside preferentially in gas rich, starburst galaxies.

In Sections 3.5.1 and 3.5.2 we showed that in our sample of local quasars with kpc ionized gas outflows and jets, there is no indication of AGN feedback having an immediate impact on the total gas reservoir once their distance to the star forming main sequence is accounted for. These observations; however, are unable to rule out a more localised impact, which can sometimes be observed using spatially-resolved molecular gas measurements (e.g. Salomé et al., 2017; Rosario et al., 2018; Fotopoulou et al., 2019; Ramakrishnan et al., 2019; Shin et al., 2019; Lutz et al., 2020). Furthermore, we can not rule out that these processes will have an impact on the global molecular gas supply on longer timescales. Specific predictions of the typical spatial scales and time frames of

[15]The picture at high redshift is somewhat less clear (e.g. Kakkad et al., 2017; Perna et al., 2018; Rosario et al., 2018; Kirkpatrick et al., 2019, Circosta et al. in prep.)

the impact on the molecular gas reservoirs are required to test different AGN feedback models (see e.g. Lapi et al. 2014), which has already started to be investigated on host galaxy star formation rates (see e.g. Harrison 2017; Scholtz et al. 2018; Schulze et al. 2019).

Figures 3.6 and 3.7 indicate that our quasars lie preferentially in molecular gas rich systems even though our only pre-selections were on the width and luminosity of [O III] and radio luminosity. Indeed, these systems are more gas rich, and are more likely to reside in starburst galaxies, than less extreme AGN host galaxies (Fig. 3.7). This is also in qualitative agreement with recent work revealing a relationship between AGN power and offset from the main sequence (at least at $z \sim 1$; Bernhard et al., 2019; Grimmett et al., 2020). Although indirectly, our work is consistent with a link between AGN activity and star formation that is driven by the underlying gas content of the host galaxy. Furthermore, similar results have been found in works considering atomic gas and high redshift sources (see e.g. Ellison et al., 2019; Rodighiero et al., 2019, respectively).

It is worth noting that one of our sources, which is undetected in our APEX data, may be exceptional in that it does have a low gas content. Using the Sun et al. (2014) CO(1–0) luminosity of L'_{CO}=1.03×10^9 K km s^{-1} pc^2 for J1356+1026 would put it amongst the most gas poor sources in our comparison sample from Tacconi et al. (2018) (M_{gas}/SFR=0.05 Gyr) and cause it to fall ∼4 times lower than the Sargent et al. (2014) starburst relation (see Fig. 3.5). This implies either that the luminosity reported in Sun et al. (2014) does not detect all of the diffuse, low surface brightness CO emission, or could imply that this source is more rapidly quenched than the rest of our sample. The most obvious exceptional property of this source, which could impact its molecular gas content compared to the rest of the sample, is the double nuclei separated by ∼2.5 kpc (Greene et al., 2012), indicating an on-going merger.

Overall the observed high molecular gas masses and incidence of starbursts in our sample are consistent with the scenario where the AGN and star formation are linked, and is in broad agreement with simple evolutionary based AGN unification models (see e.g. Sanders et al., 1988; Hopkins et al., 2006; Hickox et al., 2009). Specifically, the well studied scenario where gas rich systems have high levels of star formation and obscured / type 2 AGN activity (possibly triggered by mergers) which is followed by feedback processes (such as outflows and jets) that

will ultimately quench the AGN activity and star formation in the galaxy. Larger, less biased samples would be needed to confirm these models however. Although we can not be sure of the fate of our galaxies, we may have caught these systems in a special evolutionary phase where the feedback processes are just beginning. We can concretely conclude that the outflows and jets we observe do not *rapidly* remove the global molecular gas in an appreciable way (i.e. on a timescale shorter than, or equal to, the observed quasars, jets or outflows).

Our findings are consistent with many previous studies of the molecular gas and star formation in low redshift AGN ($z \lesssim 0.2$). For example, Husemann et al. (2017) find gradually increasing amounts of molecular gas going from AGN in bulge dominated to disc dominated to major merger host galaxies and a trend to higher molecular gas masses in systems with more luminous AGN. Similarly, Bertram et al. (2007) find that the Seyferts in their sample have molecular gas content consistent with normal star forming galaxies, while the powerful quasars are more consistent with starbursts. Luminous AGN are known to generally reside in galaxies with more recent star formation than their lower luminosity counterparts (see e.g. Balmaverde et al., 2016; Bernhard et al., 2019; Grimmett et al., 2020; Kim et al., 2020). Finally, there is evidence that obscured AGN lie in more gas rich systems than their un-obscured counterparts (Wylezalek & Zakamska, 2016; Rosario et al., 2018) and that the most extreme outflows may be preferentially found in rapidly star-forming, gas rich systems (see e.g. Rodríguez Zaurín et al., 2013; Harrison et al., 2014; Wylezalek & Zakamska, 2016).

To summarize, we find that our sample, selected to be luminous type 2 AGN hosting ionized outflows, lie preferentially in gas rich galaxies, with high levels of simultaneous star formation, which is consistent with the evolutionary framework described above. However, the small size of this sample and the two non-detections limit our ability to expand these findings to the quasar population in general. By selecting systems with fast, prominent kpc ionized gas outflows we might have expected these outflows to be able to remove the molecular gas, resulting in a deficit. However, the data suggest that if these outflows or jets will ultimately have an impact on the global molecular gas content, it is subtle, or we have captured them too early in the feedback process for this effect to be measurable.

3.6 Conclusions

Using APEX observations of the CO(2–1) emission line we have explored the global molecular gas content of nine $z \sim 0.1$ galaxies selected to host powerful type 2 quasars ($\log[L_{\rm AGN}/{\rm erg\,s^{-1}}] \gtrsim 45$) with galaxy-wide ionized outflows and radio jets (see Fig. 3.1; Harrison et al., 2014; Jarvis et al., 2019). We detected seven of the nine targets in CO(2–1), with corresponding $L'_{\rm CO}$(2–1) values of (1.4–7)$\times10^9$ K km s^{-1} pc^2. For a subset of three targets we used APEX to obtain upper limits on the CO(6–5)/CO(2–1) emission-line ratios. Our main conclusions are:

1. For at least seven of the nine quasars in our sample, the total molecular gas reservoirs show no indication of being rapidly depleted due to AGN feedback, despite being selected to have powerful ionized gas outflows and jets. Firstly, we find CO luminosities consistent (within 0.3 dex) with what would be predicted for the general galaxy population given their $L_{\rm IR}$ and distance to the star-forming main sequence (see Fig. 3.5 and Section 3.5.1). Secondly, the derived gas fractions and depletion times of our seven CO(2–1) detected sources (i.e. $M_{\rm gas}/M_\star \approx 0.1$–$1.2$ and $M_{\rm gas}/{\rm SFR} \approx 0.16$–$0.95$ Gyr, respectively) are comparable to those of redshift-matched non-AGN star-forming galaxies when taking into account their stellar mass, specific star formation rate and distance from the main sequence (see Fig. 3.6 and Section 3.5.1).

2. Galaxies hosting powerful AGN (i.e. $\log([{\rm O\,III}]/{\rm H}\beta) \gtrsim 0.6$) tend to have systematically higher gas fractions than those with less powerful AGN and star-forming galaxies in general, when our sample is considered together with those from the xCOLD GASS survey (Saintonge et al., 2017). Galaxies across these samples with the highest gas fractions appear to contain the most powerful AGN and highest levels of concurrent star formation (in relation to the star-forming main sequence; see Fig. 3.7 and Section 3.5.1).

3. The AGN are not having an extreme impact on the global CO excitation in at least two of the three sources for which we have upper limits on the $L'_{\rm CO}$(2–1)/CO(6–5) emission-line ratios (i.e. $r_{62} \lesssim 0.66$; see Fig. 3.8 and Section 3.5.2).

In summary, we find that the majority of our sample of quasars have gas rich, starburst host galaxies, even though we did not select the sample based on these properties. Furthermore, we find that their gas masses are consistent with what would be expected for their observed levels of star formation. There are no signs of an instantaneous depletion of the total molecular gas reservoir by the AGN in our sample, despite their high bolometric luminosities, strong ionized gas outflows and the presence of kpc scale jets in many. Our results are consistent with a requirement for high molecular gas fractions to feed both quasar activity and intense periods of star formation. Indeed, by selecting luminous AGN with powerful ionized gas outflows, we may have predominantly selected galaxies in a phase in their evolution where intense star formation and AGN activity are powered by large molecular gas reservoirs and the "feedback" in the form of jets and outflows is relatively young and these processes have not yet had any global impact upon the host galaxies.

Future, higher resolution CO observations and observations of more CO transitions will help determine if these processes have a more subtle and / or localised impact upon the molecular gas properties. Furthermore, galaxy formation models should work towards specific predictions of the molecular gas properties (e.g. gas fractions, depletion times, excitation) to compare to observations, such as ours, to aid understanding of the expected physical scales and time frames of any impact caused by different AGN feedback model prescriptions.

Acknowledgements

We thank the referee for their prompt and constructive comments. APEX is a collaboration between the Max-Planck-Institut für Radioastronomie, the European Southern Observatory, and the Onsala Observatory. PJ acknowledges funding from the European Research Council (ERC) under the European Union's Horizon 2020 research and innovation programme under grant agreement No 724857 (Consolidator Grant ArcheoDyn). D.M.A. acknowledges the support of the UK Science and Technology Facilities Council (STFC) through grants ST/P000541/1 and ST/T000244/1.

Chapter 4

The Quasar Feedback Survey: the origin of the radio emission and its connection to the ionized gas

Abstract: We present the first results from the Quasar Feedback Survey: a sample of 42 z<0.2 [O III] and radio luminous AGN ($L_{[O\ III]}>10^{42}$ ergs s^{-1} and $L_{1.4GHz} > 2\times10^{23}$ W Hz^{-1}). Using high spatial resolution (~0.25 – 1 arcsec) 1 – 6 GHz radio images from the Very Large Array, we find that 28 (66 percent) of the sources have spatially extended (~1–60 kpc) radio features, and at least nine have a flat-spectrum core, likely from the base of a radio jet. Of the 20 for which we have the requisite data, we show that at least 11 have excess radio emission above what would be expected from star formation. Overall, we confirm that for a minimum of 55 percent of the sample, the AGN dominates the production of the radio emission, with the origin of the radio emission in the remainder still unclear. This is despite that fact that only 7 – 12 percent of the sample are classified as radio AGN using traditional criteria (Xu et al., 1999; Best & Heckman, 2012). By combining these results with archival data we uncover that [O III] luminous AGN are more likely to be associated with spatially extended radio sources than their less extreme counterparts. Finally, we demonstrate a correlation between radio size and the FWHM of the [O III] line. Our results demonstrate that the AGN, and compact jets in particular, can contribute significantly to the radio emission of traditionally 'radio-quiet' AGN and suggest that jets may play a key role driving feedback even in radiatively powerful quasars. This work lays the foundation for deeper investigations into the feedback properties of this unique AGN sample.

4.1 Introduction

Active galactic nuclei (AGN) are amongst the most powerful phenomenon in the observable universe and are generally accepted to play a vital role in the evolution of galaxies (e.g. see reviews in Alexander & Hickox, 2012; Fabian, 2012; Harrison, 2017). Over the years, our understanding of the physical processes at play in and around AGN has grown immensely, however several key questions remain. For example, the conditions necessary for the launching of powerful jets are still unknown. Additionally, there is significant debate about the specific mechanisms through which AGN transfer energy to their host galaxies.

About 10 percent of AGN have powerful, relativistic jets that are strong radio emitters ($L_{1.4GHz} \gtrsim 10^{25}$ W Hz^{-1}; see e.g. Zakamska et al., 2004). However the origin of the radio emission in the majority of AGN (so called 'radio-quiet' AGN) is widely debated (e.g. Panessa et al., 2019). On one hand, the radio emission could be dominated by synchrotron emission caused by shocks from exploding supernovae and hence be directly related to the star formation in the galaxy (see e.g. Condon, 1992; Condon et al., 2013). Alternatively, the majority of the radio emission could originate from the AGN, namely in the form of radio jets, coronal emission or shocks from radiatively driven winds (see e.g. Kukula et al., 1998; Laor & Behar, 2008; Nims et al., 2015; Zakamska et al., 2016; Behar et al., 2018; Jarvis et al., 2019).

Although the origin of the radio emission is unclear, multiple works have shown that it is strongly connected to the presence of ionized outflows in the AGN host galaxies (see e.g. Mullaney et al., 2013; Zakamska & Greene, 2014; Villar Martín et al., 2014). In particular, Molyneux et al. (2019) found more extreme outflows in sources with compact radio emission. This radio – outflow connection could be caused by star formation, jets or winds, which are all capable of driving powerful outflows in the galaxy. Therefore, determining the origin of the radio emission in 'radio-quiet' AGN will also constrain the driving mechanism for outflows.

In our previous work (Harrison et al. 2014, 2015 and Chapter 2, Jarvis et al. 2019), we used spatially resolved radio observations and integral field spectroscopy (IFS) to find ~kpc jet-like radio features, galaxy wide ionized gas outflows, and signatures of jet-gas interactions in a sample of 10 radio quiet quasars with powerful outflows ([O III] full width half max – FWHM $> 700\,\mathrm{km\,s^{-1}}$). In

Chapter 2 (Jarvis et al., 2019) in particular, we demonstrated that radio emission originating from the AGN can be effectively identified by combining spatially resolved radio observations and the identification of radio excess beyond what is predicted from the radio–*IR* correlation for star-forming galaxies.

This work expands upon that presented in Chapter 2 (Jarvis et al., 2019), by increasing the sample size by a factor of ∼4 and removing the pre-selection for powerful outflows. Specifically, we present the first results of our new Quasar Feedback Survey. This sample of 42, predominantly radio quiet, local AGN was selected to form an ideal laboratory for studying AGN feedback, by selecting powerful AGN ($L_{[O\ III]} > 10^{42}$ erg s^{-1}; corresponding to bolometric luminosities of $L_{bol} \gtrsim 10^{45}$ erg s^{-1}) that are close enough to allow for detailed spatially resolved studies (z<0.2).

We present high spatial resolution (∼0.25 arcsec) radio observations of the full 42 sources in the Quasar Feedback Survey, which we use in combination with archival data to constrain the origin of the radio emission and to explore the radio – outflow connection. In Section 4.2, we present the sample, and the selection criteria, then in Section 4.3 we describe our NSF's Karl G. Jansky Very Large Array (VLA) data, its reduction and imaging. Section 4.4 presents our results, which we discuss in Section 4.5. We summarize our conclusions in Section 4.6. We adopt H_0=70km s^{-1}Mpc^{-1}, Ω_M=0.3, Ω_Λ=0.7 throughout, and define the radio spectral index, α, using $S_\nu \propto \nu^\alpha$. We assume a Chabrier (2003) initial mass function (IMF).

4.2 Target selection

The quasars presented in this work were selected from the parent sample of 24 264 z<0.4 spectroscopically identified AGN from the Sloan Digital Sky Survey (SDSS) presented in Mullaney et al. (2013). We restrict our sample to z<0.2 AGN with $L_{[O\ III]}$>10^{42} ergs s^{-1} (i.e. quasars) and $L_{1.4GHz} > 2\times10^{23}$ W Hz^{-1} (see Fig. 4.1 and Table 4.1). We use values from the NRAO VLA Sky Survey (NVSS; Condon et al., 1998) consistently throughout this work when referring to the total radio luminosity of our sources ($L_{1.4GHz}$) and selected our radio luminosity cut to be above the NVSS flux limit (see Fig. 4.1). Within these conditions, the sample consists of all sources that are observable from the VLA (i.e. 10<RA<300 and

24<Dec<44 degrees). This sample is designed to allow for spatially resolved studies such as this work (with 1 arcsec $\approx$ 3.3 kpc at z = 0.2), and the moderate radio luminosities ensure that our targets can be detected with short integration times (see Section 4.3). Additionally, the high [O III] luminosities of the sample correspond to bolometric luminosities ($\sim 10^{45}$ ergs s^{-1}) typical of AGN at the peak cosmic epoch of growth ($z \approx 1$–2; Hopkins et al., 2007; Aird et al., 2015), even though they represent only the top 2 percent [O III] luminous AGN at z<0.2. Based on Mullaney et al. (2013), our sample is representative of the ~30 percent of z<0.2 quasars with $L_{1.4GHz} > 2\times10^{23}$ W Hz^{-1}. 24 of the sources are type 2 AGN (57 percent) and the other 18 (43 percent) are type 1 (broad line) AGN.

The majority (37/42) of the sample are 'radio-quiet' as defined by the [O III] and radio luminosity division of Xu et al. (1999), consistent with the 'radio-quiet' fraction of the overall AGN population (i.e. ~90 percent Zakamska et al., 2004). Furthermore, this sample has no pre-selection on the presence of ionized gas outflows (e.g. no criteria based on the FWHM of the [O III] line; see Fig. 4.1).

4.3 Observations and data reduction

We observe our entire sample with the VLA to produce spatially resolved radio maps with ~1 and 0.25 arcsec resolution. The VLA data for nine of the sample have previously been presented in Chapter 2 (Jarvis et al., 2019) (see also Harrison et al., 2015). These observations were taken under proposal id. 13B-127 [PI. Harrison], with observations carried out between 2013 December 1 and 2014 May 13 in four configuration – frequency combinations: (1) A-array in L-band (1–2 GHz; ~1.0 arcsec resolution); (2) A-array in C-band (4–8 GHz; ~0.25 arcsec resolution); (3) B-array in L-band (1–2 GHz; ~4.0 arcsec resolution) and (4) B-array in C-band (4–8 GHz; ~1.0 arcsec resolution). For more details about these observations and the reduction of these data see Chapter 2 (Jarvis et al., 2019).

The remainder of the sample were observed under proposal id. 18A-300 [PI. Jarvis] using the A-array in the L- and C-bands (~1.0 and ~0.25 arcsec resolution at 1–2 and 4–8 GHz respectively), and were observed between 2018 March 2 – 22.

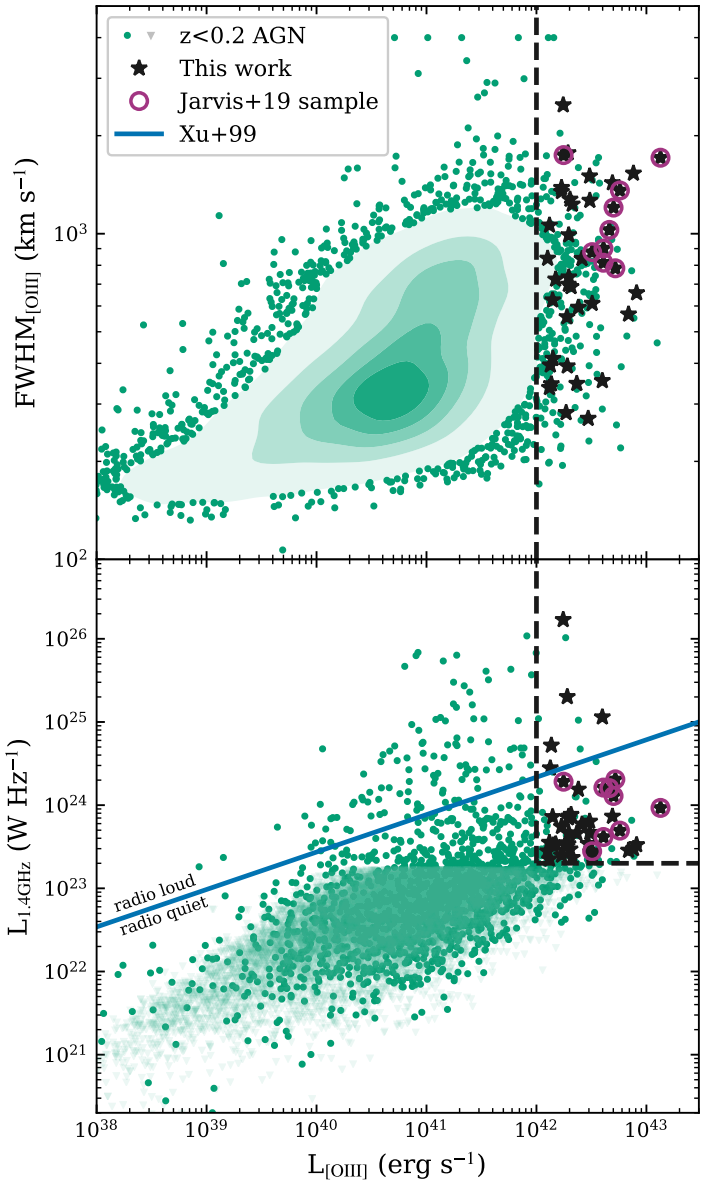

Figure 4.1: The basic properties of the Quasar Feedback Survey sample (black stars) and the criteria used to select them (black dashed lines) compared to the overall Mullaney et al. (2013) z<0.2 AGN population plotted as green circles and density contours. The sources previously presented in Chapter 2 (Jarvis et al., 2019) are further marked with magenta circles. *Top:* from the two Gaussian [O III]λ5007 line fits from Mullaney et al. (2013), we plot the FWHM of the broadest, luminous [O III] component (see Table 4.1) versus the total observed luminosity. *Bottom:* the 1.4 GHz radio luminosity from NVSS versus the total observed [O III] luminosity from Mullaney et al. (2013). The blue line marks the division between 'radio-loud' and 'radio-quiet' AGN from Xu et al. (1999), and the pale green triangles are Mullaney et al. (2013) AGN with upper limits on their radio luminosity.

Table 4.1: The Quasar Feedback Survey sources and their basic properties.

Name	Alt name	RA (J2000)	Dec (J2000)	z	$\log(L_{1.4GHz})$ (W Hz^{-1})	$S_{1.4GHz}$ (mJy)	$\log(L_{[O\,III]})$ (erg s^{-1})	$FWHM_{[OIII]}$ (km s^{-1})	Type
(1)	(2)	(3)	(4)	(5)	(6)	(7)	(8)	(9)	(10)
J0749+4510		07:49:06.50	+45:10:33.9	0.192	25.1	147.1	42.60	354	1
J0752+1935		07:52:17.84	+19:35:42.2	0.117	23.9	24.9	42.69	1432	1
J0759+5050		07:59:40.96	+50:50:24.0	0.055	23.5	44.9	42.31	1275	2
J0802+4643		08:02:24.35	+46:43:00.6	0.121	23.4	8.9	42.10	840	2
J0842+0759		08:42:05.57	+07:59:25.5	0.134	23.8	16.6	42.48	1502	1
J0842+2048		08:42:07.50	+20:48:40.1	0.181	23.4	3.6	42.23	1385	1
J0907+4620		09:07:22.36	+46:20:18.0	0.167	24.4	47.1	42.13	395	2
J0909+1052		09:09:35.49	+10:52:10.5	0.166	23.5	6.0	42.27	282	2
J0945+1737†		09:45:21.33	+17:37:53.2	0.128	24.2	45.6	42.66	1027	2
J0946+1319		09:46:52.57	+13:19:53.8	0.133	23.5	7.9	42.88	1533	1
J0958+1439†		09:58:16.88	+14:39:23.7	0.109	23.4	10.9	42.51	878	2
J1000+1242†		10:00:13.14	+12:42:26.2	0.148	24.2	34.8	42.61	815	2
J1010+0612†		10:10:43.36	+06:12:01.4	0.098	24.3	92.4	42.25	1743	2
J1010+1413†		10:10:22.95	+14:13:00.9	0.199	24.0	11.1	43.13	1711	2
J1016+0028		10:16:53.82	+00:28:57.1	0.116	23.5	11.8	42.17	725	2
J1016+5358		10:16:23.76	+53:58:06.1	0.182	23.4	3.2	42.12	1062	2
J1045+0843		10:45:05.16	+08:43:39.0	0.125	23.8	17.6	42.41	839	1
J1055+1102		10:55:55.34	+11:02:52.2	0.145	23.4	5.7	42.51	611	2
J1100+0846†		11:00:12.38	+08:46:16.3	0.100	24.1	59.8	42.70	1203	2
J1108+0659		11:08:51.03	+06:59:01.4	0.181	23.9	11.1	42.31	688	2
J1114+1939		11:14:23.81	+19:39:15.8	0.199	23.8	8.4	42.29	699	2
J1116+2200		11:16:25.34	+22:00:49.3	0.143	23.7	10.5	42.37	347	2
J1222-0007		12:22:17.85	-00:07:43.7	0.173	23.5	4.5	42.84	566	2
J1223+5409	4C+54.2	12:23:13.21	+54:09:06.5	0.156	25.3	387.6	42.28	392	1
J1227+0419		12:27:39.83	+04:19:32.4	0.180	23.7	6.8	42.49	1265	1
J1300+0355		13:00:07.99	+03:55:56.5	0.184	24.2	21.6	42.38	594	1
J1302+1624	Mrk783	13:02:58.83	+16:24:27.7	0.067	23.5	32.9	42.28	555	1
J1316+1753†		13:16:42.90	+17:53:32.5	0.150	23.7	10.3	42.76	1357	2

Continued on next page

Continuation from previous page

J1324+5849		13:24:18.25	+58:49:11.6	0.192	23.7	7.1	42.23	1346	1
J1347+1217	4C+12.50	13:47:33.36	+12:17:24.3	0.121	26.2	5397.2	42.24	2484	1
J1355+2046		13:55:50.20	+20:46:14.5	0.196	23.5	4.2	42.29	1770	1
J1356+1026†		13:56:46.10	+10:26:09.0	0.123	24.3	62.9	42.72	783	2
J1430+1339†		14:30:29.88	+13:39:12.0	0.085	23.6	26.5	42.61	901	2
J1436+4928		14:36:07.21	+49:28:58.5	0.128	23.5	9.4	42.15	414	2
J1454+0803		14:54:34.35	+08:03:36.7	0.130	23.7	12.7	42.29	736	1
J1509+1757		15:09:13.79	+17:57:10.0	0.171	23.9	11.8	42.29	991	1
J1518+1403		15:18:56.27	+14:03:19.0	0.139	23.6	8.6	42.12	337	2
J1553+4407		15:53:15.94	+44:07:49.3	0.197	23.5	4.2	42.47	271	2
J1555+5403		15:55:01.44	+54:03:26.9	0.180	23.4	3.4	42.33	1231	1
J1655+2146		16:55:51.37	+21:46:01.8	0.154	23.5	6.6	42.91	658	1
J1701+2226		17:01:58.24	+22:26:41.9	0.197	24.7	64.0	42.14	346	1
J1715+6008		17:15:44.05	+60:08:35.6	0.157	23.9	13.8	42.15	625	2

Notes: (1) Source name; (2) Alternative name that this source is published under (if any); (3)–(4) Optical RA and Dec positions from SDSS (DR7); (5) Redshift of the source from SDSS (DR7); (6) Rest-frame 1.4 GHz radio luminosities from NVSS using a spectral index of $\alpha = -0.7$ and assuming $S_\nu \propto \nu^\alpha$; (7) 1.4 GHz flux of the target from NVSS; (8) Total observed [O III]λ5007 luminosity from Mullaney et al. (2013); (9) FWHM of the broadest component of the [O III] line from Mullaney et al. (2013) two Gaussian fits, that contains at least 30 percent of the total line flux (following Harrison et al., 2014); (10) AGN type from Mullaney et al. (2013), with 1 = broad line (type 1) and 2 = type 2.

† These sources have been previously studied by our group (see e.g. Harrison et al. 2014 and Chapters 2 and 3 ,Jarvis et al. 2019; Jarvis et al. 2020)

We observed for 7.1 hours in the L-band (5–10 minutes per source) and 9.5 hours in C-band (5–25 minutes per source). To improve the *uv* coverage, each source was observed in at least two scans spread across the 1–2 hours observing blocks.[1] We began each observing block with a ∼10 minute scan of a standard calibration source (3C147, 3C286 or 3C138). We performed ∼3 minute scans (including slew-time) of nearby (typically within ∼10°) phase calibrators every 10–15 minutes.

4.3.1 Data reduction and imaging

We reduced and imaged the VLA 18A-300 data using CASA version 5.1.2-4. Specifically, we used the VLA CASA Calibration Pipeline default VLA recipe for Stokes I continuum. We then split each of the science targets into their own measurement set using 3 s time binning. To remove RFI from the L-band data specifically (where it is stronger than in the C-band), we then used the CASA task 'flagdata' in 'tfcrop' mode to apply additional flags to each L-band measurement set.

In order to take into account the broad and varying bandwidths of our observations, all of the VLA images we present were made using the Multi-Frequency Synthesis (MFS) mode of the 'clean' function. We weighted the baselines using the Briggs weighting scheme with a robustness parameter of 0.5 (Briggs, 1995). For the C-band data we performed this imaging using two Taylor terms to model the frequency dependence of the sky emission in order to simultaneously generate in-band (i.e. 4–8 GHz) spectral index maps. These images, together with cutouts from the VLA 'Faint Images of the Radio Sky at Twenty-cm' survey FIRST; Becker et al., 1995[2] and archival optical images are shown in Appendix C.1.

Throughout this work we use three sets of images for each source which we refer to as low resolution (LR), medium resolution (MR) and high resolution (HR) throughout, defined as:

- LR: We used 2 arcmin cutouts from FIRST to characterise the low resolution (∼5 arcsec; 1.4 GHz) radio properties of our sample.

[1] For J1045+0843 and J1108+0659, only the second scan was used for the final images due to badly calibrated data in the first scans.

[2] `https://third.ucllnl.org/cgi-bin/firstcutout`

- MR: Images from the new VLA data presented here and in Chapter 2 (Jarvis et al., 2019) with ∼1 arcsec resolution. Specifically, this is the C-band (6 GHz) B-array images for the nine sources in Chapter 2 as these were the images primarily used for the analysis in that work (e.g. to measure the size; see Fig. 2.5 and Table 2.3 of that work). For the remainder of the sample (i.e. those observed under proposal id. 18A-300) we use the L-band (1.4 GHz) A-array images discussed above. We note that instead using the L-band A-array images for the Chapter 2 sources would not change the results of this Chapter.

- HR: The highest resolution images used in this work are the C-band (6 GHz) A-array VLA data presented here and in Chapter 2 (Jarvis et al., 2019) (∼0.25 arcsec resolution).

We note additionally, that J1347+1217 is a VLA calibrator and so we did not observe it with the sample presented here, relying on the extensive archival information available (see e.g. O'Dea, 1998). This source is discussed in more detail in Appendix C.1.8.

4.4 Results

Our primary goals were to constrain the origin of the radio emission and explore in more detail the relationship between the radio and outflow properties of 'radio-quiet' AGN (see Section 4.5). To that end, we made five key measurements presented below. Firstly, we classified the observed radio morphology at the three spatial resolutions discussed above (Section 4.4.1) and measured the largest observed radio size (Section 4.4.2). We then used our high resolution radio images to measure the spectral index and brightness temperature of the observed radio cores in order to identify luminous, compact, flat spectrum cores indicative of the base of radio jets (Section 4.4.3 and Section 4.4.4). Finally, we measured the 'radio excess' of our sources to identify radio emission above what can be explained by the star formation of the host galaxies (Section 4.4.5).

4.4.1 Radio morphology

To aid in our identification of the source of the radio emission in our targets (see section 4.5.1) we classify by eye the morphology observed in the FIRST images (LR) as well as our VLA MR and HR images for each source. Our classification scheme roughly follows those used in Baldi et al. (2018) and Kimball et al. (2011a), with the classifications used illustrated with examples from this work in Fig. 4.2 and described below:

- Compact: this is given if the source in this radio image shows no visible extension or spatially resolved features.
- Jet: these sources are composed of one contiguous, visibly spatially extended, feature. Such features are defined as not containing multiple closed contours and are often asymmetric. We note that this definition is purely to describe the morphology, and may not be physically associated with an AGN-driven jet (see Section 4.5.1).
- Double: sources showing two distinct peaks in the radio emission (i.e. the radio can be well described by a fit with two two-dimensional Gaussian components).
- Triple: given for sources with three distinct radio peaks (i.e. the radio emission can be well described by a three component Gaussian fit).
- Irregular: encompasses all other spatially extended, irregular, radio morphologies.

We additionally note that one source (J1016+0028) was undetected in our HR image and so it is given the classification of 'Undetected'. Furthermore, although we did not observe J1347+1217, its published size of 0.16 kpc (O'Dea, 1998) corresponds to ∼0.07 arcsec at the redshift of this source ($z = 0.121$), and so it would be unresolved (classified as compact) in all three resolutions considered here. The classification given to each source in each of the three images considered are given in Table 4.2 and the overall distribution of classifications is shown in Fig. 4.2.

This work demonstrates the importance of the spatial resolution, maximum resolvable scale and depth of the images used when determining the morphology

of radio sources. Specifically, we see many more extended structures in our HR data than in either our MR images or FIRST (37/42 are classified as C in the FIRST (LR) images compared to just 19/42 in our HR images). On the other hand, for some sources (e.g. J1016+0028 and J0907+4620; see Figs. C.10 and C.7) spatially diffuse extended features, visible at low resolutions, are resolved out in our higher resolution images.

Overall, we find that 28/42 (66 percent) of our sources show extended features (i.e. any morphological classifications except for compact) in at least one of the spatial resolutions observed. We discuss this in the context of other AGN samples in Section 4.5.2.

Table 4.2: Summary of the radio properties used throughout this work.

Name	LLS (kpc)	α	FIRST	MR	HR	*qir*	Radio-AGN
(1)	(2)	(3)	(4)	(5)	(6)	(7)	(8)
J0749+4510†	66.5	**0.3**	D	I	C	–	yes
J0752+1935	3.58	-1.2	C	C	I	<**1.24**	yes
J0759+5050	0.85	-1.2	C	C	D	**1.31**	yes
J0802+4643	0.76	-1.1	C	C	J	<2.13	maybe
J0842+0759	1.77	-0.7	C	C	C	–	maybe
J0842+2048	0.46	-0.8	C	C	C	–	maybe
J0907+4620†	35.05	**-0.6**	D	I	I	–	yes
J0909+1052	0.99	-1.1	C	C	C	–	maybe
J0945+1737	11.0	-0.8	C	D	I	**1.32**	yes
J0946+1319	1.66	-1.2	C	C	C	**1.26**	yes
J0958+1439	0.9	-0.7	C	C	D	<1.81	yes
J1000+1242	25.0	**-0.4**	C	I	I	<**1.14**	yes
J1010+0612	0.21	-0.9	C	C	C	**0.89**	yes
J1010+1413	15.0	**-0.6**	C	I	I	<1.67	yes
J1016+0028	33.79	–	D	D	U	–	yes
J1016+5358	1.12	-1.3	C	C	J	<2.13	maybe
J1045+0843	0.43	-1.1	C	C	C	–	maybe
J1055+1102	3.46	-1.1	C	J	C	–	maybe
J1100+0846	0.27	-0.7	C	C	C	**1.09**	yes
J1108+0659	6.9	-0.8	C	J	D	1.93	yes*
J1114+1939	0.62	-0.9	C	C	C	–	maybe
J1116+2200	1.33	-1.2	C	C	J	–	maybe
J1222-0007	8.16	-0.9	C	J	D	2.05	maybe
J1223+5409†	11.0	**-0.3**	C	D	T	–	yes
J1227+0419	0.46	-1.1	C	C	C	–	maybe
J1300+0355	16.47	**0.5**	C	D	C	–	yes
J1302+1624	5.51	-0.8	C	I	C	<**1.2**	yes
J1316+1753	1.4	**-0.3**	C	C	T	–	yes

Continued on next page

Continuation from previous page

J1324+5849	0.73	-1.0	C	C	C	–	maybe
J1347+1217†	0.16††	–	C	C	C	**-0.32**	yes
J1355+2046	1.92	-0.9	C	C	J	<2.15	maybe
J1356+1026	5.6	-0.8	C	I	C	**1.16**	yes
J1430+1339	19.0	-0.9	J	I	D	**1.26**	yes
J1436+4928	0.76	-1.2	C	C	C	–	maybe
J1454+0803	1.73	-1.2	C	C	C	–	maybe
J1509+1757	7.28	-1.4	C	D	D	2.01	maybe
J1518+1403	13.16	-1.1	C	D	J	–	maybe
J1553+4407	22.92	**-0.1**	C	T	D	–	yes
J1555+5403	1.13	-1.0	C	C	J	–	maybe
J1655+2146	1.8	-1.2	C	C	D	<2.11	maybe
J1701+2226†	19.24	**-0.1**	I	I	I	–	yes
J1715+6008	0.69	-1.1	C	C	C	–	yes*

Notes: (1) Source name; (2) Largest linear size (LLS) in kpc (see Section 4.4.2). For sources classified as compact (C) in all three resolutions considered in columns (4–6), the deconvolved size from CASA's 'imfit' is given; (3) Spectral index (α) defined as $S_\nu \propto \nu^\alpha$ (see Section 4.4.3). A flat spectral index ($\alpha \geq -0.6$) is a strong indicator that we are observing the base of a radio jet, and these values are highlighted in bold (see Section 4.5.1); (4–6) Morphological classification from the FIRST image (LR; 4), our VLA MR image (5) and our VLA HR image (6). The possible classifications are: C = compact, D = double, T = triple, J = one sided jet (no closed contours), I = irregular / complex, and U = undetected (see Section 4.4.1); (7) *qir* of the source (see Section 4.4.5). *qir* <1.64 indicates that the radio emission is dominated by the AGN and these are highlighted in bold; (8) Our overall verdict on if this source is a Radio-AGN (i.e. the radio emission is dominated by the AGN; in which case the value in this column is 'yes'). For all other sources we were unable to determine the origin of the radio emission, and so they are marked as 'maybe' (see Section 4.5.1).

† these are the classical 'radio-loud' sources according to the Xu et al. (1999) division.

* denotes sources where the final classification was aided by extra information from the literature (see Section 4.5.1).

†† the size used here for this source was taken from O'Dea (1998). Since this size would make it unresolved even at the smallest resolution considered here (~0.25 arcsec) we classify it as compact (C) in all three columns (see Section 4.4.1).

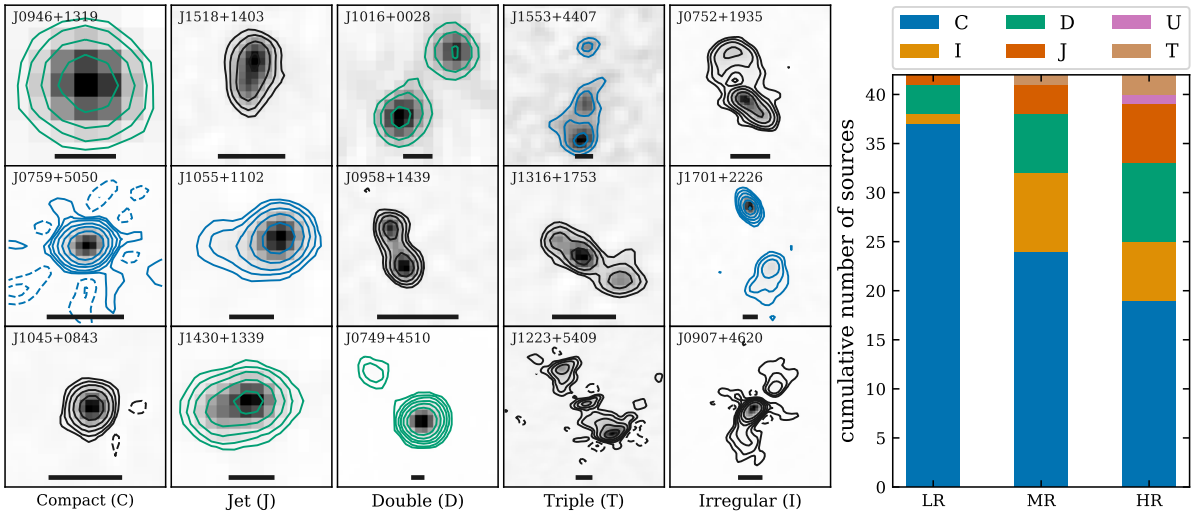

Figure 4.2: *Left:* examples of each of the morphological classifications used in this work. Each radio map is plotted in greyscale with contours whose colour denotes the data used: green for FIRST (LR), blue for our MR data and black for our HR data. Contours are plotted at ±[4, 8, 16, 32, 64, 128]σ. The size bar in each frame is 11, 4 or 2 kpc long for the LR, MR and HR data respectively. These data are displayed in the context of the other radio data considered and the optical images for each source in Appendix C.1. *Right:* distribution of the various morphological types for each resolution of radio data available (see Section 4.3.1). In addition to those classifications shown on the left, U is used when the source is undetected.

4.4.2 Radio size

In order to compare to previous works and explore the relation between the radio size and ionized gas properties (see Section 4.5.2), we measure the largest linear size (LLS) following common approaches in the literature (e.g. Kunert-Bajraszewska & Labiano 2010; also see Chapter 2, Jarvis et al. 2019). Firstly, we define LLS as the distance between the farthest peaks in the lowest resolution image where the source is not classified as compact (C). The peaks used to determine the size for each source are shown as part of the showcase images in Appendix C.1. Secondly, in the case where the source is compact in all three spatial resolutions considered, we use the major axis size, deconvolved from the beam from CASA 'imfit'. The largest linear size calculated for each source is listed in Table 4.2.

In more detail, we used peaks detected with $\geq 8\sigma$ significance, except for when data at other resolutions confirmed that the feature was real, in which case $\geq 4\sigma$ peaks were used (see e.g. J1518+1403, Fig. C.28). For J1108+0659 and J1222−0007 (see Figs. C.14 and C.17) we used our HR data to measure the size, since our MR image, although extended, did not show distinct peaks. We identified peaks using the Photutils 'find_peaks' function (Bradley et al., 2019). For many sources which were classified as having jet-like morphology (see Section 4.4.1)[3] the secondary peak(s) were identified using the residual image, after fitting the core emission with a Gaussian, whose width was fixed to the beam major and minor axes. For the Chapter 2 (Jarvis et al., 2019) sources, we did not repeat this analysis and simply use the largest published size for each source.[4] Finally for J1347+1217 we use the size published in O'Dea (1998) (0.16 kpc), since it is unresolved in FIRST and we do not have our own higher resolution images.

The sizes of our sources range from 0.16–66.5 kpc[5], with none of the sources being unresolved at all resolutions (i.e. compact in all three images and determined unresolved by CASA's 'imfit' to the HR core). Combining this with the total radio luminosities from NVSS ($L_{1.4GHz}$; see Table 4.1) we compare the radio properties

[3]Specifically, J1555+5403, J0752+1935, J1055+1102, J1355+2046 and J0802+4643.

[4]With the exception of J1100+0846 where we used the deconvolved size from CASA's 'imfit' to the C-band A-array data, not the distance between the peaks in the eMERLIN data which was used in Chapter 2 (Jarvis et al., 2019), to be consistent with the rest of the sample presented here.

[5]We note that the smallest size measured from our VLA data is 0.2 kpc.

of our sample to those of traditional radio galaxies from An & Baan (2012) in Fig. 4.3.

The sizes we measure for our sample are broadly consistent with those found in samples of compact radio galaxies. Specifically, typical sizes for GHz-Peaked Spectrum (GPS) and Compact Steep Spectrum (CSS) radio galaxies are ∼0.1–10 kpc (see Fig. 4.3). However, our sources have significantly lower radio luminosities than typical CSS / GPS sources. This is most likely due to selection effects. CSS / GPS sources have traditionally been defined as luminous (i.e. $L_{1.4GHz} > 10^{25}$ W Hz^{-1}; Orienti 2016). Even without this prerequisite, the need for detections in multiple bands, in relatively shallow radio surveys, to identify the distinguishing inverted spectrum of these sources, biases these samples towards high radio luminosities (see e.g. Callingham et al., 2017). In comparison, our radio luminosity cut is $L_{1.4GHz} > 2{\times}10^{23}$ W Hz^{-1}, with a median value of $L_{1.4GHz} = 4.8 \times 10^{23}$ W Hz^{-1}.

The largest sources in our sample (i.e. those with radio sizes $\gtrsim$10 kpc) overlap with the tail of the smallest, dimmest Fanaroff-Riley class I galaxies (FRI; Fanaroff & Riley, 1974). The smallest FRI sources in the An & Baan (2012) sample are from Fanti et al. (1987) which has spatial resolutions down to ∼1 arcsec (in comparison, our highest resolution is ∼0.25 arcsec), and sources which were not visibly extended on these scales are excluded from the catalogue. This means that at their mean redshift of $z = 0.06$ sizes $\lesssim$1 kpc (i.e ∼1/3 of our sample) could not be measured. Additionally, Fanti et al. (1987) define their sizes using the lowest reliable contour, rather than the peak-to-peak size as we do, which would result in Fanti et al. (1987) typically reporting a larger size than we do for the same source. Thus the smaller sizes in our sample compared to typical FRI sources is likely a resolution effect. We note that deeper radio images would be needed to reliably classify the majority of our sources as having FRI or FRII like morphologies (i.e. to determine the relative contributions of jets, lobes and hot spots).

Within our sample we see a noticeable difference between the type 1 and type 2 targets. The median radio size of the type 2 AGN in our sample is 2.4 kpc, slightly larger than the median size of the type 1's (1.8 kpc). This would be expected if the radio emission comes from AGN driven winds or jets which are expanding perpendicular to the AGN's obscuring torus, since the radio emission from the

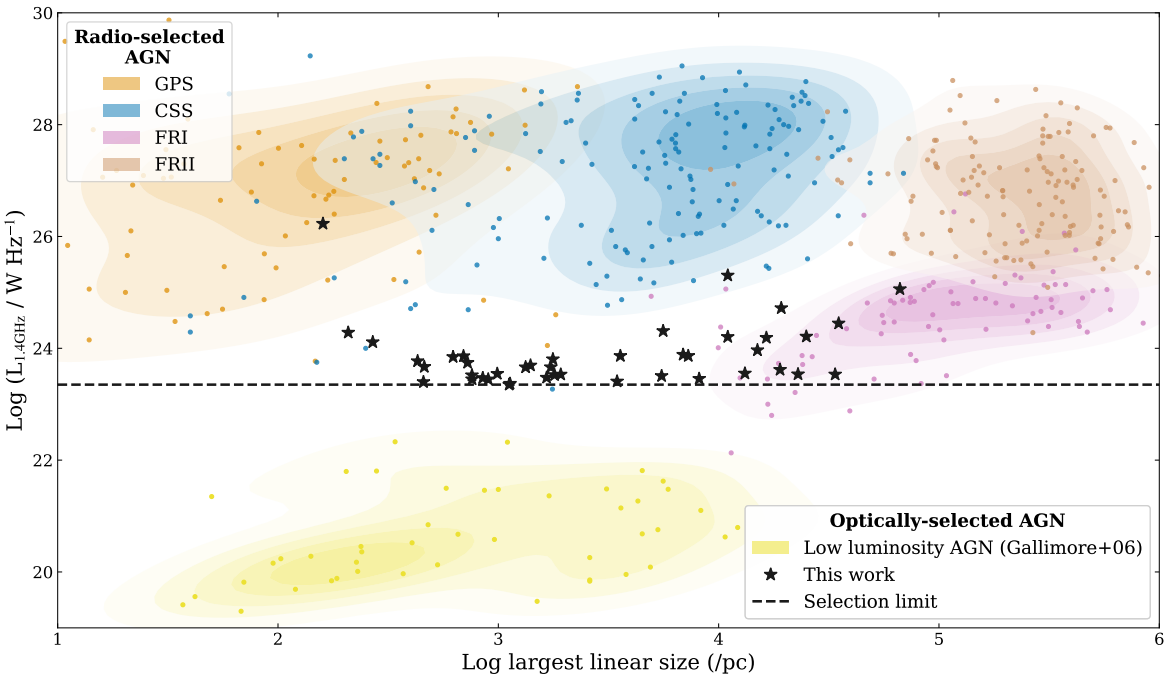

Figure 4.3: Radio luminosity versus largest linear size for the complete sample presented here (black stars) compared to the radio-selected AGN compiled by An & Baan (2012) (points and density contours of the appropriate colour; see also Chapter 2, Jarvis et al. 2019). Seyfert and LINER galaxies ('low luminosity AGN'; Gallimore et al., 2006) are shown for additional comparison. The black dashed line marks the radio luminosity selection criteria for our sample ($L_{1.4GHz} > 2 \times 10^{23}$ W Hz^{-1}). Our quasars share properties with the lowest luminosity compact radio galaxies (CSS / GPS) and low luminosity, most compact FRI radio galaxies. We suggest that at least some of the separation of the different populations are driven by selection effects (see Section 4.4.2).

type 1's would then be shortened due to projection effects. This is potentially consistent with the fact that the type 1's also have slightly higher median radio luminosities than the type 2s (5.7 versus 4.4×10^{23} W Hz^{-1}), since for the type 1's the radio luminosity of a radio jet would be increased due to Doppler boosting.

4.4.3 Core spectral index

The identification of a flat spectrum radio core is often considered key to positively identifying an object as an active radio jet (see e.g. Orienti & Dallacasa, 2014; Panessa et al., 2019). As such, we measured the spectral index of the radio component best identified as the 'core' from our HR VLA images. We used the

spectral index (α) maps discussed in Section 4.3.1 for this analysis. We took the median value of the α image within the 16σ contour from the total intensity images. In the cases where there are multiple peaks in the HR image, we defined the core to be either the brightest peak or the component, if any, with $\alpha > -0.6$. This method reliably ensures that if we have detected the radio core, we report its spectral index and not that of another component.

In a few cases we were not able to use the 16σ contour to reliably isolate the candidate core. For J1108+0659 and J1553+4407 (see Figs. C.14 and C.29) the 16σ contours contained fewer than five pixels (i.e. not enough to get a meaningful median), and so the 8σ contour was used. For many of the sources which are close doubles or have a jet-like morphology in our HR images (see Section 4.4.1) the 16σ contour contained multiple components; in these cases the 32 or 64σ contour was used.[6] We note that using the higher sigma contours for these sources does not significantly change the derived spectral index, and in particular does not cause any to change from steep ($\alpha < -0.6$) to flat ($\alpha \geq -0.6$).

We note that, for the sources studied in Chapter 2 (Jarvis et al., 2019) we do not repeat the analyses and use the core spectral indices derived in that work (see Chapter 2, Table 2.4), similarly using either the component with $\alpha > -0.6$, or the brightest where applicable.

The core spectral index for each source is listed in Table 4.2. We have no measurement of the spectral index for J1347+1217 which we did not observe with the rest of this sample or for J1016+0028 since this source was wholly undetected in our HR image (see Fig. C.10). As such, we can state, that at the flux and resolution limits of our data we detect flat spectrum ($\alpha \geq -0.6$) cores in 9/41 of our sources. This is one of the key parameters in our identification of AGN dominated radio emission in Section 4.5.1 and is a strong indication of the presence of a relativistic jet in the nine sources where we detected a flat spectrum core. Of particular interest is, that of the nine sources with flat spectrum cores, five are classified as 'radio-quiet' by the Xu et al. (1999) division. This strongly demonstrates the limitations of this 'radio-quiet' versus 'radio-loud' definition for identifying emission from jets in AGN (see also Padovani, 2016).

[6]Specifically the 32σ contour was used for J1355+2046 and the 64σ contour was used for J0759+5050, J0802+4643, J1655+2146, J1701+2226 and J0907+4620.

4.4.4 Brightness temperature

The bases of jets are expected to have high brightness temperatures due to non-thermal processes from relativistic electrons (see e.g. Neff & de Bruyn, 1983; Preuss & Fosbury, 1983; Blundell & Beasley, 1998; Ulvestad et al., 2005). Specifically, the brightness temperature (T_B) in K is defined as:

$$T_B = \frac{1.8 \times 10^9 (1+z) S_\nu}{\Theta_{maj} \Theta_{min} \nu^2}, \tag{4.1}$$

where S_ν is the peak flux in mJy/beam, ν is the frequency in GHz, and Θ_{maj} and Θ_{min} are the source major and minor axis sizes respectively, deconvolved from the beam, in milliarcsec (following Doi et al., 2013; Berton et al., 2018). We calculated these values for each of our sources from our VLA HR images using CASA Gaussian fits (using the 'imfit' routine) to the central component. For those with multiple central components in our HR image either the brightest or the one with $\alpha > -0.6$ was used (as in Section 4.4.3). All of our sample have brightness temperatures $< 10^6$ K which is generally accepted as the limit above which the emission must be due to AGN (Falcke et al., 2000). Therefore the brightness temperature is not a constraining value for the source of the radio emission for our sample. This is not unexpected given the low fluxes of our targets and relatively low spatial resolution of our observations. Higher spatial resolution radio observations (e.g. very long baseline interferometry – VLBI) would be needed to provide more constraining measurements of the brightness temperature. We note that the cores of two sources (J0749+4510 and J1300+0355) are reported as point sources using 'imfit'. For these we used 1/2 of the beam size for our T_B calculation and both had $T_B < 10^6$ K, although since we did not actually measure a size, these are lower limits. Since these also have flat spectral indices and jet-like morphologies the compactness of the core further supports their identification as Radio-AGN (see Section 4.5.1).

4.4.5 Radio excess

Finally, using archival spatially unresolved radio and infrared data we can effectively constrain if the AGN is contributing significantly to the total radio emission for the sources in our sample. Specifically, both star formation and AGN related

processes are capable of producing 1.4 GHz radio luminosities comparable to those observed in our sample (see e.g. Condon, 1992). Those where star formation dominates the radio emission can be separated from those where the AGN dominates (so called 'Radio-AGN') by comparing the relative strength of the star formation to the radio luminosity.

In Chapter 2 (Jarvis et al., 2019) we used the correlation found between the radio and infrared emission (*IR*) for normal star-forming galaxies (i.e. the radio–*IR* correlation) to identify the sources with more radio emission than would be predicted based on their star formation (radio excess). This well studied method makes use of the fact that if both the infrared and radio emission in a galaxy are dominated by stellar processes they follow a tight relation, with radio-loud AGN scattering to higher radio luminosities (e.g. Helou et al., 1985; Bell, 2003; Padovani, 2016). Although in Chapter 2 (Jarvis et al., 2019) we used spectral energy distribution (SED) fitting to extract the infrared luminosity without the AGN contribution, because of the increased difficulty of performing SED fits for type 1 AGN, for this work, we calculated the far infrared flux (S_{FIR}; 42.5–122.5 μm) for each source following Helou et al. (1985):

$$S_{FIR} = 1.26 \times 10^{-14}(2.58 S_{60\mu\mathrm{m}} + S_{100\mu\mathrm{m}})\mathrm{W\ m^{-2}}, \tag{4.2}$$

where $S_{60\mu\mathrm{m}}$ and $S_{100\mu\mathrm{m}}$ are the rest frame 60 and 100 μm fluxes in Jy (see also Marvil et al., 2015). We calculated these by linearly interpolating the Infrared Astronomical Satellite (IRAS; Neugebauer et al., 1984) 60 and 100 μm fluxes or the ESA *Herschel* Space Observatory PACS point source catalogue's (Pilbratt et al., 2010; Poglitsch et al., 2010) 70 and 100 μm fluxes where the IRAS data was unavailable or the sources was undetected. We note that for the two sources detected in both bands in IRAS and PACS (J1356+1026 and J0759+5050), we get consistent results using either set of data.

Specifically, we used IRAS fluxes from the faint source catalogue (Moshir et al., 1992). We followed a log likelihood method of matching IRAS to the closest Wide-field Infrared Survey Explorer (WISE) all-sky survey (Wright et al., 2010) source to the SDSS position (< 2 arcsec) to account for the large and asymmetric IRAS beam following Wang et al. (2014). For the sources that were observed by IRAS but were not detected, we estimated conservative maximum upper limits of 0.3, and 3 mJy for the 60, and 100 μm bands respectively.

It is possible that the L_{FIR} measured in this way is artificially boosted due to contribution from the AGN luminosity (Shi et al., 2007; Shimizu et al., 2017). We confirm that the values used in this work are reliable by comparing to the values presented in Chapter 2 (Jarvis et al., 2019). In that work we used *UV* to *IR* SED fitting to isolate the 8–1000 μm infrared luminosity (L_{IR}) from star formation. Using L_{IR}=1.5L_{FIR}(Yun et al., 2001), we find that the values from Equation 4.2 are smaller than the SED derived values by a median of 0.03 dex (maximum 0.14, minimum −0.3); i.e. within the 0.3 dex systematic uncertainty expected on the SED derived values, for the five sources in both samples which were detected at 60 and 100 μm in IRAS or PACS. Furthermore, the upper limits derived from Equation 4.2 are larger than the SED derived values for the three sources in both samples where we were only able to get an upper limit.

The offset of a source relative to the radio–*IR* correlation is commonly quantified via *qir* defined as:

$$qir = \log\left(\frac{S_{FIR}}{3.75\times10^{12}\mathrm{W\ m^{-2}}}\right) - \log\left(\frac{S_{1.4\mathrm{GHz}}}{\mathrm{W\ m^{-2}Hz^{-1}}}\right), \tag{4.3}$$

where $S_{1.4\mathrm{GHz}}$ is the 1.4GHz radio flux, and qir<1.64 indicates an excess of radio emission compared to the relation for star-forming galaxies (Helou et al., 1985).[7] We note that only 20/42 of our sources (48 percent of the sample) were observed by IRAS or PACS and so can be classified based on this diagnostic. Of these, we find that eleven are defined as radio excess using this metric (i.e. qir<1.64, including those with upper limits <1.64), six have non-constraining limits and three sources have *qir* values that fall within the region occupied by star-forming galaxies[8] (qir>1.64; see Fig. 4.4 and Table 4.2). Overall this means that *at least* 11/42 (26 percent) of our sample have excess radio emission above what can be explained by star formation with 11/20 (55 percent) of those for which we have any constraints on the *FIR* emission being radio excess.

[7]We note that this is equivalent to a limit of qir<1.8 when *qir* is defined in terms of the 8–1000 μm infrared luminosities and using L_{IR}=1.5L_{FIR}(Yun et al., 2001).

[8]Although, as is discussed further in Section 4.5.1, this does not necessarily mean that their radio emission is dominated by star formation, if their *FIR* emission has a significant contamination from the AGN.

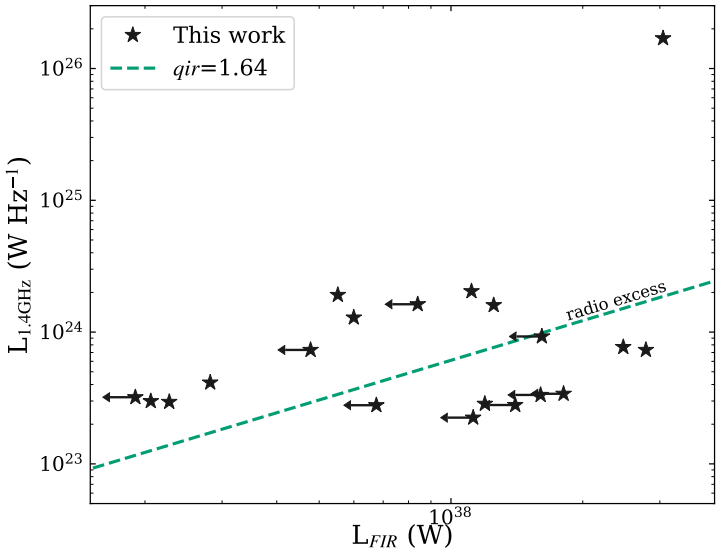

Figure 4.4: The observed radio luminosity from NVSS compared to the 42.5–122.5 μm infrared luminosity calculated from the observed IRAS / PACS fluxes for the 20 sources with the required data (black stars). The green dashed line marks qir=1.64 and divides sources where the radio emission is consistent with that from star formation from radio excess sources. See Section 4.4.5 for more details.

4.5 Discussion

Here we discuss the implications of the above results and put them into the context of previous work. Specifically, we consider the origin of the radio emission in Section 4.5.1, identifying, where possible, sources with radio emission dominated by the AGN (Section 4.5.1) and comparing this to the commonly used Best & Heckman (2012) classifications (Section 4.5.1). We then explore the relationship between the ionized gas and radio properties of our sources in Section 4.5.2, comparing the sizes measured in Section 4.4.2 to the FWHM of the [O III] line (Section 4.5.2) and the [O III] luminosity (Section 4.5.2).

4.5.1 Origin of radio emission

By constraining the dominant physical mechanisms contributing to the radio emission in our sample we gain deeper understanding of the energetics of the galaxy and the possible drivers of outflows. Specifically, we combine the qir value, the radio morphologies and spectral indices presented in Section 4.4

to identify the sources with a significant contribution from the AGN to their radio emission (Section 4.5.1). In Section 4.5.1 we compare our findings to the commonly applied criteria of Best & Heckman (2012).

Final classifications

Our identification of so called 'Radio-AGN' in our sample is based on the spectral index of the radio feature identified as 'core' in Section 4.4.3, the value of *qir* (radio excess; see Section 4.4.5), and the radio morphology (see e.g. Padovani, 2016; Panessa et al., 2019).

A flat spectral index ($\alpha \gtrsim -0.5$) is typically associated with the optically thick launching region at the base of a jet (Blandford & Königl, 1979; Reynolds, 1982). Using the core spectral indices defined in Section 4.4.3, we take $\alpha \geq -0.6$ as indicative of a flat spectrum core, where the slightly steeper than typical value of -0.6 was selected to ensure that J1010+1413, which was previously identified as a Radio-AGN in Chapter 2 (Jarvis et al., 2019) with $\alpha = -0.55$, is also classified as a Radio-AGN here and note that no other source would be classified differently if we used the more typical value of -0.5. Steep spectral indices are less constraining for the origin of the radio emission, with star formation, jets and AGN winds all typically producing $\alpha \approx -0.7$. We note that we do not have a core spectral index for J1016+0028 since it was undetected in our HR image or J1347+1217 as we do not have HR VLA data for this source. We classify nine sources as Radio-AGN based on the identification of a flat spectrum core ($\alpha \geq -0.6$).

Our second indicator that a source was a Radio-AGN was $qir < 1.64$ (radio excess). We find that eight of our sources have measured values of $qir < 1.64$ with an additional three having upper limits < 1.64 making them also certainly Radio-AGN. Three sources (J1108+0659, J1222−0007 and J1509+1757) have *qir* values (not upper limits) which place them in the star-forming region of the radio–*IR* correlation (see Fig. 4.4 and Table 4.2). However, the AGN can contribute to the measured *FIR* luminosity, which is known to cause AGN to sometimes artificially fall on the radio–*IR* correlation (Morić et al., 2010; Zakamska et al., 2016). As such, a source falling above the radio–*IR* correlation (i.e. $qir < 1.64$) indicated that its radio emission must have a significant contribution from the AGN, however, being on the relation (i.e. $qir > 1.64$) does not rule out

an AGN contribution and as such does not place significant constraints on the origin of the radio emission in these sources. For the remaining sources, six of which have upper limits on *qir* which are above the constraining value of 1.64, and 22 which were not observed at all with either IRAS or PACS, we can put no constraints on the origin of the radio emission based on the radio–*IR* correlation. In summary, using radio excess we are able to classify 11/42 of our targets as Radio-AGN, only one of which was previously classified as a Radio-AGN based on having a flat spectrum core, bringing our total number of Radio-AGN in this sample up to 19.

Although the radio emission from star formation and AGN related sources (jets, winds and coronal emission) are expected to have different morphologies (e.g. Panessa et al., 2019), they can often be hard to distinguish, particularly for barely resolved radio features or in galaxies undergoing mergers (see e.g. Condon, 1992; Bondi et al., 2016; Chen et al., 2020). As such we lay out two, fairly conservative scenarios for confidently identifying radio emission from the AGN based on the observed morphology. Firstly, in order to have radio emission from star formation, there must be a population of young stars, therefore such radio emission should be coincident with bright optical continuum. As such, radio emission without an optical counterpart is likely of AGN origin. This condition results in J0749+4510, J0907+4620, J0945+1737, J1000+1242, J1016+0028, J1553+4407 and J1701+2226 (see Figs. C.1, C.7, A.2, A.8, C.10, C.29 and C.32) being classified as Radio-AGN, with only J1016+0028 not having been classified as one already. Unfortunately the radio emission in most of our targets is confined within the host galaxy, meaning that higher spatial resolution images sensitive to star formation (e.g. infrared or *UV*) would be needed to make full use of this distinction (see e.g. Bondi et al., 2016; Chen et al., 2020). Secondly, *symmetric* triple and double structures are most likely associated with a jet or loosely collimated wind (see e.g. Alexandroff et al., 2016; Baldi et al., 2018; Kimball et al., 2011a). This results in all three sources which were classified as triple (T) in Section 4.4.1 (see Table 4.2) being now classified as Radio-AGN (all three were previously classified as Radio-AGN based on their flat spectra cores). Finally, we define symmetric doubles as those classified as a double (D) in at least one of the resolutions considered in Section 4.4.1 (see Table 4.2) and where the two radio lobes are additionally, roughly centred around the peak of

the host galaxy emission from the optical images and have roughly the same flux (i.e. they peak at the same contour level). By this classification J0958+1439 and J1016+0028 (see Figs. A.5 and C.10) are classified as Radio-AGN, with J0958+1439 not having been previously so classified (see also Chapter 2, Jarvis et al., 2019). Overall, 12 sources are classified as Radio-AGN by their morphology, adding two which were not previously classified as Radio-AGN based on the flat spectrum core and radio excess criteria, bringing the total up to 21.

There are additionally, two sources which are not classified as Radio-AGN by the method described above, but which have been identified as hosting compact jets in the literature using higher spatial resolution radio observations than those presented here. Specifically, Bondi et al. (2016) identified a core-jet structure in J1108+0659, and Müller-Sánchez et al. (2015) identified a 0.11 arcsec jet in J1715+6008. Based on this additional information we classify these sources as tentative Radio-AGN in Table 4.2 (marked with yes*; see Appendix C.1.5 and C.1.9 for more details). Adding these to our Radio-AGN count brings the total up to 23.

Overall, 23/42 (55 percent) of the sample are classified as Radio-AGN (21/42 if only the information presented in this Chapter is considered). For the rest of the sample, the origin of the radio emission is unclear, with star formation or the AGN still being viable possibilities.

Comparison to other radio AGN diagnostics

We now compare our Radio-AGN identification to other common methods. As already discussed, the 'radio-loud' division of Xu et al. (1999) only identify 5 of the 23 Radio-AGN that we identified in the previous section (see Fig. 4.1). This supports the general move away from these classical 'radio-loud' versus 'radio-quiet' divisions (see e.g. Padovani, 2016). Another widely adopted method for identifying 'radio-loud' AGN are the criteria of Best & Heckman (2012) (see also Sabater et al., 2019). Specifically: the Hα luminosity versus the radio luminosity and the "D_n4000 versus $L_{\rm rad}$ / $M_\star$" plane. Like the radio-*IR* correlation, these diagnostics compare the observed radio emission to that which would be expected for normal star-forming galaxies to determine the origin of the radio emission. We compare our classification from Section 4.5.1 to what we would have found using these diagnostics.

Hα is a common star formation rate indicator. We use the three Gaussian fits to the Hα line from Mullaney et al. (2013), summing the narrow and intermediate components (i.e. for the type 1 sources, excluding emission associated with the broad line region). We compare our results to the diagnostic cut from Best & Heckman (2012) in Fig. 4.5, namely: $\log(\mathrm{H}\alpha)=1.12(\log(\mathrm{L}_{1.4\mathrm{GHz}})-17.5)$, where H$\alpha$ is in $\mathrm{L}_{\odot}$ and $\mathrm{L}_{1.4\mathrm{GHz}}$ is in W Hz^{-1}. However, this cut is known to be conservative in its identification of Radio-AGN (see e.g. Sabater et al., 2019). Only J1223+5409, and J1347+1217 would be classified as Radio-AGN by this method. Using Hα as a star formation diagnostic is likely to be particularly poor for the most radiatively luminous AGN, such as our sample, since the Hα emission will have a strong, potentially dominant, contribution from the AGN (e.g. Kewley et al. 2001).

D_n4000 is a measurement of the strength of the spectral break at 4000 Å and is a good tracer of the mean stellar age (for ages $\lesssim$ Gyr), and the ratio of the radio luminosity and stellar mass also depends strongly on the specific star formation rate of the galaxy if the radio emission is dominated by star formation effects. We use the division from Best & Heckman (2012) for this comparison (see also Best et al., 2005; Kauffmann et al., 2008), which is derived from the Bruzual & Charlot (2003) stellar synthesis models. We take both D_n4000 and $\mathrm{M}_{\star}$ from MPA-JHU SDSS DR8 measurements[9] converted from a Kroupa to Chabrier IMF (Madau & Dickinson, 2014). We note that these stellar masses are calculated using optical SED fitting without considering AGN emission, and so are particularly unreliable for the type 1 AGN in this sample (where the optical emission is expected to be dominated by the AGN). As such, the type 1's are excluded from this diagnostic. As can be seen from Fig. 4.5, only one source, J0907+4620, is classified as a Radio-AGN via this method. We note that this classification requires the use of uncertain stellar mass measurements. To investigate this, we checked the MPA-JHU stellar masses against those derived from the independent *UV* to *IR* SED fits from Chapter 2 (Jarvis et al., 2019). For the nine shared targets we found that the MPA-JHU masses are on average 0.3 dex higher than those from our SED fitting with a maximum difference of 0.9 dex. However, all our type 2 sources fall in a region of the parameter space in Fig. 4.5 where the final classification is highly *insensitive* to the exact stellar mass measurements, with deviations of $\gtrsim$0.6 dex

[9] https://www.sdss.org/dr12/spectro/galaxy_mpajhu/

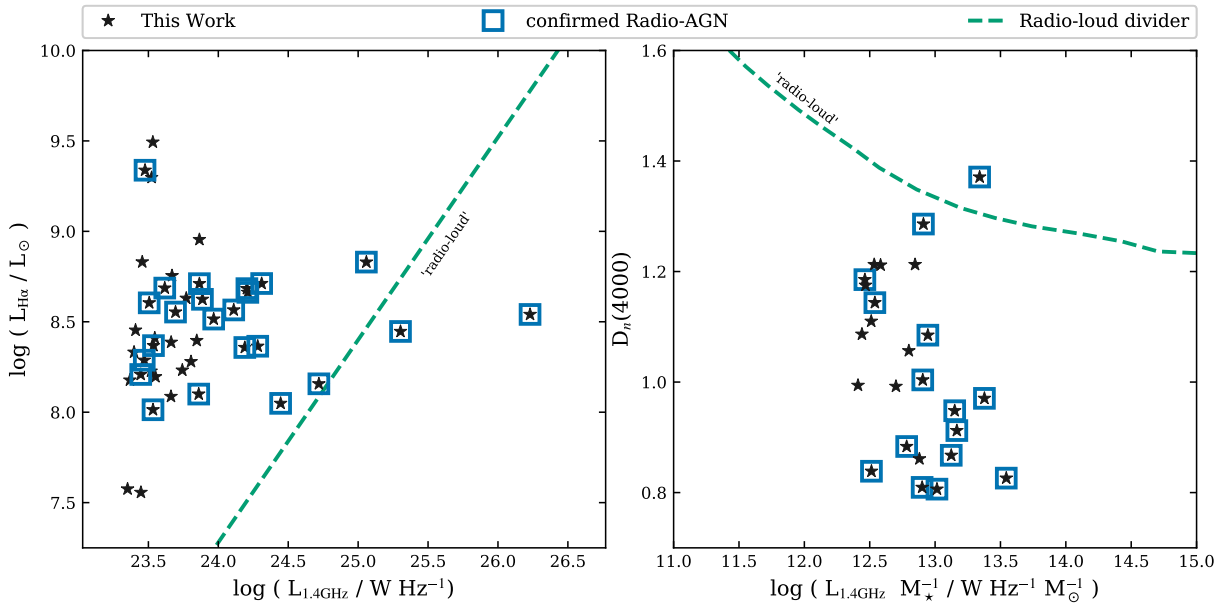

Figure 4.5: Two of the Best & Heckman (2012) diagnostic plots (see Section 4.5.1). All but three of the sources presented here (black stars) fall in the 'radio-quiet' / star formation area of each. Those that are confirmed as Radio-AGN in this Chapter (Section 4.5.1) are further marked with blue squares. In each panel, 'radio-loud' sources are divided from the remainder of the population by the green dashed line. *Left:* Hα versus the 1.4 GHz radio luminosity. *Right:* the D$_n$4000 versus the ratio of the 1.4 GHz radio luminosity and the stellar mass. Type 1 AGN are not included in this comparison.

needed to change any of the classifications. Indeed, all but two of our sources have a stable classification for deviations in the stellar mass of $\gtrsim$1 dex. We conclude that the stellar masses used are unlikely to influence this classification.

In summary, only 3 of the AGN in our sample would be classified as 'radio-loud' by the Best & Heckman (2012) classifications, which are a subset of the five classical 'radio-loud' sources identified by the Xu et al. (1999) division (see Table 4.2 and Fig. 4.1). Consistent with our findings in Chapter 2 (Jarvis et al., 2019), the Hα and D$_n$4000 diagnostics fail to identify the majority of the AGN dominated radio sources in our sample, indicating that the Best & Heckman (2012) criteria are unreliable for AGN with the strongest emission lines. A combination of the radio–*IR* correlation and radio morphology / spectral index seem to provide a more complete identification of Radio-AGN in this moderate radio luminosity, [O III] luminous sample.

4.5.2 The ionized gas – radio connection

There is mounting evidence of a connection between the radio and ionized gas properties of 'radio-quiet' AGN. For example, Mullaney et al. (2013), which uses the parent population of our sample (Section 4.2), found a higher incidence of outflows in the higher radio luminosity sources ($L_{1.4GHz} > 10^{23}$ W Hz^{-1}; see also Zakamska & Greene, 2014). In Molyneux et al. (2019) we studied all of the Mullaney et al. (2013) sources with FIRST or NVSS counterparts, and discovered a trend towards lower [O III] FWHM values for larger radio sources, with those where the radio was confined within the SDSS fibre being twice as likely to contain an extreme outflow (FWHM > 1000 km s^{-1}). We use the ∼20 times higher spatial resolution radio images presented in this work to study the connection between the ionized gas and radio properties of this sample.

FWHM

In Fig. 4.6 we compare the size of the sources from our sample (see Table 4.2) to the FWHM of their broadest, luminous [O III] emission-line component (Table 4.1; Mullaney et al., 2013). From our data, there is evidence for a negative correlation between the FWHM and the radio size, with a Spearman rank correlation coefficient of −0.45 and p-value for a null hypothesis of uncorrelated data of 0.003. If only our confirmed Radio-AGN are considered, the correlation strengthens, with a coefficient of −0.64 and a p-value of just 0.0009. For comparison / to guide the eye we plot the qualitatively similar relation found by Labiano (2008) whose CSS / GPS sample span a similar range of [O III] luminosities and radio sizes to the sample presented here (approximately $10^{41} < L_{[O\ III]} < 10^{44}$ erg s^{-1} and 0.1 < LLS < 10 kpc) but with significantly higher radio luminosities ($L_{1.4GHz} \gtrsim 10^{25}$ W Hz^{-1}).

Both radio jets and radiation driven winds could produce such a correlation. Specifically, as the jet / wind expands through the galaxy, interactions with the interstellar medium (ISM) would cause deceleration, which would result in the observed lower outflow speeds (traced by the FWHM of the [O III] emission) for larger radio sources (see e.g. Labiano, 2008; Mukherjee et al., 2018). Furthermore, in the case of the jet scenario, one would expect a sharp decrease in jet–gas interactions once the size of the radio jet expands past the host galaxy (see e.g.

Holt et al., 2008; Molyneux et al., 2019). If the radio emission is larger than the SDSS fibre (3 arcsec diameter, or 7.8 kpc at $z = 0.15$, the mean redshift of our sample), any interactions with the ISM might not be detected, resulting in radio sources with sizes larger than the fibre size having significantly smaller FWHM values than the rest of the sample. We do not see any strong indication of this effect. We note however, that many of our sources show complex radio morphologies, so that the largest radio structure observed may not always be the main source of interaction with the ionized gas (see e.g. J0749+4510 and J1701+2226 – Figs. C.1 and C.32, which show radio features at multiple spatial resolutions). This is further demonstrated by Chapter 2 (Jarvis et al., 2019), in which our IFS observations revealed direct interactions between the smaller scale radio features observed and the ionized gas (e.g. J0945+1737 and J1430+1339 in Fig. 2.10 of that work; see also Harrison et al. 2015). This highlights the need for IFS data for the whole sample in order to constrain jet-gas interactions more directly and on multiple scales. Additionally, we note that all of our confirmed Radio-AGN in Fig. 4.6 which are smaller than the SDSS fibre have relatively high FWHM values (i.e. 625–2483 km s^{-1}). We additionally note that all but one lie above the Labiano (2008) relation. This could be because our sample are primarily weak jets (based on their radio luminosity) which may interact more efficiently with the host galaxy ISM than stronger jets (see e.g. Mukherjee et al., 2018). In contrast, the confirmed Radio-AGN with sizes larger than the fibre, occupy the full range of observed FWHM (i.e. 270–1711 km s^{-1}), as some may still be interacting on smaller scales (as discussed above) while others have passed outside of the fibre and so are no longer impacting the observed FWHM.

[O III] luminosity

In Fig. 4.7 we show the [O III] luminosity versus radio size, combining our sample with the SDSS matched GPS / CSS sample of Liao & Gu (2020). From this figure we observe a lack of compact radio sources (i.e. $\lesssim$0.1 kpc) at the most extreme [O III] luminosities (i.e. $L_{[OIII]} \gtrsim 10^{42}$ erg s^{-1}). Combining these samples is justified, since our targets represent a natural expansion of the CSS / GPS population (see Fig. 4.3). Specifically, the Liao & Gu (2020) sources have an average radio luminosity of $L_{1.4GHz} \approx 3 \times 10^{26}$ W Hz^{-1}, in contrast to the median value of $L_{1.4GHz} = 4.8 \times 10^{23}$ W Hz^{-1} for our sample. Most importantly,

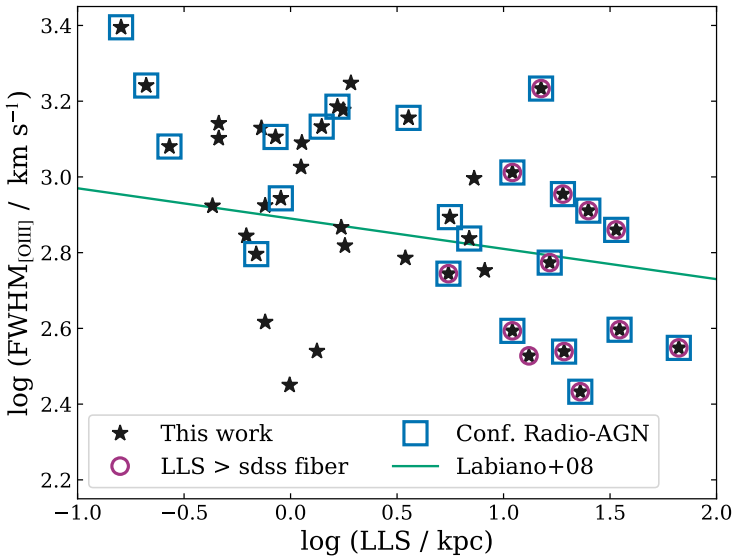

Figure 4.6: The FWHM of the broadest, luminous [O III] emission-line component from the Mullaney et al. (2013) fits for our data (see Table 4.1) compared to the largest linear size (LLS) calculated in this work (see Table 4.2; black stars). Magenta circles additionally mark those whose LLS is larger than the SDSS fibre. The sources where we were able to confirm that the AGN is contributing significantly to the radio emission (Radio-AGN; see Section 4.5.1) are further marked with blue squares. For comparison / to guide the eye we include the linear fit to archival CSS and GPS data from Labiano (2008) (green line).

our sample alone spans only a small range of $L_{[O\ III]}$. By including the Liao & Gu (2020) sources, we expand our [O III] coverage down to $\sim 10^{39}$ erg s^{-1}. We note that Kunert-Bajraszewska & Labiano (2010) and Labiano (2008) show qualitatively similar results, i.e. that the most [O III] luminous sources are all also among the largest radio sources. This is also consistent with Leipski et al. (2006), who find larger radio sizes in the quasars in their sample compared to the Seyferts.

That sources with high $L_{[O\ III]}$ seem to be associated preferentially with extended radio sources (Fig. 4.7) could explain why we find a larger fraction of spatially extended sources than e.g. Pierce et al. (2020). Specifically we find that 66 percent of our sample show spatially extended features compared to 44 percent in Pierce et al. (2020), whose selection criteria are almost identical to those in this work with the exception that their sample all have $L_{[O\ III]}<10^{42}$ erg s^{-1} (see also Kukula et al., 1998; Gallimore et al., 2006). This could also help explain why we found a higher fraction of spatially extended sources in Chapter 2 (Jarvis et al., 2019) (~80–90 percent), since the subset of targets in that work all fall at the higher [O III] luminosity end of the current sample (median $L_{[O\ III]} = 4.3\times10^{42}$ erg s^{-1}, compared to 2.1×10^{42} erg s^{-1} for the complete sample presented here; see Fig. 4.1).

A connection between the [O III] luminosity and radio emission could be expected for both jet and wind models. Specifically, photon pressure driven winds could cause shocks in the galactic interstellar medium (ISM), resulting in extended, likely bi-conical radio emission (Nims et al., 2015; Jiang et al., 2010), or AGN jets can interact with and ionize the ISM (Bicknell et al., 1997; Mukherjee et al., 2018). In either case, as the wind / jet passes through the ISM it triggers or enhances the [O III] emission (see e.g. Labiano, 2008). Specifically, compact radio sources can only excite the gas in the central parts of the galaxy which places a limit on the total luminosity, whereas larger sources can ionize larger volumes of gas. At the same time, large radio sizes are possible with lower [O III] luminosities if the jet / wind can pass through or out of the galaxy with minimal interaction with the ISM, depending on the orientation and power of the jet / wind and the properties of the ISM (see e.g. Mukherjee et al., 2018). This warrants further investigation.

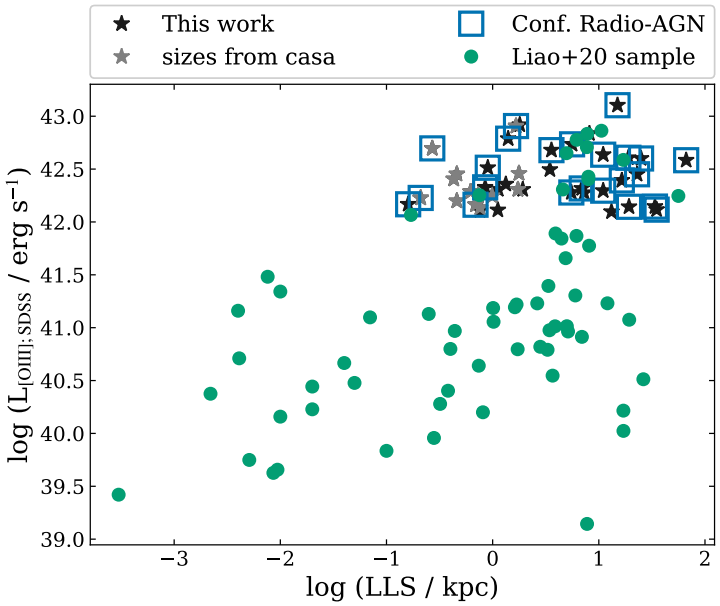

Figure 4.7: The [O III] luminosity (from SDSS single Gaussian fits) versus largest linear size (LLS) of the radio emission, for the sample presented here (black stars / grey for those where the LLS was calculated using Guassian fits from CASA) and for the SDSS matched GPS / CSS sample of Liao & Gu (2020) (green circles). The sources in our sample which we were able to confirm as Radio-AGN (see Section 4.5.1) are additionally marked with blue squares. High $L_{[O\ III]}$ AGN all tend to be associated with larger radio sources, where less [O III] luminous AGN can be associated with a wide range of radio sizes.

4.6 Conclusions

We present spatially resolved radio observations at 1.5 and 6 GHz with ∼1 and 0.25 arcsec resolution for the 42 z<0.2 [O III] and radio luminous AGN of the Quasar Feedback Survey ($L_{[O\ III]} > 10^{42}$ ergs s^{-1} and $L_{1.4GHz} > 2\times10^{23}$ W Hz^{-1}). By combining this with archival information, we investigate the source of the radio emission and the relationship between the radio and ionized gas properties of this sample. In particular we find:

1. 28/42 (66 percent) of the sample show spatially extended radio features on resolutions $\gtrsim$0.25 arcsec (see Table 4.2 and Fig. 4.2). In our ∼0.25 arcsec resolution images in particular, we find that 19 of our sources are compact, eight show a double lobed radio morphology, two show a triple lobe–core–lobe structure, six show a jet-like, elongated structure, six have complex, irregular morphologies and one is undetected. Additionally, six of the sources that are compact or undetected in these images show extended, diffuse radio structures in our lower resolution images, emphasising the requirement for both high spatial resolution and short baselines to construct a complete morphological picture.

2. the largest linear radio sizes of the sample are 0.16 < LLS < 66.5 kpc. These sizes are comparable to those observed for CSS / GPS sources, however, with radio luminosities ∼2 orders of magnitude lower (median $L_{1.4GHz} = 4.8\times10^{23}$ W Hz^{-1}). Additionally, the larger (∼kpc) sources in our sample could represent a compact tail to classical FRI radio sources (see Fig. 4.3). This places our sample in a largely unexplored region of the parameter space, distinct from classical 'radio-loud' AGN, although this distinctness is likely, at least in part, due to selection effects (see Section 4.4.2).

3. at least, 23/42 (55 percent) have a strong indication that the radio emission is dominated by the AGN (see Table 4.2 and Section 4.5.1). Although we can not perform all analyses on all targets, we find that, at the flux and resolution limits of our VLA data 9/41 have flat spectrum ($\alpha \geq -0.6$) cores and 11/20 sources are radio excess based off of the *qir* parameter (see Fig. 4.4). We are unable to draw definitive conclusions on the origin of the radio emission

in the remainder of the targets because of the similar morphologies and spectral indices possible of the radio emission from star formation and AGN, and the possibility that the AGN contaminate the infrared emission used to calculate qir. Importantly, we find that the Xu et al. (1999) and Best & Heckman (2012) criteria to select radio AGN fail to identify the majority of the confirmed Radio-AGN in our sample (only identifying five and three of our confirmed radio AGN respectively; see Figs. 4.1 and 4.5).

4. a negative correlation between the width of the [O III] line and the radio size (Spearman rank correlation coefficient of -0.45 and p-value of 0.003; see Fig. 4.6). If only our confirmed radio AGN are considered the correlation strengthens, with a coefficient of -0.64 and a p-value of just 0.0009. This confirms that there is a relationship between the radio emission and the ionized gas kinematics for these 'radio-quiet' AGN, with jets / winds confined within the host galaxy being more likely to interact with the ionized gas, and possibly indicates a deceleration of the jet / wind as it passes through the galaxy.

5. by combining our sample with archival AGN samples, we find that the most [O III] luminous sources (i.e. $L_{[O\ III]} \gtrsim 10^{42}$ erg s^{-1}) are all associated with extended radio emission (i.e. LLS $\gtrsim$ 0.1 kpc; see Fig. 4.7). This could explain the higher incidence of spatially extended radio structures in this work than has been seen in similar studies which do not preferentially select sources with high [O III] luminosities / optically powerful AGN (e.g. Pierce et al., 2020).

In summary, we find that radio jets and / or AGN winds are significant contributors to the radio emission in this sample of [O III] and radio luminous, optically selected AGN. Additionally, we expand upon the work in Molyneux et al. (2019), showing that more compact radio sources have a larger impact on the ionized gas within their host galaxies as probed by the SDSS fibre, than their more spatially extended counterparts. This work highlights the importance of considering the radio emission and compact radio jets in order to build a complete picture of AGN feedback, even in classical 'radio-quiet', optically powerful AGN, where feedback is generally believed to be dominated by radiative processes.

This work is the first to examine the properties of the full Quasar Feedback

Survey sample. Future work will explore the radio SED's (Jarvis et al. in prep) and present higher spatial resolution radio observations from eMERLIN. We will also present MUSE and ALMA data for subsets of the sample, to explore in more detail the multi-phase outflows and ISM properties, building on the preliminary work presented in Chapters 2 and 3 (Jarvis et al., 2019; Jarvis et al., 2020) (e.g. Girdhar et al. in prep). As such this Chapter represents a first step towards a detailed understanding of the mechanisms and impact of AGN feedback in this unique sample of local quasars.

Acknowledgements

The National Radio Astronomy Observatory is a facility of the National Science Foundation operated under cooperative agreement by Associated Universities, Inc. This research made use of Photutils, an Astropy package for detection and photometry of astronomical sources Bradley et al. (2019).

Chapter 5

Summary & Outlook

This thesis explores the ways in which powerful ($L_{AGN} \gtrsim 10^{45}$ erg s^{-1}), local ($z < 0.2$) AGN are able to impact their host galaxies, by investigating both the physical mechanisms responsible for driving outflows and the observable effects of feedback, using multi-wavelength analyses. In this Chapter I summarize the main results of the thesis while placing them in the context of larger open questions. Additionally, I discuss my ongoing and future work, building on the results of this thesis.

5.1 What is the origin of the radio emission in quasars?

The radio emission in classical 'radio-loud' AGN is known to originate from powerful radio jets (see Section 1.3.1), however, the physical mechanisms behind the radio emission in 'radio-quiet' AGN is less clear, with star formation, jets, radiation driven winds and coronal emission all possibly contributing (see e.g. Panessa et al., 2019). Specifically, 'radio-quiet' AGN, such as those studied in this thesis, are typically unresolved at the spatial resolution of current radio surveys (~5 arcsec). In Chapter 2 (Jarvis et al., 2019), high spatial resolution radio imaging (~0.25 arcsec) was used to identify spatially resolved, often jet-like radio structure in 77–88 percent of the quasars observed. These were selected to be [O III] luminous ($L_{[O\ III]} > 10^{42}$ erg s^{-1}) with moderate radio luminosities ($L_{1.4GHz} > 10^{23}$ W Hz^{-1}) and powerful ionized gas outflows (FWHM > 700 km s^{-1}). Chapter 4 increased the sample size with high spatial resolution radio observations by a factor of about four without a pre-selection on outflow properties, and again found a high incidence of spatially resolved, jet-like

radio emission (66 percent). Additionally, in both Chapters the majority of the sources (∼90 and $\gtrsim$55 percent for Chapters 2 and 4 respectively) show excess radio emission compared to what would be expected from star formation alone. This established the AGN and compact jets in particular as a dominant source of radio emission in moderate radio luminosity quasars, and demonstrated a continuity between the traditional 'radio-loud' and 'radio-quiet' classes of AGN.

Further work is needed to fully establish the relative contribution of jets, radiatively driven winds and coronal emission to the radio emission of these 'radio-quiet' quasars and by so doing constrain the mechanism(s) by which AGN can influence their host galaxies (see Section 5.2). To that end, I am actively working on a paper using the low frequency radio SEDs of the Quasar Feedback Survey sample of 42 sources introduced in Section 1.6 and Chapter 4 (see Fig. 5.1). By comparing the radio SEDs to wind models (e.g. Jiang et al., 2010; Nims et al., 2015) and literature samples of AGN with known jets, I will put constraints on the origin of the radio emission. Specifically, compact steep spectrum and gigahertz peaked-spectrum radio sources are known to follow a tight correlation of their peak frequency and their linear radio size. Therefore, if any of the Quasar Feedback Survey sources follow the same trend, this suggest that the radio is emitted via the same processes (i.e. young or disrupted jets; see e.g. Orienti & Dallacasa, 2014). This work is centred around Giant Metrewave Radio Telescope (GMRT) data for which I was the principal investigator (PI), with preliminary results shown in Fig. 5.1. Another project I am working on will determine the relative contributions of jets and hot coronas to the 100 GHz emission in a pilot study of three sources from the Quasar Feedback Survey using ALMA data I obtained as PI. Preliminary results suggest an excess of 100 GHz emission in these sources compared to what would be expected from coronal emission alone, likely due to the influence of radio jets (see Fig. 5.2 and 5.4). Looking forward, observations with ∼pc resolution (i.e. using very-long-baseline interferometry) could probe the radio emission directly around the black hole, opening up the possibility of measuring the speed and collimation of outflowing material, which will prove crucial in disentangling jets from radiatively driven winds.

In Chapter 4 I discovered that the pre-selection of [O III] luminous quasars might provide an explanation for why the Quasar Feedback Survey sources show a higher incidence of spatially resolved radio structures on ∼kpc scales than other

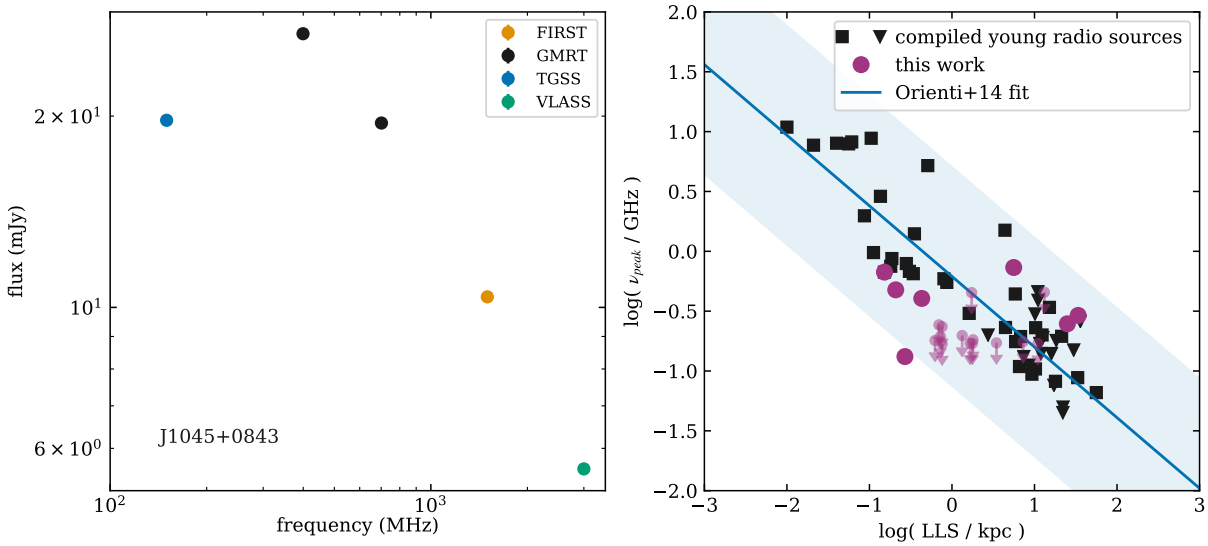

Figure 5.1: This figure shows preliminary work from a paper in preparation presenting my PI GMRT data. *Left:* an example radio SED for one of the Quasar Feedback Survey sources that shows a peaked radio spectrum (J1045+0843). Data is shown from my GMRT observations, and archival data form the TIFR GMRT Sky Survey (TGSS), FIRST and the Very Large Array Sky Survey (VLASS). *Right:* the peak frequency (ν_{peak}) versus largest linear size (LLS) relation for young radio AGN. Specifically, I show the compiled data (black squares, and triangles for sources with only an upper limit on their peak frequency) and fit (blue line and shaded region representing the 3σ scatter) of Orienti & Dallacasa (2014). The Quasar Feedback Survey sources with a measured peak in their SEDs (e.g. J1045+0843 shown to the left) are shown as magenta circles, with those where only a flattening of the low frequency SED is measured are shown as smaller and translucent upper limits.

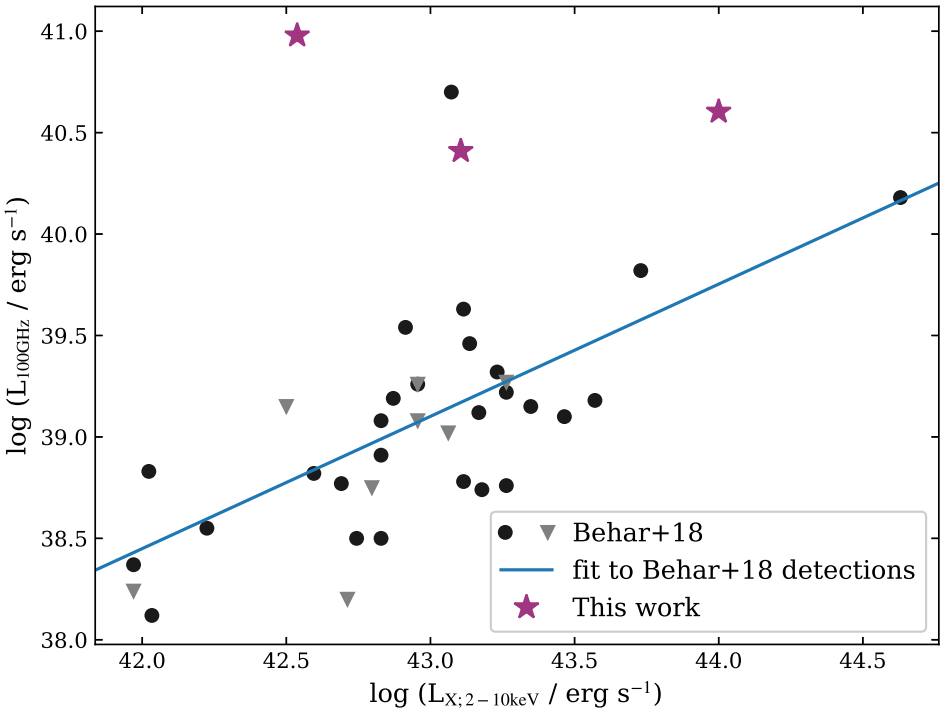

Figure 5.2: The 100 GHz emission versus the X-ray luminosity of the Quasar Feedback Survey sources in this pilot sample (magenta stars) are compared to the sample of Behar et al. (2018) (black circles / grey triangles for L_{100GHz} upper limits) with a fit to their detected sources shown as a blue line. The Behar et al. (2018) sources follow a similar correlation as coronally active stars, suggesting that the their 100 GHz emission is also coronal. The excess 100 GHz emission found in the Quasar Feedback Survey sources and the one main outlier from Behar et al. (2018) is likely due to a jet contribution.

similar samples. This represents a critical first step in an investigation of what factors determine whether an AGN forms a jet or not as well as the power and size of the potential jet. Future work will combine the VLA data presented in Chapters 2 and 4 with publicly available data to examine how the presence and size of jets correlates with the host galaxy and black hole properties. Additionally, my collaboration has eMERLIN data for the entire Quasar Feedback Survey which is currently being reduced. These observations will allow for the identification of more compact (~100 pc) radio structures, providing a more accurate account of the frequency and sizes of the jets.

5.2 How do quasars impact their host galaxies?

AGN are generally accepted to drive outflows in their host galaxies, and contribute to the global shutdown of star formation (see Section 1.5). In this thesis I used two different gas phases to trace feedback in the Quasar Feedback Survey sample: the warm ionized and cold molecular gas.

5.2.1 Ionized gas

Chapter 2 demonstrated that the jets observed are driving warm ionized gas outflows in their host galaxies. Specifically, optical IFS data was combined with radio images to discover the spatial coincidence and alignment of disrupted [O III] gas with the observed radio components. Although there is no IFS data for the complete Quasar Feedback Survey sample presented in Chapter 4, I used the SDSS fibre spectra to find a negative correlation between the FWHM of the [O III] line and the size of the radio source, indicating that the ionized gas kinematics and radio properties are linked. Similar results were found using low spatial resolution radio data (FIRST) in Molyneux et al. (2019), a paper written by a science intern during a project I co-supervised during my PhD. All this contradicts the commonly held assumption that jet–gas interactions do not play a significant role in feedback in traditional 'radio-quiet' AGN and will have a resounding impact upon future studies of AGN outflows and how feedback is implemented in simulations.

To fully explore the impact of the AGN and radio jets on the ionized gas in

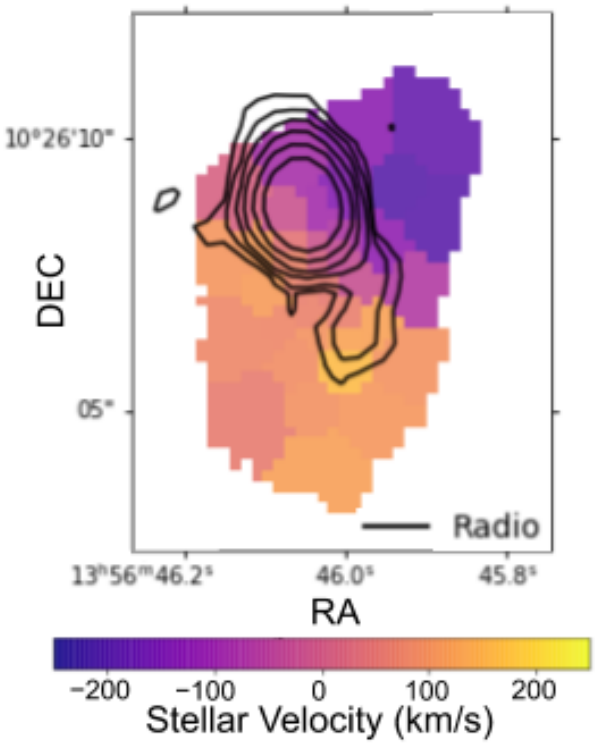

Figure 5.3: The stellar velocity map of J1356+1026 using MUSE data, with VLA radio contours (∼1 arcsec resolution) overlaid in black. The rotation of the galaxy can be clearly seen in the stellar kinematics. Combining these data with the type of analysis presented in this thesis will help to study the behaviour of the ionized gas with the stellar contributions removed. This will reveal the exact relationship between the observed radio features and the ionized gas. This figure shows preliminary work from Girdhar et al. in prep.

the Quasar Feedback Survey sample, requires IFS observations of the complete sample. Specifically, IFS observations are needed with high enough spatial resolution to identify distinct kinematic structures associated with the radio features observed in this thesis, and a large enough field of view to observe the whole galaxy. To that end my collaboration has obtained observations with ESO's Multi Unit Spectroscopic Explorer (MUSE) for the 17 type 2 AGN in the Quasar Feedback Survey visible from the Very Large Telescope (VLT), and will propose for equivalent data for the remainder of the sample. In addition to the higher spatial resolution, these data have sufficient signal-to-noise to decouple the stellar kinematics (see Fig. 5.3) from the gas kinematics, which will be key for reliably determining the velocity structure and energetics of the outflows, granting deeper insight into the impact and physical drivers of AGN feedback in these systems.

5.2.2 Molecular gas

In order to asses the impact of AGN on the star formation in their host galaxies, it is crucial to investigate the cold molecular gas, which is the primary fuel for star formation. In particular, AGN are generally accepted to remove, destroy or heat the molecular gas in their host galaxies, facilitating the quenching of star formation (see Section 1.5). Chapter 3 (Jarvis et al., 2020) revealed that at least seven of the nine Quasar Feedback Survey sources studied reside in molecular gas rich (average M_{gas}=1.3×10^{10} $M_{\odot}$), high star formation rate (average SFR = 42 $M_{\odot}yr^{-1}$) host galaxies. This is an indication that these AGN are in an early phase of their evolution and have not yet had a global impact on the molecular gas, despite the observed ionized gas outflows and the jets or winds visible in the radio emission. This suggests that commonly held assumptions about AGN feedback may need to be reevaluated and presents many further questions: Are the nine AGN studied in Chapter 3 special compared to the rest of the Quasar Feedback Survey sample? Are these quasars driving massive, extended molecular gas outflows? What can simulations tell us about the exact impact expected by quasars on the molecular gas of their host galaxies, and the timescales this effect can be seen on?

To answer these questions, my collaboration has had proposals accepted to obtain total (i.e. unresolved) CO observations in the (1–0), (2–1) and (3–2) transition for the 17 type 2 AGN in the Quasar Feedback Survey with MUSE data. These data will allow for the measurement of the total molecular gas mass in this larger sample and provide constraints on the gas properties through the use of multiple transitions (e.g. density and temperature; see e.g. Kamenetzky et al., 2018). My collaborators and I have also begun a preliminary study using spatially resolved ALMA observations of the CO(3–2) transition, which combined with publicly available archival data (Sun et al., 2014), cover the full sample presented in Chapter 3. This will allow for the study of the kinematics of the molecular gas and constrain the molecular phase of the outflows. By combining these data with the optical IFS data presented in Chapter 2 or the MUSE data subsequently obtained, and the radio maps from Chapters 2 and 4, the kinematics of the cold molecular can be compared to the warm ionized gas and the impact of the jets can be traced (see Fig. 5.4).

Finally, concrete predictions of what the expected impact of AGN on the molecular gas should be, are needed to strengthen the interpretation of studies

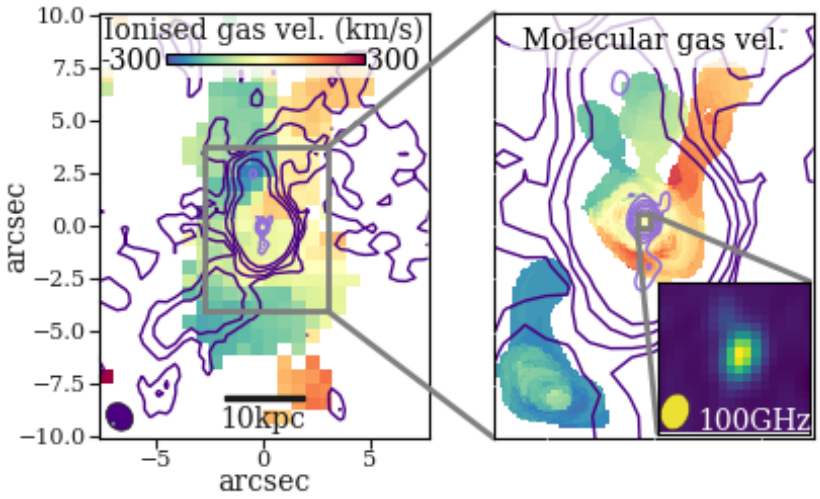

Figure 5.4: Velocity maps of the warm ionized and cold molecular gas (left and right respectively; using the same colour scale) for one of the Quasar Feedback Survey AGN (J1000+1242), with radio contours overlayed (high / low spatial resolution in light / dark purple respectively). This galaxy shows giant (galaxy sized) radio lobes and signatures of jet - gas interactions in both gas phases (see Chapter 2; Jarvis et al., 2019). In the bottom right is a further zoom in with my PI 100 GHz data (ALMA), sensitive to jets (extension in the top left) and hot coronal emission (possibly contributing to the bright core).

such as the work presented in Chapter 3. For example, recent work examining the impact of AGN on the SFR in galaxies in the widely used EAGLE cosmological simulations found that no immediate impact is expected, completely changing how observational studies on the topic must be interpreted (Harrison, 2017; Scholtz et al., 2018). However, there are currently no parallel studies focusing on the molecular gas content. As such, I have begun an investigation into the impact of AGN feedback on the molecular gas, using the IllustrisTNG cosmological simulations. Specifically, I am investigating the molecular gas in galaxies, looking for variations with instantaneous AGN luminosity, the accretion state of the black hole and the specific star formation rate of the galaxy, and the interplay between these four parameters. Preliminary results suggest that for massive galaxies, powerful AGN are found in galaxies with larger gas masses and higher specific star formation rates than less powerful AGN (see Fig. 5.5), which is in agreement with the results presented in Chapter 3 of this thesis. I am currently working on understanding how the numerical methods implemented in the simulations (e.g. the resolution limits and black hole accretion and feedback prescriptions) might impact this work.

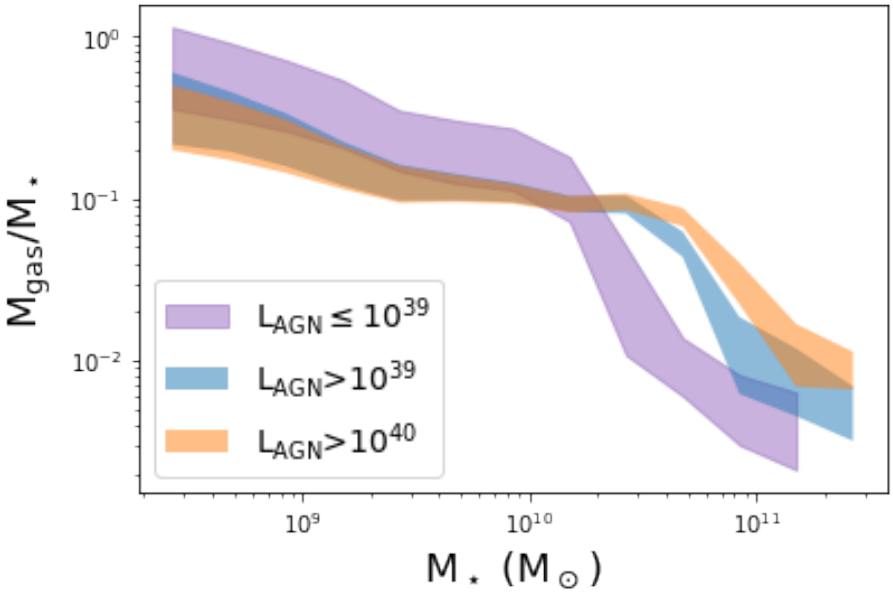

Figure 5.5: Preliminary results from my work studying the impact of AGN on the molecular gas in the IllustrisTNG simulations. The gas fraction (ratio of molecular gas mass to stellar mass – $M_{gas}/M_\star$) is plotted as a function of stellar mass for three bins of instantaneous AGN luminosity (L_{AGN}) in erg s^{-1}. Data are taken from the TNG100-1 simulation at $z = 0$ following Diemer et al. (2019). Preliminary analysis suggests that the trend with increasing AGN luminosity might be driven by different specific star formation rates in the different bins rather than by the influence of the AGN directly, in agreement with the results of Chapter 3 of this thesis (Jarvis et al., 2020).

5.3 Final remarks

This thesis presents unique insights into the physical drivers and impact of AGN feedback in local quasars through a combination of spatially resolved and multi-wavelength approaches. Specifically, I establish radio jets as a critical component to feedback in 'radio-quiet' quasars and demonstrate that significant AGN activity does not appear to lead to an immediate decrease in the amount of available molecular gas. Additionally, I present the first results on the full Quasar Feedback Survey, which is a growing international collaboration that I am co-leading. This large and unique sample of luminous local AGN presents huge opportunities for continued scientific discoveries, by enabling detailed spatially resolved analysis of quasars powerful enough to drive the large scale quenching expected primarily of higher redshift AGN.

Multi-wavelength and spatially resolved investigations into galaxy evolution, such as those presented in this thesis, are the future of extra-galactic astronomy. In particular, this thesis, and the Quasar Feedback Survey for which this thesis is the foundation, examine feedback in powerful quasars, which although rare in the local universe are typical at higher redshift ($z \approx 1$–3), where the majority of star formation and black hole growth occurred (see Section 1.5). As such, this thesis and the ongoing work building upon it, will serve as a benchmark for similar high sensitivity spatially resolved surveys at high redshift as the progress of instrumentation makes such work possible. Specifically, deep, high spatial resolution radio surveys planned with the Square Kilometre Array (SKA) combined with next generation spectroscopic surveys such as the "Multi Object Optical and Near-infrared Spectrograph" for the VLT will provide an overview of AGN and AGN feedback in galaxies, especially at high redshift. Additionally, detailed observations of individual high redshift galaxies in multiple wavelengths will be enabled by, for example, the James Webb Space Telescope, ESO's Extremely Large Telescope and the SKA. By combining the statistical power of large surveys and the wealth of information provided by in-depth analysis of smaller samples, the details of AGN feedback at high redshift will be revealed. The Quasar Feedback Survey and the work presented in this thesis will be vital as a local comparison sample for such future work.

Finally, as the quality of both simulations and observations improves, the need for increased communication between these two branches of astrophysics is

becoming more urgent. Specific predictions from simulations are vital for meaningful interpretation of data, as discussed above. Furthermore, observations such as those presented in this thesis will be key in ensuring that the implementation of feedback in simulations reflects reality.

Galaxies are complex systems, and those with AGN doubly so. This makes detailed, spatially resolved studies across the electro-magnetic spectrum, such as those presented in this thesis vital to achieving an understanding of the processes involved in their evolution.

Appendix A

Appendix to Chapter 2

This appendix provides more details on the *UV* to *FIR* SED fitting used in this work as well as a detailed presentation of our radio data and IFS data used for the analyses in the main paper. We also show additional radio and IFS data for two targets that were not included in the final primary sample (see Section 3.1).

A.1 SED Analysis

Here we describe the photometric data and SED fitting procedure used to derive stellar masses, AGN luminosities and far-infrared luminosities due to star formation presented in Section 2.2.

A.1.1 Photometry

We gathered archival data from the *UV* to *FIR* (0.1516–350 μm). In the *UV* we used data from The Galaxy Evolution Explorer (GALEX; far-*UV* at 1516Å and near-*UV* at 2267Å; Bianchi et al., 2014; Martin et al., 2005), and in the optical SDSS (*u*, *g*, *r*, *i* and *z* bands; Abolfathi et al., 2018). In the near infrared we took values from the Extended Source Catalogue of The Two Micron All Sky Survey 2MASS; J, H and K_s bands Skrutskie et al., 2006[1] , the Wide-field Infrared Survey Explorer (WISE) all-sky survey (3.4, 4.6, 12, and 22 μm Wright et al., 2010), and the Infrared Astronomical Satellite (IRAS; 12, 25, 60 and 100 μm

[1]For J1338+1503, which was not in the Extended 2MASS source catalogue, we used the values from the point source catalogue.

Neugebauer et al., 1984) faint source catalogue (Moshir et al., 1992)[2]. We added in quadrature 30 per cent of the measured flux densities to the quoted WISE uncertainties to account for calibration uncertainties in the WISE data (Wright et al., 2010). Finally, where available we used data from the ESA *Herschel* Space Observatory (Pilbratt et al., 2010) using data from the PACS (Poglitsch et al., 2010) and SPIRE (Griffin et al., 2010) point source catalogues at 70, 100, 160 and 250, 350 μm respectively, in the far infrared.

For the WISE and 2MASS surveys we took the closest positional match to the SDSS position (all are < 2 arcsec). For GALEX we searched for all catalogue entries within 6.5 arcsec and took the detection with the lowest error in case of multiple observations (from the different GALEX surveys). For IRAS we followed a log likelihood method of matching IRAS to WISE counterparts to account for the large and asymmetric IRAS beam following Wang et al. (2014). For the sources that were observed by IRAS but that we were not able to obtain IRAS flux density measurements we estimated conservative maximum upper limits of 0.25, 0.4, 0.3, and 3 mJy for the 12, 25, 60, and 100 μm bands respectively.[3] Finally we applied corrections for galactic extinction to all photometry at wavelengths shorter than (and including) 2MASS, at which point the corrections are already smaller than the errors. Specifically, we used the Schlafly & Finkbeiner (2011) absorption values.[4]

A.1.2 SED fitting

In order to fit the SEDs we used the CIGALE code (version 0.12.0), which takes into account the energy balance between the absorption due to dust in the *UV*–optical regime and the corresponding re-emission in the *FIR*. The output parameters and their uncertainties are computed through a Bayesian statistical analysis: for each parameter of interest the code builds a probability distribution function (PDF) by summing the term $\exp(-\chi^2/2)$, associated to each model, in given bins of the parameter space. The procedure we applied and the input values we used closely follow Circosta et al. (2018), but we give some specific details

[2]We also searched for significant detections using the SCANPI tool to inspect the data (`http://irsa.ipac.caltech.edu/applications/Scanpi`).

[3]One source (J1100+0846) falls into an area of the sky that was not observed by IRAS and we therefore cannot place photometric constraints on the IRAS bands for this source.

[4]`https://irsa.ipac.caltech.edu/applications/DUST/`

here.

We modelled the stellar emission, which dominates the wavelength range 0.3–5 μm with the Bruzual & Charlot (2003) stellar population models, and assuming a delayed exponentially declining star formation history (SFH). The metallicity is fixed to solar (0.02) and the stellar population ages are constrained to be younger than the age of the Universe at the redshift of the targets. To account for attenuation we applied to the stellar contribution a modified version of the Calzetti et al. (2000) curve multiplied in the *UV* range by a power law with variable slope δ. Negative slopes of the additional power law produce steeper attenuation curves and a slope equal to 0 reproduces the Calzetti et al. (2000) curve. Differential reddening undergone by young stars (<10 Myr) and old stars (>10 Myr) was taken into account by applying the reduction factor, $E(B-V)_{\rm old}/E(B-V)_{\rm young}$, fixed to 0.44.

The emission from dust heated by star formation, dominating the *FIR* regime, is reproduced using the library of Dale et al. (2014). We set the AGN contribution to these dust models equal to zero, in order to model the AGN emission separately using the models presented by Fritz et al. (2006). We only considered the AGN templates representative of type 2 AGN (see Circosta et al., 2018). Templates reproducing nebular emission from H II regions based on the models by Inoue (2011) were also included. We note that repeating the fits without nebular lines changes our output values of interest (see Table 2) by at most a factor of 1.3 with the stellar mass being the most effected.

A.2 Additional figures

In this section we provide three sets of figures to present our data and analyses for each of the primary targets (Fig. A.1–A.30) as follows:

1. The first set of figures shows the radio images used for calculating the spectral index for each feature we identified (see Section 4.1.1). Alongside, we show the Gaussian model fits (and data−model residuals) used to calculate the flux densities from the images. We also show the radio SEDs for each feature. Table A.1 gives the details of how each of these radio images was constructed and the corresponding properties of the synthesised beams and noise (see Section 3.1.2). Finally, we show the broad-band *UV*-to-*FIR* SEDs

used to calculate stellar masses, star-formation rates and AGN luminosities (see Section 2.2).

2. The second set of figures compares the SDSS or when available, *HST* imaging, ionized gas kinematics from our IFS data, and the radio morphologies to complement the discussion presented in Section 5.3. We also show [O III] emission-line profiles extracted from our IFS data at locations of interest motivated by the ionized gas and radio features observed. When numbers are quoted in relation to the [O III] kinematics in the main manuscript they are taken from, or motivated by, the line profiles shown in these figures. These figures also show the non-parametric kinematic maps extracted from the IFS data (see Section 4.2). When we have both VIMOS and GMOS data for a target we show the maps derived from both sets of data.

3. The final set of figures for each target presents narrow-band images from the IFS data, stepping through various wavelength slices (optionally in an animated format) to further highlight how different velocity components of the ionized gas relate to the radio features seen. Video formats of these figures are also included as separate .mp4 files with this supplementary information.

Table A.1: Summary of radio images shown in Appendix A

Name	Fig.	res.	Frq. (GHz)	Beam HPBW (arcsec)	Beam PA (deg)	Noise (μJy/beam)	Data	Weighting
(1)	(2)	(3)	(4)	(5)	(6)	(7)	(8)	(9)
J0945+1737	A.1	HR	1.5	0.23×0.23	31	254	e-MERLIN	
		HR	5.2	0.26×0.26	-32	29	C-A	uniform
		HR	7.2	0.22×0.2	-16	20	C-A	briggs 0.0
		LR	1.5	1.59×1.11	68	77	L-A	briggs 0.5
		LR	5.2	1.52×1.3	43	17	C-A + C-B	natural & 160 kλ taper
		LR	7.2	1.45×1.31	47	16	C-A + C-B	natural & 120 kλ taper
J0958+1439	A.4	HR	1.5	0.23×0.21	-27	319	e-MERLIN	
		HR	5.2	0.27×0.26	-50	18	C-A	uniform
		HR	7.2	0.23×0.21	-19	13	C-A	briggs 0.0
		LR	1.5	1.73×1.11	64	30	L-A	briggs 0.5
		LR	5.2	1.48×1.23	45	10	C-A + C-B	natural & 200 kλ taper
		LR	7.2	1.36×1.14	45	9	C-A + C-B	natural & 150 kλ taper
J1000+1242	A.7	HR	1.5	0.27×0.22	-40	227	e-MERLIN	
		HR	5.2	0.28×0.26	-20	34	C-A	uniform
		HR	7.2	0.27×0.24	-8	27	C-A	briggs 0.6
		LR	1.5	1.63×1.12	63	48	L-A	briggs 0.5
		LR	5.2	1.45×1.14	23	21	C-A + C-B	natural & 200 kλ taper
		LR	7.2	1.31×1.16	40	21	C-A + C-B	natural & 140 kλ taper
J1010+1413	A.10	HR	1.5	0.24×0.22	-11	156	e-MERLIN	
		HR	5.2	0.27×0.26	-47	19	C-A	uniform
		HR	7.2	0.24×0.22	-14	13	C-A	briggs 0.2
		LR	1.5	1.55×0.83	84	79	L-A	uniform
		LR	5.2	1.32×1.19	44	13	C-A + C-B	natural & 200 kλ taper
		LR	7.2	1.29×1.09	46	9	C-A + C-B	natural & 160 kλ taper
J1010+0612	A.13	HR	1.5	0.32×0.18	25	3438	e-MERLIN	
		HR	5.2	0.3×0.28	-54	89	C-A	uniform
		HR	7.2	0.22×0.2	-69	87	C-A	uniform
		LR	1.5	1.99×0.9	59	508	L-A	briggs 0.5

Continued on next page

Continuation from previous page

		LR	5.2	1.57×1.11	48	60	C-A + C-B	natural & 200 kλ taper
		LR	7.2	1.5×1.12	46	51	C-A + C-B	natural & 150 kλ taper
J1100+0846	A.16	HR	1.5	0.3×0.18	26	549	e-MERLIN	
		HR	5.2	0.28×0.27	-35	53	C-A	uniform
		HR	7.2	0.25×0.22	-20	50	C-A	briggs 0.2
		LR	1.5	1.57×1.12	61	109	L-A	briggs 0.5
		LR	5.2	1.54×1.29	37	33	C-A + C-B	natural & 160 kλ taper
		LR	7.2	1.27×1.12	39	36	C-A + C-B	natural & 150 kλ taper
J1316+1753	A.19	HR	1.5	0.3×0.17	27	136	e-MERLIN	
		HR	5.2	0.32×0.27	78	20	C-A	uniform
		HR	7.2	0.25×0.22	-70	13	C-A	briggs 0.0
		LR	1.5	1.16×1.06	20	28	L-A	briggs 0.5
		LR	5.2	1.16×1.13	-28	12	C-A + C-B	natural & 200 kλ taper
		LR	7.2	1.12×1.07	30	10	C-A + C-B	natural & 160 kλ taper
		LR	5.2	1.0×0.92	43	13	C-B	uniform
		LR	7.2	0.93×0.83	54	7	C-B	briggs 0.6
J1356+1026	A.25	HR	1.5	0.32×0.17	24	570	e-MERLIN	
		HR	5.2	0.35×0.29	-83	86	C-A	uniform
		HR	7.2	0.27×0.23	-69	88	C-A	briggs 0.0
		LR	1.5	1.18×1.06	21	97	L-A	briggs 0.5
		LR	5.2	1.3×0.99	-1	32	C-A + C-B	natural
		LR	7.2	1.19×1.02	-178	32	C-A + C-B	natural & 200 kλ taper
J1430+1339	A.28	HR	1.5	0.31×0.16	24	205	e-MERLIN	
		HR	5.2	0.4×0.28	-84	32	C-A	uniform
		HR	7.2	0.32×0.24	-71	22	C-A	briggs 0.2
		LR	1.5	1.15×1.06	13	42	L-A	briggs 0.5
		LR	5.2	1.22×1.16	52	15	C-A + C-B	briggs 0.5 & 120 kλ taper
		LR	7.2	1.18×1.1	71	14	C-A + C-B	briggs 0.5 & 100 kλ taper
J1355+1300	A.31	LR	6.2	1.01×0.92	43	6	C-B	briggs 0.5
J1504+0151	A.31	LR	6.2	0.85×0.78	60	12	C-B	uniform

Continued on next page

Continuation from previous page

Notes: For each target (name in column 1) and for each of the resolution matched images created for measuring flux densities (figure number, resolution and frequency given in columns 2, 3 and 4), the synthesised beams and noise are given (columns 5-7), as well as the noise level (7). (8) describes the measurement set used, where C-A indicates a VLA C-band A-configuration image (etc.). 'C-A + C-B' means a concatenation of the C-band A and B-configuration data was used with relative weighting of 4:1; (9) describes the weighting scheme used to image the data. The last two rows, separated by a line, give the details for the two VLA images shown in Appendix A.3 for the sources not in our primary sample.

A.3 Non-primary sample

From our incomplete 16A-182 VLA run we obtained C-band B-configuration data for two quasar targets not included in the primary sample (see Section 3.1). These data are presented in Fig. A.31.

There is not much of note in either the radio or IFS data for J1504+0151 except that the wide [O III] line (~900 km s^{-1}) suggest the presence of an outflow. Our radio images for J1355+1300 however reveal extensive possibly jet-like features which seem to be aligned with kinematic features seen in our IFS data, although the GMOS FOV is smaller than the radio features seen. In particular we see line splitting in the south-east corner possibly related to a jet-launched bubble, similar to that seen in J1000+1242 and J1356+1026. We have no spectroscopic information for the extended radio features seen to the west in J1355+1300, so cannot comment if it is related or a background source.

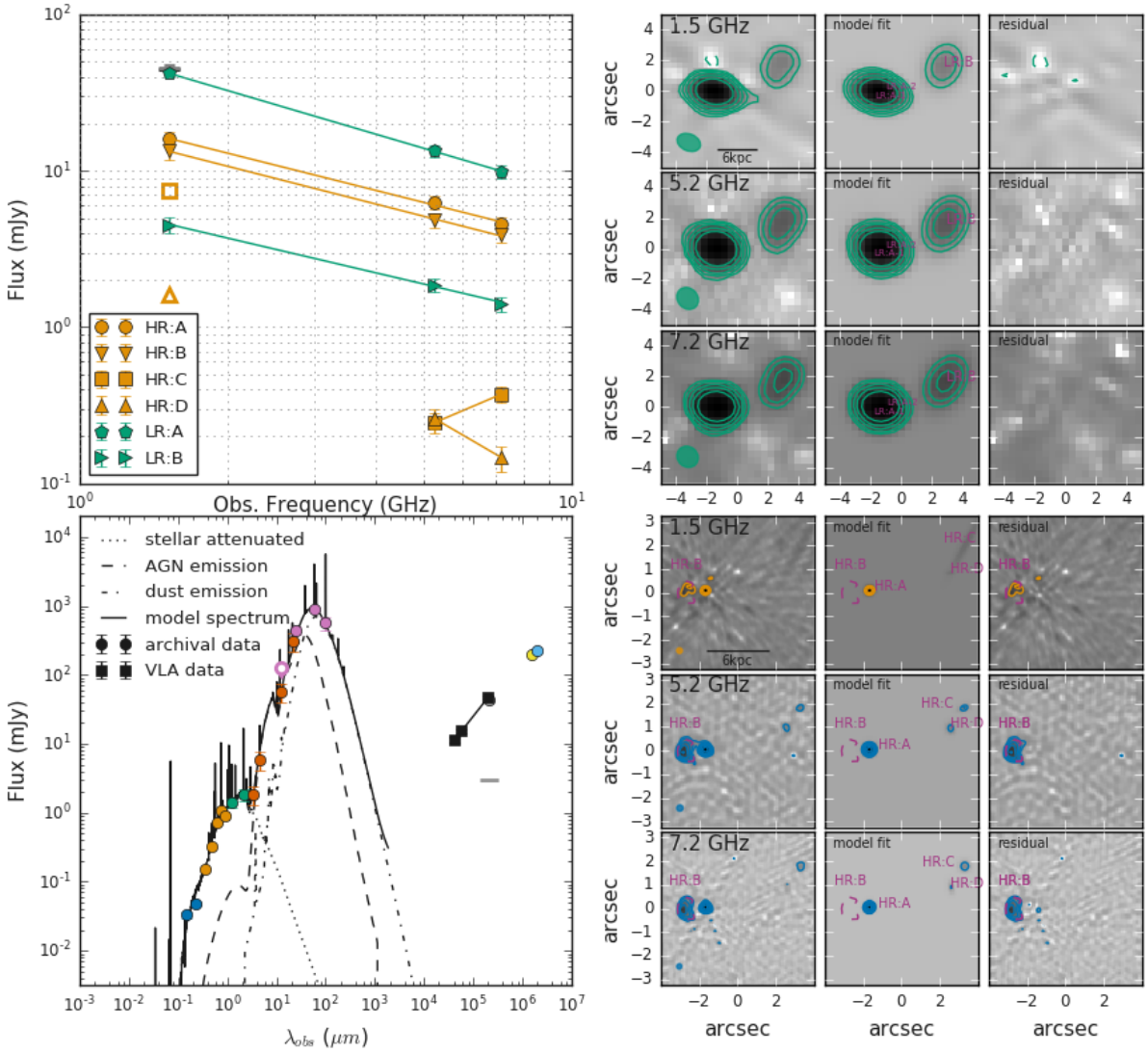

Figure A.1: Broadband SED, multi-frequency radio images including model fits, and the radio SEDs for the individual radio features in J0945+1737. The data points in the broadband SED (bottom left) are colour coded by instrument / survey and the various components of the fits are shown by different styled lines, as in Fig. 4. The radio SED (top left) shows the flux densities for each morphological component marked by a distinct symbol, with the high resolution (HR) components in orange and the low-resolution (LR) components in green. The FIRST and NVSS fluxes (galaxy integrated) are also shown in black and grey, respectively. For both the radio and *UV-FIR* SEDs, upper limits are represented by open symbols, while detections are filled. The multi-frequency radio images, Gaussian fits and model−data residuals are shown as the remaining columns with the LR images as the top three rows and the HR on the bottom three rows. The colour coding, contour levels and the morphological component labels are the same as in Fig. 5, with additional labels for the individual LR Gaussians components when multiple Gaussians were used. The scale bar (shown in the bottom of the 1.5 GHz image at each resolution) represents 6 kpc. For this source, in our high resolution images, we observe a nuclear component (HR:A) and jet/lobe structure to the east (HR:B). In the e-MERLIN image HR:B has the appearance of a bent jet. We note that LR:B, which we interpret as a second jet/lobe to the east, is mostly resolved out in the high resolution images, except for two very weak (HR:C and HR:D) features with uncertain flux density measurements and an unclear interpretation (see Fig. A.2).

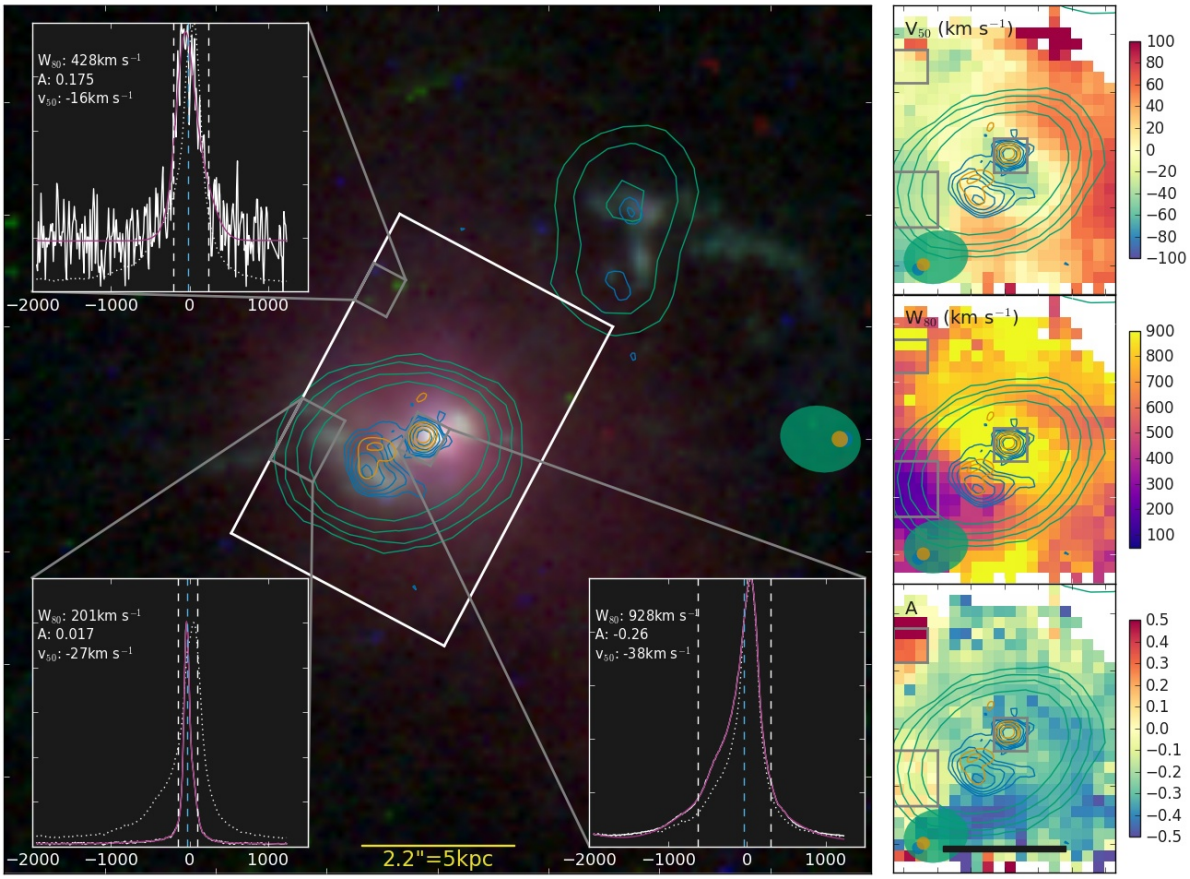

Figure A.2: A comparison of the broad-band image, ionized gas and radio features for J0945+1737. The panel on the left shows the radio contours from Fig. 5 colour coded as they are in that figure with the synthesised beams represented by ellipses in the middle right of the figure. The background three-colour image is from archival HST data; with continuum from the F814W filter in red (Cui et al., 2001), [O III] and Hβ narrow-band image from the FR551N filter in green, and Hα+[N II] narrow-band image from the FR716N filter in blue (observing proposal id.13741). The FOV of the GMOS IFS observations is overlaid in white. [O III] emission-line profiles are extracted from the regions of the data shown in grey boxes and are plotted in their respective corners. The weighted average of the pixels included is shown in white with the fit in magenta and the total spectra across the cube is shown as a dotted white curve for reference. The vertical white dashed lines mark v_{10} and v_{90} with the light-blue dashed line showing v_{50}, which is also written, along with the W_{80} and asymmetry (A) for the extracted emission-line profile in the top left of each inset (see Section 4.2 for definitions). The second column shows the maps of v_{50}, W_{80} and A with the boxes used for the extracted spectrum overlaid, the scale bar in the asymmetry plot the same as in the main panel. As can be seen from the *HST* data, LR:B is coincident to a line emission dominated region and therefore it is likely related to the host galaxy. We propose that it is a secondary jet/lobe. The GMOS data reveals a bright, narrow, largely symmetric [O III] region just beyond HR:B, and we suggest that this kinematically distinct [O III] region has deflected the jet. The lack of an alignment between the positional angle of the two jet/lobes (LR:B and HR:B), and the differences in their distance to the probable core (HR:A), suggests that these could be due to multiple episodes of jet activity (see e.g., Kharb et al., 2006; Gallimore et al., 2006; Orienti, 2016).

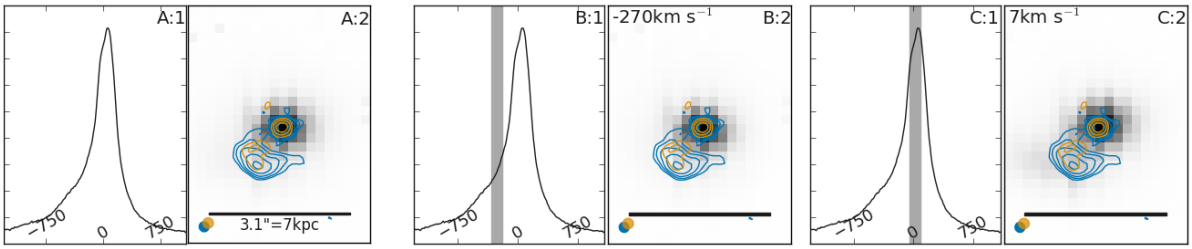

Figure A.3: A:1: The total [O III] emission line profile of J0945+1737 across all spaxels, with wavelength given in km s^{-1}. A:2: an image from the IFS data, created by summing over the entire emission-line profile in A:1 for each spaxel. Radio contours from Fig. 5 are over-plotted, colour coded as in that figure. Panels B and C show individual wavelength slices, with sub-panel 1 showing the total [O III] emission-line profile with a grey bar marking the wavelength range over which the [O III] image in panel 2 is summed. The central velocity of each slice is shown in the top left corner of panel 2. In each image the synthesised beams are represented with ellipses in the bottom left. For this source, the slice shown in panel C (∼7km s^{-1}) shows the distinct kinematic component associated with HR:B.

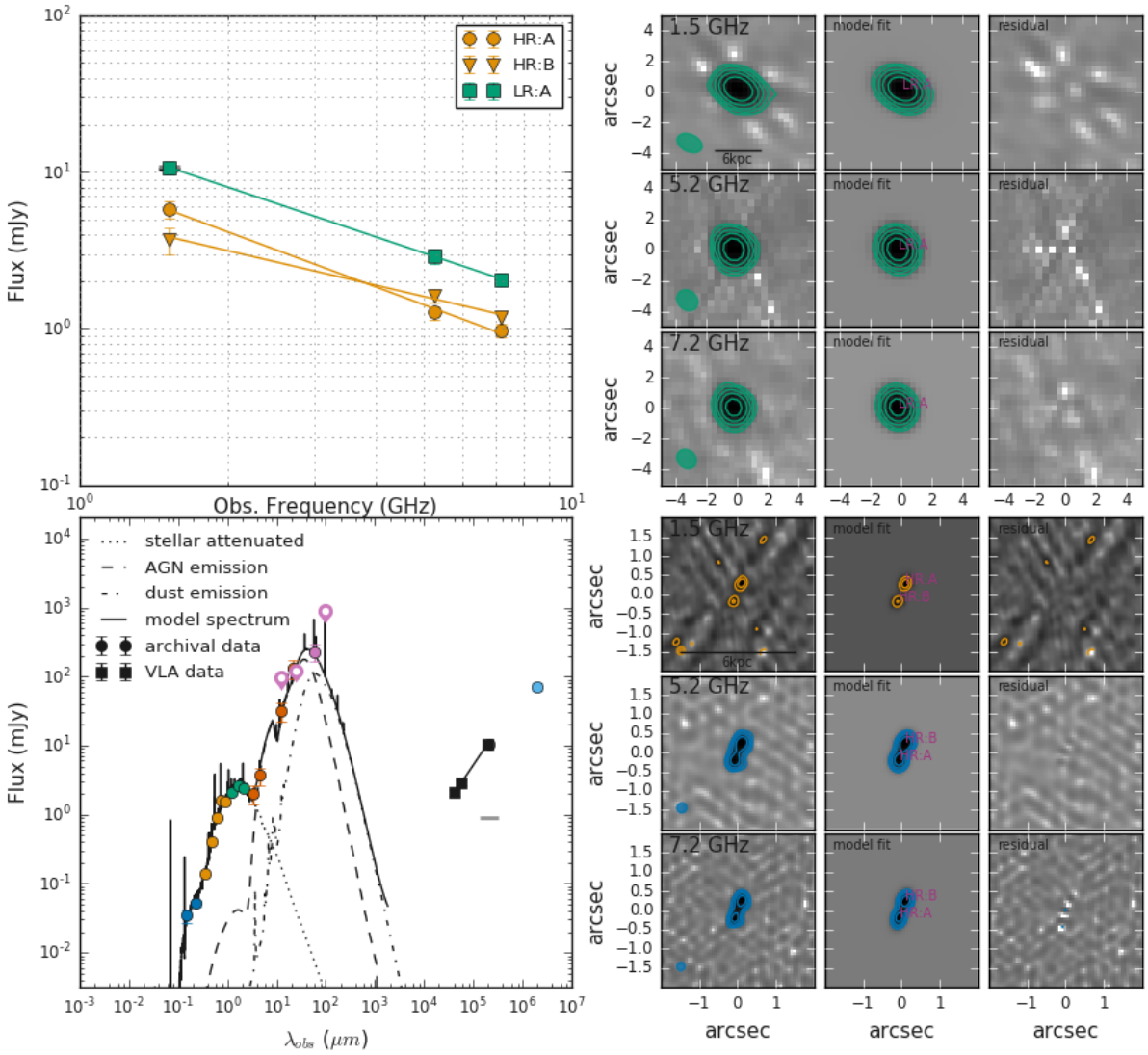

Figure A.4: As Fig. A.1 but for J0958+1439. In the high resolution images this source is resolved into two steep spectrum ($\alpha \sim -0.9$) components which we interpret as roughly symmetric radio lobes around an undetected central AGN core.

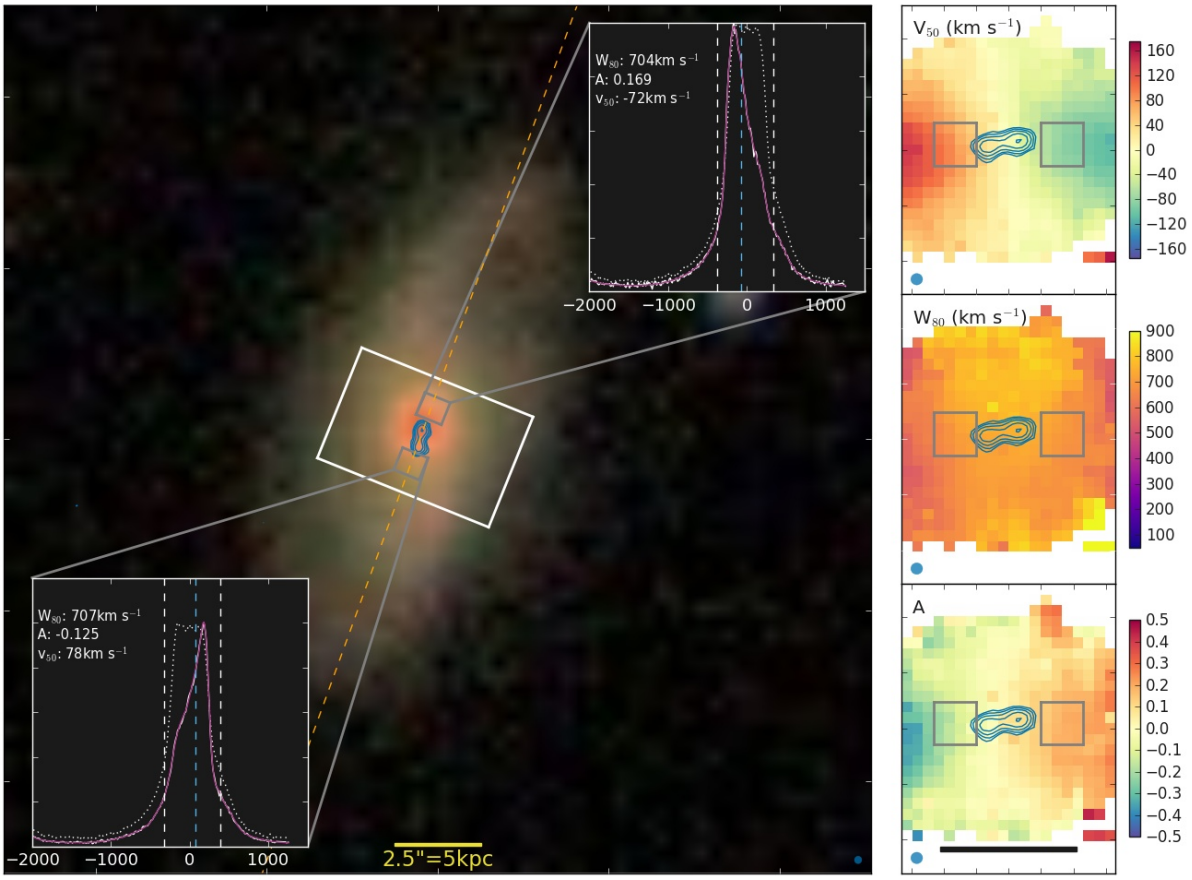

Figure A.5: As Fig. A.2 but for J0958+1439. Since there is no *HST* data for this source the SDSS three-colour image is used instead, as in Fig. 2. The orange dashed line marks the approximate direction of the velocity gradient from our [O III] measurements, which additionally, by eye, lies in the plane of the galactic disc. This means that the jet axis defined between HR:A and HR:B is into the galactic disc. At the location of each radio lobe we see a high-velocity ($\approx\pm75$ km s^{-1}) ionized gas component, as can be seen from the inset emission-line profiles.

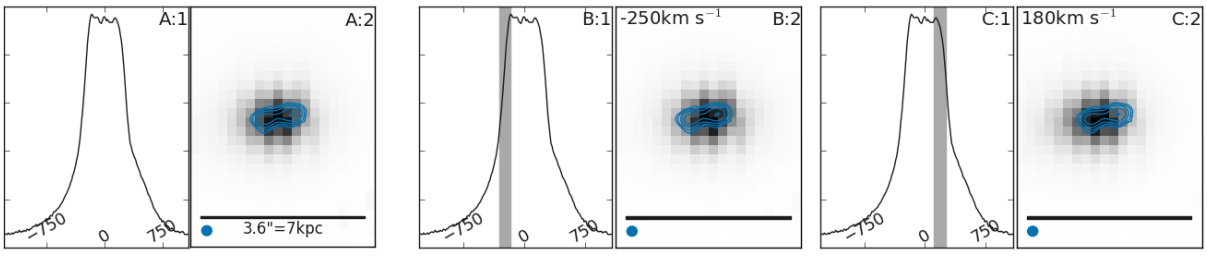

Figure A.6: As Fig. A.3 but for J0958+1439.

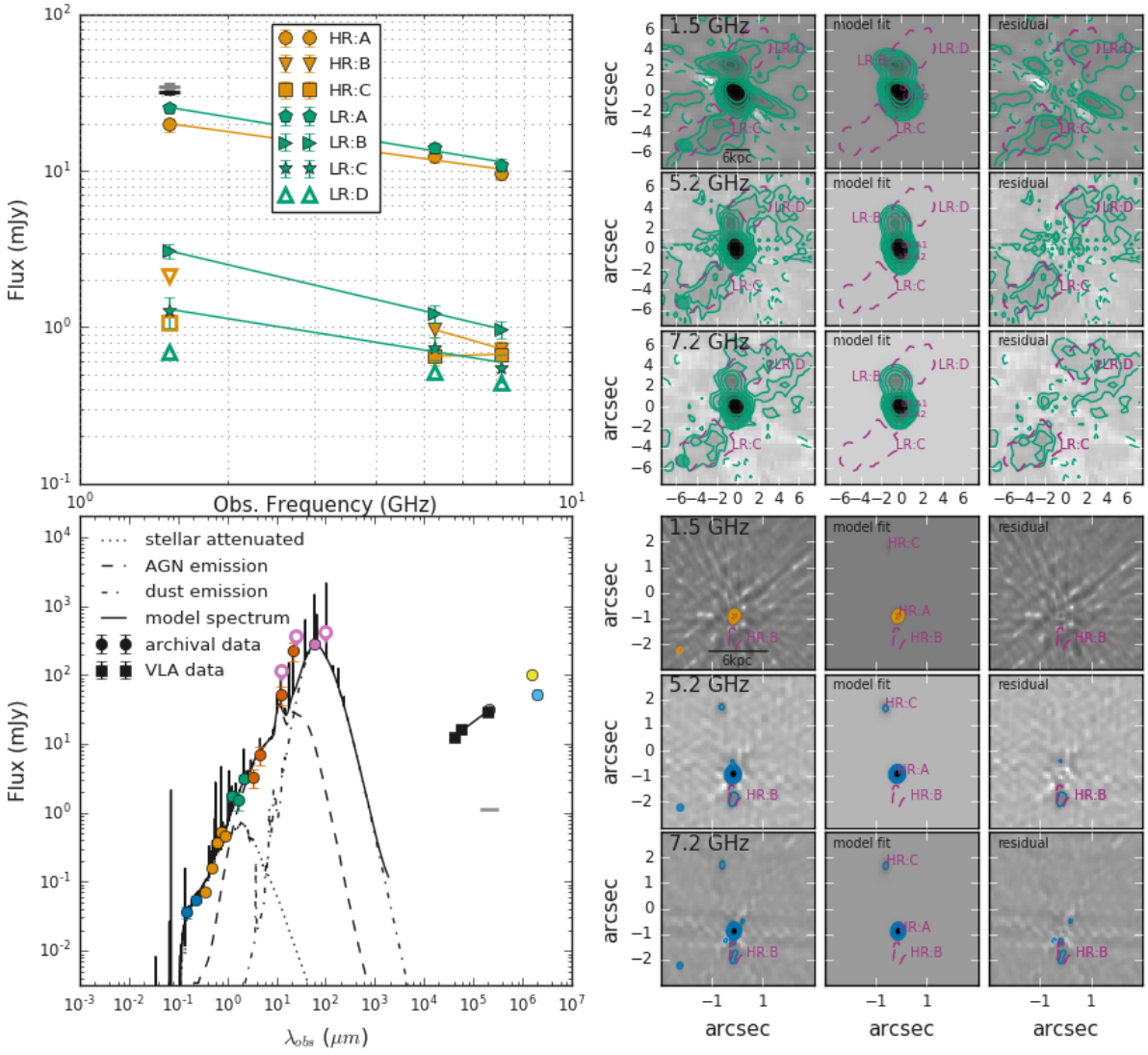

Figure A.7: Same as Fig. A.1 but for J1000+1242. We interpret the radio features in this source as jet/lobe structures with a flat spectrum hot spot (HR:C; $\alpha = 0.1$) embedded in one of the lobes (LR:B). Furthermore, LR:C and LR:D are likely signs of deflection (see e.g., Heesen et al., 2014). HR:A, with a relatively flat spectral index of -0.4, most likely contains the radio core and possibly unresolved jet or lobe components. HR:B appears to be a jet. The GLEAM and TGSS data for this source (see bottom left panel) suggest that its radio spectrum turns over somewhere between 1.4 and 0.15 GHz, which, following the turnover - size relation from CSS/GPS sources (Orienti & Dallacasa, 2014) corresponds to a size from 0.2–9kpc, consistent with the HR total size given in Table 4.

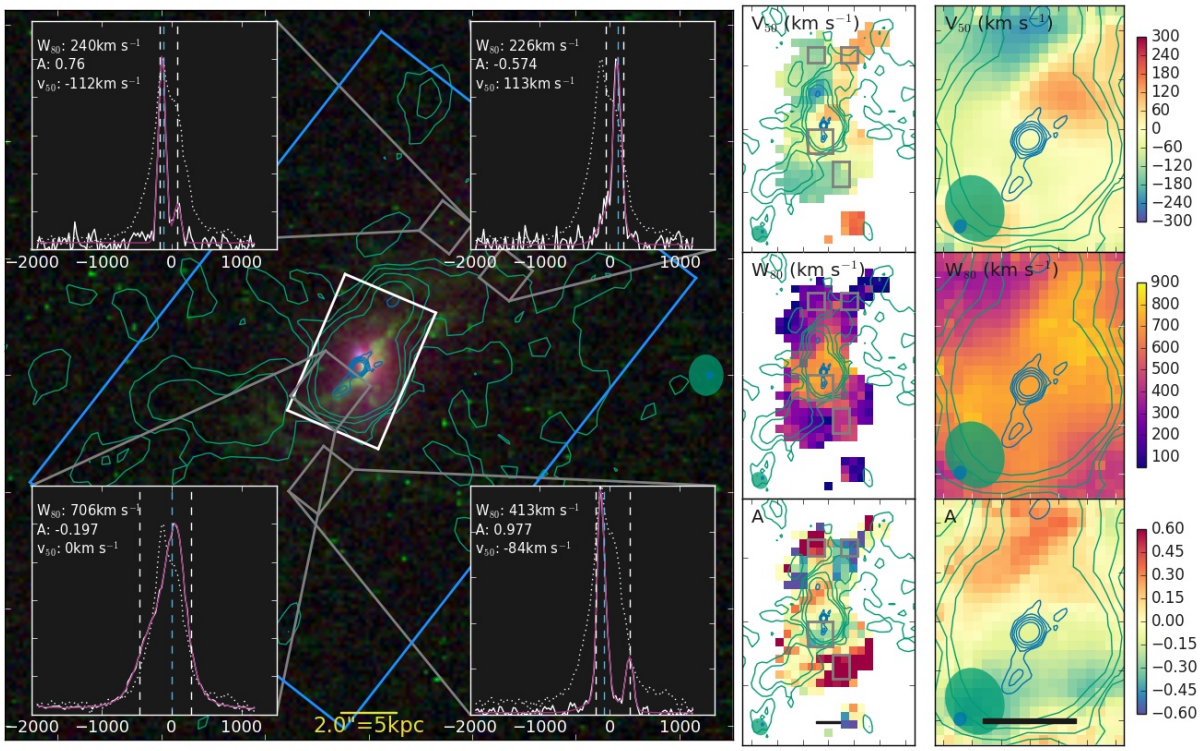

Figure A.8: As Fig. A.2 but for J1000+1242. The background three-colour image is from archival HST data (observing proposal id.14730), with IR continuum from the F160W filter in red, optical continuum from the F621M filter in blue and [O III] from the FQ575N filter in green. The VIMOS data is also shown as the middle column with the area covered by the displayed kinematics maps shown on the main image in light blue. The extracted emission-line profiles in the main panel are from the VIMOS data. Both the radio morphology and [O III] kinematics for this source are complex. Most notable is the line splitting shown in the lower right [O III] emission-line profile and by the high positive asymmetry in the same region, which we show to be due to a ∼10 kpc scale outflowing bubble (see Fig. 11; also see in Fig. A.9). The HST data show that [O III] is enhanced along the southern jet and possibly along a corresponding northern jet, which is not observed in our radio images.

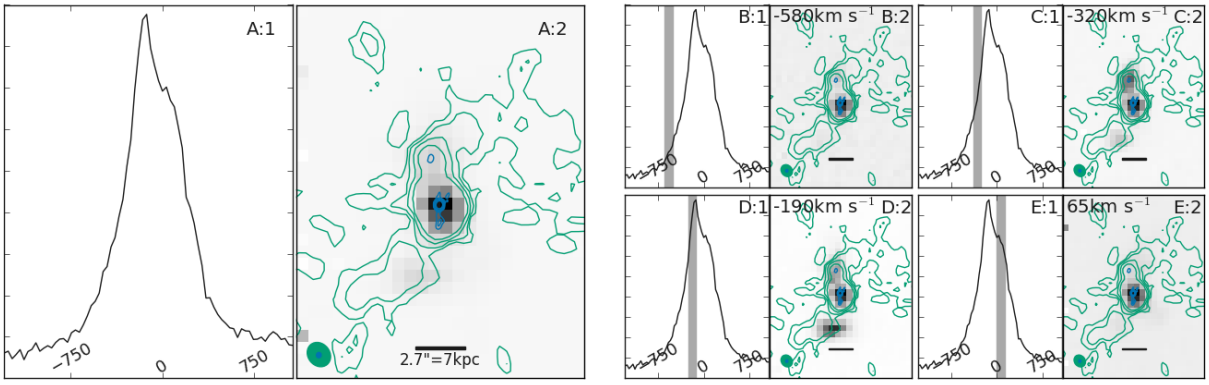

Figure A.9: As Fig. A.3 but for J1000+1242. Panels C and D show that the southern radio features are associated with kinematically distinct regions of ionized gas.

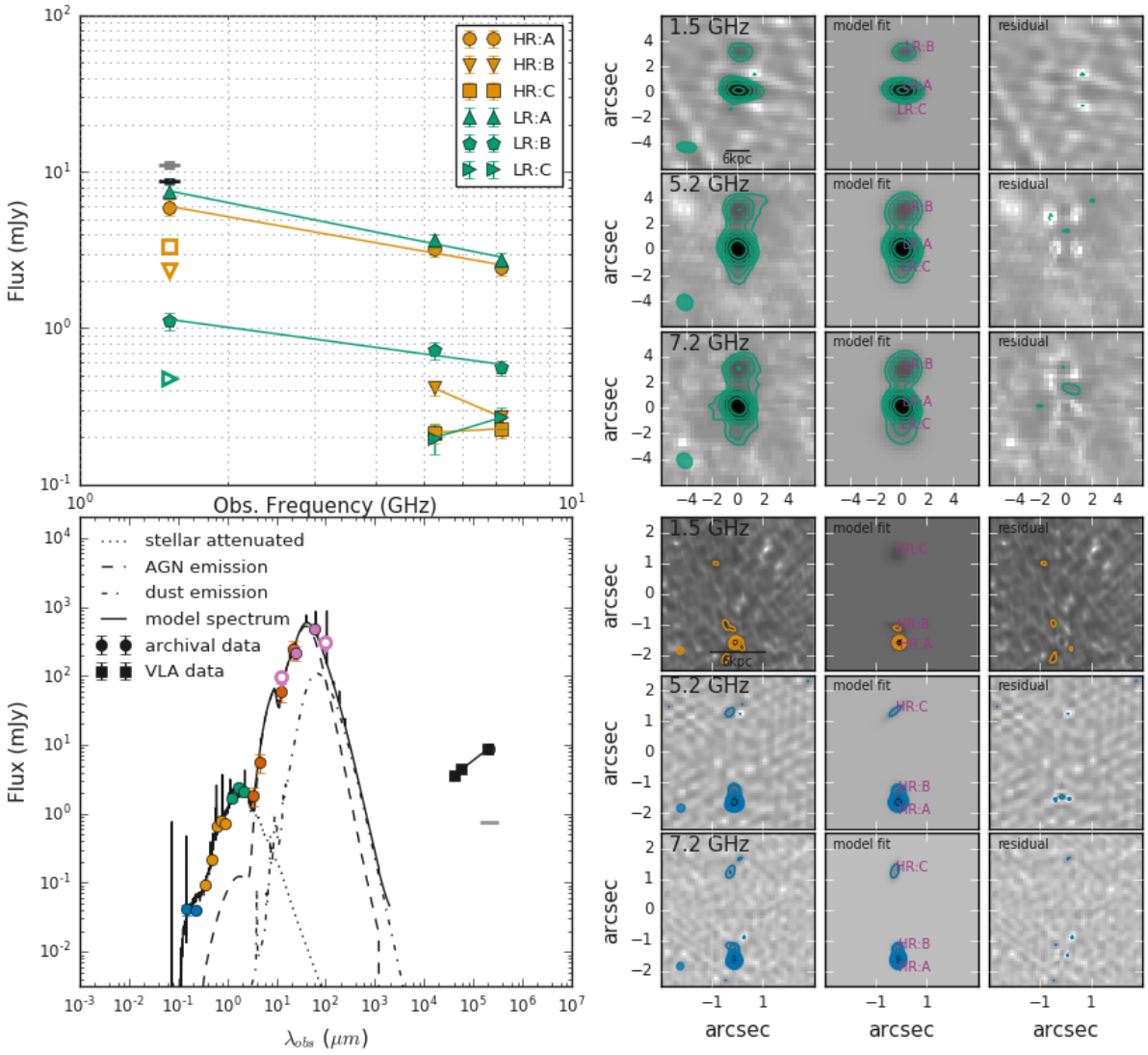

Figure A.10: Same as Fig. A.1 but for J1010+1413. The morphology of this source suggests a simple lobe (LR:B and LR:C) core structure with HR:C (with a relatively flat spectral index of $\alpha = 0.2$) as a hot spot and HR:B the base of the jet. The steepness ($\alpha = -0.6$) of HR:A however makes it difficult to identify as being dominated by an AGN core, possibly suggesting the presence of unresolved jet / lobe / wind features.

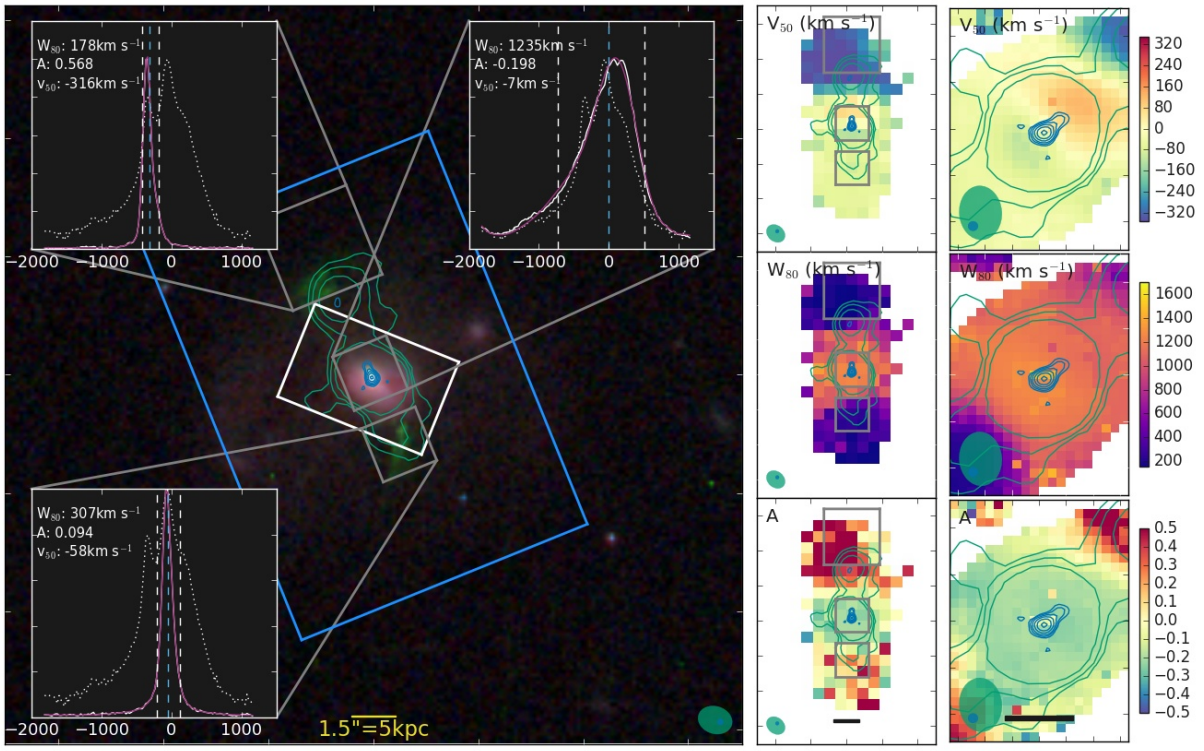

Figure A.11: As Fig. A.2 but for J1010+1413. The background three-colour image is from archival HST data (observing proposal id.14730), with IR continuum from the F160W filter in red, optical continuum from the F689M filter in blue and [O III] from the F621M filter in green. The VIMOS data is also shown as the middle column with the area covered by the kinematic maps derived from the VIMOS data shown on the main image in light blue. The extracted emission-line profiles are from the VIMOS data. The [O III] profile at the base of the jet (around HR:A and HR:B) is wide with a blue wing, indicative of outflows. The gas just beyond the extent of LR:B and LR:C is narrow and in both cases slightly blue shifted with respect to the peak central. For the gas in the north in particular this kinematically distinct [O III] feature could be responsible for the jet bending tentatively seen in HR:C and jet-gas interactions could be the cause of the velocity offset. Similarly, the southern jet could be truncated by the bright [O III] feature in the south, seen most clearly in the HST data.

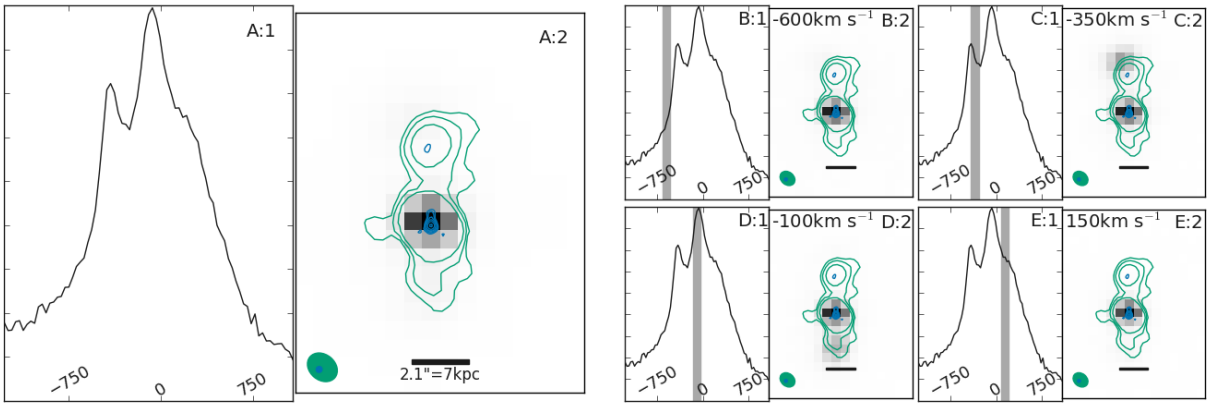

Figure A.12: As Fig. A.3 but for J1010+1413. The two main peaks seem to be associated with LR:B and LR:C (highlighted in panels C and D) with the wide central component (co-spatial to LR:A) slightly redshifted.

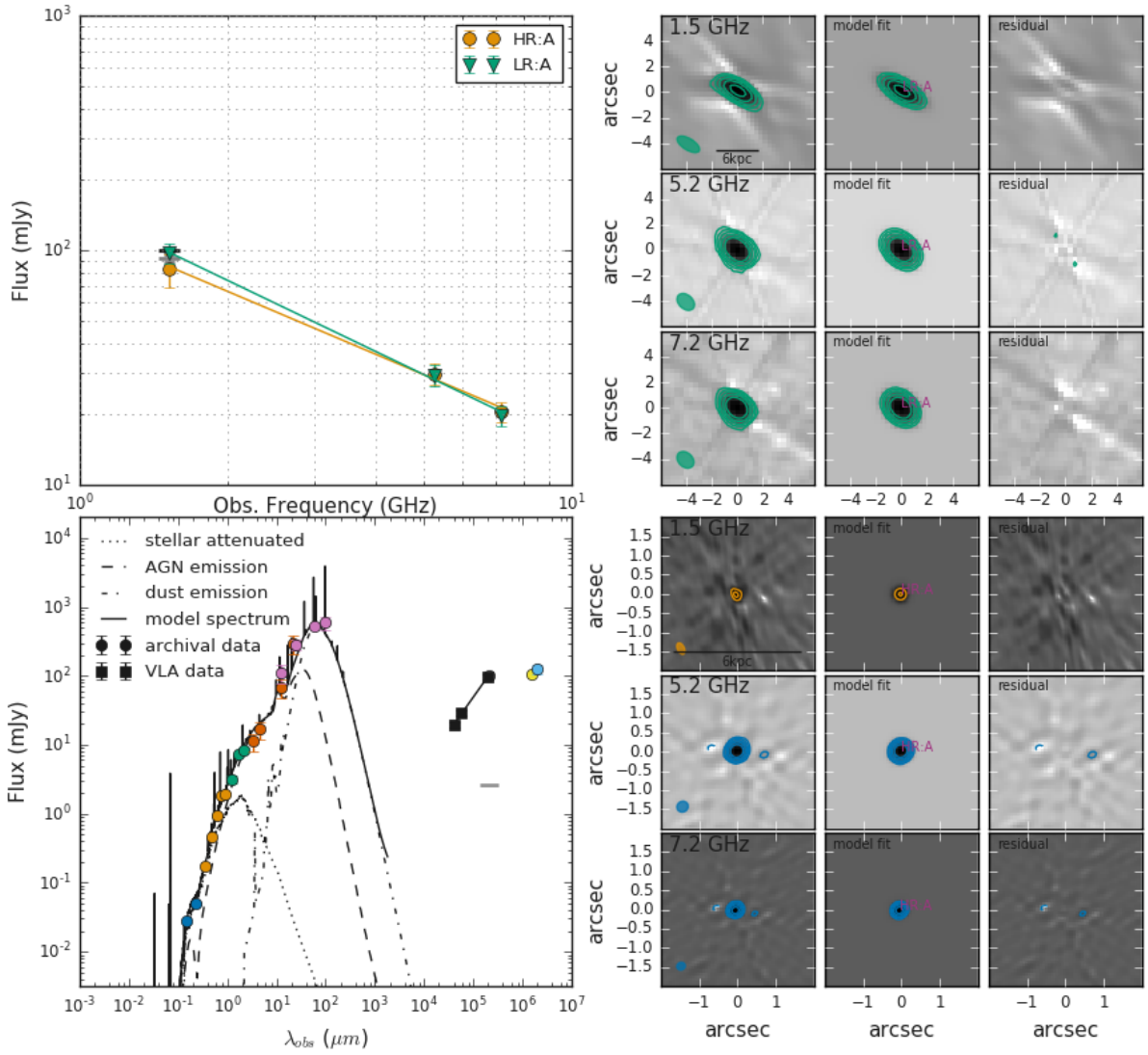

Figure A.13: Same as Fig. A.1 but for J1010+0612. Although there are no morphological features in the radio for this source, the GLEAM and TGSS data suggest either an unusual spectral shape (a peak between 1.4 and 0.15 GHz then rising again; see e.g., Hogan et al., 2015) or variability. A peak within those frequencies would mean a size of 0.2–10.5 kpc according to the turnover - size relation from CSS/GPS sources (Orienti & Dallacasa, 2014), consistent with the deconvolved size of 0.2 kpc we measured (see Section 4.1.2).

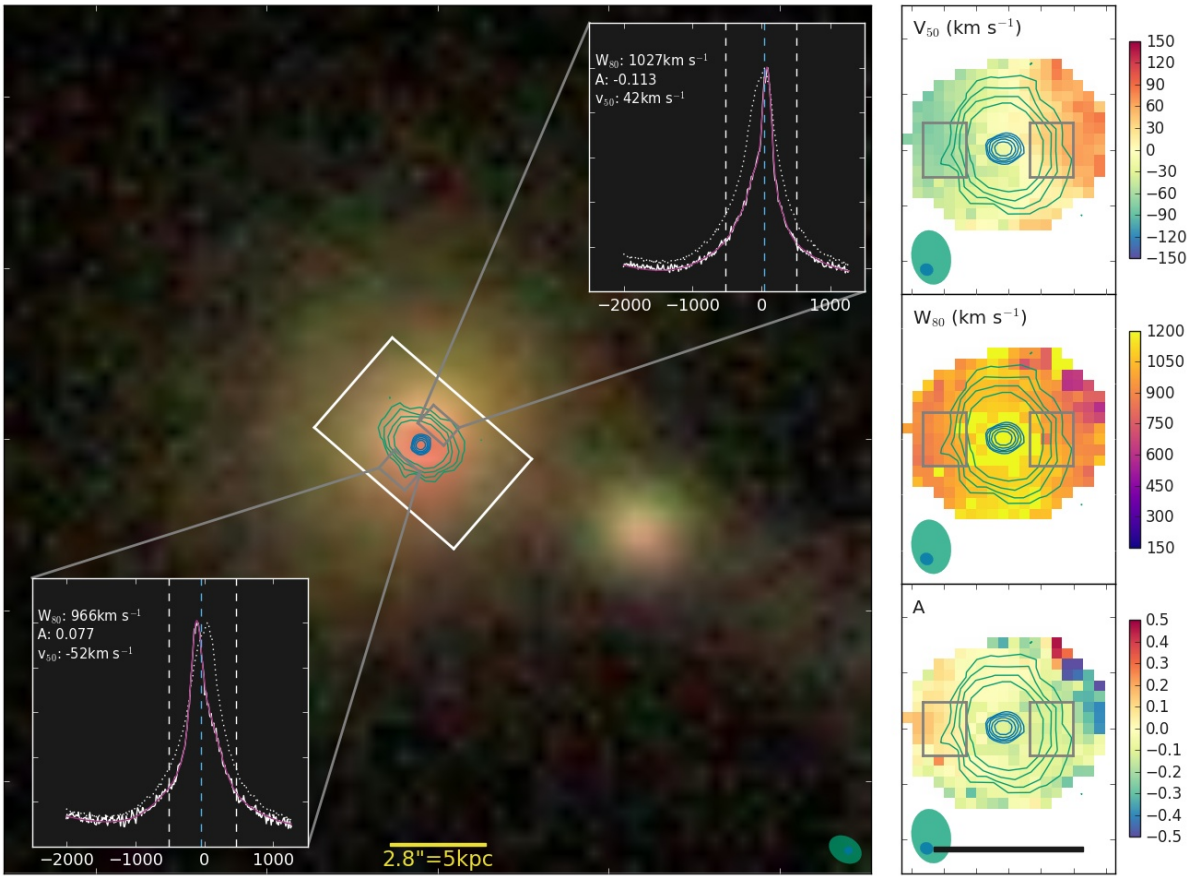

Figure A.14: As Fig. A.2 but for J1010+0612 except with the three-colour SDSS image shown in the main panel. Although there are no morphological features seen in this source at the spatial scales we are sensitive to, the width of the [O III] profile is indicative of fast ($\gtrsim$1000km s^{-1}) outflows. However, we do see a tentative alignment between the position angles calculated for the ionized gas and from the radio image (see Section 5.3), suggesting the presence of barely resolved features.

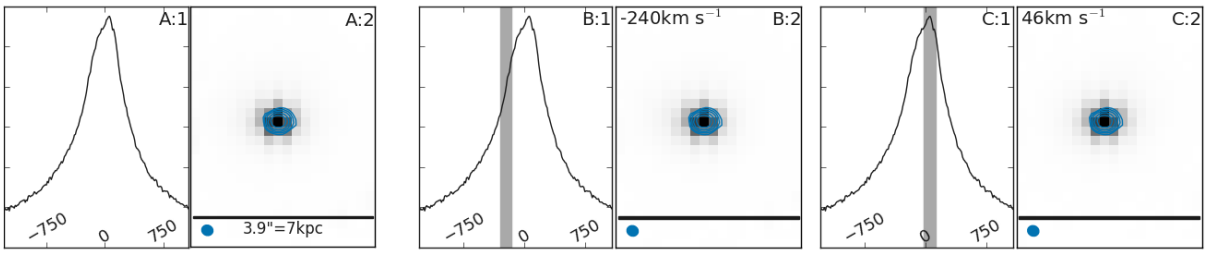

Figure A.15: As Fig. A.3 but for J1010+0612.

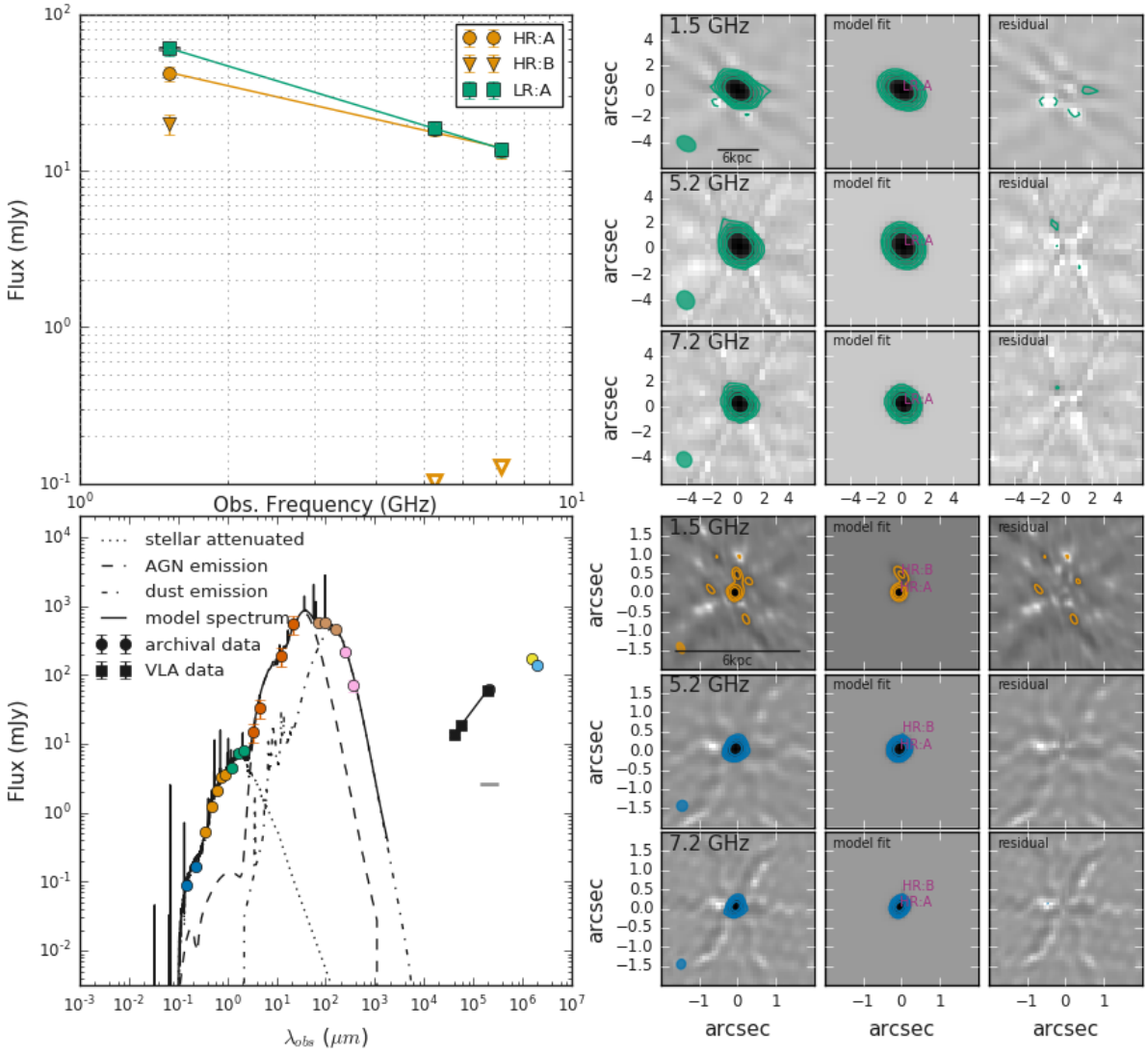

Figure A.16: Same as Fig. A.1 but for J1100+0846. HR:B is only detected in the e-MERLIN data. Although it is a 7σ detection in e-MERLIN (see Table 4) and there are wings in the synthesised beam with a similar percentage of the peak flux density, the lack of a symmetric feature in the image suggests this could be real, in which case it would be a highly variable radio structure (see Section 5.2.4). The GLEAM and TGSS data suggest that the radio SED peaks somewhere between 1.4 and 0.14 GHz which would correspond to sizes between 0.2 and 10.5 kpc assuming the source follows the size - turnover frequency relation from CSS and GPS sources (Orienti & Dallacasa, 2014). This would be consistent with the 0.8 kpc size measured between HR:A and HR:B.

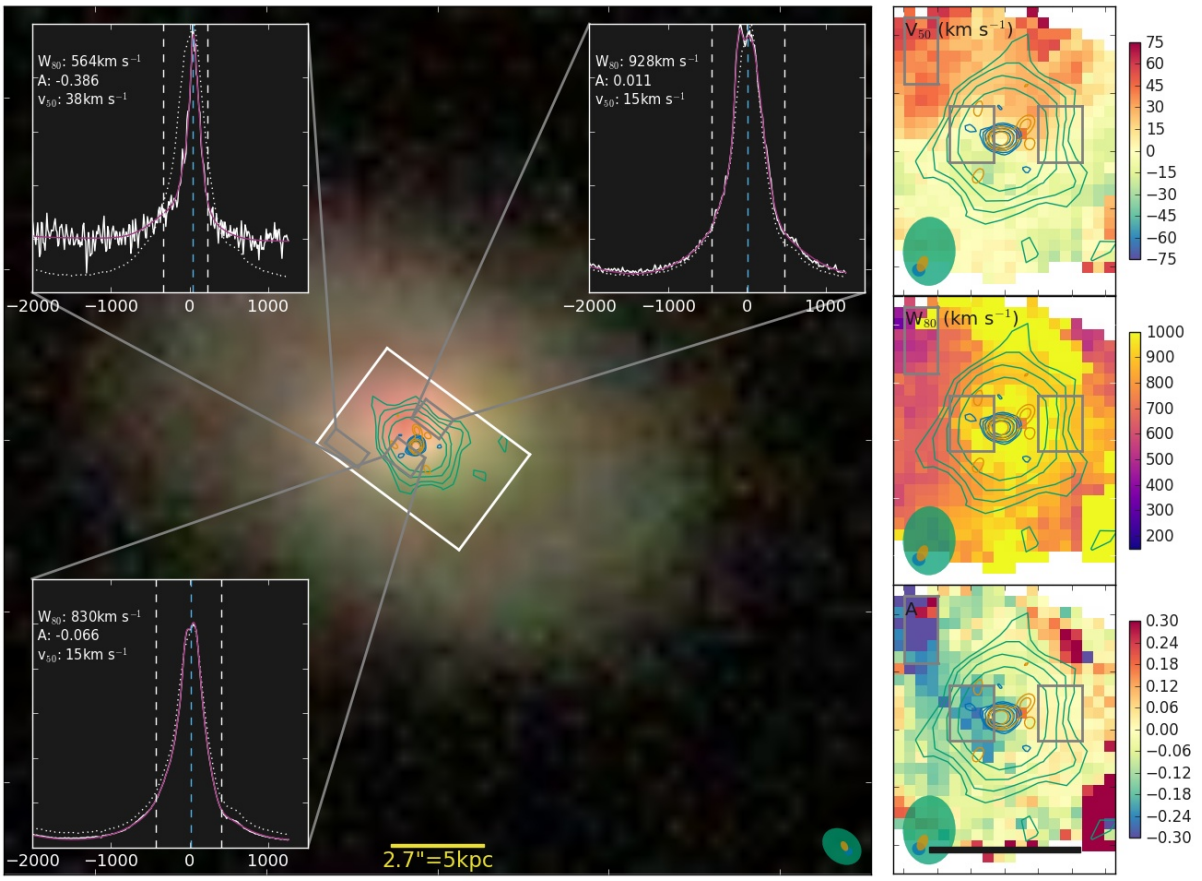

Figure A.17: Same as Fig. A.2 but for J1100+0846, with the the SDSS three-colour image in the main panel. The [O III] emission-line profile in this source is both wide (W_{80}≈1000) and disturbed (irregular velocity, width and asymmetry maps). However, we are unable to see a clear connection between the ionized gas kinematics and radio morphology in this source with the current data.

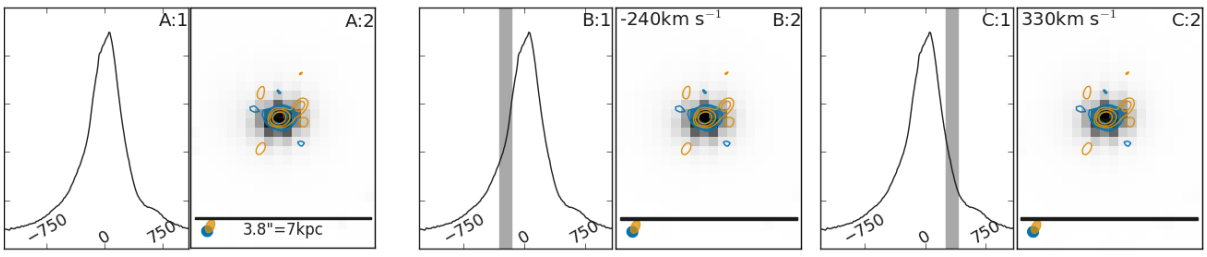

Figure A.18: As Fig. A.3 but for J1100+0846.

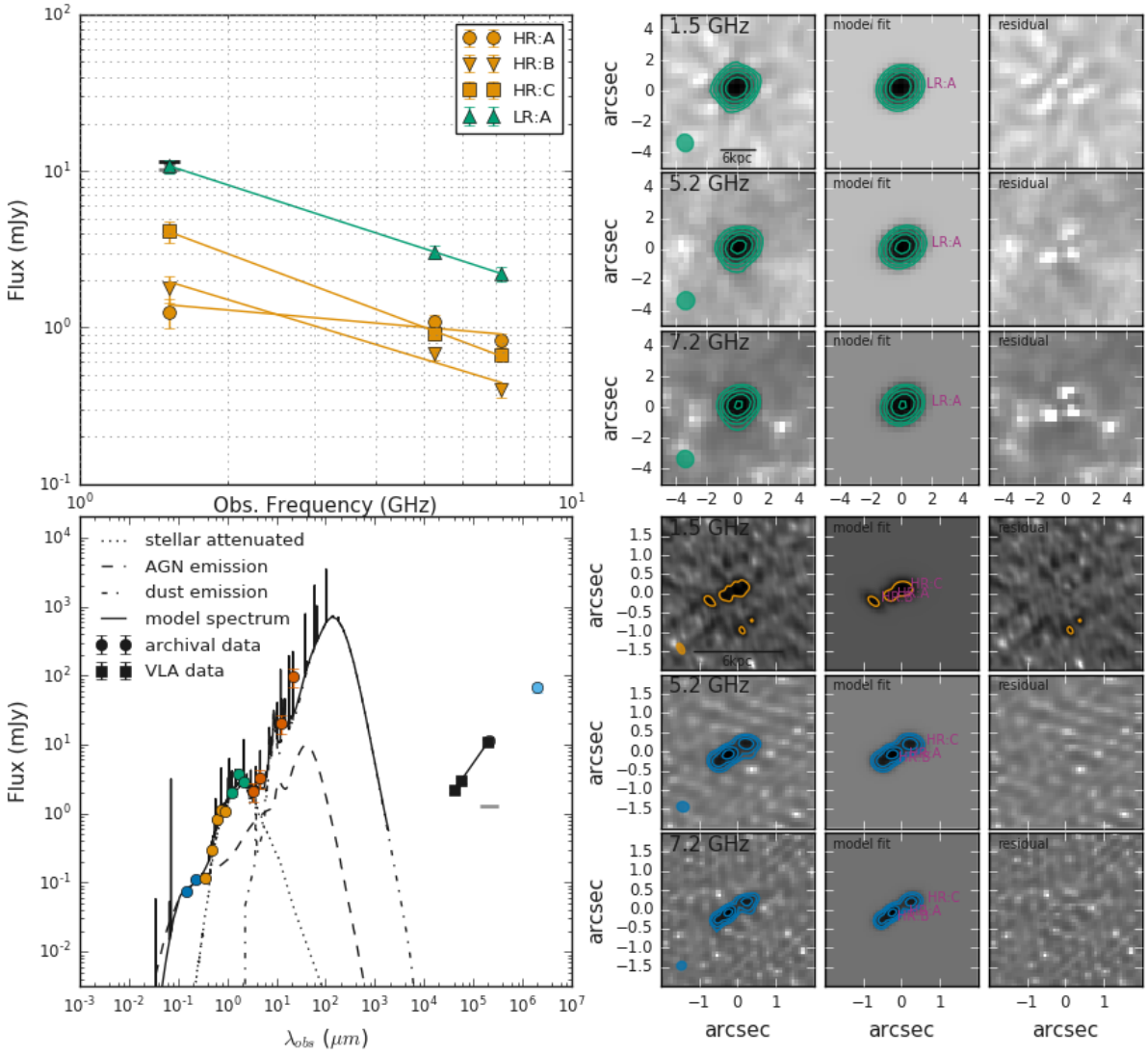

Figure A.19: Same as Fig. A.1 but for J1316+1753. The three morphological features in the high resolution images for this source have a distinctive triple (lobe-core-lobe) morphology. The relative flatness of the spectral index of HR:A ($\alpha = -0.3$) and steepness of the HR:B and HR:C components (each with $\alpha \approx -1$) is consistent with this interpretation.

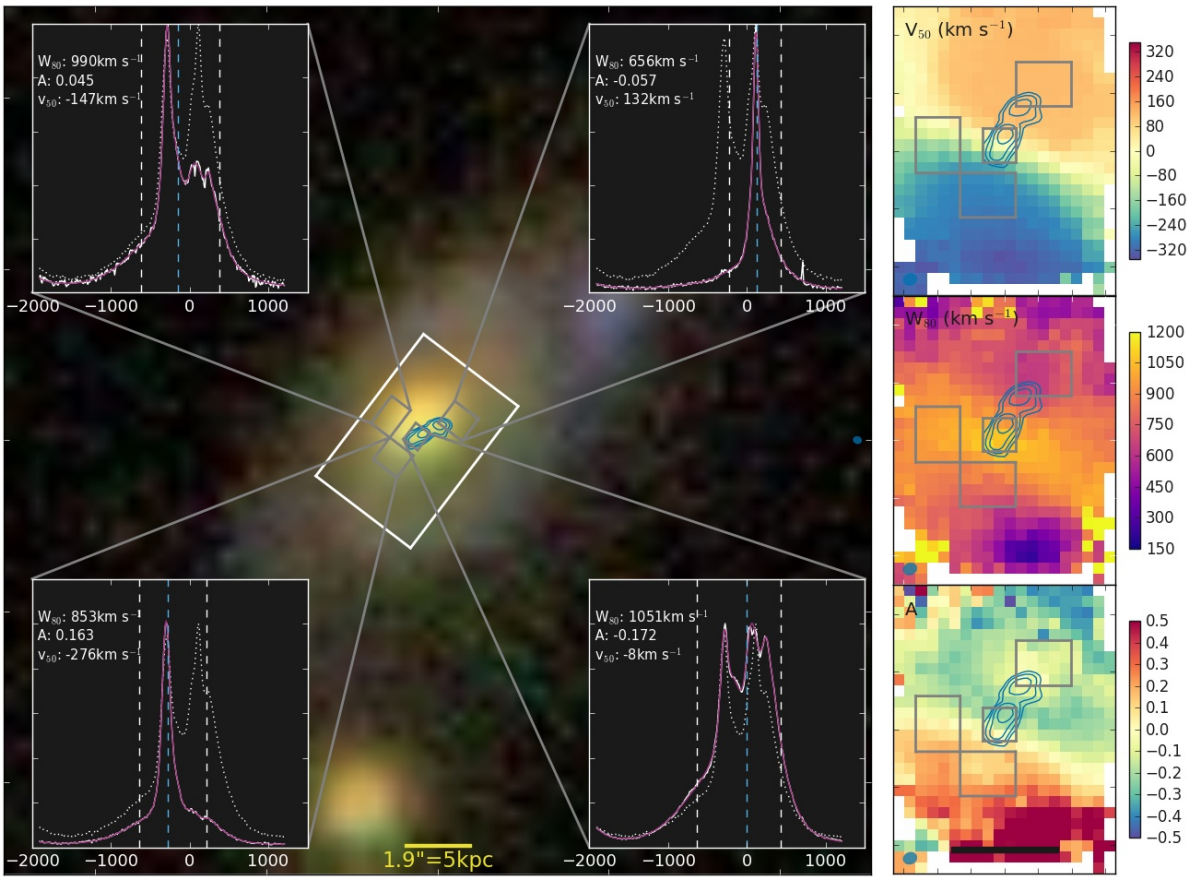

Figure A.20: As Fig. A.2 but for J1316+1753 with the SDSS three-colour image in the main panel. The velocity gradient seen could be a biconical outflow driven by the jets. The outflow interpretation is supported by the large (∼1000 km s^{-1}) line widths and the association between the location of the jets and [O III] kinematic components (also see Fig. A.21).

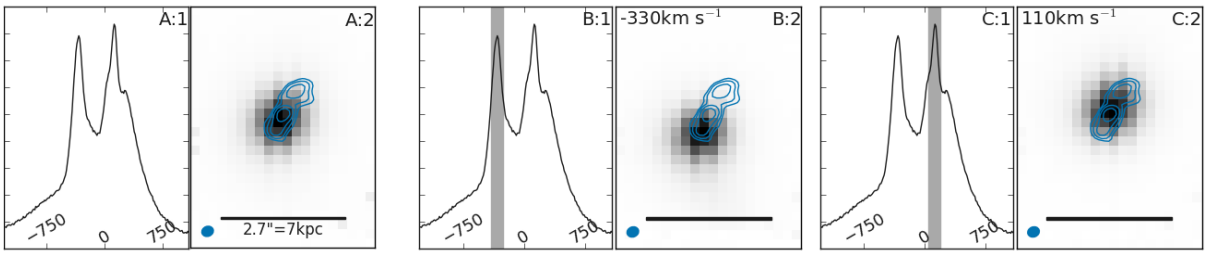

Figure A.21: As Fig. A.3 but for J1316+1753. Panels B and C show that the blue and red [O III] components roughly lie on either side of the radio features.

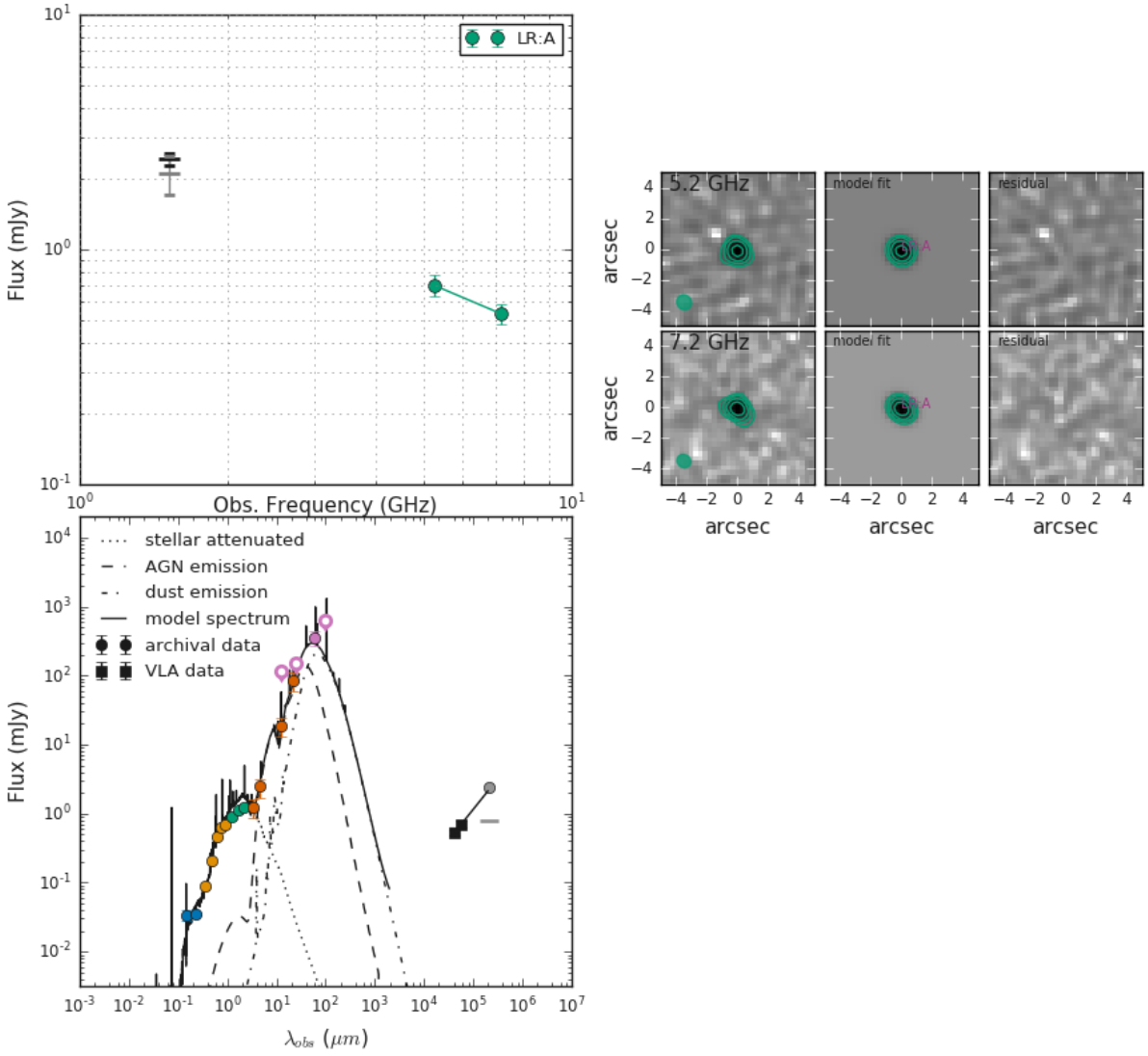

Figure A.22: Same as Fig. A.1 but for J1338+1503. We only have VLA C-band B-configuration data for this object (see Section 3) and hence can not comment on the presence of $\lesssim$kpc scale features similar to what we see in many of the other targets. We see a single morphological component with $\alpha = -0.9$.

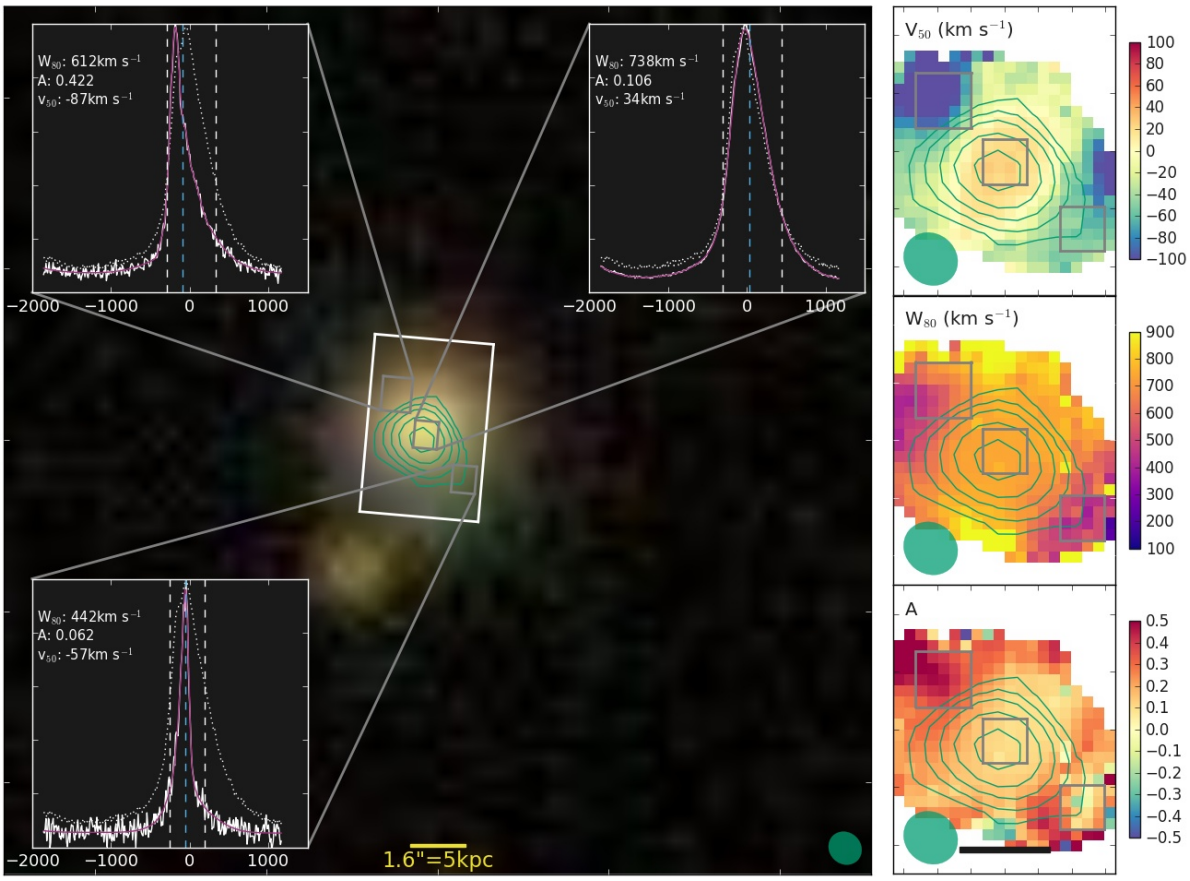

Figure A.23: As Fig. A.2 but for J1338+1503, with the three-colour SDSS image shown in the main panel. The ionized gas in this source is disturbed (seen in the velocity, width and asymmetry maps), possibly related to unresolved jet and/or quasar wind driven outflows. The alignment measured between the radio and [O III] features from our fitting, but not visible by eye (see Section 5.3.1) suggest there might be unresolved radio features in this target.

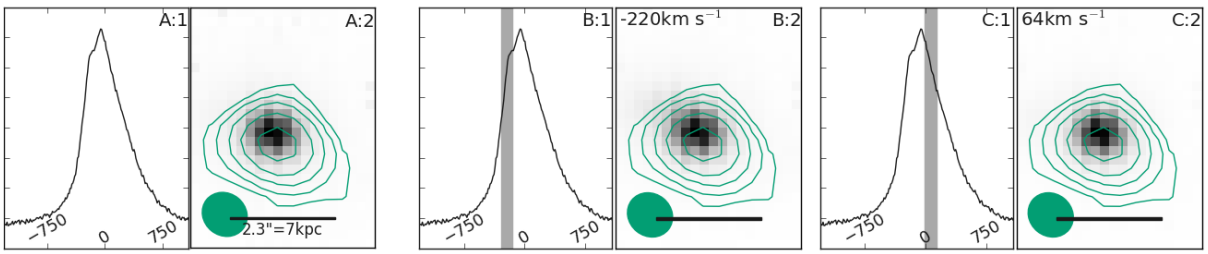

Figure A.24: As Fig. A.3 but for J1338+1503.

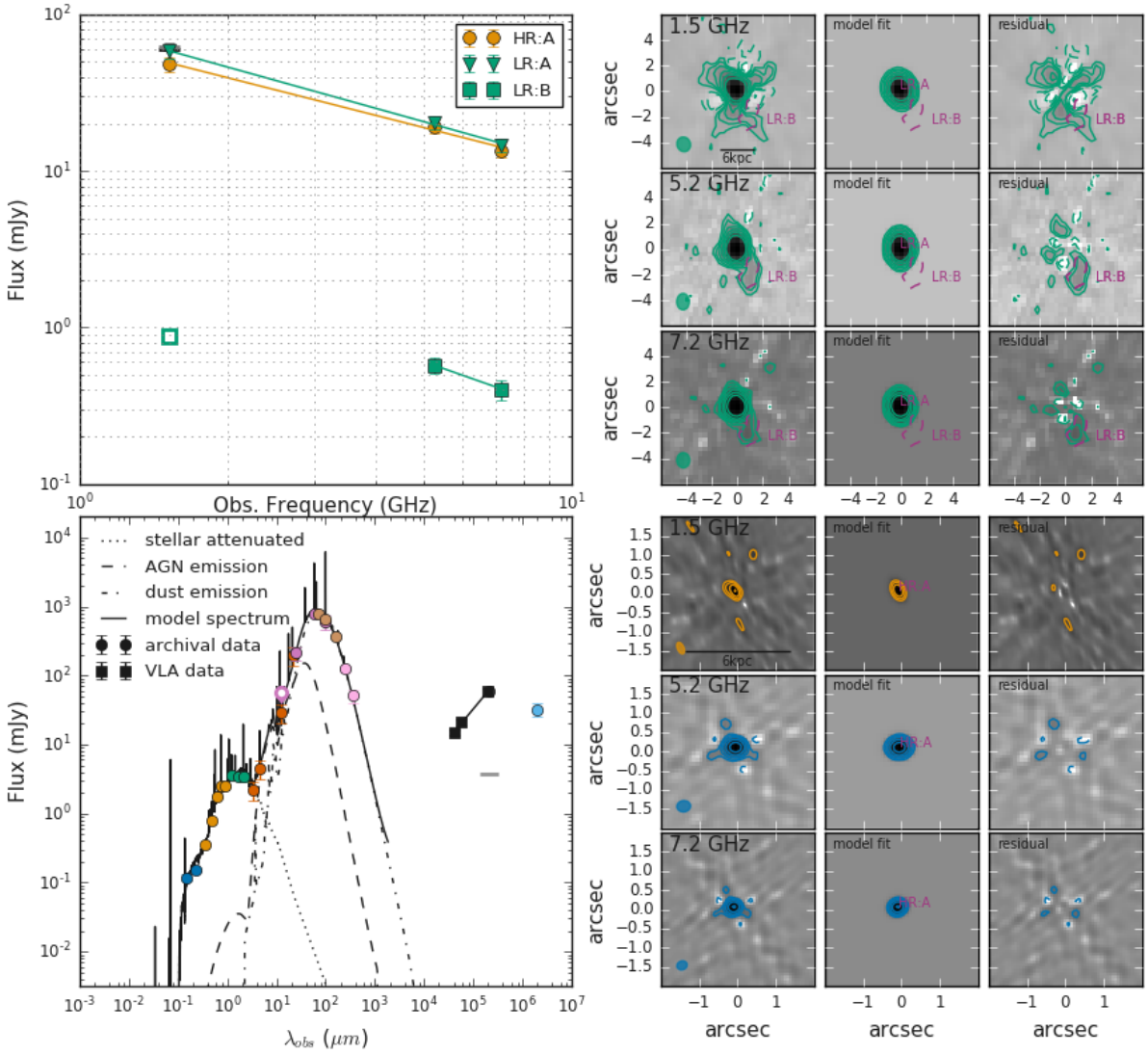

Figure A.25: Same as Fig. A.1 but for J1356+1026. LR:B is a diffuse (not visible in the HR data), steep spectrum ($\alpha = -1.1$) component whose exact nature is unclear but which might be a deflected jet or a tail of star formation (see Section 5.2.4). The nuclear component (HR:A / LR:A) also has a steep spectrum ($\alpha \approx -0.8$), which may suggest that the nuclear component contains a still unresolved jet. Furthermore, the turnover in the radio SED (which is dominated by the nuclear HR:A component), implies a size between 0.2 and 10 kpc, assuming the size – turnover frequency relation from Orienti & Dallacasa 2014), consistent with the deconvolved size measured in Section 4.1.2 (0.3 kpc).

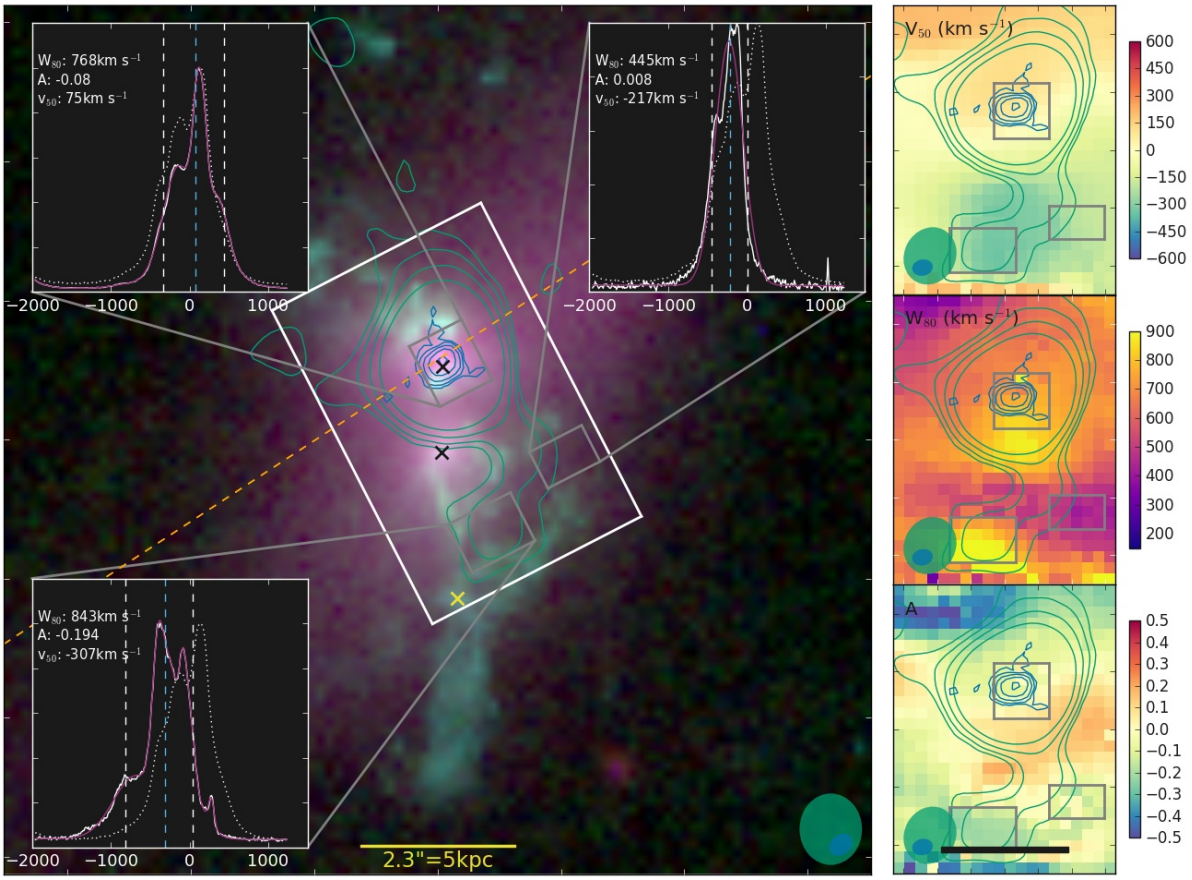

Figure A.26: Same as Fig. A.2 but for J1356+1026. The background image is from archival HST data with F160W (continuum) in red, the F814W filter (mix of Hα and continuum) in blue and the F438W ([O II] dominated) filter in green (Comerford et al., 2015). This source has been identified to host two AGN, which are marked by black x's with their locations taken from the peaks in the F814W image. The yellow x marks the approximate position of the base of the quasi-spherical outflow / bubble identified by Greene et al. (2012), that is not covered by our GMOS observations. LR:B terminates just at the base of the bubble, suggesting the two features could be related. The lack of line emission coincident with LR:B challenges its interpretation as due to star formation. The orange dashed line marks the direction of the velocity gradient in the cold gas disc from ALMA data (Sun et al., 2014).

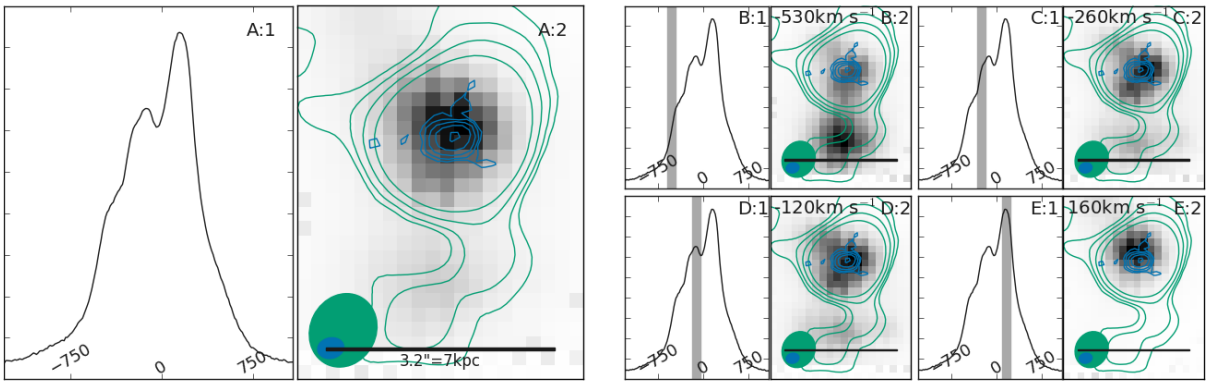

Figure A.27: As Fig. A.3 but for J1356+1026. Panel B shows that the broad [O III] emission in the vicinity of the extended radio structure is kinematically distinct from the rest of the ionized gas, potentially due to interactions with a jet. Panels C and D show that the prominent blue wing in the emission-line profile is mostly associated with a region of [O III] emission extended to the north-east of the brightest nuclei.

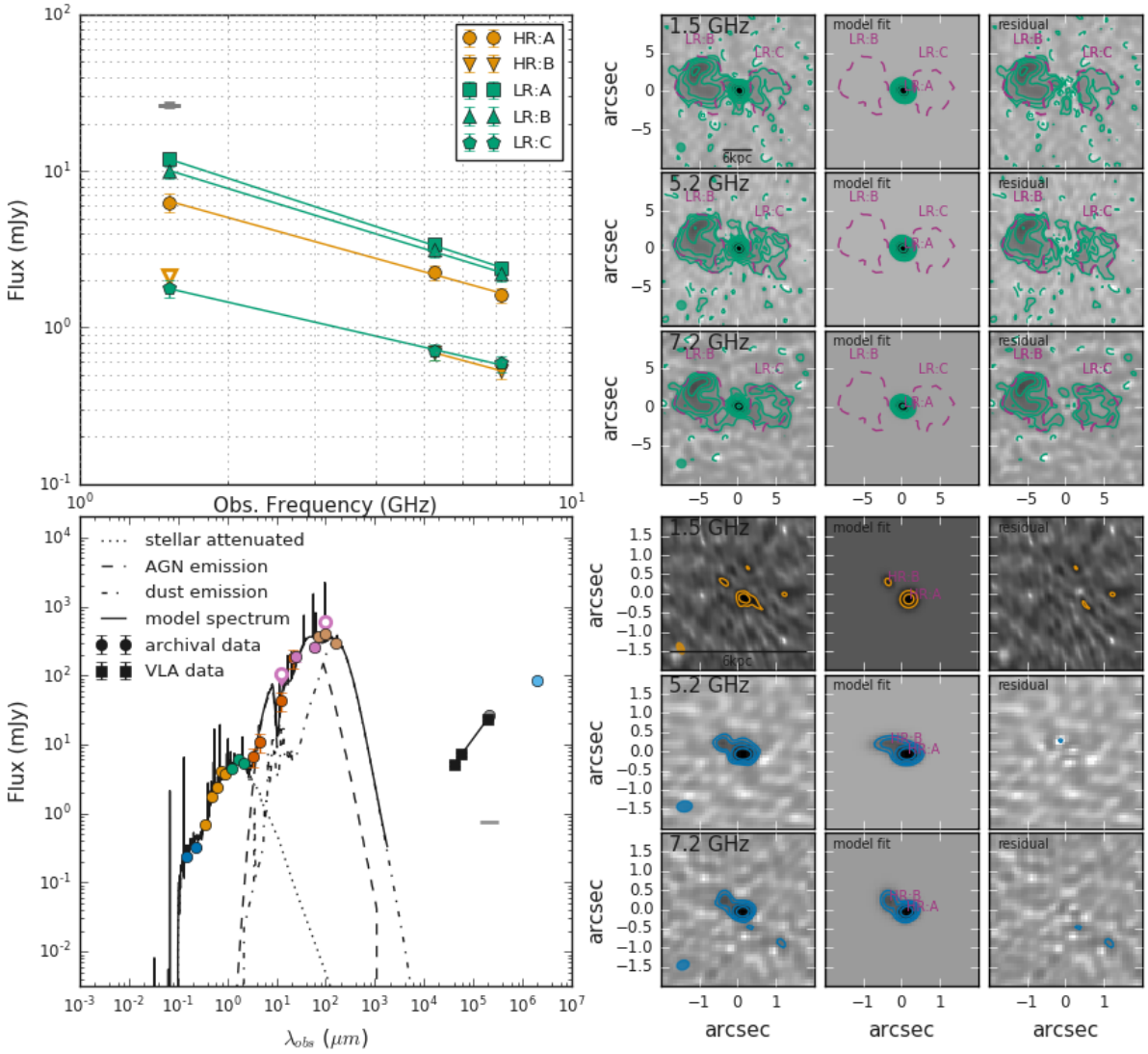

Figure A.28: Same as Fig. A.1 but for J1430+1339. The hollow radio bubbles seen in this source (LR:B and LR:C) are unique among this sample. HR:A and HR:B could be compact (LLS=0.8 kpc) radio jet/lobes. All of the radio components have steep spectral indices ($-0.7 < \alpha < -1$).

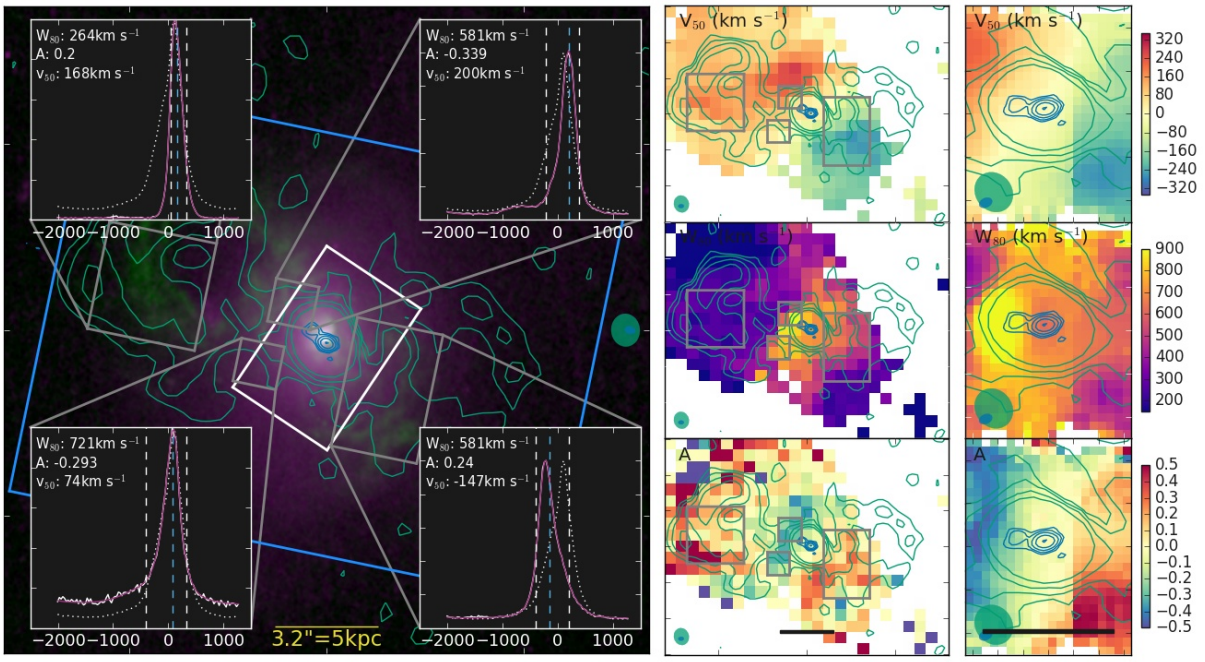

Figure A.29: Same as Fig. A.2 but for J1430+1339. The background image is from archival HST data (continuum in purple and Hα in green Keel et al., 2015). As was identified in Harrison et al. (2015) the radio bubbles (LR:B and LR:C) are coincident with similarly shaped structures in the ionized gas each with a distinct velocity (better seen in Fig. A.30). It has also been identified that the bubbles are bright in soft X-rays, whose spectrum is consistent with shocked gas (Lansbury et al., 2018). There is a wide and blue shifted ionized gas component, indicative of an outflow, just beyond HR:B (shown in the top right [O III] line profile). This source is discussed in more detail in Harrison et al. (2015).

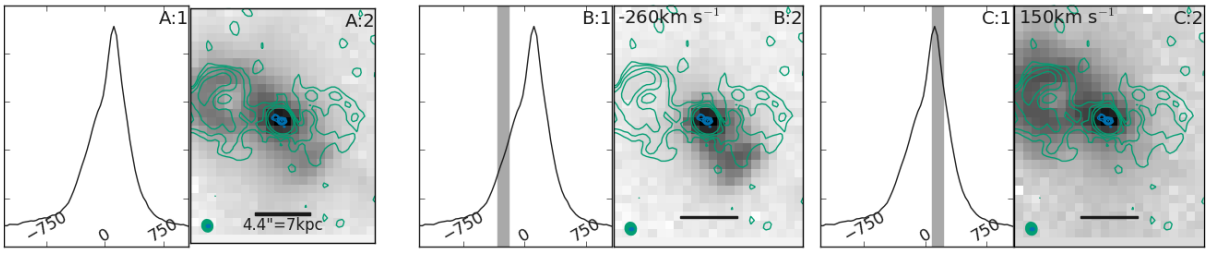

Figure A.30: As Fig. A.3 but for J1430+1339. The ionized gas components coincident with the radio bubbles are kinematically distinct (also see Villar-Martín et al., 2018).

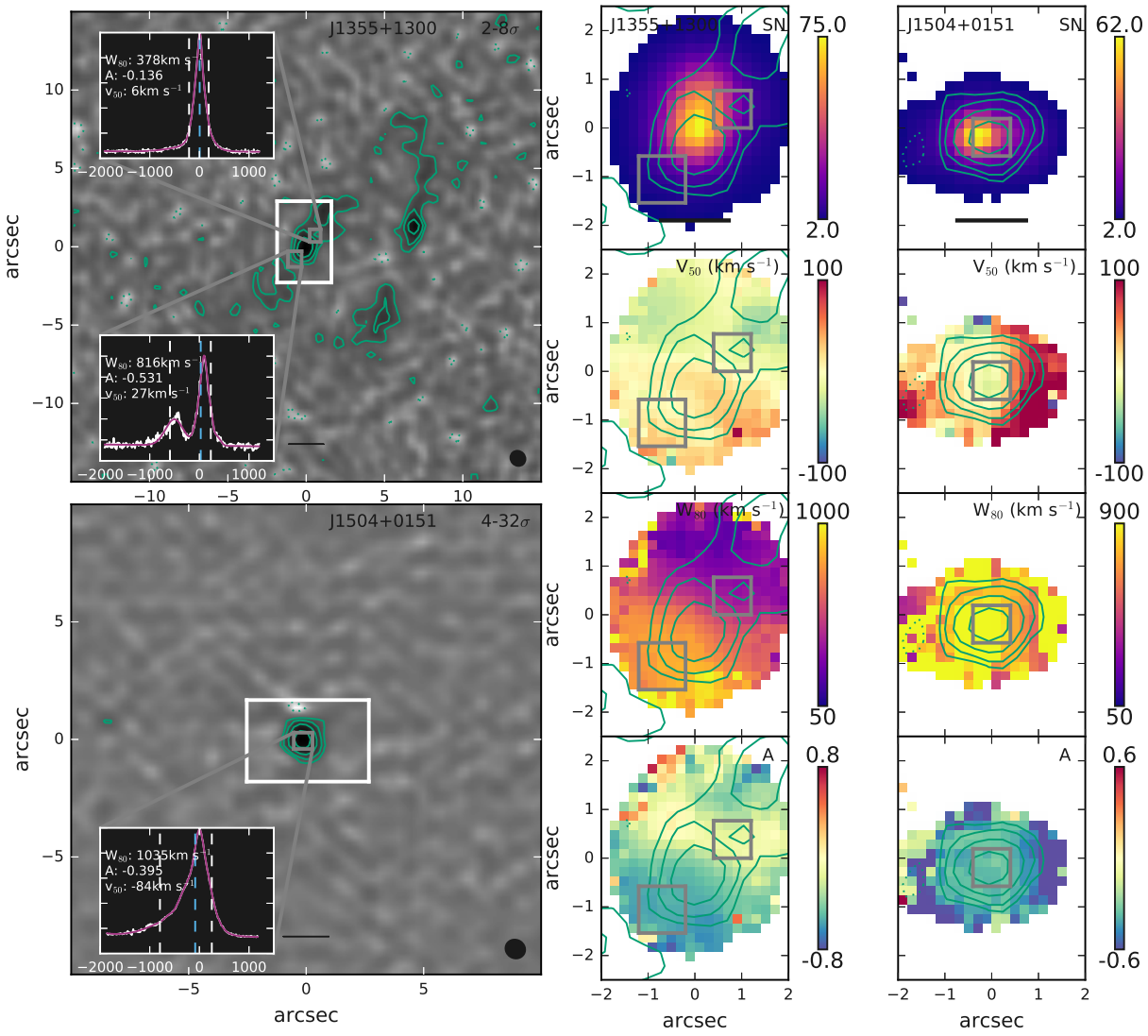

Figure A.31: Our VLA and GMOS IFS data for the two AGN in the original Harrison et al. (2014) sample for which we have VLA C-band B-configuration data but which were not in the primary sample discussed here. The left column contains the VLA images for each (the details of which are in Table A.1), and the black scale bar in the bottom centre represents 6 kpc. A white rectangle marks the GMOS FOV and the [O III] emission-line profiles shown in various corners are extracted from the regions shown in grey boxes. The weighted average of the spaxels included is shown in white with the fit in magenta; the vertical white dashed lines mark v_{10} and v_{90} with the light blue dashed line showing v_{50}, which is also written, along with the W_{80} and asymmetry for the extracted [O III] line profile in the top left of each line profile overlay (see Section 4.2 for parameter definitions). The second and third columns show the GMOS maps of S/N, v_{50}, W_{80} and A with the boxes used for the extracted line profiles overlaid, the scale bar in S/N image for each source is the same as in the main panel.

Appendix B

Appendix to Chapter 3

B.1 Bayesian fitting

This section provides further details about our Bayesian fits to our APEX CO observations. The values quoted in Table 3.3 are derived from these fits. The corner plots showing the posterior probability distributions of each of the parameters for each source are given in the online supplementary data to this paper ('Supplement to Appendix A'; A1–A12; Jarvis et al. 2020).

For the seven CO(2–1) detected targets (see Section 3.4), we used initial guess parameters from reduced χ^2 Gaussian fits to the emission-line data using 100 km s^{-1} bins. For the initial guess parameters for the two CO(2–1) undetected targets (J0958+1439 and J1356+1026) we used the average σ (line width) from the detected targets (170 km s^{-1}) and v_p=0. For J0958+1439 we chose an initial guess flux derived from the $L'_{CO} - L_{IR}$ starburst relation (see Section 3.5.1; f≈6 Jy km s^{-1}) and for J1356+1026 we used the Sun et al. (2014) ALMA CO(1–0) and CO(3–2) total fluxes for a rough estimate (f≈6 Jy km s^{-1}). For the initial guess parameters for fitting the CO(6–5) data we used the values found through our Bayesian analysis for the CO(2–1) data, multiplying the fluxes by 1.4 to convert to the CO(6–5) transition (for typical LIRGs; Papadopoulos et al., 2012). By fitting sources multiple times with the initial guesses varied by approximately an order of magnitude, we confirmed that the results, within errors do not depend strongly on the initial guess used.

We adopted weak priors for our fitting procedure. We limited the flux and σ_N (noise) to be greater than zero, v_p to be within +/−2000 km/s for CO(2–1) and +/−1500 km/s for the CO(6–5) data (i.e. the velocity coverage of the data).

We constrained σ (line width) to be greater than zero and used slightly different maximum values of σ for different cases. Specifically, for the CO(2–1) detections we limited the line width to be less than 3 times the width of the initial guess from the reduced χ^2 Gaussian fit (corresponding to upper values of 360–680 km s^{-1}), and for the non-detections we used the largest limit from the detected lines (i.e. $\sigma \leq$680 km s^{-1}). For the CO(6–5) data we limited σ (line width) to be less than 3 times the CO(2–1) line width from this Bayesian analysis (i.e. the values quoted in Table 3.3). We note that using more complicated or more constraining priors could lower the errors on our fits and our upper limits; however this would risk introducing bias into the results.

Our fitting code is designed to be completely general and therefore, our likelihood is composed of a single Gaussian with both Poisson and Gaussian noise considered. However, Poisson and Gaussian likelihoods become indistinguishable even for very moderate values of the mean parameter (>10). Our priors are uniform distributions which drop to 0 outside of the bounds described above. We use 100 walkers for the MCMC analysis and run it for 500 steps with the first 300 steps later cropped as burn in (visual inspection of the trace plots were used to confirm the burn in period for all fits). We determine the starting position for each walker using the initial guesses described above with a random offset added drawn from a uniform distribution limited to within ± 3 orders of magnitude less than the initial guess.

For each source where the CO(2–1) line is detected (all except J0958+1439 and J1356+1026) the posterior distributions for all 4 parameters show clear peaks. In contrast, the non detections do not show clear peaks in one or more of the parameters (the posteriors for σ in particular do not have a clear peaks for any of the non detected CO lines), as is shown in the corner plots in the online 'Supplement to Appendix A' (Jarvis et al., 2020). Further details on the individual fits can be found in the corner plots and captions in that supplemental document to the published work.

B.2 $\alpha_{\rm CO}$ and molecular gas mass calculations

Here we provide specific details about how we calculated $\alpha_{\rm CO}$ and the molecular gas masses. We also present these derived values for each source, using the two

different methods that are discussed in this paper (see Table B.1). In each case $r_{21} = 0.8$ is used to convert from CO(2–1) to CO(1–0) (see Section 3.5.1).

For a comparison with the values from Tacconi et al. (2018) (Section 3.5.1 and Fig. 3.6) we follow the α_{CO} calculation from that work (as in Genzel et al., 2015), taking the geometric mean of the metallicity dependent α_{CO} recipes of Bolatto et al. (2013) and Genzel et al. (2012):

$$\alpha_{CO} = 4.36 \times \sqrt{0.67 \times \exp(0.36 \times 10^{-1\times(12+\log(O/H)-8.67)} \times 10^{(-1.27\times(12+\log(O/H)-8.67)})}, \quad \text{(B.1)}$$

where α_{CO} has units $M_\odot$ (K km s^{-1} $pc^2)^{-1}$. Also following Tacconi et al. (2018) we use the following mass metallicity relation from Genzel et al. (2015):

$$12 + \log(O/H) = a - 0.087 \times (\log M_\star - b)^2, \quad \text{(B.2)}$$

where a=8.74 and

$$b = 10.4 + 4.46 \times \log(1 + z) - 1.78 \times (\log(1 + z))^2. \quad \text{(B.3)}$$

For the comparison with the xCOLD GASS samples in Section 3.5.1 we calculate α_{CO} following Saintonge et al. (2017). Specifically, they use the metallicity and Δ_{MS} dependent α_{CO} correlation from Accurso et al. (2017):

$$\log \alpha_{CO} = 14.752 - 1.623 \times [12 + \log((O/H)] + 0.062 \times \log \Delta_{MS}. \quad \text{(B.4)}$$

To keep consistent with the methods adopted in the comparison sample, we calculate the metallicity (12+log(O/H)) following the Pettini & Pagel (2004) 'O3N2' consistent mass–metallicity relation of Kewley & Ellison (2008):

$$12 + \log(O/H) = a + b \times \log M_\star + c \times \log M_\star^2 + d \times \log M_\star^3, \quad \text{(B.5)}$$

where a=32.1488, b=−8.51258, c=0.976384, d=−0.0359763 and $M_\star$ is in $M_\odot$. For additional consistency we do not use the Δ_{MS} (i.e. the ratio of the sSFR of the galaxy and its local main sequence) derived in the main paper, but re-calculate this value for use in the α_{CO} calculation, using the same method as in Saintonge et al. (2017). That is, using the star forming main sequence from Accurso et al. (2017):

$$\log \mathrm{sSFR}_{MS}[\mathrm{Gyr}] = -1.12+1.14\times z-0.19\times z^2-(0.3+0.13\times z)\times(\log M_\star-10.5). \quad \text{(B.6)}$$

Table B.1: The values α_{CO} and M_{gas} for each source in this sample using the two methods used in this work to be consistent with the literature comparisons.

	Tacconi et al. comparison (Fig.3.6)		xCOLD GASS comparison (Fig.3.7)	
Name	α_{CO}	log M_{gas}/ $M_\odot$	α_{CO}	log M_{gas}/ $M_\odot$
(1)	(2)	(3)	(4)	(5)
J0945+1737	4.1	$10.07^{+0.1}_{-0.08}$	5.3	$10.18^{+0.1}_{-0.08}$
J0958+1439	4.0	<10.0	3.4	<10.0
J1000+1242	4.2	$9.99^{+0.08}_{-0.06}$	6.0	$10.14^{+0.08}_{-0.06}$
J1010+1413	4.1	$10.54^{+0.07}_{-0.06}$	3.7	$10.5^{+0.07}_{-0.06}$
J1010+0612	4.0	$10.03^{+0.1}_{-0.09}$	3.9	$10.01^{+0.1}_{-0.09}$
J1100+0846	4.0	$10.15^{+0.08}_{-0.06}$	3.7	$10.1^{+0.08}_{-0.06}$
J1316+1753	4.1	10.1±0.2	3.7	10.1±0.2
J1356+1026	4.0	<10.0	3.9	<10.0
J1430+1339	4.1	$9.9^{+0.2}_{-0.1}$	3.3	$9.8^{+0.2}_{-0.1}$

Notes: (1) Object name; (2) α_{CO} calculated to be consistent with Tacconi et al. (2018); (3) log M_{gas} calculated to be consistent with Tacconi et al. (2018); (4) α_{CO} calculated to be consistent with xCOLD GASS (Saintonge et al., 2017); (5) log M_{gas} calculated to be consistent with xCOLD GASS (Saintonge et al., 2017).

As described in Accurso et al., 2017, this α_{CO} relation is only valid within 7.9<12+log(O/H)<8.8 and $-0.8<\log\Delta_{MS}<1.3$. Using the Δ_{MS} values for these calculations J0945+1737, J1000+1242 and J1356+1026 all fall outside (or at the edge of) of the allowed Δ_{MS} range (with log Δ_{MS}=1.6, 1.4 and 1.3 respectively). However using the recommended starburst α_{CO} from Accurso et al. (2017) of 1 for these sources does not change the conclusions of this work.

We note that the gas masses derived from both of the methods described above are consistent within errors.

Appendix C

Appendix to Chapter 4

C.1 Images and notes on individual objects

In this appendix we provide images showcasing the data used in Chapter 4 for each source (Fig C.1 – C.33), the captions of which contain brief discussions of the features seen. We additionally discuss our findings compared to the literature available for individual sources where needed (Sections C.1.1 – C.1.9). For the sources which were previously discussed in Chapter 2, we refer the reader to Appendix A.

C.1.1 J0749+4510

This source is one of the five radio-loud sources in this sample according to the (Xu et al., 1999) division. Additionally, it has been well studied in previous literature. Specifically it is a known gamma ray source and is optically variable (Nolan et al., 2012; Hovatta et al., 2014). Combined with the flat spectrum core identified in this work (see Table 4.2 and Fig. C.1), this source is almost certain to host a powerful jet. The radio morphology for this source however is very unusual, with a possible lobe visible in the FIRST image 66.5 kpc from the core towards the south-east, while our VLA L-band image shows a diffuse curved structure in the north-west possibly indicating procession or bending of the jet.

We summarize the data used in this work for this source in Fig. C.1.

C.1.2 J0752+1935

This source shows a complex radio morphology in our C-band image (see Fig. C.2). This could be due to a disrupted jet. This would be consistent with our finding that this source is radio excess (see Table 4.2), its wide [O III] line (FWHM=1432 km s^{-1}; Table 4.1) and the fact that it is possibly associated with a *Fermi* γ-ray source (Massaro et al., 2012).

We summarize the data used in this work for this source in Fig. C.2.

C.1.3 J0759+5050

This source was studied by Villar Martín et al. (2014), who identified it as a radio excess source, and attribute its high [O III] FWHM (1275 km s^{-1}; Table 4.1) to an unseen <5 kpc jet. Indeed, our VLA C-band data for this source reveal a lobe–core or jet-like structure with a LLS of ∼0.85 kpc.

We summarize the data used in this work for this source in Fig. C.3.

C.1.4 J1016+0028

We summarize the data used in this work for this source in Fig. C.10.

This source has been previously identified as a compact double (Jimenez-Gallardo et al., 2019). It was undetected in our VLA C-band images and has no observed core component in FIRST or our L-band image. Higher frequency data could allow for the identification of a flat spectrum core in this source. However, the clear symmetric double radio morphology centred on the target AGN-host galaxy and with no optical emission observed in the lobes, makes its classification as a radio jet fairly unambiguous, even though it would be classified as 'radio-quiet' by Xu et al. (1999).

C.1.5 J1108+0659

This source was well studied in Bondi et al. (2016). Specifically, they used a higher spatial resolution (0.22×0.21 arcsec) radio image at 8.5 GHz to identify a flat spectrum core and a steeper spectrum lobe within the central component visible in our VLA C-band data. Additionally, they use *HST UV* imaging to associate the spatially resolved features visible to the north and south in our

VLA data with star formation. This highlights the importance of getting similar spatially resolved star formation tracers for the remainder of the sample.

We summarize the data used in this work for this source in Fig. C.14.

C.1.6 J1222−0007

This source has been previously studied using long slit spectroscopy by Greene et al. (2011), where it was identified as an ongoing merger with signatures of AGN driven disruption in the ionized gas throughout the host galaxy.

Although too low significance to impact the morphological classifications presented in table 4.2, our C-band data shows a possible triple (lobe – core –lobe) structure.

Taken together this could indicate that this source has a jet / wind triggered by a merger which is interacting strongly with the host galaxy ISM.

We summarize the data used in this work for this source in Fig. C.17.

C.1.7 J1302+1624

This source has been previously studied as Mrk783. Specifically, Doi et al. (2013) used VLBI observations of this source to measure a brightness temperature of 7.7×10^7 K indicating a non-thermal process driven by a central jet (see also Section 4.4.4). Congiu et al. (2017) identified the extended curved structure visible in our VLA L-band data. They measure a steep spectral index (α=−2.02) for this radio structure, and use this to identify the emission as a relic from a past period of jet activity. VLBI and eMERLIN imaging for this source (Congiu et al. Submitted) reveal a kpc jet-like structure, suggesting a precessing intermittent jet in this source. This all confirms our identification of this source as a Radio-AGN based on the observed radio excess.

We summarize the data used in this work for this source in Fig. C.21.

C.1.8 J1347+1217

This source is one of the GPS sources used to originally define the population (see e.g. O'Dea, 1998; Stanghellini et al., 1998). We use the published size of this source of 0.16 kpc throughout this work (O'Dea, 1998).

This source is additionally a VLA calibrator and so we did not observe it with the sample presented here. The data that we did consider directly are presented in Fig. C.23.

C.1.9 J1715+6008

This source is studied in Müller-Sánchez et al. (2015). In that work long slit spectroscopy, HST imaging and high resolution radio imaging (0.22×0.11 arcsec beam at 11.5 GHz) were used to identify both a radio jet with a largest angular size of 0.11±0.03 arcsec and jet driven [O III] outflows. We note that this is smaller than the deconvolved size used in this work of 0.256±0.0059 arcsec.

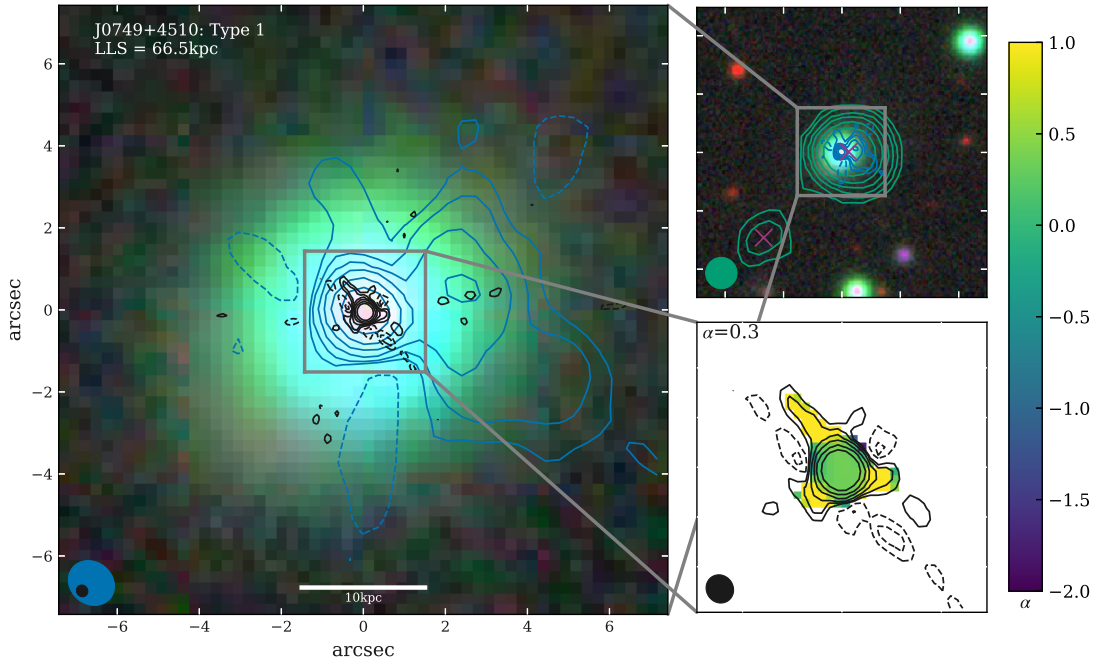

Figure C.1: This figure highlights the observed properties of J0749+4510 and the data used in Chapter 4. To the left is an rgb image from the DESI Legacy Imaging Survey in the (z,r,g) bands, with contours from our VLA L-band data (∼1 arcsec resolution) in blue and our C-band data (∼0.25 arcsec resolution) in black. North is up and east is to the left. In the top-right is a zoom-out with FIRST survey radio contours overlayed (green) in addition to the L-band contours. The magenta X's mark the peaks used to calculate the size for this source in Table 4.2. The bottom-right is a zoom-in showing the spectral index map (colour bar to the right) from our C-band data, with flux contours (as to the left) overlayed. Radio contours for all data are plotted at ±[4, 8, 16, 32, 64, 128]σ and the beams for the relevant radio images are shown in the bottom left of each sub-plot in the matching colour. This source shows two clear peaks in the FIRST image, the core, and a secondary component in the south-east possibly the lobe from an asymmetric jet. Since this component is not observed in either of our higher resolution radio images it is likely diffuse. Our L-band data for this source reveals a diffuse roughly curved structure to the west of the core, possibly indicating a disrupted or bent jet. In our C-band image, only the core is detected. The in-band spectral index shows the core to be flat, supporting our interpretation of the lower resolution features as originating from a jet.

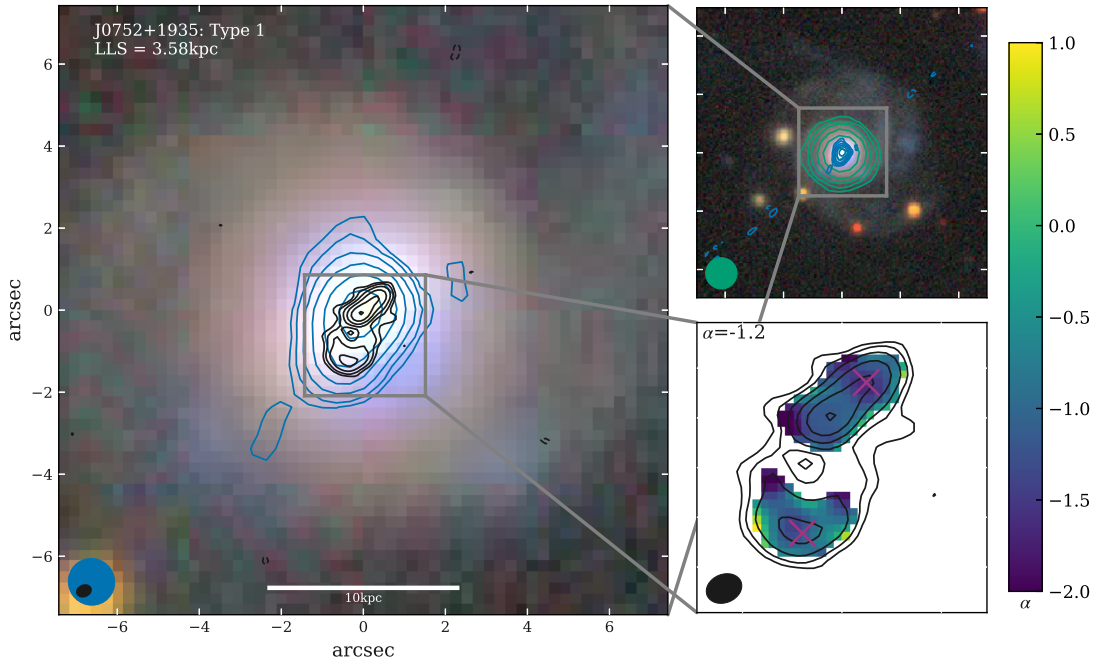

Figure C.2: As Fig. C.1 but for J0752+1935. This source is extended in our L-band image, although not resolved into distinct components. Our C-band image for this source shows a complex morphology possibly indicative of a bent / disrupted jet, although a radiatively driven wind could produce similar irregular morphologies.

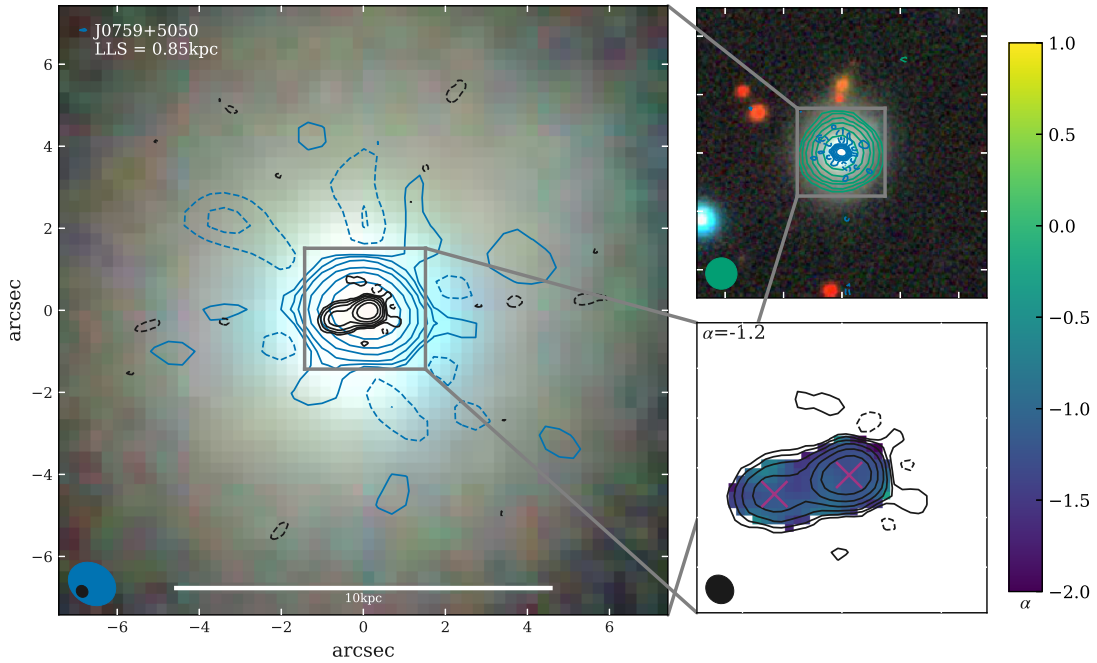

Figure C.3: As Fig. C.1 but for J0759+5050. This source is unresolved in all but our C-band image where it shows a 0.85 kpc double or jet structure. Since this source is also radio excess (Table 4.2), these features are most likely associated with the AGN and not star formation.

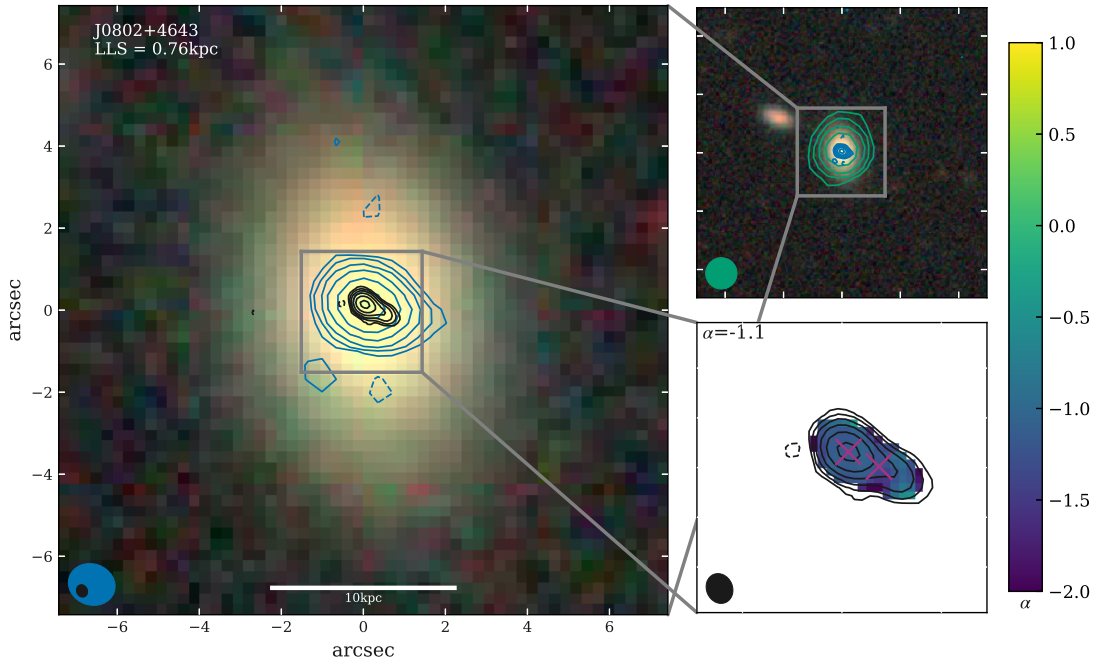

Figure C.4: As Fig. C.1 but for J0802+4643. This source is unresolved in all but our C-band image where it shows a jet-like structure extending to the south-west of the core.

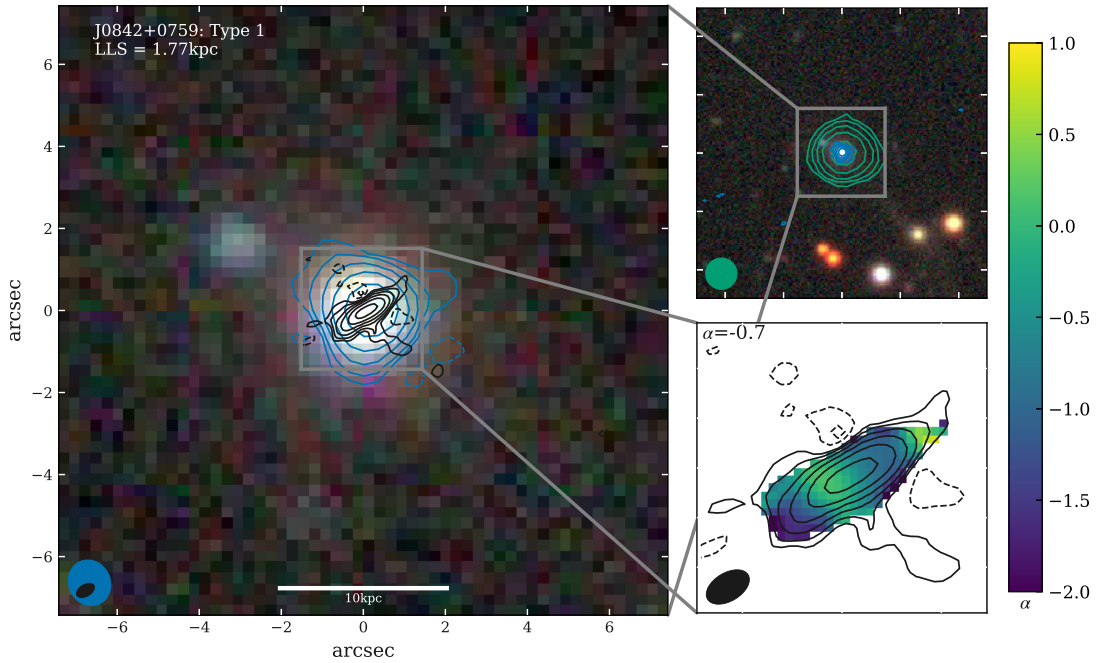

Figure C.5: As Fig. C.1 but for J0842+0759. Although there are no distinct features, the C-band data seems to be marginally extended (deconvolved size from of 0.74±0.02 arcsec). Although the spectral index measured in Section 4.4.3 is steep (−0.7) the visible flattening of the spectral index map to the south-east of the peak could indicate a flat spectrum core. Higher resolution radio images would be needed to confirm this.

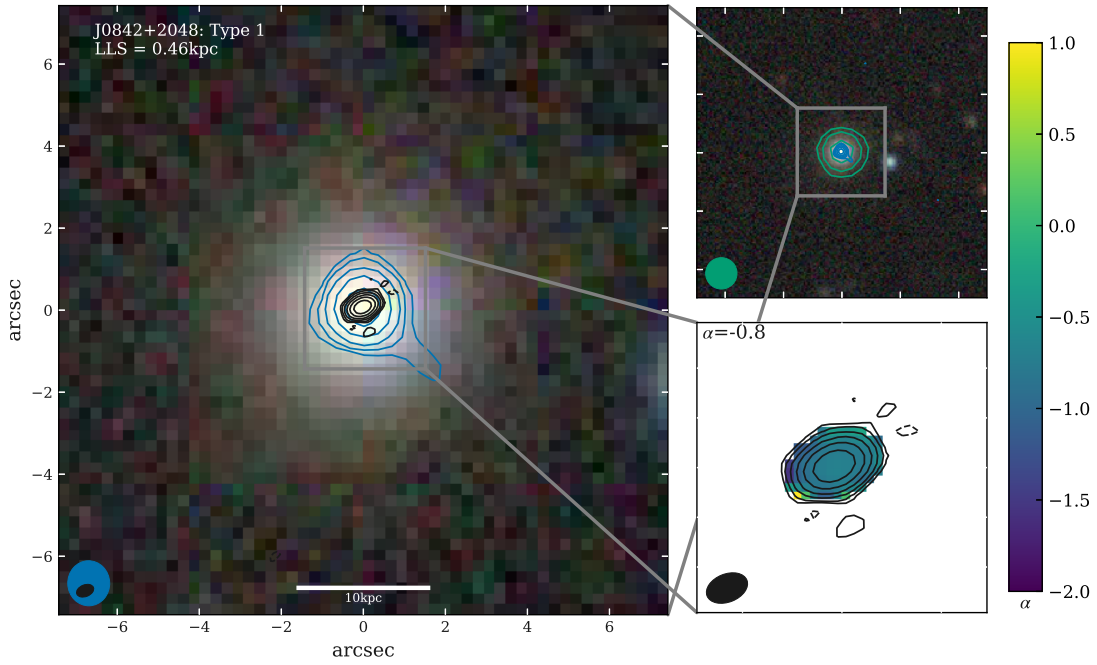

Figure C.6: As Fig. C.1 but for J0842+2048. This source shows no notable features.

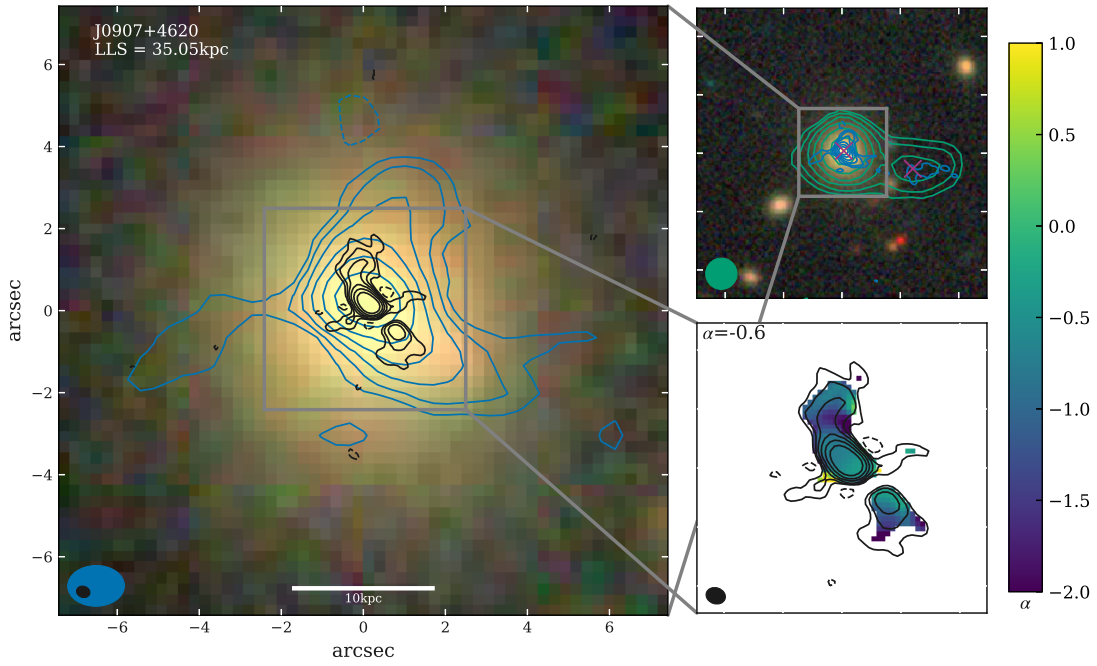

Figure C.7: As Fig. C.1 but for J0907+4620. The FIRST image shows a lobe-like feature 35 kpc to the west, which is detected with low significance in our L-band data and not at all in our C-band data marking it as diffuse emission. The lack of an optical counterpart for this radio emission suggests that it likely originates from a jet. The jet interpretation is supported by the observation of a relatively flat core from our C-band spectral index map (α=−0.6). Both our L-band and C-band image of the central region suggest a bent jet-like morphology.

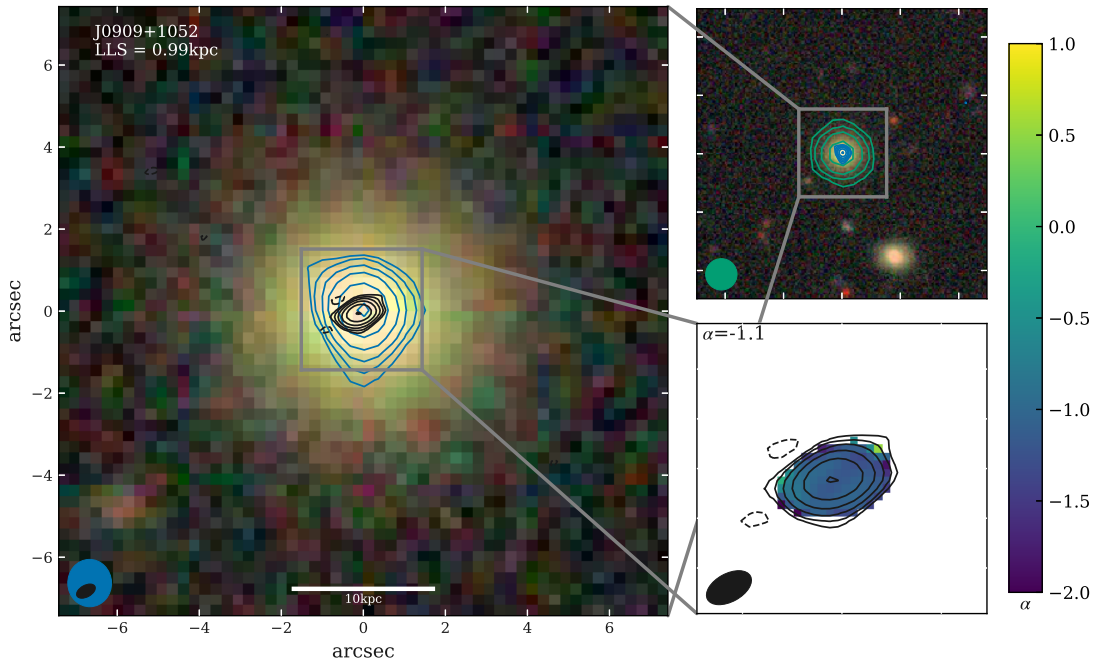

Figure C.8: As Fig. C.1 but for J0909+1052. This source shows no notable features.

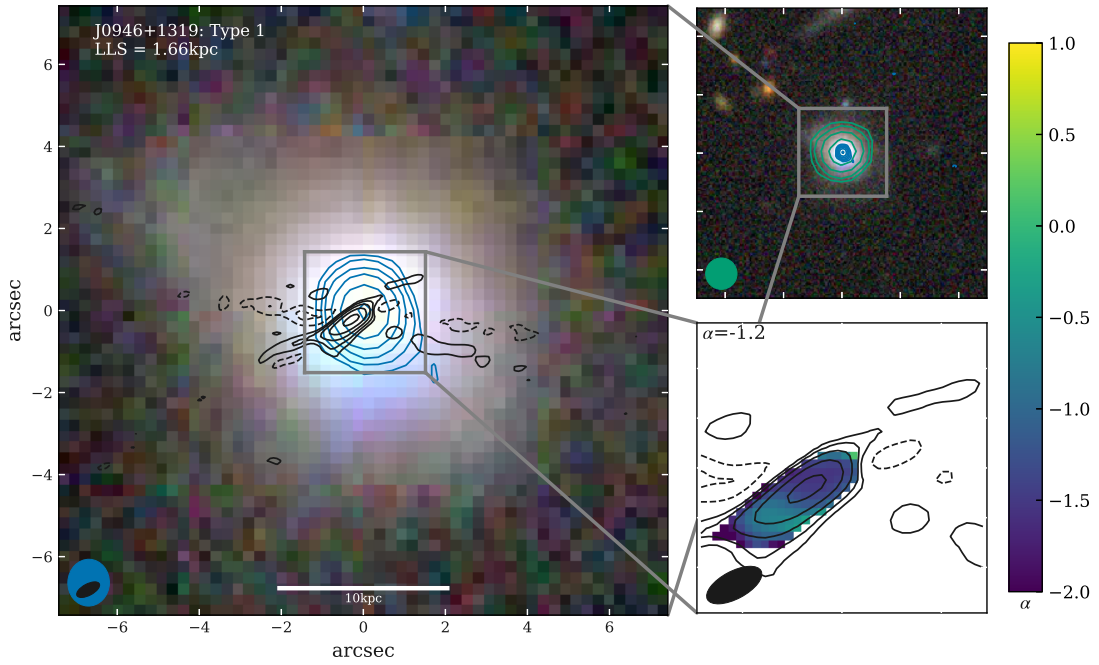

Figure C.9: As Fig. C.1 but for J0946+1319. This source shows no notable features. We note however, that there is a slight positional offset between our L and C-band data. Combined with the potential structure visible in the spectral index map (flattening towards the south-east) and the deconvolved size from casa of 0.7 arcsec, this could be evidence of barely resolved radio features in our C-band data.

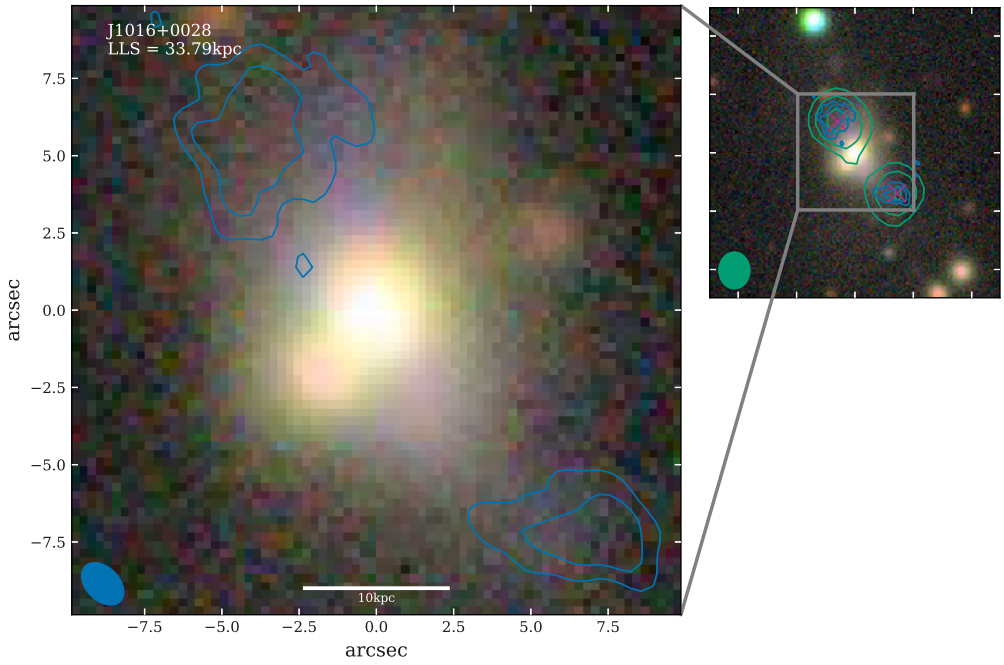

Figure C.10: As Fig. C.1 but for J1016+0028. This source clearly shows two radio lobes (visible in FIRST and our L-band data) roughly symmetric about the optical galaxy with no visible optical counterparts. This suggests that these are radio lobes emitted from an undetected jet in this source (see Section C.1.4). This source was completely undetected in the C-band and so no spectral index map is shown.

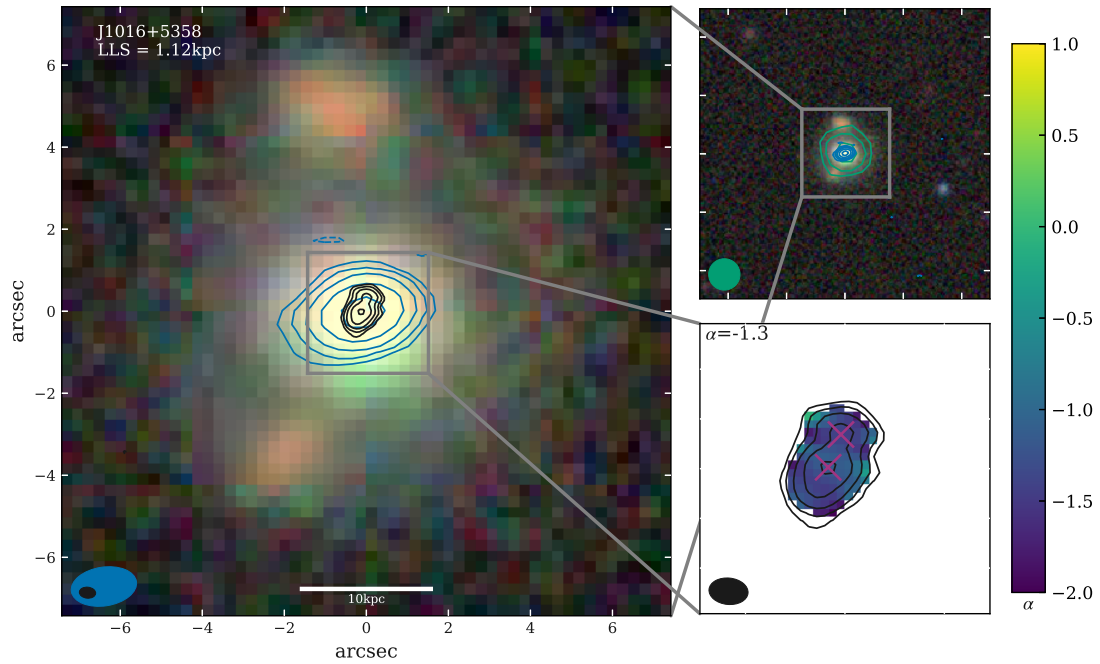

Figure C.11: As Fig. C.1 but for J1016+5358. This source is unresolved in all but our C-band image where it shows a double peaked structure.

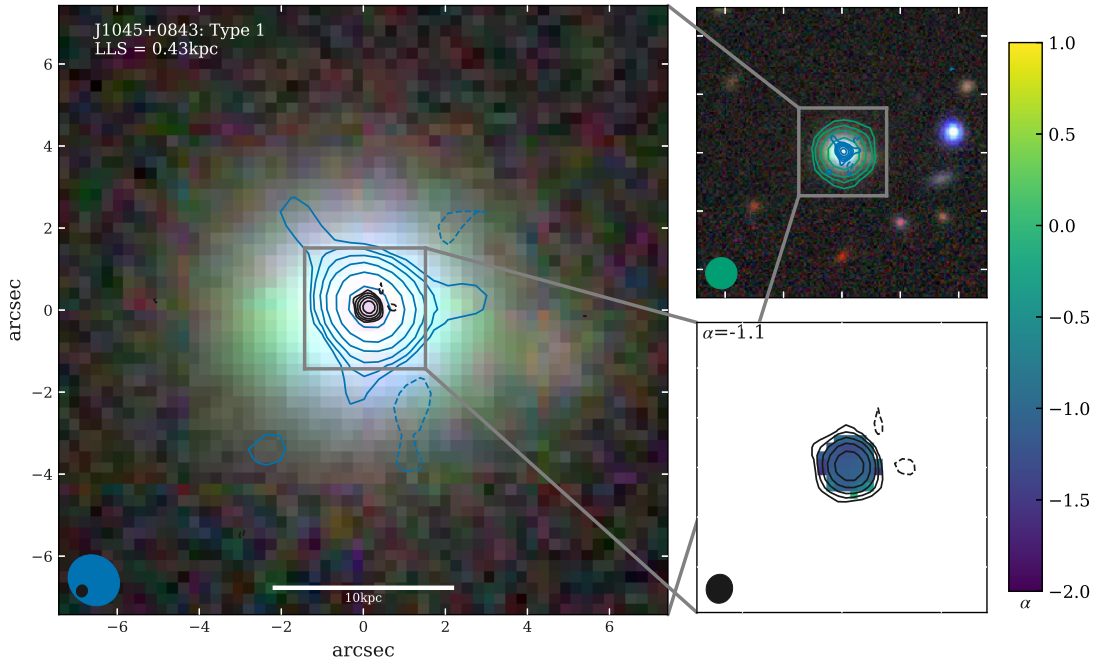

Figure C.12: As Fig. C.1 but for J1045+0843. This source shows no notable features.

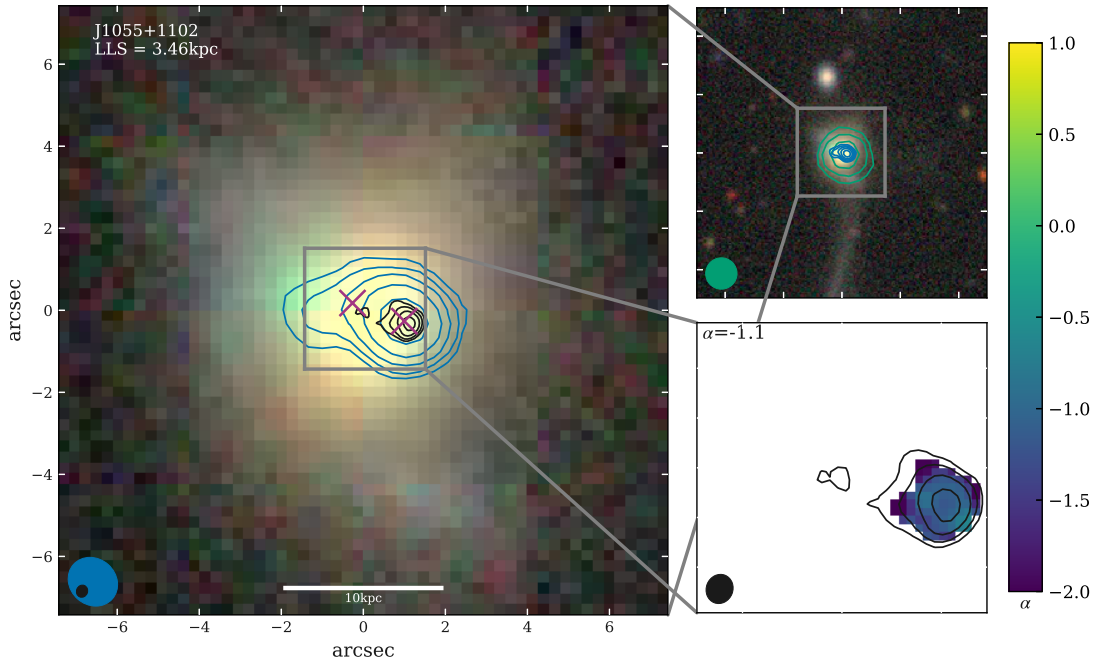

Figure C.13: As Fig. C.1 but for J1055+1102. This source shows a jet-like extension to the east in our L-band data which is also marginally detected in our C-band image. The origin of the radio emission in this source is unclear.

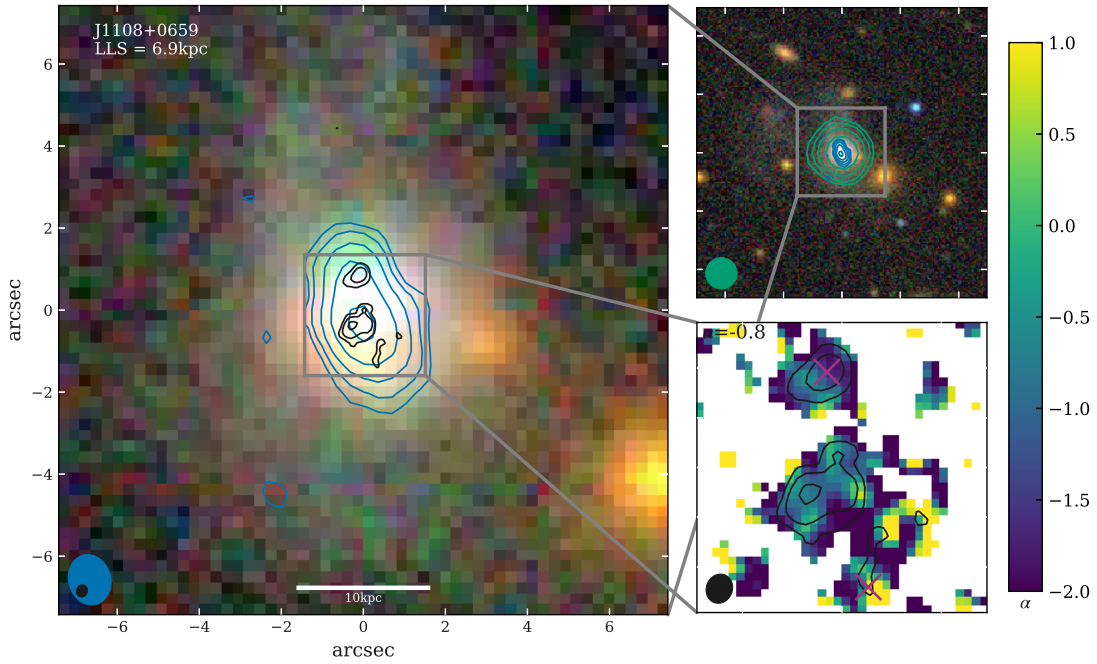

Figure C.14: As Fig. C.1 but for J1108+0659. This source is extended but with no distinct spatially resolved features in our L-band data. In the C-band it is resolved into three (low significance) features which were identified by Bondi et al. (2016) as being due to star formation. This source is discussed in more detail in Section C.1.5.

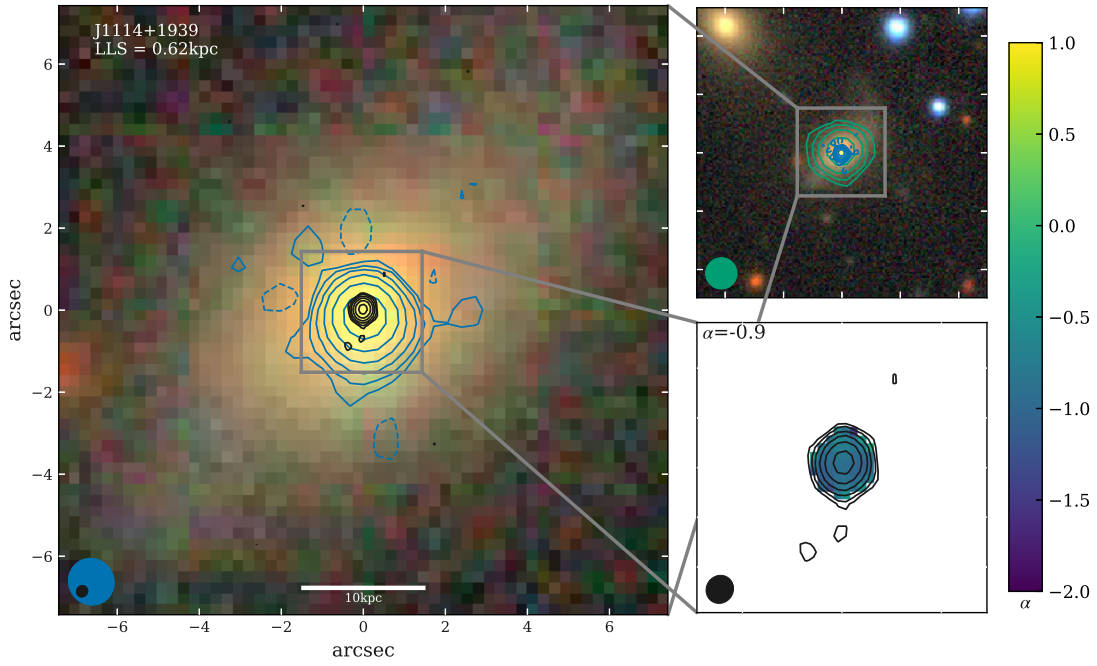

Figure C.15: As Fig. C.1 but for J1114+1939. This source shows no notable features.

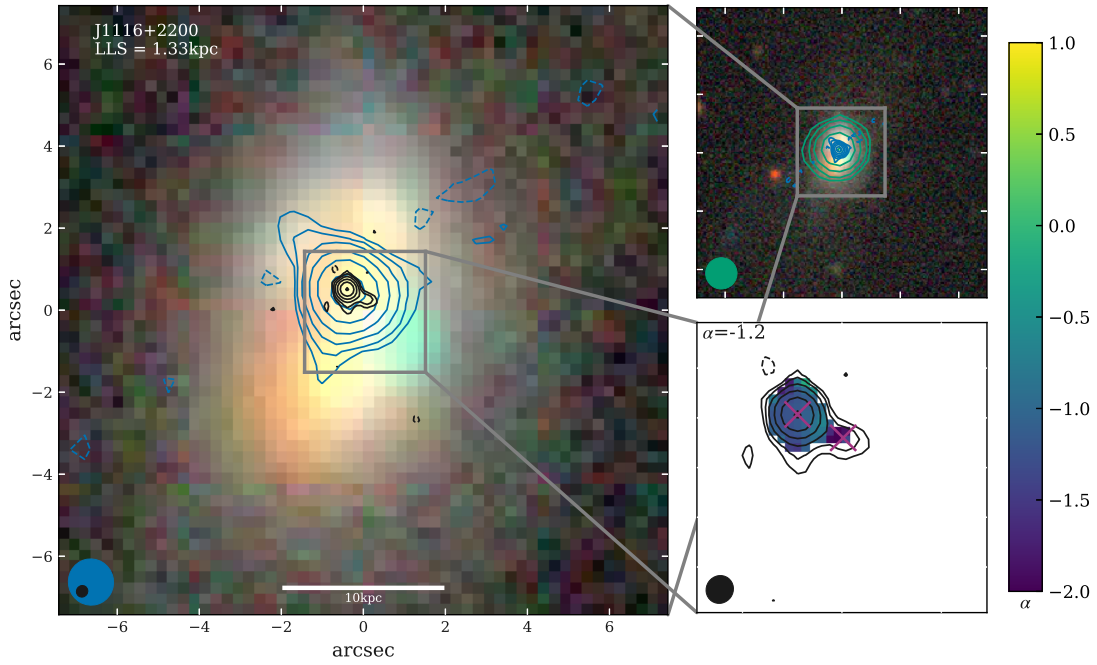

Figure C.16: As Fig. C.1 but for J1116+2200. This source is compact in all but our C-band image, where it shows a slight extension to the south-west. The origin of the radio emission in this source is unclear.

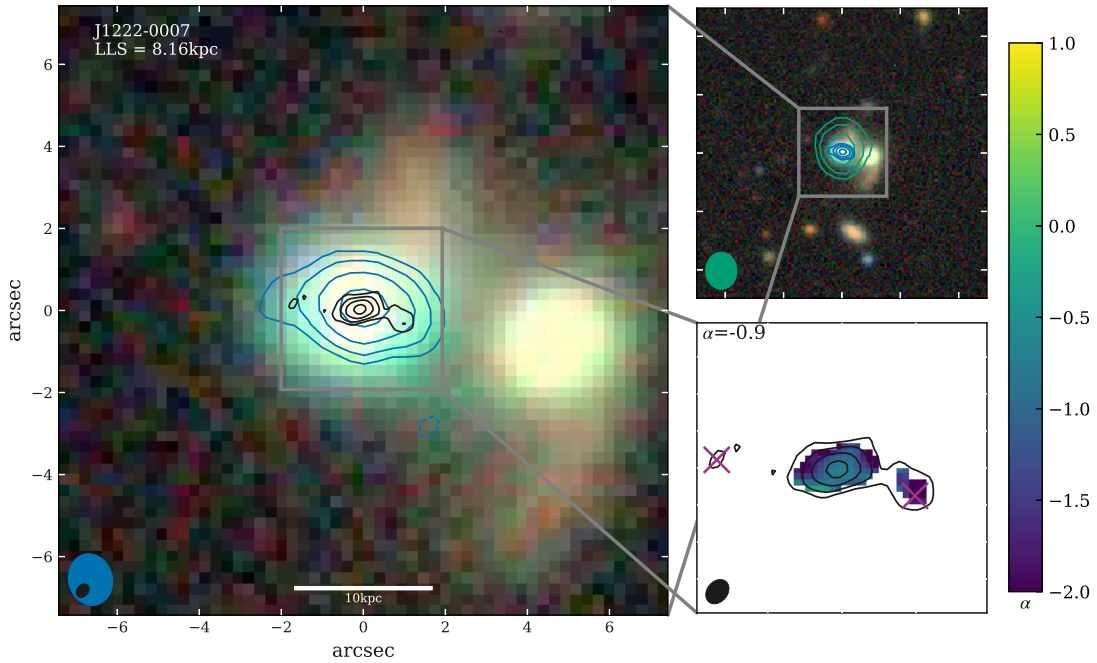

Figure C.17: As Fig. C.1 but for J1222-0007. This source is extended but with no distinct spatially resolved features in our L-band data. In the C-band it is resolved into three (low significance) features possibly showing a slight bending. Although the core component has a steep spectral index (−0.9) the morphology looks strongly like a lobe - core - lobe jet structure. More data would be needed to confirm the origin of the radio emission in this source.

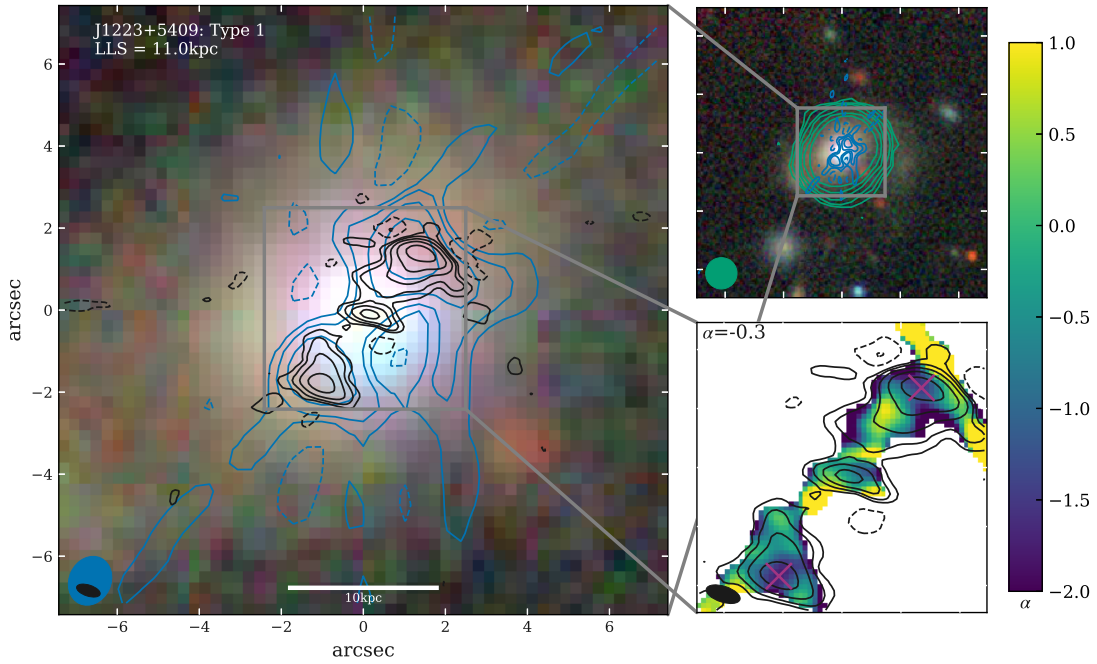

Figure C.18: As Fig. C.1 but for J1223+5409. This is one of the radio-loud sources in our sample by the Xu et al. (1999) division. Although unresolved in FIRST, it shows a distinct triple (lobe - core - lobe) morphology in both our L and C-band images, with a flat spectrum core (α=−0.3). This suggests that this source contains a radio jet.

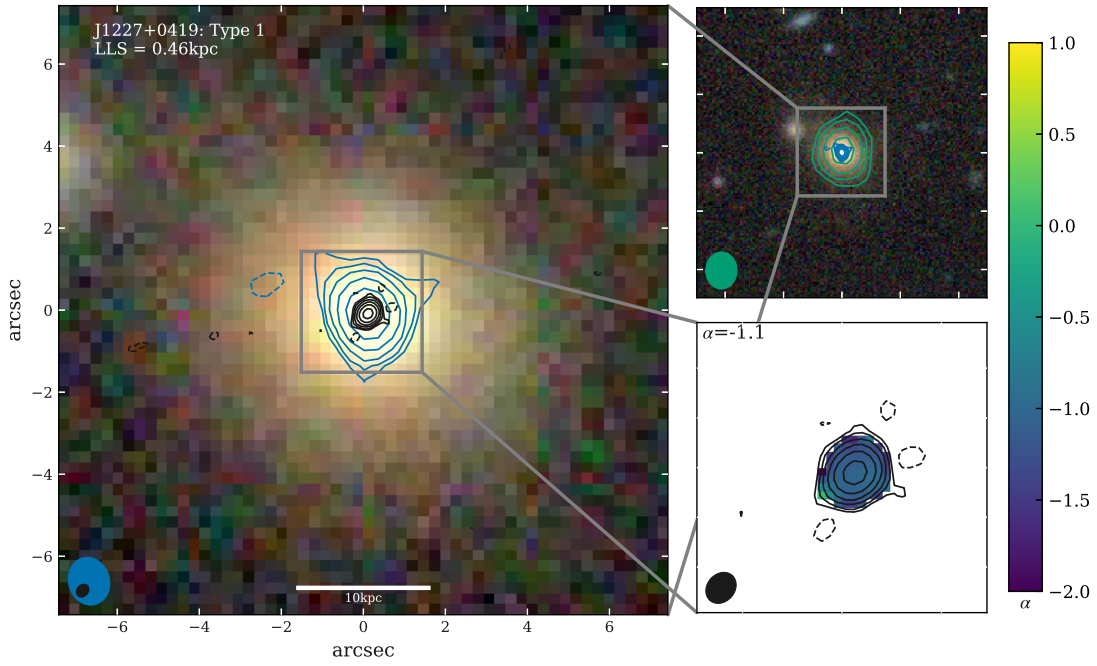

Figure C.19: As Fig. C.1 but for J1227+0419. This source shows no notable features.

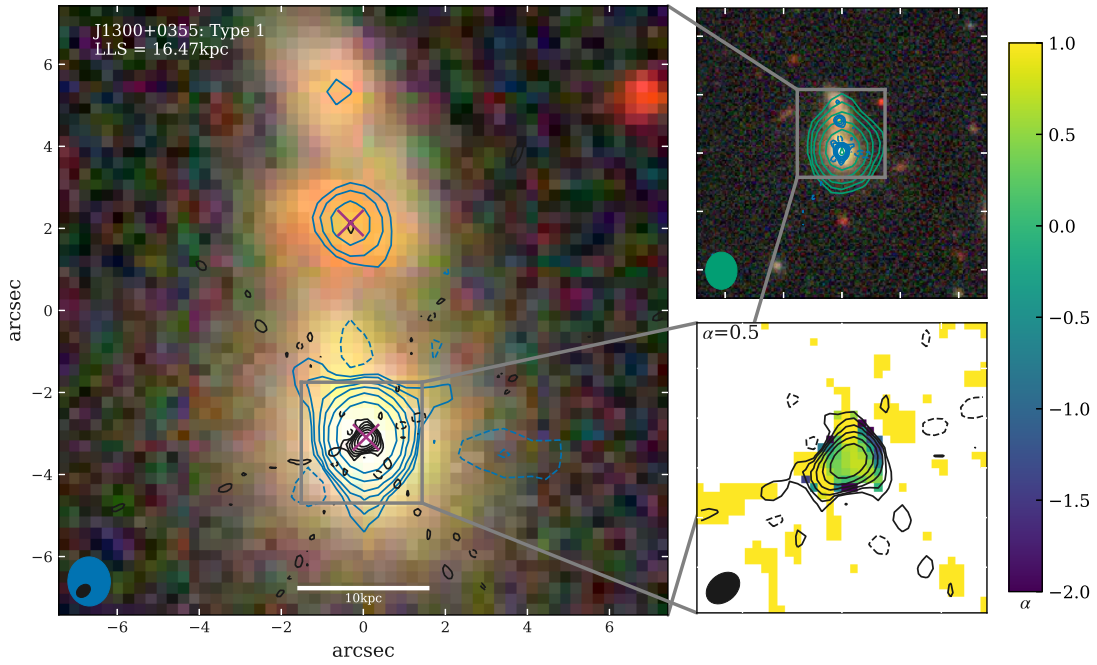

Figure C.20: As Fig. C.1 but for J1300+0355. The core of this source observed in our C-band spectral index image is inverted (α=0.5) suggesting that it is the base of a jet. Our L-band data reveals 2 additional radio components to the north, with the first 16.47 kpc from the core being additionally barely detected in our C-band data. The more distant component is only detected at 4σ in our L-band data and hence is not used to calculate the LLS of this source. Both of these radio components have distinct optical counterparts suggesting that they are related to an interacting system and are not lobes from the radio jet.

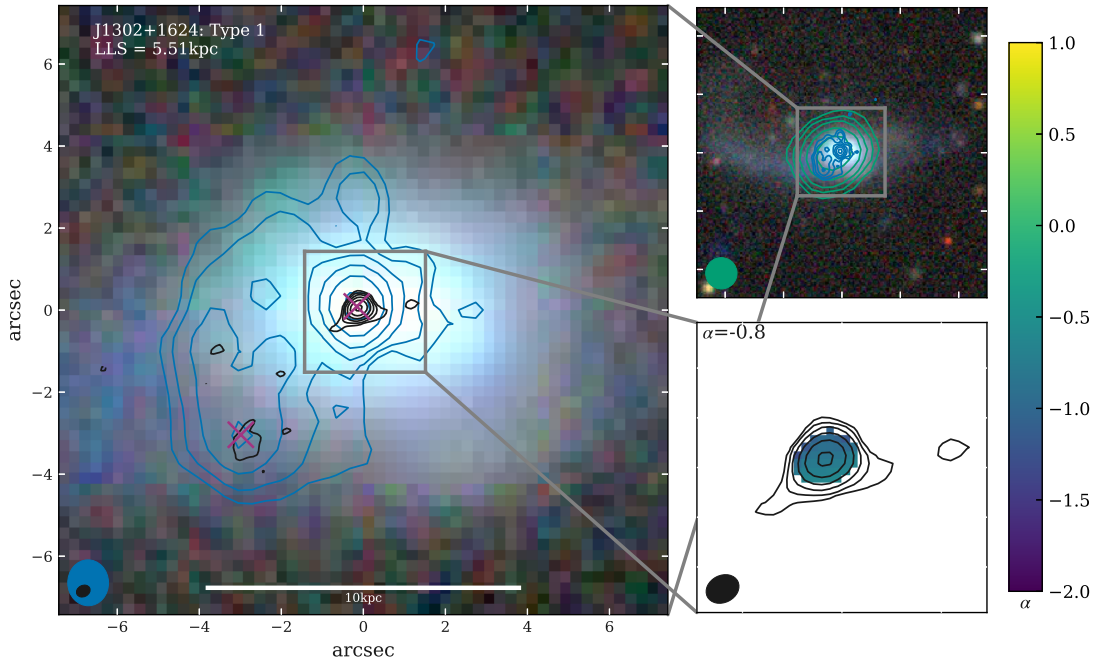

Figure C.21: As Fig. C.1 but for J1302+1624. This source shows an extended 'C' shaped structure in our L-band image, which has been previously identified as a radio relic in Congiu et al. (2017). This source has been well studied in the literature and is discussed in more detail in Section C.1.7.

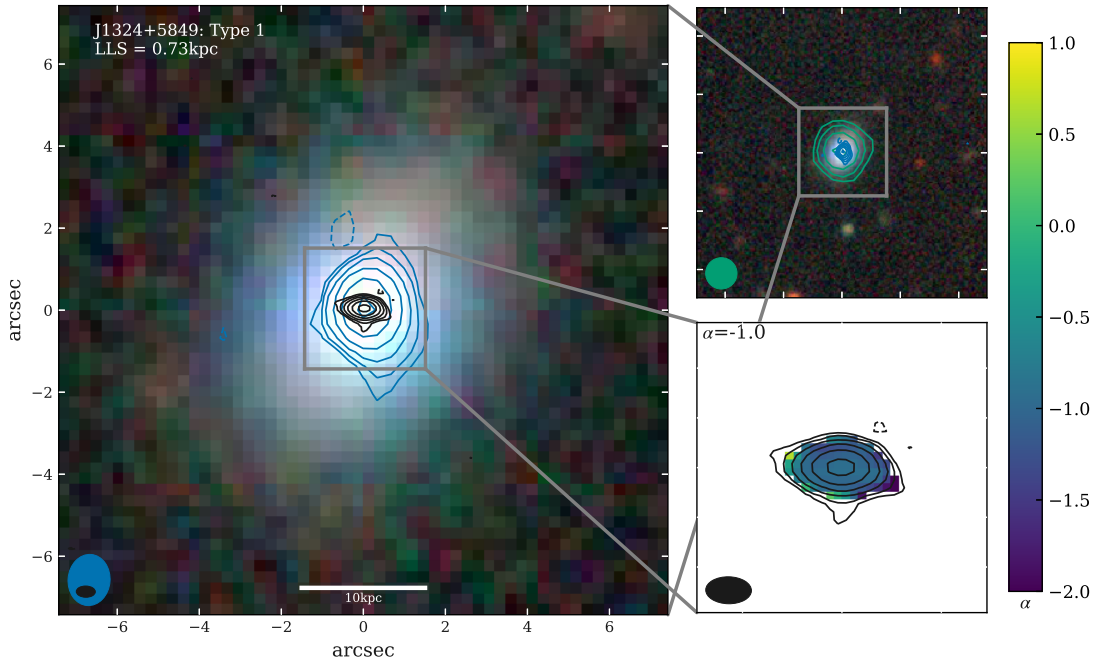

Figure C.22: As Fig. C.1 but for J1324+5849. This source shows no notable features.

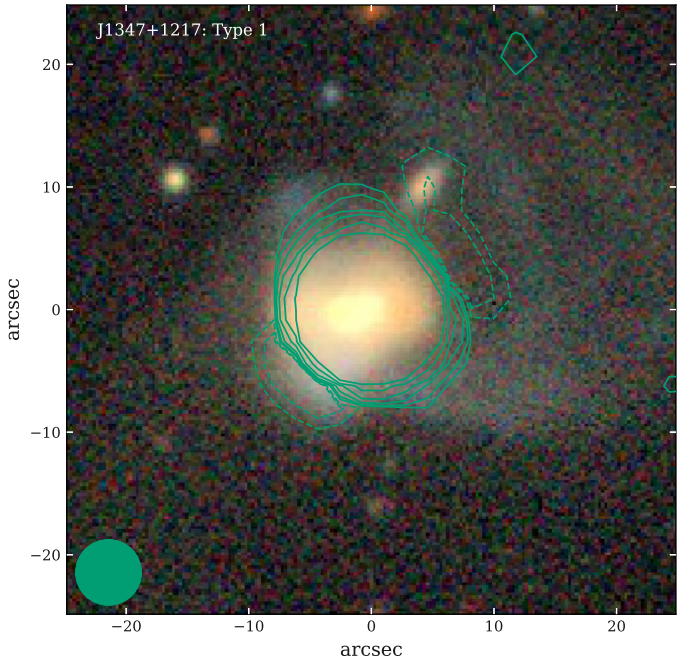

Figure C.23: For this source we show only the FIRST image (green contours) and the DESI Legacy Imaging Survey *rgb* image. It was not observed with the VLA with the remainder of the sample since it is one of the VLA calibrators. This source is discussed in more detail in Section C.1.8.

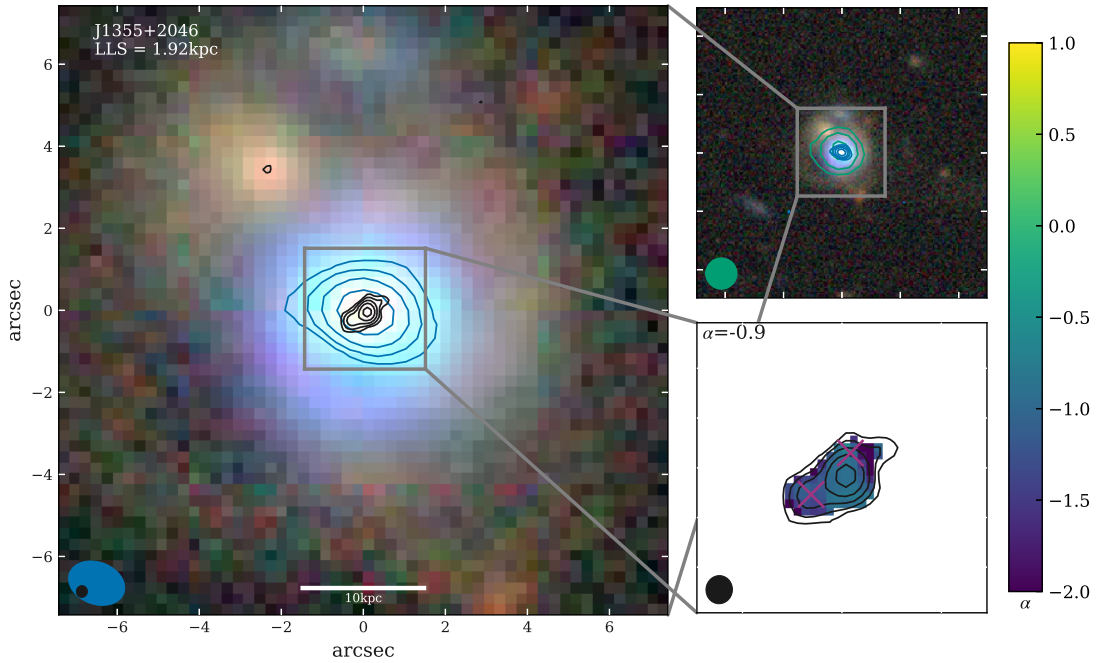

Figure C.24: As Fig. C.1 but for J1355+2046. This source is unresolved in all but our C-band image where it shows a jet-like morphology extending to the south-east with an additional, lower significance jet-like extension to the north-west. The source of these radio features is unclear.

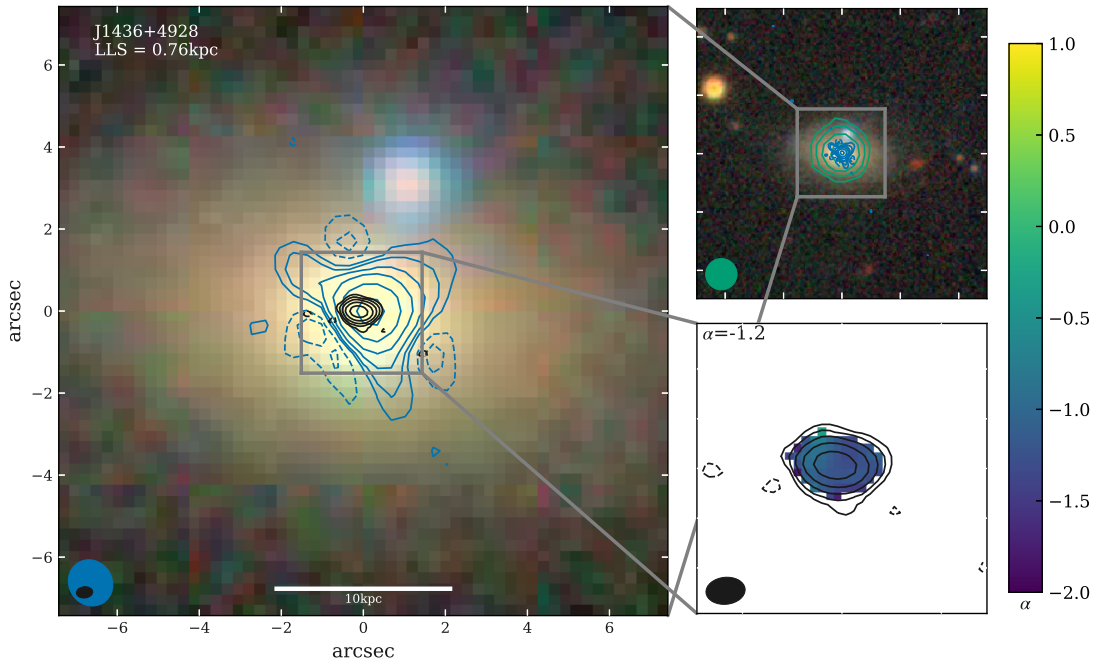

Figure C.25: As Fig. C.1 but for J1436+4928. This source shows no notable features.

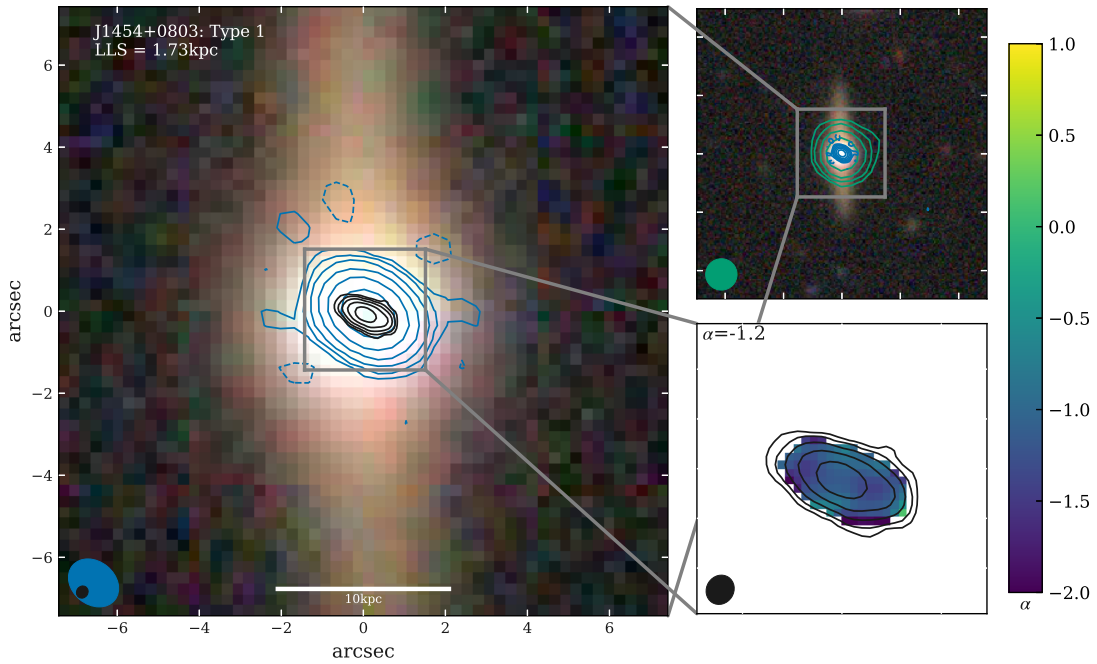

Figure C.26: As Fig. C.1 but for J1454+0803. This source shows no notable features.

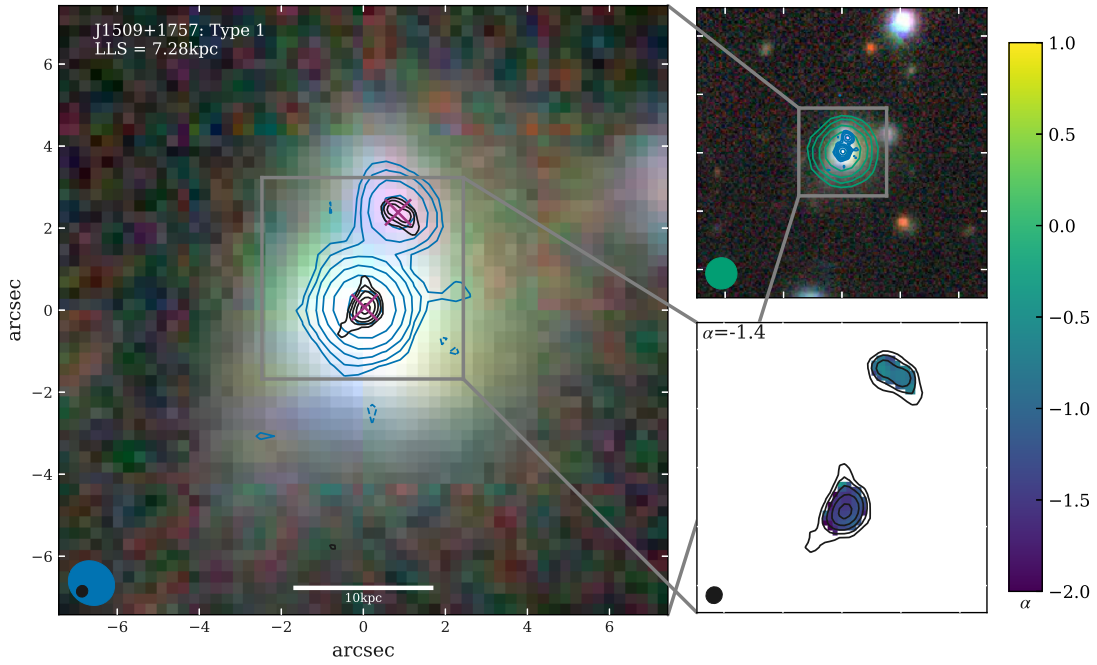

Figure C.27: As Fig. C.1 but for J1509+1757. This source shows a double peaked structure in both our L and C-band data. The potential lobe component in the north appears slightly extended and is coincident with an optically bright sub-component of the galaxy, supporting a wind or star formation explanation.

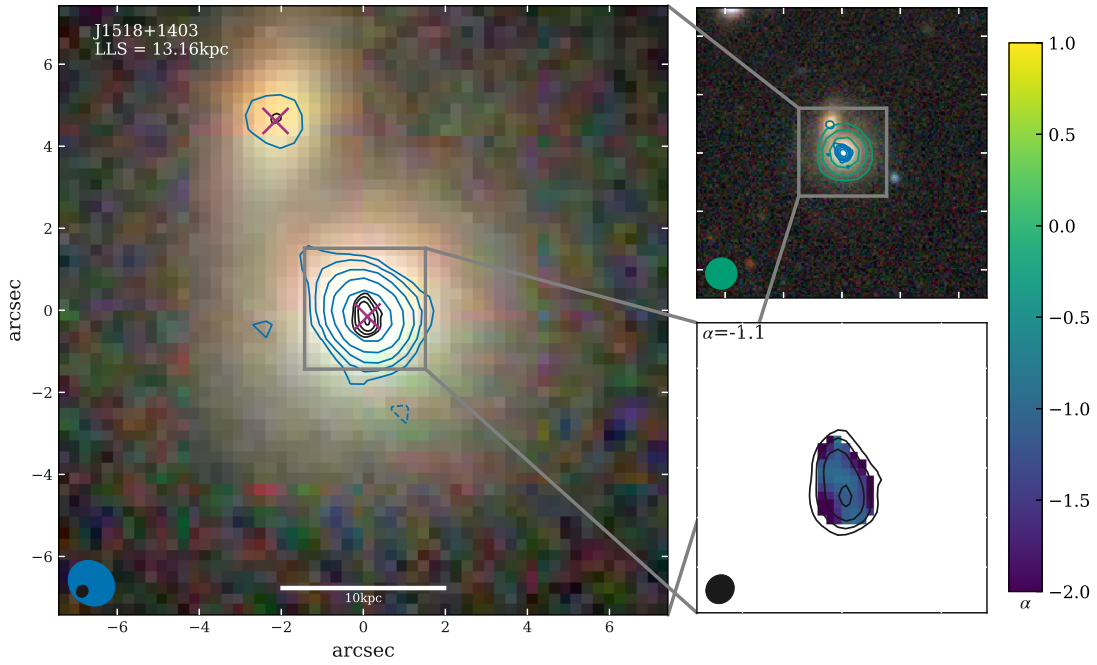

Figure C.28: As Fig. C.1 but for J1518+1403. There is a low significance feature 13.16 kpc to the north-east in our L and C-band data, coincident with a bright optical source, suggesting that this might be radio emission associated with a companion galaxy. The C-band data additionally shows a jet-like extension of the central radio emission.

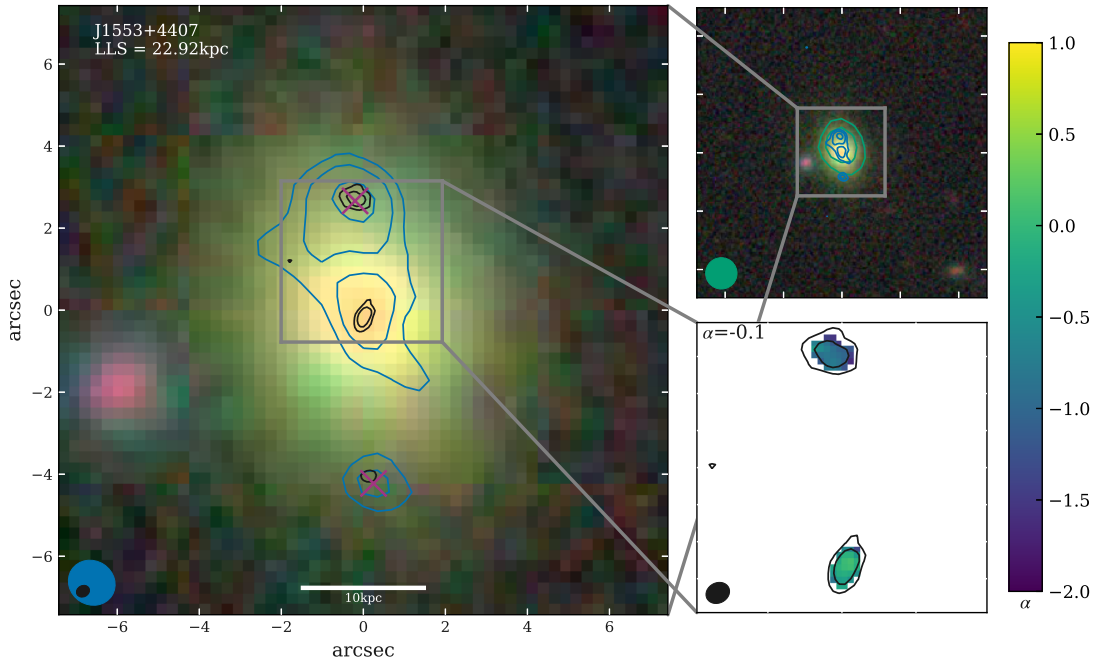

Figure C.29: As Fig. C.1 but for J1553+4407. This source source shows a classical 'triple' lobe – core – lobe structure from a radio jet in both our L and C-band data. The jet interpretation is further supported by the flat spectrum core ($\alpha = -0.1$).

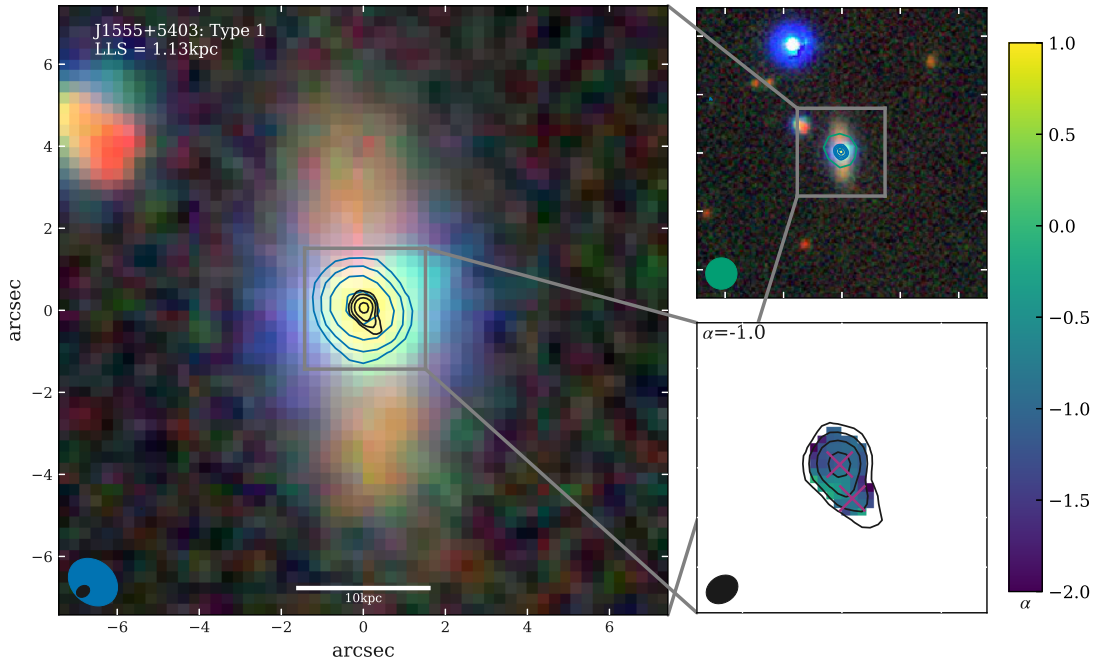

Figure C.30: As Fig. C.1 but for J1555+5403. This source has a jet-like structure in our C-band image, roughly aligned with the galactic disc. If the radio emission originates from a jet / wind driving into the disc this could explain the extreme [O III] velocities in this source (FWHM=1231 km s^{-1}).

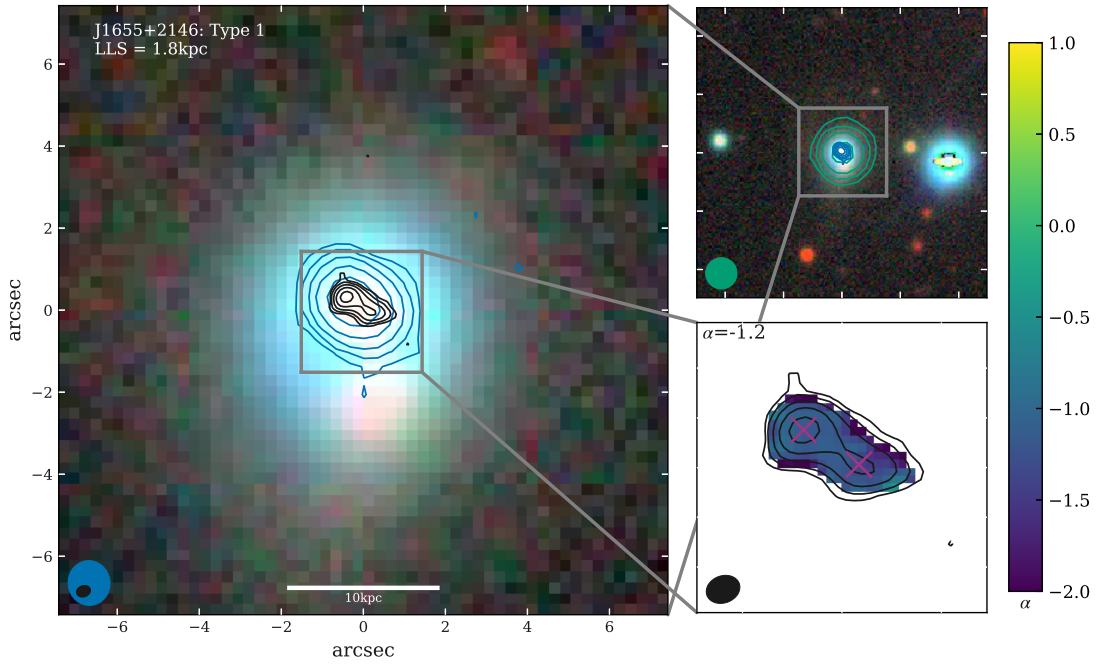

Figure C.31: As Fig. C.1 but for J1655+2146. This source is unresolved in all but our C-band image where it reveals a double peaked structure, the origin of which is unclear.

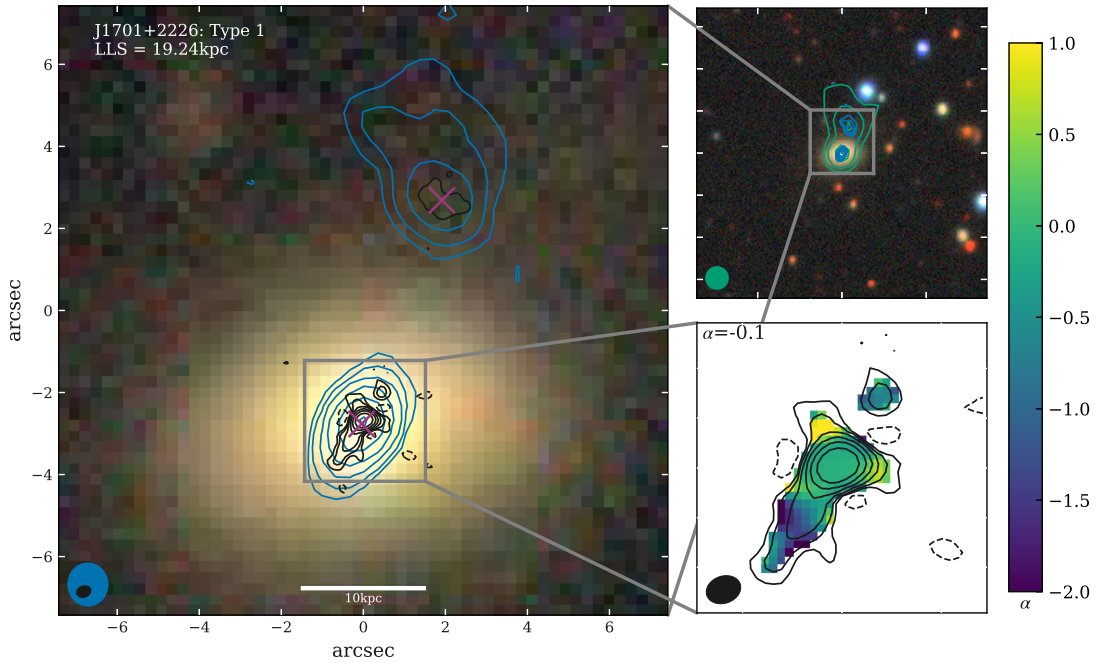

Figure C.32: As Fig. C.1 but for J1701+2226. In FIRST and our L-band data there is a peak to the north-west with diffuse emission curving up. In our C-band data the north-west peak is marginally detected and the central component is resolved into a jet-like structure with a flat spectrum core (α=−0.1). This source may be a jet, where the outer lobe is being swept back due to motion relative to an external medium (see e.g. Rudnick & Owen, 1977).

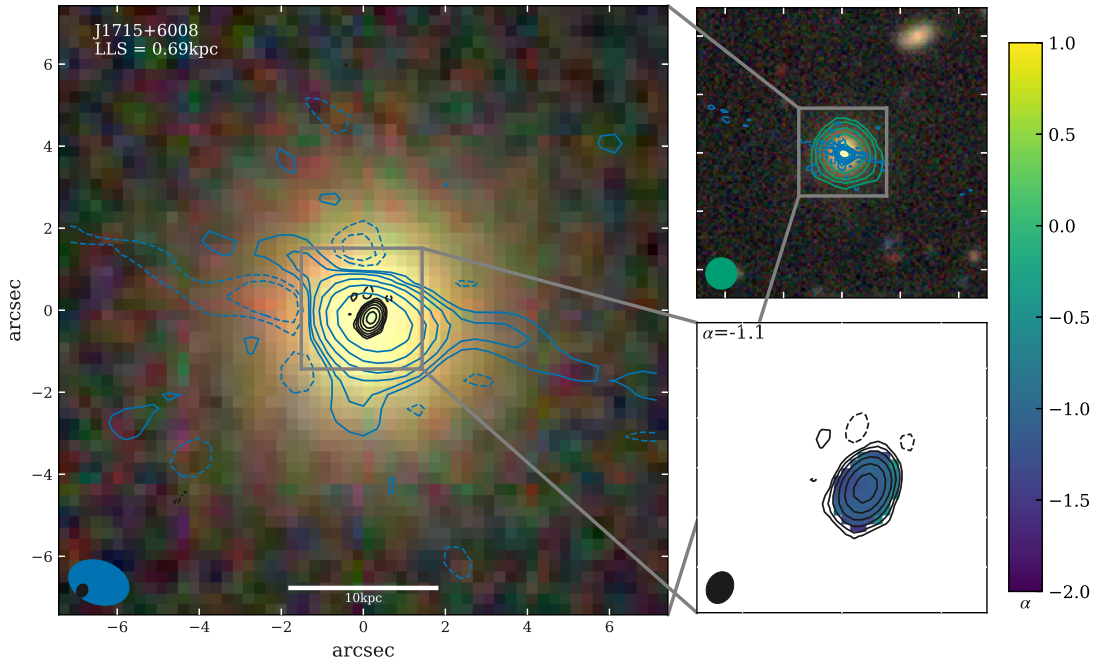

Figure C.33: As Fig. C.1 but for J1715+6008. This source shows no notable features in our radio data, however has an known jet-like structure on ~pc scales, below the spatial resolution of our data (see Section C.1.9; Müller-Sánchez et al., 2015).

Bibliography

Abazajian, K. N. et al., 2009, ApJS, 182, 543
Abolfathi, B. et al., 2018, The Astrophysical Journal Supplement Series, 235, 42
Accurso, G. et al., 2017, MNRAS, 470, 4750
Aird, J. et al., 2010, MNRAS, 401, 2531
Aird, J. et al., 2015, MNRAS, 451, 1892
Alam, S. et al., 2015, ApJS, 219, 12
Alatalo, K. et al., 2011, ApJ, 735, 88
Alexander, D. M., & Hickox, R. C., 2012, New Astronomy Review, 56, 93
Alexandroff, R. M. et al., 2016, MNRAS, 463, 3056
Alhassan, W. et al., 2018, MNRAS, 480, 2085
An, T., & Baan, W. A., 2012, ApJ, 760, 77
Argo, M., 2015, ArXiv e-prints, arXiv:1502.04936
Armus, L. et al., 2009, Publications of the ASP, 121, 559
Bae, H.-J., & Woo, J.-H., 2018, ApJ, 853, 185
Baldi, R. D. et al., 2018, MNRAS, 476, 3478
Baldwin, J. A. et al., 1981, Publications of the ASP, 93, 5
Balmaverde, B. et al., 2016, A&A, 585, A148
Barvainis, R. et al., 2005, ApJ, 618, 108
Bauermeister, A. et al., 2013, ApJ, 768, 132
Becker, R. H. et al., 1995, ApJ, 450, 559
Behar, E. et al., 2018, MNRAS, 478, 399
Belitsky, V. et al., 2018, A&A, 612, A23
Bell, E. F., 2003, ApJ, 586, 794
Bernhard, E. et al., 2019, MNRAS, 483, L52
Berton, M. et al., 2018, A&A, 614, A87
Bertram, T. et al., 2007, A&A, 470, 571
Best, P. N., & Heckman, T. M., 2012, MNRAS, 421, 1569
Best, P. N. et al., 2005, MNRAS, 362, 9
Bianchi, L. et al., 2014, Advances in Space Research, 53, 900
Bicknell, G. V. et al., 2018, MNRAS, 475, 3493
Bicknell, G. V. et al., 1997, ApJ, 485, 112
Bieri, R. et al., 2017, MNRAS, 464, 1854
Bîrzan, L. et al., 2004, ApJ, 607, 800

Bischetti, M. et al., 2019, A&A, 628, A118
Blandford, R. D., & Königl, A., 1979, ApJ, 232, 34
Blandford, R. et al., 2019, ARA&A, 57, 467
Blundell, K. M., & Beasley, A. J., 1998, MNRAS, 299, 165
Blundell, K. M., & Rawlings, S., 2001, ApJ, 562, L5
Bolatto, A. D. et al., 2013, Annual Review of Astronomy and Astrophysics, 51, 207
Bondi, M. et al., 2016, A&A, 588, A102
Bongiorno, A. et al., 2012, MNRAS, 427, 3103
Bonzini, M. et al., 2013, MNRAS, 436, 3759
Boroson, T., 2005, AJ, 130, 381
Bower, R. G. et al., 2006, MNRAS, 370, 645
Bower, R. G. et al., 2012, MNRAS, 422, 2816
Bradley, L. et al. 2019, astropy/photutils: v0.6 (Zenodo)
Braine, J. et al., 1993, A&AS, 97, 887
Briggs, D. 1995, "High Fidelity Deconvolution of Moderately Resolved Sources", -, PhD thesis (-: The New Mexico Institute of Mining and Technology, Socorro, New Mexico)
Brinchmann, J. et al., 2004, MNRAS, 351, 1151
Brinkmann, W. et al., 2000, A&A, 356, 445
Bruzual, G., & Charlot, S., 2003, MNRAS, 344, 1000
Buat, V. et al., 2015, A&A, 577, A141
Burtscher, L. et al., 2013, A&A, 558, A149
Calistro Rivera, G. et al., 2016, ApJ, 833, 98
Calistro Rivera, G. et al., 2018, ApJ, 863, 56
Callingham, J. R. et al., 2017, ApJ, 836, 174
Calzetti, D. et al., 2000, ApJ, 533, 682
Capetti, A. et al., 1996, ApJ, 469, 554
Carilli, C. L., & Barthel, P. D., 1996, A&ARv, 7, 1
Carilli, C. L., & Walter, F., 2013, ARA&A, 51, 105
Carilli, C. L. et al., 1991, ApJ, 383, 554
Carniani, S. et al., 2019, MNRAS, 489, 3939
Chabrier, G., 2003, Publications of the ASP, 115, 763
Chen, S. et al., 2020, MNRAS, 498, 1278
Choi, E. et al., 2018, ApJ, 866, 91
Churazov, E. et al., 2000, A&A, 356, 788
Churazov, E. et al., 2005, MNRAS, 363, L91
Cicone, C. et al., 2014, A&A, 562, A21
Cicone, C. et al., 2018, Nature Astronomy, 2, 176
Cielo, S. et al., 2018, MNRAS, 477, 1336
Ciesla, L. et al., 2015, A&A, 576, A10
Ciotti, L. et al., 2010, ApJ, 717, 708
Cirasuolo, M. et al., 2003, MNRAS, 341, 993
Circosta, C. et al., 2018, A&A, 620, A82
Colbert, E. J. M. et al., 1996, ApJ, 467, 551

Combes, F. et al., 2011, A&A, 528, A124
Combes, F., 1999, in H2 in Space, ed. F. Combes, & G. Pineau des Forêts, E.46
Comerford, J. M. et al., 2015, ApJ, 806, 219
Condon, J. J., 1992, ARA&A, 30, 575
Condon, J. J. et al., 1991, ApJ, 376, 95
Condon, J. J. et al., 1998, AJ, 115, 1693
Condon, J. J. et al., 2013, ApJ, 768, 37
Congiu, E. et al., 2017, A&A, 603, A32
Costa, T. et al., 2018a, MNRAS, 473, 4197
—, 2018b, MNRAS, 479, 2079
Crenshaw, D. M. et al., 2003, ARA&A, 41, 117
Cresci, G., & Maiolino, R., 2018, Nature Astronomy, 2, 179
Croton, D. J., 2009, MNRAS, 394, 1109
Croton, D. J. et al., 2006, MNRAS, 365, 11
Cui, J. et al., 2001, AJ, 122, 63
Daddi, E. et al., 2007, ApJ, 670, 173
Daddi, E. et al., 2015, A&A, 577, A46
Dale, D. A. et al., 2014, ApJ, 784, 83
Dallacasa, D. et al., 2013, MNRAS, 433, 147
Dasyra, K. M., & Combes, F., 2012, A&A, 541, L7
Dasyra, K. M. et al., 2016, A&A, 595, L7
Davies, R. et al., 2020, MNRAS
Davis, S. W., & Laor, A., 2011, ApJ, 728, 98
de Jong, T. et al., 1985, A&A, 147, L6
Del Moro, A. et al., 2013, A&A, 549, A59
Delhaize, J. et al., 2017, A&A, 602, A4
Delvecchio, I. et al., 2014, MNRAS, 439, 2736
Diemer, B. et al., 2019, MNRAS, 487, 1529
Doi, A. et al., 2013, ApJ, 765, 69
Dressler, A., 1989, in IAU Symposium, Active Galactic Nuclei, ed. D. E. Osterbrock, & J. S. Miller, Vol. 134, 217
Dubois, Y. et al., 2013, MNRAS, 433, 3297
Dunn, J. P. et al., 2010, ApJ, 709, 611
Eddington, A. S., 1916, MNRAS, 77, 16
Elbaz, D. et al., 2007, A&A, 468, 33
Elbaz, D. et al., 2011, A&A, 533, A119
Ellison, S. L. et al., 2016, MNRAS, 458, L34
Ellison, S. L. et al., 2019, MNRAS, 482, 5694
Emonts, B. H. C. et al., 2005, MNRAS, 362, 931
Fabian, A. C., 2012, ARA&A, 50, 455
Falcke, H. et al., 2000, ApJ, 542, 197
Fanaroff, B. L., & Riley, J. M., 1974, MNRAS, 167, 31P
Fanti, C. et al., 1987, A&AS, 69, 57

Faucher-Giguère, C.-A., & Quataert, E., 2012, MNRAS, 425, 605
Ferrarese, L., & Merritt, D., 2000, ApJ, 539, L9
Ferruit, P. et al., 1998, ApJ, 509, 646
Ferruit, P. et al., 1999, MNRAS, 309, 1
Feruglio, C. et al., 2010, A&A, 518, L155
Fiore, F. et al., 2017, A&A, 601, A143
Floyd, D. J. E. et al., 2006, ApJ, 639, 23
Fluetsch, A. et al., 2019, MNRAS, 483, 4586
Foreman-Mackey, D. et al., 2013, PASP, 125, 306
Forman, W. et al., 2007, ApJ, 665, 1057
Fotopoulou, C. M. et al., 2019, A&A, 629, A30
Fritz, J. et al., 2006, MNRAS, 366, 767
Gallimore, J. F. et al., 2006, AJ, 132, 546
Ganguly, R., & Brotherton, M. S., 2008, ApJ, 672, 102
García-Burillo, S. et al., 2014, A&A, 567, A125
Gaspari, M. et al., 2011, MNRAS, 411, 349
Gebhardt, K. et al., 2000, ApJ, 539, L13
Gelderman, R., & Whittle, M., 1994, ApJS, 91, 491
Genzel, R. et al., 1997, MNRAS, 291, 219
Genzel, R. et al., 2010, MNRAS, 407, 2091
Genzel, R. et al., 2012, ApJ, 746, 69
Genzel, R. et al., 2015, ApJ, 800, 20
Gillessen, S. et al., 2010, in Society of Photo-Optical Instrumentation Engineers (SPIE) Conference Series, Proceedings of the SPIE, Vol. 7734, 77340Y
Giroletti, M. et al., 2017, A&A, 600, A87
Gott J. Richard, I. et al., 2005, ApJ, 624, 463
Gravity Collaboration et al., 2018, A&A, 618, L10
Greene, J. E. et al., 2012, ApJ, 746, 86
Greene, J. E., & Ho, L. C., 2005, ApJ, 627, 721
Greene, J. E. et al., 2011, ApJ, 732, 9
Greve, T. R. et al., 2014, ApJ, 794, 142
Griffin, M. J. et al., 2010, A&A, 518, L3
Grimmett, L. P. et al., 2020, MNRAS, 495, 1392
Gruppioni, C. et al., 2008, ApJ, 684, 136
Gürkan, G. et al., 2018, MNRAS, 475, 3010
Gürkan, G. et al., 2019, A&A, 622, A11
Haardt, F., & Maraschi, L., 1991, ApJ, 380, L51
Hainline, K. N. et al., 2013, ApJ, 774, 145
Hao, C.-N. et al., 2011, ApJ, 741, 124
Harrison, C. M., 2017, Nature Astronomy, 1, 0165
Harrison, C. M. et al., 2014, MNRAS, 441, 3306
Harrison, C. M. et al., 2015, ApJ, 800, 45
Harrison, C. M. et al., 2018, Nature Astronomy, 2, 198

Harrison, C. 2014, "Observational constraints on the influence of active galactic nuclei on the evolution of galaxies", PhD thesis (Durham University)
Harwood, J. J. et al., 2017, MNRAS, 469, 639
Heckman, T. M. et al., 1981, ApJ, 247, 403
Heckman, T. M. et al., 2004, ApJ, 613, 109
Heesen, V. et al., 2014, MNRAS, 439, 1364
Helou, G. et al., 1985, ApJ, 298, L7
Henriques, B. M. B. et al., 2015, MNRAS, 451, 2663
Hickox, R. C. et al., 2009, ApJ, 696, 891
Hirschmann, M. et al., 2014, MNRAS, 442, 2304
Ho, L. C., & Ulvestad, J. S., 2001, ApJS, 133, 77
Hogan, M. T. et al., 2015, MNRAS, 453, 1201
Holt, J. et al., 2008, MNRAS, 387, 639
Holt, J. et al., 2011, MNRAS, 410, 1527
Hopkins, P. F. et al., 2006, ApJS, 163, 1
Hopkins, P. F. et al., 2010, MNRAS, 401, L19
Hopkins, P. F. et al., 2007, ApJ, 654, 731
Hovatta, T. et al., 2014, MNRAS, 439, 690
Hubble, E. P., 1926, ApJ, 64, 321
Hurley-Walker, N. et al., 2017, MNRAS, 464, 1146
Husemann, B. et al., 2013, A&A, 549, A43
Husemann, B. et al., 2016, A&A, 594, A44
Husemann, B. et al., 2017, MNRAS, 470, 1570
Hwang, H.-C. et al., 2018, MNRAS, 477, 830
Inoue, A. K., 2011, MNRAS, 415, 2920
Inoue, Y., & Doi, A., 2018, ApJ, 869, 114
Intema, H. T. et al., 2017, A&A, 598, A78
Ishibashi, W., & Fabian, A. C., 2015, MNRAS, 451, 93
Jarvis, M. E. et al., 2019, MNRAS, 485, 2710
Jarvis, M. E. et al., 2020, MNRAS, 498, 1560
Jiang, Y.-F. et al., 2010, ApJ, 711, 125
Jimenez-Gallardo, A. et al., 2019, A&A, 627, A108
Kakkad, D. et al., 2016, A&A, 592, A148
Kakkad, D. et al., 2017, MNRAS, 468, 4205
Kamenetzky, J. et al., 2016, ApJ, 829, 93
Kamenetzky, J. et al., 2017, MNRAS, 471, 2917
Kamenetzky, J. et al., 2018, ApJ, 859, 9
Kang, D., & Woo, J.-H., 2018, ApJ, 864, 124
Karouzos, M. et al., 2016, ApJ, 819, 148
Kauffmann, G. et al., 2003a, MNRAS, 341, 33
Kauffmann, G. et al., 2003b, MNRAS, 346, 1055
Kauffmann, G. et al., 2008, MNRAS, 384, 953
Keel, W. C. et al., 2015, AJ, 149, 155

Kellermann, K. I. et al., 1989, AJ, 98, 1195
Kellermann, K. I. et al., 1994, AJ, 108, 1163
Kellermann, K. I. et al., 2007, Ap&SS, 311, 231
Kennicutt Robert C., J., 1998, ApJ, 498, 541
Kennicutt Robert C., J. et al., 2009, ApJ, 703, 1672
Kennicutt, R. C., & Evans, N. J., 2012, ARA&A, 50, 531
Kewley, L. J. et al., 2001, ApJ, 556, 121
Kewley, L. J., & Ellison, S. L., 2008, ApJ, 681, 1183
Kewley, L. J. et al., 2006, MNRAS, 372, 961
Kharb, P. et al., 2006, ApJ, 652, 177
Kim, M. et al., 2020, MNRAS, 491, 4045
Kimball, A. E. et al., 2011a, AJ, 141, 182
Kimball, A. E. et al., 2011b, ApJ, 739, L29
King, A., & Pounds, K., 2015, ARA&A, 53, 115
Kirkpatrick, A. et al., 2019, ApJ, 879, 41
Komossa, S. et al., 2008, ApJ, 680, 926
Kormendy, J., 1993, in The Nearest Active Galaxies, ed. J. Beckman et al., 197
Kormendy, J., & Ho, L. C., 2013, ARA&A, 51, 511
Krips, M. et al., 2012, ApJ, 753, 135
Kukula, M. J. et al., 1998, MNRAS, 297, 366
Kukula, M. J. et al., 1995, MNRAS, 276, 1262
Kunert-Bajraszewska, M., & Labiano, A., 2010, MNRAS, 408, 2279
Labiano, A., 2008, A&A, 488, L59
Laing, R. A. et al., 2008, MNRAS, 386, 657
Lamperti, I. et al., 2020, ApJ, 889, 103
Lansbury, G. B. et al., 2018, ApJ, 856, L1
Laor, A., & Behar, E., 2008, MNRAS, 390, 847
Laor, A. et al., 2019, MNRAS, 482, 5513
Lapi, A. et al., 2014, ApJ, 782, 69
Le, H. A. N. et al., 2017, ApJ, 851, 8
Le Petit, F. et al., 2006, ApJS, 164, 506
Lehnert, M. D. et al., 2011, A&A, 532, L3
Leipski, C. et al., 2006, A&A, 455, 161
Leroy, A. K. et al., 2009, AJ, 137, 4670
Liao, M., & Gu, M., 2020, MNRAS, 491, 92
Liu, D. et al., 2019, ApJ, 887, 235
Liu, G. et al., 2013, MNRAS, 430, 2327
Lu, N. et al., 2017, ApJS, 230, 1
Lutz, D. et al., 2020, A&A, 633, A134
Madau, P., & Dickinson, M., 2014, ARA&A, 52, 415
Mahony, E. K. et al., 2013, MNRAS, 435, L58
Mancini, C. et al., 2011, ApJ, 743, 86
Maraschi, L. et al., 1992, ApJ, 397, L5

Marconi, A. et al., 2004, MNRAS, 351, 169
Marscher, A. P., 2006, in American Institute of Physics Conference Series, Relativistic Jets: The Common Physics of AGN, Microquasars, and Gamma-Ray Bursts, ed. P. A. Hughes, & J. N. Bregman, Vol. 856, 1
Martin, D. C. et al., 2005, ApJ, 619, L1
Marvil, J. et al., 2015, AJ, 149, 32
Mashian, N. et al., 2015, ApJ, 802, 81
Massaro, F. et al., 2012, ApJ, 752, 61
May, D. et al., 2018, MNRAS, 481, L105
McCarthy, I. G. et al., 2010, MNRAS, 406, 822
McNamara, B. R., & Nulsen, P. E. J., 2012, New Journal of Physics, 14, 055023
Meisenheimer, K. et al., 1989, A&A, 219, 63
Middelberg, E. et al., 2004, A&A, 417, 925
Mingozzi, M. et al., 2018, MNRAS, 474, 3640
Moe, M. et al., 2009, ApJ, 706, 525
Molyneux, S. J. et al., 2019, A&A, 631, A132
Morganti, R., 2017, Frontiers in Astronomy and Space Sciences, 4, 42
Morganti, R. et al., 2005, A&A, 439, 521
Morganti, R. et al., 2007, A&A, 476, 735
Morganti, R. et al., 2015, A&A, 580, A1
Morganti, R. et al., 2018, ArXiv e-prints, arXiv:1807.07245
Morganti, R. et al., 2016, A&A, 593, A30
Morić, I. et al., 2010, ApJ, 724, 779
Moshir, M. et al. 1992, IRAS Faint Source Survey, Explanatory supplement version 2
Mukherjee, D. et al., 2016, MNRAS, 461, 967
Mukherjee, D. et al., 2018, MNRAS, 479, 5544
Mullaney, J. R. et al., 2013, MNRAS, 433, 622
Müller-Sánchez, F. et al., 2015, ApJ, 813, 103
Murray, N. et al., 2005, ApJ, 618, 569
Narayanan, D., & Krumholz, M. R., 2014, MNRAS, 442, 1411
Neff, S. G., & de Bruyn, A. G., 1983, A&A, 128, 318
Nesvadba, N. P. H. et al., 2017, A&A, 599, A123
Netzer, H., 1990, in Active Galactic Nuclei, ed. R. D. Blandford et al., 57
Neugebauer, G. et al., 1984, ApJ, 278, L1
Nims, J. et al., 2015, MNRAS, 447, 3612
Noeske, K. G. et al., 2007, ApJ, 660, L43
Nolan, P. L. et al., 2012, ApJS, 199, 31
Noll, S. et al., 2009, A&A, 507, 1793
Ocaña Flaquer, B. et al., 2010, A&A, 518, A9
O'Dea, C. P., 1998, Publications of the ASP, 110, 493
O'Dea, C. P. et al., 1991, ApJ, 380, 66
Oosterloo, T. et al., 2019, A&A, 632, A66
Orienti, M., 2016, Astronomische Nachrichten, 337, 9

Orienti, M., & Dallacasa, D., 2014, MNRAS, 438, 463
Padovani, P., 2016, A&ARv, 24, 13
—, 2017, Nature Astronomy, 1, 0194
Padovani, P. et al., 2011, ApJ, 740, 20
Padovani, P. et al., 2015, MNRAS, 452, 1263
Padovani, P. et al., 2017, A&ARv, 25, 2
Panessa, F. et al., 2015, MNRAS, 447, 1289
Panessa, F. et al., 2019, Nature Astronomy, 3, 387
Papadopoulos, P. P. et al., 2010, ApJ, 715, 775
Papadopoulos, P. P., 2010, ApJ, 720, 226
Papadopoulos, P. P. et al., 2012, MNRAS, 426, 2601
Pedlar, A. et al., 1989, MNRAS, 238, 863
Pereira-Santaella, M. et al., 2013, ApJ, 768, 55
Perna, M. et al., 2015, A&A, 574, A82
Perna, M. et al., 2018, A&A, 619, A90
Peterson, B. M. et al., 2004, ApJ, 613, 682
Pettini, M., & Pagel, B. E. J., 2004, MNRAS, 348, L59
Pierce, J. C. S. et al., 2020, MNRAS, 494, 2053
Pilbratt, G. L. et al., 2010, A&A, 518, L1
Poglitsch, A. et al., 2010, A&A, 518, L2
Preuss, E., & Fosbury, R. A. E., 1983, MNRAS, 204, 783
Raginski, I., & Laor, A., 2016, MNRAS, 459, 2082
Ramakrishnan, V. et al., 2019, MNRAS, 487, 444
Renzini, A., & Peng, Y.-j., 2015, ApJ, 801, L29
Reyes, R. et al., 2008, AJ, 136, 2373
Reynolds, S. P., 1982, ApJ, 256, 13
Richards, G. T. et al., 2006, ApJS, 166, 470
Richings, A. J., & Faucher-Giguère, C.-A., 2018, MNRAS, 478, 3100
Riffel, R. A. et al., 2014, ApJ, 780, L24
Rodighiero, G. et al., 2011, ApJ, 739, L40
Rodighiero, G. et al., 2019, ApJ, 877, L38
Rodríguez-Ardila, A. et al., 2017, MNRAS, 470, 2845
Rodríguez Zaurín, J. et al., 2013, MNRAS, 432, 138
Roettiger, K. et al., 1994, ApJ, 421, L23
Romero, G. E. et al., 2017, Space Science Reviews, 207, 5
Rosario, D. J. et al., 2010, ApJ, 716, 131
Rosario, D. J. et al., 2018, MNRAS, 473, 5658
Rosenberg, M. J. F. et al., 2015, ApJ, 801, 72
Rudnick, L., & Owen, F. N., 1977, AJ, 82, 1
Rupke, D. S. N., & Veilleux, S., 2013, ApJ, 768, 75
Rupke, D. S. N., & Veilleux, S., 2011, ApJ, 729, L27
Sabater, J. et al., 2019, A&A, 622, A17
Saez, C. et al., 2009, ApJ, 697, 194

Saintonge, A. et al., 2017, ApJS, 233, 22
Salim, S. et al., 2007, ApJS, 173, 267
Salomé, Q. et al., 2017, A&A, 608, A98
Salvato, M. et al., 2004, ApJ, 600, L31
Sanders, D. B. et al., 1988, ApJ, 325, 74
Sandstrom, K. M. et al., 2013, ApJ, 777, 5
Santini, P. et al., 2015, ApJ, 801, 97
Sargent, M. T. et al., 2014, ApJ, 793, 19
Sauvage, M., & Thuan, T. X., 1992, ApJ, 396, L69
Scannapieco, E., 2017, ApJ, 837, 28
Schawinski, K. et al., 2007, MNRAS, 382, 1415
Schaye, J. et al., 2015, MNRAS, 446, 521
Schiminovich, D. et al., 2007, ApJS, 173, 315
Schirmer, M. et al., 2013, ApJ, 763, 60
Schlafly, E. F., & Finkbeiner, D. P., 2011, ApJ, 737, 103
Schmidt, M., 1963, Nature, 197, 1040
Schmitt, H. R. et al., 2001, ApJS, 132, 199
Scholtz, J. et al., 2018, MNRAS, 475, 1288
Schreiber, C. et al., 2015, A&A, 575, A74
Schulze, A. et al., 2019, MNRAS, 488, 1180
Shakura, N. I., & Sunyaev, R. A., 1973, A&A, 500, 33
Shangguan, J. et al., 2020, ApJS, 247, 15
Shankar, F. et al., 2009, ApJ, 690, 20
Shi, Y. et al., 2007, ApJ, 669, 841
Shimizu, T. T. et al., 2017, MNRAS, 466, 3161
Shin, J. et al., 2019, ApJ, 881, 147
Silk, J., & Rees, M. J., 1998, A&A, 331, L1
Simpson, J. M. et al., 2012, MNRAS, 426, 3201
Skrutskie, M. F. et al., 2006, AJ, 131, 1163
Sol, H. et al., 1989, MNRAS, 237, 411
Solomon, P. M. et al., 1997, ApJ, 478, 144
Soltan, A., 1982, MNRAS, 200, 115
Somerville, R. S. et al., 2008, MNRAS, 391, 481
Speagle, J. S. et al., 2014, ApJS, 214, 15
Stanghellini, C. et al., 1998, A&AS, 131, 303
Steffen, W. et al., 1997, ApJ, 491, L73
Stern, D. et al., 2005, ApJ, 631, 163
Stockton, A., 1976, ApJ, 205, L113
Suh, H. et al., 2019, ApJ, 872, 168
Sun, A.-L. et al., 2014, ApJ, 790, 160
Sun, A.-L. et al., 2017, ApJ, 835, 222
Tacconi, L. J. et al., 2018, ApJ, 853, 179
Tadhunter, C. N. et al., 1989, MNRAS, 240, 225

Tadhunter, C., 2016, A&ARv, 24, 10
Taylor, P., & Kobayashi, C., 2015, MNRAS, 448, 1835
Thompson, T. A. et al., 2005, ApJ, 630, 167
Thompson, T. A. et al., 2015, MNRAS, 449, 147
Tombesi, F. et al., 2012, MNRAS, 422, L1
Tremonti, C. A. et al., 2004, ApJ, 613, 898
Ulvestad, J. S., & Wilson, A. S., 1983, ApJ, 264, L7
Ulvestad, J. S. et al., 1981, ApJ, 247, 419
Ulvestad, J. S. et al., 2005, ApJ, 621, 123
Urry, C. M., & Padovani, P., 1995, Publications of the ASP, 107, 803
Vallini, L. et al., 2019, MNRAS, 490, 4502
van Breugel, W. et al., 1984, AJ, 89, 5
van der Werf, P. P. et al., 2010, A&A, 518, L42
Vassilev, V. et al., 2008, A&A, 490, 1157
Veilleux, S. et al., 2013, ApJ, 776, 27
Veilleux, S. et al., 2020, A&ARv, 28, 2
Veron, M. P., 1981, A&A, 100, 12
Villar-Martín, M. et al., 2013, MNRAS, 434, 978
Villar Martín, M. et al., 2014, MNRAS, 440, 3202
Villar-Martín, M. et al., 2018, MNRAS, 474, 2302
Vogelsberger, M. et al., 2014, Nature, 509, 177
Wagner, A. Y. et al., 2012, ApJ, 757, 136
Walcher, J. et al., 2011, Ap&SS, 331, 1
Wang, L. et al., 2014, MNRAS, 442, 2739
Wang, R. et al., 2006, ApJ, 645, 890
Weedman, D. W., 1970, ApJ, 159, 405
Weiß, A. et al., 2005, A&A, 438, 533
Whitaker, K. E. et al., 2014, ApJ, 795, 104
White, S. V. et al., 2017, MNRAS, 468, 217
Whittle, M., & Wilson, A. S., 2004, AJ, 127, 606
Whittle, M. et al., 1986, MNRAS, 222, 189
Wright, E. L. et al., 2010, AJ, 140, 1868
Wu, X.-B. et al., 2015, Nature, 518, 512
Wyder, T. K. et al., 2007, ApJS, 173, 293
Wylezalek, D., & Morganti, R., 2018, Nature Astronomy, 2, 181
Wylezalek, D., & Zakamska, N. L., 2016, MNRAS, 461, 3724
Wylezalek, D. et al., 2017, MNRAS, 467, 2612
Xia, X. Y. et al., 2012, ApJ, 750, 92
Xu, C. et al., 1999, AJ, 118, 1169
York, D. G. et al., 2000, AJ, 120, 1579
Yun, M. S. et al., 2001, ApJ, 554, 803
Zakamska, N. L., & Greene, J. E., 2014, MNRAS, 442, 784
Zakamska, N. L. et al., 2016, MNRAS, 455, 4191

Zakamska, N. L. et al., 2004, AJ, 128, 1002
Zhang, C.-P. et al., 2019, A&A, 631, A110
Zhang, K. et al., 2011, ApJ, 737, 71
Zubovas, K., & King, A., 2012, ApJ, 745, L34

Acknowledgements

I am extremely grateful to Chris Harrison and Vincenzo Mainieri for supervising this PhD and all of the help, support and guidance they have offered along the way. I couldn't have asked for better supervisors. Thanks also to Eiichiro Komatsu for being my official supervisor at MPA and opening doors for me when one was closed. Thank you to the rest of my PhD defence committee for volunteering their time for me. I'd also like to thank all of my co-authors on my papers and co-Investigators on my telescope proposals for all of their feedback and help.

I would not have been able to do this without the friendship and support of my fellow astronomy PhD students (and similar such folk) in Munich. I'm afraid that if I tried naming them all I'd miss someone and be terribly embarrassed so I'll limit this to the few who helped me proof read this thesis in order of the sections they edited: Simon, Aoife, Max, Stephen, Aishwarya and Rob. I'd also like to thank everyone who organised or came to the weekly MPA and ESO game nights, which were always a high point of my week.

Finally I'd like to thank my family, especially my parents for always believing in me and being there when I needed them. I've missed you so much these years in Germany! And special thanks to my amazing Julian for loving me and being there for me these last 4+ years and putting up with all my moods and thesis writing stress!